Multi-Field Modelling and Simulation of the Human Hip Joint

Von der Fakultät Bau- und Umweltingenieurwissenschaften
der Universität Stuttgart zur Erlangung der Würde
eines Doktor-Ingenieurs (Dr.-Ing.)
genehmigte Abhandlung

Vorgelegt von

DDipl.-Ing. Joffrey Mabuma

aus

Lille, Frankreich

Hauptberichter: Prof. Dr.-Ing. Wolfgang Ehlers
1. Mitberichter: Prof. Dr.-Ing. Bernd Markert
2. Mitberichter: Prof. Dr.-Ing. Udo Nackenhorst

Tag der mündlichen Prüfung: 31. Juli 2014

Institut für Mechanik (Bauwesen) der Universität Stuttgart
Lehrstuhl für Kontinuumsmechanik
Prof. Dr.-Ing. W. Ehlers
2014

Report No. II-28
Institut für Mechanik (Bauwesen)
Lehrstuhl für Kontinuumsmechanik
Universität Stuttgart, Germany, 2014

Editor:
Prof. Dr.-Ing. W. Ehlers

Institut für Mechanik (Bauwesen)
Lehrstuhl für Kontinuumsmechanik
Universität Stuttgart
Pfaffenwaldring 7
70569 Stuttgart, Germany

Printed by DIP – Digital Print, Witten, Germany, 2014

ISBN 978 – 3 – 937399 – 28 – 3
(D 93 – Dissertation, Universität Stuttgart)

Acknowledgements

The work presented in this thesis was carried out in the years between 2009 and 2014 when I was working as a research associate and a doctoral candidate at the Institute of Applied Mechanics (Civil Engineering) at the University of Stuttgart. In the following, I would like to thank the people who contributed directly or indirectly to my work.

First of all, a thank you to my supervisor, Professor Wolfgang Ehlers for giving me the opportunity to work on my thesis at the institute and for his guidance, particularly at the end of my research. His major works in the field of continuum mechanics were essential foundations of this thesis. Furthermore, I owe my gratitude to my co-supervisor, Professor Bernd Markert for his active interest in my work and his substantial contribution to my progress in solving complex problems. I am also very grateful to Professor Udo Nackenhorst for taking the co-chair in my promotion procedure.

Then, I would like to acknowledge the associated research units of Professor Udo Nackenhorst (Leibniz University of Hannover), PD Christof Hurschler (Medical School of Hannover) and Professor Fritz Schick (University Hospital of Tübingen) for the collaboration during the research project funded by the German Research Foundation (DFG).

Next, I want to thank all my fellow workers at the institute for the very friendly atmosphere and the many interesting discussions we had on theoretical and numerical fundamentals. Special thanks to Dr. rer. nat Rudolf Jäger and Seyedmohammad Zinatbakhsh for the fruitful scientific cooperation.

Last but not least, I would like to express my durable affection to my siblings and my mother for their support all over the years. Finally, my dear father who always boosted me, is probably the very essence of my motivation in life.

Stuttgart, August 2014 Joffrey Mabuma

"Wisdom is like a baobab tree; no one individual can embrace it." (African Proverb)

Contents

Deutschsprachige Zusammenfassung

Motivation

Die langsame Selbstheilungs- und Regenerationsfähigkeit des Knorpels ist ein aktuelles Problem in der Biomechanik. Grund dafür ist, dass Knorpelgewebe sehr anfällig gegen Degenerierung ist, was zu starken Schmerzen und Arbeitsunfähigkeit bei Menschen mittleren und höheren Alters führt. Insbesondere ist die Osteoarthrose (OA) eine verbreitete Form der Knorpeldegenerierung, an der weltweit etwa 630 Millionen Menschen leiden, was 15% der gesamten Weltbevölkerung entspricht.

Das Robert-Koch-Institut für Gesundheit berichtet, dass in Deutschland über 1,6% der unter dreißigjährigen Menschen Symptome der OA aufweisen. Bis zum 50. Lebensjahr erreicht die Prävalenz von OA 14,9% und nach dem 60. Lebensjahr ist ein Drittel der weiblichen Bevölkerung und ein Viertel der männlichen Bevölkerung davon betroffen. Außerdem sind die eingetragenen OA-Fälle zwischen 2003 und 2010 von 22,6% auf 27,1% bei Frauen und von 15,5% auf 17,9% bei Männern gestiegen. Dieser deutliche Anstieg der OA-Fälle ist eng mit der Kostenerhöhung des Gesundheitssystems verbunden. Im Jahr 2004 belegten Krankheiten des Muskelknochensystems den dritten Platz in Bezug auf die verursachten Kosten von 24,46 Milliarden Euro nach den Herz-Kreislauf-Erkrankungen und Verdauungsstörungen. Von den Kosten der Muskelknochensystem-Erkrankungen beziehen sich 6,77 Milliarden Euro auf die OA. Außerdem lassen sich 39% der Arbeitsunfähigkeitsfälle wegen OA im Jahr 2012 auf OA im Hüftgelenk zurückführen.

Eines der Ziele dieser Arbeit besteht darin, dem Arzt eine neuartige Möglichkeit zu bieten, die Diagnose zu sichern. Zu diesem Zweck wurde ein numerisches Werkzeug entwickelt, um eine korrekte Darstellung des OA-Vorkommens und den Einfluss auf die Hüftgelenkanatomie zu gewährleisten. Dies setzt eine geometrisch und konstitutiv hochkomplexe Modellierung voraus, um die *In-vivo*-Eigenschaften, die entsprechenden Randbedingungen sowie die Beschreibung des anisotropen und heterogenen hydratisierten Weichgewebes darstellen zu können. Hierzu wird ein thermodynamisch konsistentes Modell im Rahmen der Theorie Poröser Medien (TPM) vorgestellt und für den speziellen Fall eines Knorpelgewebes angepasst.

Dies führt zum zweiten Ziel der Arbeit, der Ausarbeitung einer konsistenten Kalibrierungsstrategie für das komplexe Rechenmodell. Im Rahmen der vorgestellten Kalibrierungsmethode werden wichtige Fragen über die Parameterindentifizierungstechniken und die Sensitivität des erhaltenen Satzes von Materialparametern angesprochen. Danach liegt der Fokus auf der Berücksichtigung von realen Randbedingungen für die Knorpeloberfläche des Femurkopfes. In diesem Zusammenhang werden die Kontaktspannungen an der Oberfläche untersucht, um den Einfluss der OA während normaler und pathologischer Ganganalysen auszuwerten.

Zielsetzung und Vorgehensweise

Modellierung des Knorpelgewebes

Seit langer Zeit interessieren sich die Wissenschaftler für die experimentelle Erforschung (Benninghoff [22], Maroudas [178]) und die Modellierung von Knorpel. Typischerweise sind Einzelphasenmodelle (Hayes *et al.* [109]) für die Modellierung des Knorpelgewebes verwendet worden. Diese Modellierungsart sorgt für eine starke Vereinfachung der Knorpelstruktur und seiner Eigenschaften. Der Fokus dieser Arbeit liegt in den Mehrphasenmodellen, welche immer mehr Popularität gewinnen. Im Allgemeinen basieren diese Modelle auf der Mischungstheorie (Lai *et al.* [152]) oder auf einer verfeinerten Version, der Theorie der Porösen Medien (TPM) (de Boer [30, 31], Bowen [34, 35], Ehlers [68-72]). Insbesondere schlagen Lai *et al.* [152] ein erstes Dreiphasenmodell vor, in dem Eigenschaften wie elektro-chemische Effekte schon berücksichtigt werden. Dieses Modell beruht auf einer getrennten Beschreibung der Festkörper- und der Flüssigkeitsphase, die anhand der Elektroneutralitätsbedingung vereinfacht wird. Weitere Dreiphasenmodelle sind aus dieser Darstellung (Frijns *et al.* [92], Acartürk *et al.* [3]) entstanden. Durch die *Lanir*sche Annahme (Lanir [154]) werden weitere Modellreduzierungen möglich, zum Beispiel Zweiphasenmodelle, die als weniger rechenintensiv gelten (Mow *et al.* [190], Huang *et al.* [124], Wieners *et al.* [253], Julkunen *et al.* [132], Karajan *et al.* [139]). Diese Modelle sind auch in Stande, osmotische Effekte zu beschreiben, die Quell- und Schrumpfprozesse hervorrufen. Zweiphasenmodelle werden auch intensiv verwendet, um Kriech- und Relaxationsverhalten im Knorpel zu simulieren. Insbesondere werden Modelle, die in der Lage sind, Kriechphänomene zu beschreiben, als poroviskoelastische Modelle (Ehlers & Markert [75], Julkunen *et al.* [133], Markert [174], Suh & Bai [239]) durch Mak [169] eingeführt.

Die Modelle von Li *et al.* [158], Wieners *et al.* [253] und Julkunen *et al.* [132] erweitern noch die numerische Darstellung von Knorpelgeweben durch das Einbeziehen von Heterogenitätseigenschaften. Basierend auf der TPM erstellen Ehlers *et al.* [73, 76–78] ein thermodynamisch konsistentes Modell für die menschliche Bandscheibe, das größenteils die oben genannten Eigenschaften berücksichtigt. Zur gleichen Zeit entwickelten die Forschungsgruppen von Julkunen *et al.* [133] und Lilledahl *et al.* [162] unterschiedliche Knorpelmodelle. In Lilledahl *et al.* [162] wurden wichtige Knorpeleigenschaften wie Kollagenfaseranordnung, ortsabhängige Heterogenitäten und anisotrope Permeabilität genau ermittelt.

Parameteridentifizierung

Im Wandel der Zeiten sind Materialmodelle eindeutig komplexer geworden. Eine hohe Modellkomplexität sorgt zwar für eine bessere Materialbeschreibung, hat aber auch Nachteile. Die Rechenzeit kann aufgrund des umfangreichen experimentellen Datensatzes für die Identifizierung problematisch sein. Eine weitere Überlegung bezieht sich auf die Anwendbarkeit solcher komplexen Modelle. Was ist die optimale Modellkomplexität? Welche gemessenen Effekte müssen untersucht werden? Welche Parameter sind nicht relevant und gehören somit nicht zum reduzierten Modell? Basierend auf der Nichtlinearität des Problems und der Anforderung eines Anfangsparametersatzes werden unterschiedliche Methoden angewandt, um diese Fragen zu beantworten. Im Rahmen dieser Arbeit wird eine gradienten-freie Optimierungstechnik basierend auf der COBYLA *Trust-region*-Methode von Powell [210] verwendet. Diese Methode beruht auf der Konstruktion eines quadratischen Modells für den Parameterraum anhand eines ausgesuchten Radius' (die *Trust*-Region). Diese Region breitet sich aus oder schrumpft schrittweise, bis der Radius einen vorgegebenen Toleranzwert erreicht hat. Diese Technik bietet Effizienz bezogen auf die Rechenzeit und die Funktionsevaluierung und ist flexibel genug, um lokale Minimalwerte zu überwinden. Weitere Optimierungsmethoden sind ausführlich in den Arbeiten von Brent [38], Dennis & Torczon [55], Johnson & Faunt [130], Markert [172] oder Nocedal & Wright [204] erläutert.

Sensitivitätsstudie

Nach einer erfolgreichen Indentifizierung der Modellparameter muss untersucht werden, welche dieser Parameter relevant sind und welche aus dem Modell entfernt werden können. Die Frage über eine mögliche Korrelation zwischen Parametern soll ebenfalls gestellt werden. Diesbezüglich werden Sensitivitätsstudien durchgeführt. In diesem Zusammenhang gibt es die sogenannte subjektive Analyse (Downing *et al.* [57]) als einfachste und intuitivste Variante der Sensitivitätsanalyse. Basierend auf dem Experiment werden die Parameter nicht berücksichtigt, die *a priori* am wenigsten Einfluss auf die Modellantwort haben. Diese qualitative Methode ist anwendbar, um die Anzahl der Parameter in umfangreichen Modellen zu erniedrigen. In dieser Arbeit wird der Fokus auf eine lokale Sensitivitätsstudie gelegt (Gardner *et al.* [94]). Insbesondere wird jeder einzelne Parameter über die Zeit variiert, während die anderen festgehalten werden.

Messung und Berechnung der Kontaktspannungen im Hüftgelenk im Bezug auf die OA

Der Zweck einer Modellkalibrierung liegt üblicherweise in einer späteren Modellanwendung. Hier richtet sich der Fokus auf numerische Untersuchungen des gesunden und des degenerierten Hüftgelenks. Die Mechanismen, die für die Knorpeldegenierung verantwortlich sind, sind noch teilweise unbekannt. Dennoch erhöhen hohe lokale Kontaktspannungen das Risiko einer möglichen Entwicklung von OA (Mavcic *et al.* [184], Maxian *et al.* [185]). Darum ist eine Berechnung dieser Spannungen klinisch relevant, um sich präoperative Konzepte ausdenken und die Effizienz der eingesetzten chirurgischen Behandlungen auswerten zu können. Allerdings ist eine direkte Messung der *In-vivo*-Kontaktspannungen technisch aufwendig. Eine Alternative dazu stellt die Modellbildung dar. In dieser Arbeit werden die Kontaktspannungen im Hüftgelenk anhand von Finite-Elemente-Analysen untersucht.

Gliederung der Arbeit

Eine ausführliche Einführung ist in **Kapitel 1** enthalten mit dem aktuellen Stand der Forschung und den Zielen der vorgestellten Arbeit sowie den angewandten Methoden.

In **Kapitel 2** werden die Grundlagen der TPM und der Mischungskinematik eingeführt mit Fokus auf die zweiphasige Modellierung weicher, biologischer Gewebe. In diesem Zusammenhang werden Bilanzgleichungen anhand bestimmter Annahmen und die Konstitutivgleichungen aufgestellt. Nach einer kurzen Beschreibung bekannter Eigenschaften, wie der Poroviskoelastizität und der osmotischen Effekte, richtet sich der Fokus auf die Erläuterung eines komplexen Filtergesetzes und der Faser-Matrix-Schubinteraktion.

Kapitel 3 beschäftigt sich mit den für die Implementierung benötigten numerischen Techniken. Nach der Herleitung der schwachen Formulierung findet eine konsistente örtliche und zeitliche Diskretisierung statt.

Kapitel 4 konzentriert sich auf die Modellverfeinerung in Bezug auf eine präzise Knorpelbeschreibung. Diesbezüglich werden zusätzliche Merkmale des Knorpels vorgestellt und nach ihrer Relevanz für die Modellierung untersucht. Hierbei werden zentrale Begriffe der Sensitivitätsanalyse und der Parameteridentifikation implizit eingeführt. Dies geschieht mithilfe von kleinen numerischen Beispielen bezogen auf die anisotrope Viskoelastizität und die Faser-Matrix-Interaktion.

In **Kapitel 5** wird eine Kalibrierungsstrategie für das komplexe Knorpelmodell aufgestellt, nachdem theoretische Grundlagen über die Parameteridentifizierung und die Sensitivitätsanalyse erläutert wurden. Danach wird die Kalibrierungsstrategie bezüglich Eindrucksversuche und richtungsabhängiger Schubversuche der Forschungsgruppe von PD Hurschler (Medizinische Hochschule Hannover) verwendet.

Relevante Anwendungen werden in **Kapitel 6** ausführlich untersucht. In diesem Rahmen wird zunächst die komplexe drei-dimensionale (3-d) Anatomie des Hüftgelenks anhand von Daten der Magnetresonanztomographie (MRT) aus der Forschungsgruppe von Prof. Schick (Universitätsklinik Tübingen) rekonstruiert. Die Ergebnisse einer Ganganalyse mit einem durch die Forschungsgruppe von PD Hurschler entwickelten Mehrkörpersystem-Modell des Unterkörpers werden als reale Randbedingungen in das FE Rechenmodell des Femurkopfes eingesetzt. Hierbei werden unterschiedliche Szenarien berücksichtigt, beispielsweise gesundes oder degeneriertes Knorpelgewebe sowie normale oder pathologische Gehbewegungen. Im Anschluss werden anhand einer stereographischen Projizierung der Kontaktspannungen die Gefahrenbereiche auf der Knorpeloberfläche visualisiert. Weiterhin werden Aspekte der Mechanobiologie diskutiert, wobei Knorpelzellen als weiche Einschlüsse modelliert werden und die lokalen Spannungen in den verschiedenen Zellpositionen berechnet werden.

Zum Schluss bietet **Kapitel 7** eine kurze Zusammenfassung der Ergebnisse und einen Ausblick auf weitere Aufgaben sowie Modellierungsalternativen aus der Forschungsgruppe von Prof. Nackenhorst (Leibniz Universität Hannover).

Desweiteren werden relevante Modellannahmen und neu eingeführte Verzerrungsenergiefunktionen im **Anhang** angesprochen.

Chapter 1: Introduction and Overview

1.1 Motivation

A major biomedical problem is the poor self-healing and regeneration of cartilage. Therefore, cartilage tissues are easily prone to degenerate, leading to pain and working disabilities in middle-aged and older people. In particular, osteoarthritis (OA), a commonly occurring form of cartilage degeneration, is estimated to affect 630 million people worldwide, representing 15% of the global population.

In Germany, the Robert-Koch Institute, responsible for national health data reporting, mentions only 1,6% of the under 30-year-old population displaying symptoms of OA. Until the age of 50, the OA prevalence reaches 14,9%, and after the age of 60, one-third of the female population and one-fourth of the male population suffer from OA, respectively. Moreover, between 2003 and 2010, the registered OA cases increased from 22,6% to 27,1% for women and from 15,5% to 17,9% for men. Obviously, the overall increase of OA cases is intimately connected to the rising cost of the healthcare. In 2004, diseases of the muscle-skeleton system occupied the third position in terms of generated costs at 24.46 billion euros, after cardiovascular and digestive diseases. From the costs related to muscle-skeleton diseases in 2012, 6.77 billion euros were incurred for OA, and 39% of the cases of missed work due to OA disease referred to hip-joint OA (see Figure 1.1).

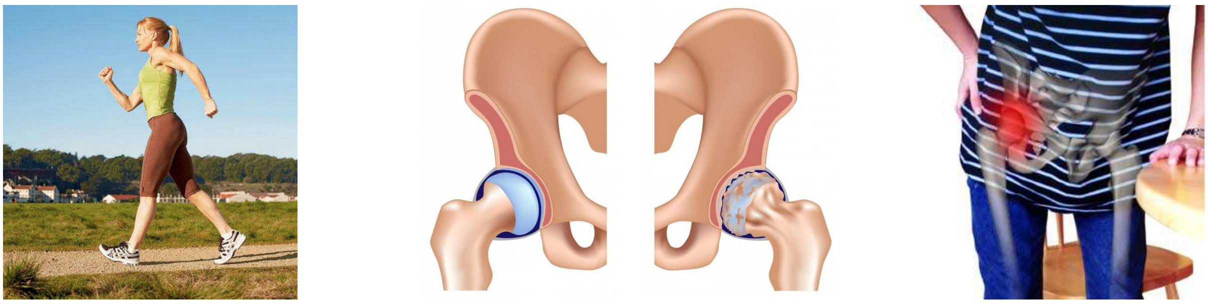

Figure 1.1: *Healthy (left) and degenerated hip joint (right) [http://www.cookinglight.com, www.hipflexor.org, www.wisegeek.org].*

In this general context, OA appears as a well-known clinical syndrome related to cartilage degeneration. Still, the mechanisms responsible for OA remain poorly understood. Up to now, the diagnoses are based on a combination of clinical, radiological and anamnestic criteria, mainly concentrating on the statistical occurrence of OA without a strong focus on the characteristics of the patient. One goal of this monograph is to extend the range of available possibilities for clinicians to strengthen their diagnoses.

For this purpose, a numerical tool is provided to guarantee a valid representation of the OA occurrence for a real hip-joint anatomy. This process naturally requires a highly complex geometrical and constitutive modelling in order to represent the patient-specific, highly anisotropic and heterogeneous features of the hydrated cartilage tissue. Therefore, a thermodynamically consistent model of soft biological tissue based on the Theory of Porous Media (TPM) is presented and adapted to the specific case of articular cartilage. In this connection, a consistent calibration strategy for the complex computational model is elaborated, which is the second objective of this work. Next, the focus lies on the consideration of realistic boundary conditions applied at the cartilage surface of the femoral head. Based on the contact stresses at the articular surface, a novel visualisation tool is introduced to evaluate the influence of OA during normal and pathological walking processes.

1.2 State of the Art

1.2.1 Articular-Cartilage Modelling

For a long time, scientists have demonstrated much interest in the experimental study (Benninghoff [22], Maroudas [178]) and modelling of cartilage. The interest in cartilage has been observed in the intense research work, particularly over the last decades, through the proliferation of numerical cartilage models on the scientific market. Classically, single-phase models have been used for the articular-cartilage modelling (Hayes *et al.* [109]). These models significantly simplified the cartilage structure and properties. However, their evident flaws came from the lack of incorporation of the pore-fluid contribution in the overall macroscopic behaviour. In this regard, multiphase models have been developed and became more popular, mostly based on the theory of mixtures (Lai *et al.* [152]) or on the more elaborate TPM (de Boer [30, 31], Bowen [34, 35], Ehlers [65–69]). Lai *et al.* [152] proposed the first triphasic model, which incorporated additional features such as electromechanical effects. In this model, a separate description of the solid and the fluid phases was adopted, including a reduction of the fluid components by using the electroneutrality condition. Further triphasic models appeared based on this description (Acartürk *et al.* [3], Frijns *et al.* [92]). Next, other considerations with respect to further model reductions were inspired by *Lanir*'s assumption (Lanir [154]). It justified the emergence of biphasic models (Huang *et al.* [124], Julkunen *et al.* [132], Karajan *et al.* [139], Mow *et al.* [190], Wilson *et al.* [253–256]), which were computationally less expensive. The models of Ehlers *et al.* [73, 74] were even able to precisely match the osmotic effects obtained from Acartürk *et al.* [3] and Frijns *et al.* [92] by means of a constitutively computed osmotic pressure. Biphasic models have been also intensively used to model creep and stress relaxation of articular cartilage. Both fluid flow-dependent and -independent phenomena were soon considered after biphasic poroviscoelastic models (Ehlers & Markert [75], Julkunen *et al.* [133], Markert [174], Suh & Bai [239]) were introduced by Mak [169]. The models of Li *et al.* [158], Wieners *et al.* [253] and Julkunen *et al.* [132] even complexified the numerical description of cartilage when incorporating supplementary features such as heterogeneities. Based on the TPM, Ehlers *et al.* [73, 76–78] proposed a thermodynamically consistent model that included most of these features but was specially designed for intervertebral discs. Simultaneously, other research groups developed various cartilage models (Julkunen *et al.* [133], Lilledahl *et al.* [162]). In Lilledahl *et al.* [162], important cartilage features such as collagen fibre disposition as well as zone-dependent heterogeneities and anisotropic permeability were precisely determined.

1.2.2 Parameter Identification

Obviously, material models are becoming more complex through the ages. A high model complexity allows for a better material description and representation despite having its downsides. The computational time for performing calculations tends to be problematic, and the high model complexity necessitates enormous experimental support for the parameters finding. Moreover, a crucial question is whether such complex models are practical. What is the optimal model complexity? Which measurable effects need to be captured? In order to answer these questions, many classifications exist based on the nonlinearity of the problem, the required convergence grade or the initial guess of the parameters. A typical distinction amongst different methods relies on the use of gradient-based identification techniques (Bock *et al.* [28], Johnson & Faunt [130]). In this monograph, the trust region method of constraint optimisation by linear approximation (COBYLA) (Powell [210]), belonging to the gradient-free methods (Brent [38], Dennis & Torczon [55], Johnson & Faunt [130], Markert [172], Nocedal & Wright [204]), is adopted. This method consists of the construction of a quadratic model for the area within a given radius (the trust region). This region expands or shrinks iteratively until the radius reaches a specified tolerance value. This method is mostly efficient in terms of the computational time and the function evaluations, and is flexible enough not to drop into local minima.

1.2.3 Sensitivity Analysis

Following this, a further question needs to be answered. What is the correlation between the parameters and the influence of a parameter variation on the numerical results? In this regard, sensitivity analyses are conducted. Here again, various classification types are presented in the literature (Bauer & Hamby [20], Box *et al.* [36], Helton [113], Helton *et al.* [114]).The easiest and most intuitive sensitivity analysis method is definitely the subjective analysis (Downing *et al.* [57]), thereby, the parameters which *a priori* slightly influence the model output are removed, based on the experience of the "simulator". This qualitative method is eventually used to reduce the number of parameters of large models but is not easily manageable with quantitative techniques. The method chosen in this monograph, is the local sensitivity analysis (Gardner *et al.* [94]). In this context, each parameter is varied at a time while holding the others fixed. The obtained sensitivity is locally defined because of its specification at a fixed point in the parameter space.

1.2.4 Measurement and Calculation of Stresses in Hip Joints

The calibration of a model generally introduces some relevant applications. In this regard, the focus lies on the numerical investigation of healthy and degenerated hip joints. Even though the mechanisms responsible for the degeneration of articular cartilage are still partially shrouded in mystery, one fact remains certain: high local contact stresses increase the risk of contracting OA (Mavcic *et al.* [184], Maxian *et al.* [185]). The calculation of contact stresses is then clinically relevant to propose pre-operative plans and evaluate the efficiency of surgical treatments. For this purpose, Hodge *et al.* [119] acquired data from telemetering inter-articular pressure measured on femoral head prostheses. Other *in-vitro* methods (Day *et al.* [54]) based on excision of concentric rings of cartilage estimated the joint pressure. Nevertheless, a direct measurement of *in-vivo* contact stresses is still technically complicated to perform. A way to predict such contact stresses resides in the development of computational models. In this framework, Abraham *et al.* [1], Genda *et al.* [96] and Yoshida *et al.* [262] performed discrete-element analyses (DEA). This discretisation using spring deformations and rigid bones led to high computational efficiency and to mostly qualitative match with experimental data. Then Anderson *et al.* [8] and Abraham *et al.* [1] proposed finite-element analyses of hip joints by means of single-phasic and biphasic models, respectively. Both teams of authors accurately estimated the contact stresses calculated for daily-life activities. The present contribution fits in the framework of finite-element analyses in order to investigate hip contact stresses.

1.3 Outline of the Thesis

As a brief overview, **Chapter 2** introduces the basics of the TPM and the mixture kinematics with a direct focus on the biphasic modelling of soft biological tissues. In this regard, balance relations are specified under given assumptions. The constitutive assumptions are then presented in a general framework. After a short description of classical features of soft biological tissues such as poroviscoelasticity and osmotic swelling, the author concentrates on the presentation of less common properties such as a complex non-*Darcy*an flow and the fibre-matrix shear interaction.

In **Chapter 3**, the numerical techniques required for implementing the constitutive model in the FE code are briefly recalled. In particular, starting from the derivation of the weak formulation of the balance relations, the domain is discretised in space and time leading to a consistent numerical procedure.

Chapter 4 focuses on the model refinement related to a precise cartilage description. In this context, additional characteristics are presented and discussed in terms of their relevance for the investigated phenomena. Important notions such as sensitivity analysis are implicitly introduced by means of short numerical examples displaying specific cartilage features such as anisotropic viscoelasticity and fibre-matrix shear interaction.

Chapter 5 aims to present a sophisticated model calibration strategy that is able to deal with the complex computational model. First, the theoretical background related to parameter identification and sensitivity analysis is recalled. In particular, a constraint optimisation by linear approximation (COBYLA) is used as a derivative-free method for identifying the material parameters. Regarding the sensitivity, correlation matrices are systematically introduced. Next, the calibration method is applied to various experimental set-ups such as multiple-indentation tests and multi-directional shear tests performed by the associated research unit of PD Hurschler at the Medical School of Hannover.

Applications of the calibrated model are presented in **Chapter 6**. A complex three-dimensional (3-d) hip-joint anatomy is reconstructed from magnetic resonance imaging (MRI) scans provided by the associated research unit of Prof. Schick at the University Hospital of Tübingen and used for test simulations. Thereafter, an introductive numerical example is presented in relation to the solid-fluid coupling in the hip joint between articular cartilage and synovial fluid. After reducing the initial geometry to the cartilage surface and its underlying femoral bone, multi-body system (MBS) calculations of the lower body part performed by the associated research unit of PD Hurschler are mixed with the presented constitutive model for a realistic representation of boundary conditions given by walking processes. In this connection, simulations are performed with consideration of different scenarios of healthy or OA-degenerated cartilage, normal or pathological walking and their combinations. Furthermore, the results are stereographically projected to allow a direct visualisation of contact stresses. Following this, aspects of mechanobiology are discussed, and the cartilage cells are modelled as weak inclusions. Then, observations on local stresses at presumed cell positions are presented.

Finally, the work done in this thesis and some future research aspects are summarised in **Chapter 7**. Therein, alternative concepts developed by the associated research unit of Prof. Nackenhorst at the Leibniz University of Hannover are addressed.

Additional information regarding various assumptions in the modelling is provided in **Appendix A**. Further aspects related to the polyconvexity of newly introduced contributions to the strain-energy function are mathematically investigated in **Appendix B**. Thereafter, **Appendix C** takes an interest in the numerical stability and the physical behaviour of the fibre-matrix shear contribution to the strain-energy function.

Chapter 2: Biphasic Modelling of Soft Biological Tissues

In this section, a broad continuum-mechanical framework is recalled. A brief overview of the Theory of Porous Media (TPM), the kinematic relations and the balance relations is presented. Then, soft biological tissues are described, leading to well-known constitutive equations. Particularly, sections 2.2 to 2.3.2 are based on previous models thoroughly described in Acartürk [2], Karajan [138] and Markert [172]. The sections thereafter concentrate on further extensions of these models and introduce the material specifications for articular cartilage and other tissues, as discussed in Chapter 4.

2.1 Theoretical Fundamentals of the Theory of Porous Media

2.1.1 Homogenisation and Volume Fractions

The TPM (de Boer [30, 31], Bowen [34, 35], Ehlers [65–69]) offers an adapted framework for macroscopically describing the complex microstructure of soft biological tissues. In this framework, the inner structure of the tissue is smeared over an arbitrarily chosen representative elementary volume (REV) by means of a volumetric averaging process. Next, the original microstructure is statistically substituted by the homogenised microstructure. In this regard, the soft biological tissue is represented by means of a binary aggregate of immiscible solid and fluid constituents φ^α denoted by $\alpha = \{S\,(\text{solid}),\ \text{F}\,(\text{fluid})\}$, leading to a model

$$\varphi = \bigcup_\alpha \varphi^\alpha = \varphi^S \cup \varphi^F \tag{2.1}$$

of superimposed and interacting continua (see Figure 2.1). In particular, the model consists of a deformable extracellular matrix (ECM) φ^S composed of proteoglycan aggregates (PGA) and a network of collagen fibres. Attached to the PGA chains are mass- and volume-free fixed charges φ^{fc} resulting from a large number of silicate or carbonate groups (Mow & Ratcliffe [194]). A further constituent of the model is the interstitial pore fluid φ^F described as a miscible mixture of its components, given by the liquid solvent (water) φ^L and the freely movable ions (Na^+) φ^+ and (Cl^-) φ^- of dissolved salt.

Hence, the overall volume V of the aggregate $\mathcal{B}$ is the sum of the partial volumes V^α of its constituents φ^α:

$$V = \int_\mathcal{B} \mathrm{d}v = \sum_\alpha V^\alpha, \quad \text{where} \quad V^\alpha = \int_\mathcal{B} \mathrm{d}v^\alpha = \int_\mathcal{B} n^\alpha \mathrm{d}v. \tag{2.2}$$

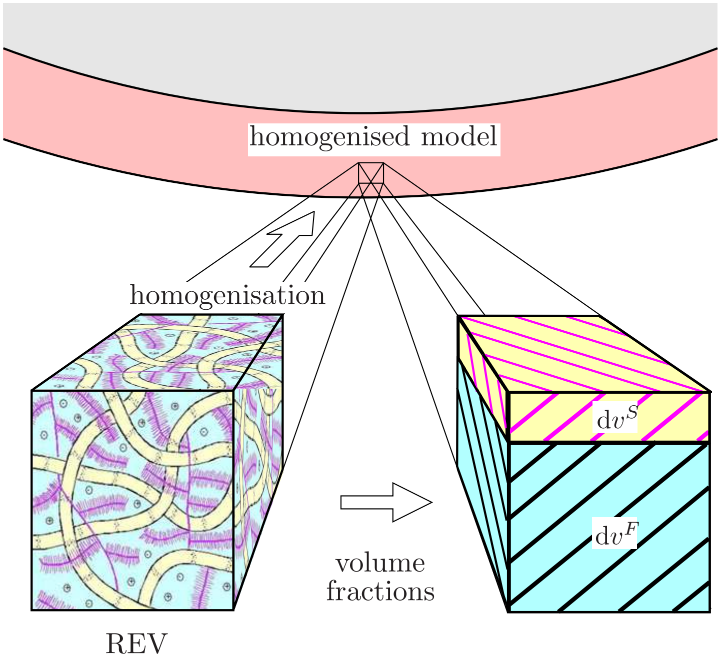

Figure 2.1: *Representative elementary volume (REV) of soft biological tissue exemplary depicted for a cartilage layer with homogenised model and concept of volume fractions.*

Therein, the local constitution of the solid-fluid aggregate is given by the volume fraction n^α defined as

$$n^\alpha = \frac{\mathrm{d}v^\alpha}{\mathrm{d}v} \tag{2.3}$$

relating the volume element $\mathrm{d}v^\alpha$ of the constituent φ^α to the volume element $\mathrm{d}v$ of the overall model φ. By summing up all volume fractions n^α, the saturation constraint is obtained as

$$\sum_\alpha n^\alpha = n^S + n^F = 1\,, \tag{2.4}$$

stating that no vacant space is existent in the overall aggregate. Herein, n^S and n^F are the so-called solidity and porosity, respectively. The solidity n^S is made up of the solid fractions n^S_{ECM} and n^S_{coll} as

$$n^S = n^S_{\mathrm{ECM}} + n^S_{\mathrm{coll}}\,, \tag{2.5}$$

where n^S_{ECM} and n^S_{coll} are the solid fractions of the ECM and the collagen fibres, respectively.

The introduction of the volume fractions motivates the definition of two different density functions, the effective density $\rho^{\alpha R}$ and the partial density ρ^α. The first one relates the mass element $\mathrm{d}m^\alpha$ of a constituent φ^α to its volume $\mathrm{d}v^\alpha$, while the second one relates $\mathrm{d}m^\alpha$ to the bulk volume $\mathrm{d}v$. Thus,

$$\rho^{\alpha R} = \frac{\mathrm{d}m^\alpha}{\mathrm{d}v^\alpha} \quad \text{and} \quad \rho^\alpha = \frac{\mathrm{d}m^\alpha}{\mathrm{d}v}\,. \tag{2.6}$$

These two densities are related to each other via

$$\rho^\alpha = n^\alpha \rho^{\alpha R}\,. \tag{2.7}$$

Note in passing that a biphasic description of soft biological tissue is justified by the combined use of the saturation condition (2.4) and *Lanir*'s assumption (Lanir [154]). It states that the mobile ions instantaneously reach their electrochemical equilibrium due to a rapid diffusion through the liquid. Following *Lanir*'s assumption, the motion of mobile ions does not have to be considered separately (Acartürk [2], Karajan [138]).

2.1.2 Kinematical Relations

According to the concept of superimposed and interacting continua, each constituent φ^α follows its own motion function starting from different positions $\mathbf{X}_\alpha$ in the reference configuration at time t_0. At time t in the actual configuration, each spatial point P^α of the body $\mathcal{B}$ is occupied simultaneously by each constituent φ^α (see Figure 2.2). This leads to the following vector-valued field functions of motion, velocity and acceleration, respectively:

$$\mathbf{x} = \boldsymbol{\chi}_\alpha(\mathbf{X}_\alpha, t), \quad \overset{\prime}{\mathbf{x}}_\alpha = \frac{\partial}{\partial t}[\boldsymbol{\chi}_\alpha(\mathbf{X}_\alpha, t)] \quad \text{and} \quad \overset{\prime\prime}{\mathbf{x}}_\alpha = \frac{\partial^2}{\partial t^2}[\boldsymbol{\chi}_\alpha(\mathbf{X}_\alpha, t)]\,. \tag{2.8}$$

Herein, $(.)'_\alpha$ and $(.)''_\alpha$ denote the first and second material time derivatives following the motion of φ^α.

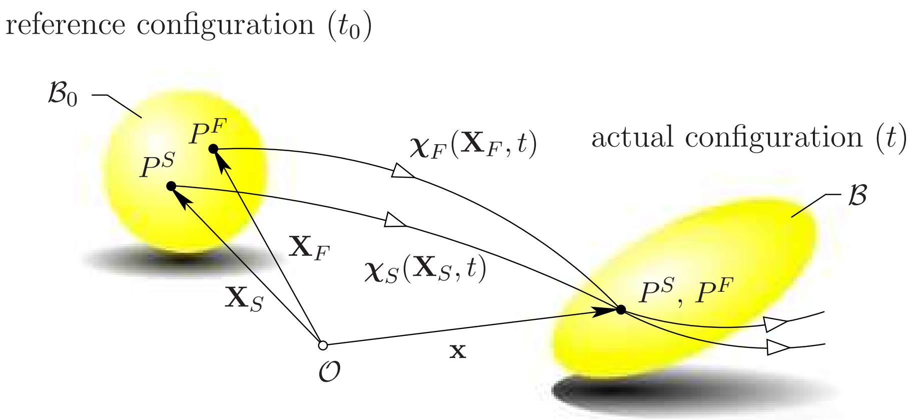

Figure 2.2: *Motion of a biphasic aggregate.*

Furthermore, the requirement of a unique and uniquely invertible motion function is

$$\mathbf{X}_\alpha = \boldsymbol{\chi}_\alpha^{-1}(\mathbf{x}, t) \quad \text{if} \quad J_\alpha = \det\frac{\partial \boldsymbol{\chi}_\alpha}{\partial \mathbf{X}_\alpha} \neq 0\,, \tag{2.9}$$

where the *Jacobi*an J_α differs from zero.
In this regard, the material deformation gradient $\mathbf{F}_\alpha$ and its inverse $\mathbf{F}_\alpha^{-1}$ are given by

$$\mathbf{F}_\alpha = \frac{\partial \boldsymbol{\chi}_\alpha}{\partial \mathbf{X}_\alpha} = \text{Grad}_\alpha\,\mathbf{x} \quad \text{and} \quad \mathbf{F}_\alpha^{-1} = \frac{\partial \boldsymbol{\chi}_\alpha^{-1}}{\partial \mathbf{x}} = \text{grad}\,\mathbf{X}_\alpha\,. \tag{2.10}$$

Here, the gradient operator "Grad$_\alpha$" represents the partial derivative with respect to the reference position vector $\mathbf{X}_\alpha$, and "grad" denotes the partial derivative with respect to the actual position vector $\mathbf{x}$.

In the framework of solid-fluid coupled problems, the solid motion is usually expressed in a *Lagrange*an description via the displacement vector $\mathbf{u}_S$, and the fluid is considered using a modified *Euler*ian description via the seepage velocity $\mathbf{w}_F$ as

$$\mathbf{u}_S = \mathbf{x} - \mathbf{X}_S \quad \text{and} \quad \mathbf{w}_F = \overset{\prime}{\mathbf{x}}_F - \overset{\prime}{\mathbf{x}}_S = \mathbf{v}_F - \mathbf{v}_S \,. \tag{2.11}$$

Here, $\mathbf{v}_F$ and $\mathbf{v}_S$ denote the velocity of the fluid and solid phases, respectively.

Generally, the solid displacement vector $\mathbf{u}_S$ is introduced as the primary kinematic variable of the solid phase. Using $(2.10)_1$ and $(2.11)_1$, the solid deformation gradient $\mathbf{F}_S$ is given as

$$\mathbf{F}_S = \mathbf{I} + \mathrm{Grad}_S \mathbf{u}_S \,, \tag{2.12}$$

where $\mathbf{I}$ represents the second-order identity tensor.

2.1.3 Strain and stress measures

Next, the deformation and strain measures of each constituent φ^α are briefly recalled, based on the transport mechanism of a line element between the reference and the actual configuration, i. e., $\mathrm{d}\mathbf{x} = \mathbf{F}_\alpha \, \mathrm{d}\mathbf{X}_\alpha$. In this context, the right $\mathbf{C}_\alpha$ and left $\mathbf{B}_\alpha$ *Cauchy-Green* deformation tensors are obtained as

$$\mathrm{d}\mathbf{x} \cdot \mathrm{d}\mathbf{x} = \mathbf{F}_\alpha \, \mathrm{d}\mathbf{X}_\alpha \cdot \mathbf{F}_\alpha \, \mathrm{d}\mathbf{X}_\alpha = \mathrm{d}\mathbf{X}_\alpha \cdot \underbrace{(\mathbf{F}_\alpha^T \, \mathbf{F}_\alpha)}_{\mathbf{C}_\alpha} \, \mathrm{d}\mathbf{X}_\alpha \tag{2.13}$$

and

$$\mathrm{d}\mathbf{X}_\alpha \cdot \mathrm{d}\mathbf{X}_\alpha = \mathbf{F}_\alpha^{-1} \, \mathrm{d}\mathbf{x} \cdot \mathbf{F}_\alpha^{-1} \, \mathrm{d}\mathbf{x} = \mathrm{d}\mathbf{x} \cdot \underbrace{(\mathbf{F}_\alpha^{T-1} \, \mathbf{F}_\alpha^{-1})}_{\mathbf{B}_\alpha^{-1}} \, \mathrm{d}\mathbf{x} \,. \tag{2.14}$$

In particular, $\mathbf{C}_\alpha = \mathbf{F}_\alpha^T \, \mathbf{F}_\alpha$ represents a deformation measure in the reference configuration, while $\mathbf{B}_\alpha = \mathbf{F}_\alpha \, \mathbf{F}_\alpha^T$ is related to the deformation in the actual configuration.

In connection to the body deformation measures, the *Green-Lagrange*an and *Almansi*an strain tensors, $\mathbf{E}_\alpha$ and $\mathbf{A}_\alpha$, are introduced as

$$\mathrm{d}\mathbf{x} \cdot \mathrm{d}\mathbf{x} - \mathrm{d}\mathbf{X}_\alpha \cdot \mathrm{d}\mathbf{X}_\alpha = \mathrm{d}\mathbf{X}_\alpha \cdot \underbrace{(\mathbf{C}_\alpha - \mathbf{I})}_{2\,\mathbf{E}_\alpha} \, \mathrm{d}\mathbf{X}_\alpha = \mathrm{d}\mathbf{X}_\alpha \cdot \underbrace{(\mathbf{I} - \mathbf{B}_\alpha^{-1})}_{2\,\mathbf{A}_\alpha} \, \mathrm{d}\mathbf{X}_\alpha \,. \tag{2.15}$$

Therein, $\mathbf{E}_\alpha = \frac{1}{2}(\mathbf{C}_\alpha - \mathbf{I})$ is expressed in the reference configuration, while $\mathbf{A}_\alpha = \frac{1}{2}(\mathbf{I} - \mathbf{B}_\alpha^{-1})$ is defined in the actual configuration. Note that for transporting a tensor from the reference to the actual configuration, a push-forward transformation is required, while a transport from the actual to the reference configuration necessitates a pull-back operation. Further information about transport mechanisms is given in Ehlers [65], Holzapfel [121] and Truesdell & Noll [242].

After formulating the deformation and strain measures, deformation and strain rates are introduced, starting from the definition of the deformation gradient $\mathbf{F}_\alpha$ (cf. equation $(2.10)_1$) and the material time derivative of the line element $\mathrm{d}\mathbf{x}$ as

$$\mathrm{d}\overset{\prime}{\mathbf{x}}_\alpha = (\mathbf{F}_\alpha)'_\alpha\,\mathrm{d}\mathbf{X}_\alpha = \underbrace{(\mathbf{F}_\alpha)'_\alpha\,\mathbf{F}_\alpha^{-1}}_{\mathbf{L}_\alpha}\,\mathrm{d}\mathbf{x}\,. \tag{2.16}$$

Herein, $\mathbf{L}_\alpha$ is defined as the spatial velocity gradient of the constituent φ^α. After some rearrangements, one obtains

$$\mathbf{L}_\alpha = \mathrm{grad}\,\overset{\prime}{\mathbf{x}}_\alpha \quad \text{and} \quad \mathbf{L}_\alpha \cdot \mathbf{I} = \mathrm{div}\,\overset{\prime}{\mathbf{x}}_\alpha\,. \tag{2.17}$$

Following this, a unique decomposition of $\mathbf{L}_\alpha$ into its symmetric part $\mathbf{D}_\alpha$ and skew-symmetric part $\mathbf{W}_\alpha$ is expressed as

$$\mathbf{L}_\alpha = \underbrace{\tfrac{1}{2}(\mathbf{L}_\alpha + \mathbf{L}_\alpha^T)}_{\mathbf{D}_\alpha} + \underbrace{\tfrac{1}{2}(\mathbf{L}_\alpha - \mathbf{L}_\alpha^T)}_{\mathbf{W}_\alpha}\,. \tag{2.18}$$

Therein, the deformation velocity or strain rate tensor is represented by $\mathbf{D}_\alpha$, and $\mathbf{W}_\alpha$ denotes the spin or vorticity tensor.

In this connection, the rate of the right *Cauchy-Green* deformation tensor $\mathbf{C}_\alpha$ is calculated from equation (2.13) via

$$(\mathbf{C}_\alpha)'_\alpha = (\mathbf{F}_\alpha^T\,\mathbf{F}_\alpha)'_\alpha = 2\,\mathbf{F}_\alpha^T\,\mathbf{D}_\alpha\,\mathbf{F}_\alpha\,. \tag{2.19}$$

From the previous relation and from equation (2.15), the *Green-Lagrangean* strain rate is obtained as

$$(\mathbf{E}_\alpha)'_\alpha = \tfrac{1}{2}(\mathbf{C}_\alpha)'_\alpha = \mathbf{F}_\alpha^T\,\mathbf{D}_\alpha\,\mathbf{F}_\alpha\,. \tag{2.20}$$

For the sake of completeness, stress measures are addressed according to the *Cauchy* theorem. In this regard, the surface traction vector $\mathbf{t}^\alpha(\mathbf{x},\mathbf{n},t)$ is related to the partial *Cauchy* stress tensor $\mathbf{T}^\alpha$ and the outward-oriented unit surface vector $\mathbf{n}$ of the body surface Γ as

$$\mathbf{t}^\alpha(\mathbf{x},\mathbf{n},t) = \mathbf{T}^\alpha(\mathbf{x},t)\mathbf{n}\,. \tag{2.21}$$

Further stress tensors can be derived from the definition of the incremental surface force $\mathrm{d}\mathbf{k}^\alpha$ as

$$\begin{aligned}\mathrm{d}\mathbf{k}^\alpha = \mathbf{t}^\alpha\,\mathrm{da} = (\mathbf{T}^\alpha\,\mathbf{n})\,\mathrm{da} = \mathbf{T}^\alpha\,(\mathbf{n}\,\mathrm{da}) &= \mathbf{T}^\alpha\,\mathrm{d}\mathbf{a}\\ &= \underbrace{J_\alpha\,\mathbf{T}^\alpha}_{\boldsymbol{\tau}^\alpha}\,\underbrace{J_\alpha^{-1}\,\mathrm{d}\mathbf{a}}_{\mathrm{d}\bar{\mathbf{a}}_\alpha}\\ &= \underbrace{J_\alpha\,\mathbf{T}^\alpha\,\mathbf{F}_\alpha^{T-1}}_{\mathbf{P}^\alpha}\,\underbrace{J_\alpha^{-1}\,\mathbf{F}_\alpha^T\,\mathrm{d}\mathbf{a}}_{\mathrm{d}\mathbf{A}_\alpha}\,,\end{aligned} \tag{2.22}$$

where $\mathrm{d}\mathbf{a}$ represents the oriented area element of the current configuration, $\mathrm{d}\bar{\mathbf{a}}_\alpha$ is the corresponding weighted area element, and $\mathrm{d}\mathbf{A}_\alpha$ is the area element in the reference configuration of φ^α. In this context, the *Cauchy* stress tensor $\mathbf{T}^\alpha$ is understood as the true stress due to its expression in the actual configuration, and the *Kirchhoff* stress tensor $\boldsymbol{\tau}^\alpha$ is the weighted *Cauchy* stress. Furthermore, the first *Piola-Kirchhoff* stress tensor $\mathbf{P}^\alpha$ relates the force vector in the current configuration to the surface element of the reference configuration of φ^α. A full pull-back transport of $\boldsymbol{\tau}^\alpha$ towards this reference configuration leads to the second *Piola-Kirchhoff* stress tensor $\mathbf{S}^\alpha$:

$$\mathbf{S}^\alpha = \mathbf{F}_\alpha^{-1}\,\mathbf{P}^\alpha = \mathbf{F}_\alpha^{-1}\,\boldsymbol{\tau}^\alpha\,\mathbf{F}_\alpha^{T-1}\,. \tag{2.23}$$

2.2 Balance Relations

Continuum mechanics rests upon equations expressing the balances of mass, linear momentum, moment of momentum and energy in a body. These balance equations apply to all bodies, independent of the material constitution. Just as time, position and velocity are primary notions in kinematics, equally important are the concepts of mass, energy and force with respect to the classical mechanics of continua. These entities can be axiomatically introduced via master balances, which give a frame for all balances. In this regard, *Truesdell*'s metaphysical principles [241] extend the classical balance laws, valid for a single-phase material, to the multiphasic materials, in which the interactions between the constituents are taken into account, as follows:
1. All properties of the mixture must be mathematical consequences of properties of the constituents.
2. In order to describe the motion of a constituent, we may imagine isolating it from the rest of the mixture, provided we properly allow for the actions of the other constituents upon it.
3. The motion of the mixture is governed by the same equations as those in a single body.

Then, the formulation of the governing equations in their global form is simplified using the following assumptions:

- mass exchange between the constituents excluded and mass production terms $\hat{\rho}^\alpha$ neglected, i. e., $\hat{\rho}^\alpha = 0$,
- material incompressibility of the constituents under physiological pressure (Bachrach *et al.* [13]), i. e., $\rho^{\alpha R} = \text{const.}$,
- uniform temperature for each constituent, i. e., $\Theta^\alpha = \Theta = \text{const.}$,
- gravitational forces neglected, i. e., $\rho^\alpha\,\mathbf{g} \approx \mathbf{0}$ (see Appendix A.1),
- quasi-static conditions, i. e., $\rho^\alpha\,\overset{\prime\prime}{\mathbf{x}}_\alpha \approx \mathbf{0}$ (see Appendix A.2).

2.2.1 Volume Balances

Under the two first assumptions, the local mass balances (Ehlers [65]) of the solid and fluid constituents transform into volume balances. The volume balance of the overall aggregate is obtained after summing up the local volume balances of its constituents yielding

$$\left.\begin{array}{lcccc} (n^S)'_S & + & n^S\,\mathrm{div}\,\overset{\prime}{\mathbf{x}}_S & = & 0 \\ (n^F)'_F & + & n^F\,\mathrm{div}\,\overset{\prime}{\mathbf{x}}_F & = & 0 \end{array}\right\} \quad\longrightarrow\quad \mathrm{div}\,[\,(\mathbf{u}_S)'_S + n^F\mathbf{w}_F\,] = 0\,. \tag{2.24}$$

The volume balance of the solid constitutent and its adhering fixed charges can be integrated analytically from the initial solidity n^S_{0S} (Ehlers [65]), yielding

$$n^S = n^S_{0S}\, J_S^{-1}\,, \tag{2.25}$$

where the *Jacobi*an $J_S = \det \mathbf{F}_S$ is the determinant of the solid deformation gradient $\mathbf{F}_S$. Note that according to the saturation equation (2.4), the initial porosity n^F_{0S} in the solid reference configuration is obtained as

$$n^F_{0S} = 1 - n^S_{0S}\,. \tag{2.26}$$

Similarly to (2.25), the molar concentration c^{fc}_m of the fixed charges is obtained, after analytical integration from the the initial value $c^{fc}_{m,0S}$ of the concentration of the fixed charges, as (Acartürk [2])

$$c^{fc}_m = c^{fc}_{m,0S}\,\frac{1 - n^S_{0S}}{J_S - n^S_{0S}}\,. \tag{2.27}$$

2.2.2 Momentum Balance

Following the first and the two last assumptions expressed in section 2.2, the momentum balance of the overall aggregate is obtained from the sum of the local momentum balances of the solid and fluid constituents (Ehlers [65]) as

$$\left.\begin{array}{lllllllll} \operatorname{div}\mathbf{T}^S & + & \rho^S\,\mathbf{g} & + & \hat{\mathbf{p}}^S & - & \rho^S\,\overset{\prime\prime}{\mathbf{x}}_S & = & \mathbf{0} \\ \operatorname{div}\mathbf{T}^F & + & \rho^F\,\mathbf{g} & + & \hat{\mathbf{p}}^F & - & \rho^F\,\overset{\prime\prime}{\mathbf{x}}_F & = & \mathbf{0} \end{array}\right\} \longrightarrow \quad \operatorname{div}\,(\mathbf{T}^S + \mathbf{T}^F) = \mathbf{0}\,. \tag{2.28}$$

Therein, the overall *Cauchy* stress tensor $\mathbf{T} = \mathbf{T}^S + \mathbf{T}^F$ is the sum of the partial *Cauchy* stresses of the solid and the pore fluid, and $\hat{\mathbf{p}}^F = -\hat{\mathbf{p}}^S$ is the momentum production term. For more details, the interested reader is referred to the works of Karajan [138] and Acartürk [2] and to Appendix A.2.

2.3 Constitutive Relations

Next to the local balance equations, the physical response of soft tissues is described by means of constitutive equations. Depending on its function, every soft tissue will exhibit a different characteristic behaviour. In this general framework, a soft tissue is described as an anisotropic, viscoelastic and osmotically swelling material. A more precise description related to a specific soft tissue such as articular cartilage will be the focus of Chapter 4.

In this context, the presented formulations are related to the partial *Cauchy* stress tensors of the solid and the pore fluid, and the momentum production term. Exploiting the material incompressibility condition, the so-called extra values $\mathbf{T}^S_E$, $\mathbf{T}^F_E$ and $\hat{\mathbf{p}}^F_E$, for which constitutive relations are needed, are as follows (Ehlers [66], Skempton [233]):

$$\begin{array}{lllll} \mathbf{T}^S_E & = & n^S\,\mathcal{P}\,\mathbf{I} & + & \mathbf{T}^S\,, \\ \mathbf{T}^F_E & = & n^F\,\mathcal{P}\,\mathbf{I} & + & \mathbf{T}^F\,, \\ \hat{\mathbf{p}}^F_E & = & -\,\mathcal{P}\,\operatorname{grad} n^F & + & \hat{\mathbf{p}}^F\,. \end{array} \tag{2.29}$$

Here, $\mathcal{P}$ is the *Lagrange*an multiplier from the entropy inequality, identified as the hydraulic pore-fluid pressure (Ehlers [66]). The hydraulic pore-fluid pressure is defined as the difference between the overall pressure p and the osmotic pressure difference $\Delta\pi$ as (Karajan [138])

$$\mathcal{P} = p - \Delta\pi \tag{2.30}$$

To account for the mechanical and osmotic properties of soft biological tissues, the extra *Cauchy* solid stress $\mathbf{T}^S_E$ can be split into a purely mechanical contribution $\mathbf{T}^S_{\text{mech}}$ and an osmotic contribution $\mathbf{T}^S_{\text{osm}}$:

$$\mathbf{T}^S_E = \mathbf{T}^S_{\text{osm}} + \mathbf{T}^S_{\text{mech}}\,. \tag{2.31}$$

The mechanical contribution $\mathbf{T}^S_{\text{mech}}$ can further be divided into an isotropic part $\mathbf{T}^S_{\text{ISO}}$ due to the ECM, an anisotropic part $\mathbf{T}^S_{\text{ANI}}$ deduced from the anisotropic structure and an interaction part $\mathbf{T}^S_{\text{INT}}$ related to the shear interaction between ECM and the anisotropic structure, i. e.,

$$\begin{aligned}
\mathbf{T}^S_{\text{mech}} &= \frac{n^S_{\text{ECM}}}{n^S}\,\mathbf{T}^S_{\text{ISO}} + \frac{n^S_{\text{coll}}}{n^S}\,\mathbf{T}^S_{\text{ANI}} + \frac{n^S_{\text{ECM}}}{n^S}\,\frac{n^S_{\text{coll}}}{n^S}\,\mathbf{T}^S_{\text{INT}} \\
&= (1 - \frac{n^S_{\text{coll}}}{n^S})\,\mathbf{T}^S_{\text{ISO}} + \frac{n^S_{\text{coll}}}{n^S}\,\mathbf{T}^S_{\text{ANI}} + (1 - \frac{n^S_{\text{coll}}}{n^S})\,\frac{n^S_{\text{coll}}}{n^S}\,\mathbf{T}^S_{\text{INT}}\,.
\end{aligned} \tag{2.32}$$

If the solid constituent is only composed of the ECM ($n^S_{\text{coll}} = 0$), a fully isotropic behaviour is expected, i. e., $\mathbf{T}^S_{\text{mech}} = \mathbf{T}^S_{\text{ISO}}$. In the extreme case of the only presence of collagen fibres ($n^S_{\text{coll}} = 1$), the purely mechanical stresses are described by $\mathbf{T}^S_{\text{mech}} = \mathbf{T}^S_{\text{ANI}}$. The contributions $\mathbf{T}^S_{\text{osm}}$, $\mathbf{T}^S_{\text{ISO}}$, $\mathbf{T}^S_{\text{ANI}}$ and $\mathbf{T}^S_{\text{INT}}$ are expressed mathematically in subsections 2.3.1 to 2.3.4. An overview of the additive splits for each contribution to $\mathbf{T}^S_E$ is provided in Figure 2.3.

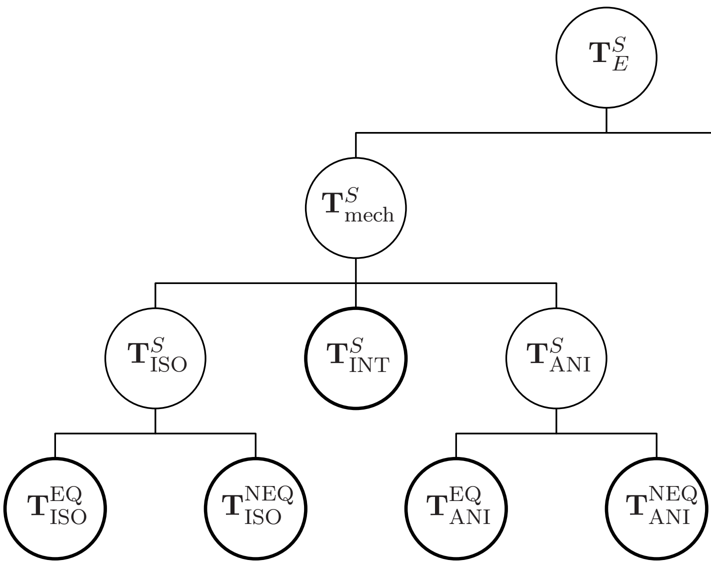

Figure 2.3: *Additive split of different Cauchy stress tensors.*

Regarding the fluid phase, the extra fluid stress $\mathbf{T}_E^F$ is neglected after a dimensional analysis (Ehlers *et al.* [72]). Following this, the overall *Cauchy* stress $\mathbf{T}$ is rearranged after substituting (2.29) in (2.28) and using the saturation condition (2.4) as

$$\mathbf{T} = \mathbf{T}^S + \mathbf{T}^F = \mathbf{T}_E^S - \mathcal{P}\,\mathbf{I}\,. \tag{2.33}$$

Finally, the remaining unspecified extra value $\hat{\mathbf{p}}_E^F$ is quantified by means of a constitutive formulation reflecting the features of a viscous, interstitial pore-fluid. After some mathematical rearrangements (Ehlers *et al.* [74]), a modified *Darcy*'s equation for the incompressible pore-fluid flow is discussed in subsection 2.3.5.

2.3.1 Osmotic Swelling

Many hydrated, soft biological tissues change their dimensions, volume and weight (Eisenberg & Grodzinsky [81, 82], Maroudas & Bannon [180], Mow & Schoonbeck [195], Myers *et al.* [198], Parsons & Black [207]). This change is due to the presence of fixed negative charges, yielding a greater ion concentration inside the tissue than that in the external bathing solution. As a consequence of the imbalance of ions, an osmotic pressure between the interstitial pore fluid and the external solution takes place, and the external fluid flows within the tissue to dilute the ionic solution of the pore fluid. This leads to a mechanical counterpressure, i. e., a pre-stress of the ECM (Grodzinsky *et al.* [98], Maroudas [179], Maroudas & Bannon [180]).
In particular, the associated osmotic pressure difference (Lai *et al.* [152], Maroudas [178]) is given by *van't Hoff*'s osmotic law as (Karajan [138])

$$\Delta\pi \;=\; R\,\Theta\left(\sqrt{4\,\bar{c}_m^{\,2} + (c_m^{fc})^2} - 2\,\bar{c}_m\right). \tag{2.34}$$

Herein, R denotes the universal gas constant, Θ is the absolute *Kelvin*'s temperature, and $\bar{c}_m$ is the molar concentration of the external salt solution surrounding the tissue. The osmotic pressure difference $\Delta\pi$ is inserted into the osmotic contribution $\mathbf{T}^S_{\text{osm}}$, yielding

$$\mathbf{T}^S_{\text{osm}} = -\Delta\,\pi\,\mathbf{I}\,. \tag{2.35}$$

Note that the mechanical relevance of osmotic swelling in the load-carrying system of soft biological tissues has been confirmed by many authors such as Best *et al.* [27], Mow *et al.* [196] and Urban *et al.* [245], amongst others.

2.3.2 Isotropic Viscoelasticity

The structural similarity of the protein-made ECM with polymeric network structures justifies the description of a viscoelastic material. In particular, the intrinsic viscoelasticity is understood by means of an adapted *Ogden*-like, finite viscoelastic formulation (Ogden [205]) for $\mathbf{T}^S_{\text{ISO}}$, which is based on previous works in the linear and nonlinear poroviscoelasticity field (Ehlers *et al.* [74], Markert [174]). In this context, the behaviour of the solid phase is described by means of a discrete relaxation spectrum associated with the generalised *Maxwell* rheological model (Markert [174]).

Hereby, use is made of a multiplicative decomposition of the deformation gradient $\mathbf{F}_S$ into elastic parts $(\mathbf{F}_{Se})_n$ and inelastic (viscous) parts $(\mathbf{F}_{Si})_n$ as

$$\mathbf{F}_S = (\mathbf{F}_{Se})_n \, (\mathbf{F}_{Si})_n \,. \tag{2.36}$$

This multiplicative split is illustrated in Figure 2.4 by a stress-free, geometrically incompatible, intermediate configuration describing the purely inelastic deformation state.

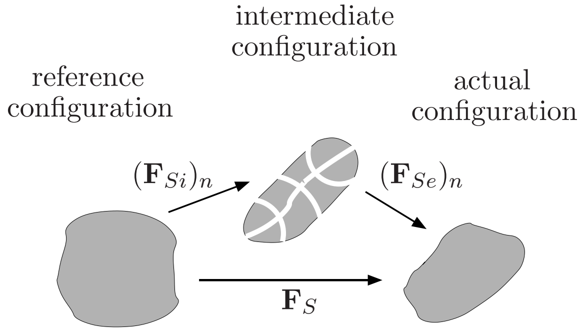

Figure 2.4: *Concept of an inelastic intermediate configuration.*

Proceeding from (2.36), the elastic $(J_{Se})_n$ and inelastic $(J_{Si})_n$ parts of the *Jacobi*an J_S, and the solid volume fractions $(n^S_{Si})_n$ of the $n = \{1, .., N\}$ *Maxwell* elements are introduced as

$$J_S = (J_{Se})_n \, (J_{Si})_n \quad \text{and} \quad n_S = (n^S_{Si})_n \, (J^{-1}_{Se})_n \quad \text{with} \quad (n^S_{Si})_n = n^S_{0S} \, (J^{-1}_{Si})_n \,. \tag{2.37}$$

Equation (2.36) also motivates the following split of $\mathbf{T}^S_{\text{ISO}}$ into an equilibrium contribution $\mathbf{T}^{\text{EQ}}_{\text{ISO}}$ and a non-equilibrium contribution $\mathbf{T}^{\text{NEQ}}_{\text{ISO}}$ as depicted in Figure 2.3, yielding

$$\mathbf{T}^S_{\text{ISO}} = \mathbf{T}^{\text{EQ}}_{\text{ISO}} + \mathbf{T}^{\text{NEQ}}_{\text{ISO}} \,. \tag{2.38}$$

In particular, the equilibrium and non-equilibrium contributions are

$$\begin{aligned}
\mathbf{T}^{\text{EQ}}_{\text{ISO}} &= J_S^{-1} \Big\{ \mu_0^S \sum_{k=1}^{3} (\lambda_{S(k)} - 1) \mathbf{N}_{S(k)} + \\
&\quad + \frac{\lambda_0^S}{\gamma_0^S - 1 + \dfrac{1}{(1 - n^S_{0S})^2}} \Big(J_S^{\gamma_0^S} - \frac{J_S}{J_S - n^S_{0S}} + \frac{J_S \, n^S_{0S}}{1 - n^S_{0S}} \Big) \mathbf{I} \Big\} \quad \text{and} \\
\mathbf{T}^{\text{NEQ}}_{\text{ISO}} &= J_S^{-1} \sum_{n=1}^{N} \Big\{ \mu_n^S \sum_{k=1}^{3} (\lambda_{Se(k)} - 1) \mathbf{N}_{Se(k)} + \\
&\quad + \frac{\lambda_n^S}{\gamma_n^S - 1 + \dfrac{1}{[1 - (n^S_{Si})_n]^2}} \Big[(J_{Se}^{\gamma_n^S})_n - \frac{(J_{Se})_n}{(J_{Se})_n - (n^S_{Si})_n} + \frac{(J_{Se})_n \, (n^S_{Si})_n}{1 - (n^S_{Si})_n} \Big] \mathbf{I} \Big\} \,.
\end{aligned} \tag{2.39}$$

The equilibrium part $\mathbf{T}^{\text{EQ}}_{\text{ISO}}$ given in $(2.39)_1$ is related to a neo-*Hooke*an formulation (Eipper [80]). The parameters λ_0^S and λ_n^S and μ_0^S and μ_n^S are identified as the first and second *Lamé* constants, respectively. Furthermore, the parameters γ_0^S and γ_n^S represent the volumetric extension term of Markert [172], as elaborately discussed in Eipper [80], Karajan [138] and Markert [172]. The eigenvalues and eigentensors of the solid deformation tensors $\mathbf{C}_S$ and $\mathbf{B}_S$ are represented by $\lambda_{S(k)}$ and $\mathbf{N}_{S(k)}$, respectively.

Regarding equation $(2.39)_2$, the eigenvalues and eigentensors of the left *Cauchy-Green* elastic deformation $(\mathbf{B}_{Se})_n = (\mathbf{F}_{Se})_n \, (\mathbf{F}^T_{Se})_n$ in the actual configuration are denoted by

$\lambda_{Se(k)}$ and $\mathbf{N}_{Se(k)}$, respectively. The inelastic evolution equation formulated by the material time derivative of the right *Cauchy-Green* inelastic deformation $(\mathbf{C}_{Si})_n = (\mathbf{F}_{Si}^T)_n\,(\mathbf{F}_{Si})_n$ in the solid reference configuration, reads (Markert [174])

$$[(\mathbf{C}_{Si})_n\,]'_S - \frac{1}{\eta_n^S}\,(\mathbf{C}_{Si})_n\,\mathbf{S}_n^S\,(\mathbf{C}_{Si})_n + \frac{\zeta_n^S}{\eta_n^S(2\eta_n^S + 3\zeta_n^S)}\,[\,\mathbf{S}_n^S\cdot(\mathbf{C}_{Si})_n\,]\,(\mathbf{C}_{Si})_n = \mathbf{0}\,. \tag{2.40}$$

Therein, $\mathbf{S}_n^S$ represents the second *Piola-Kirchhoff* non-equilibrium stress tensor contribution related to the n-th *Maxwell* element, and η_n^S and ζ_n^S are defined as the respective macroscopic shear and bulk viscosities (Markert [172, 174]).

2.3.3 Anisotropic Viscoelasticity

The viscoelastic behaviour of collagen fibres was demonstrated by means of tensile tests by Li & Herzog [156]. In the modelling, the anisotropic viscoelasticity of the collagen fibre network is considered within a continuum-mechanical description. In this context, the anisotropic structure is represented by structural tensors $\boldsymbol{\mathcal{N}}^S$ and $\boldsymbol{\mathcal{M}}^S$, based on unit vectors $\mathbf{a}_0^S$ (Spencer [236]) pointing, in the solid reference configuration, in the fibre direction. Thus,

$$\boldsymbol{\mathcal{N}}^S = \mathbf{F}_S\,\boldsymbol{\mathcal{M}}^S\,\mathbf{F}_S^T = \mathbf{F}_S\,(\mathbf{a}_0^S\otimes\mathbf{a}_0^S)\,\mathbf{F}_S^T = \mathbf{F}_S\,\mathbf{a}_0^S\otimes\mathbf{F}_S\,\mathbf{a}_0^S \equiv \mathbf{a}^S\otimes\mathbf{a}^S\,. \tag{2.41}$$

Here, $\mathbf{a}^S$ is the vector pointing, in the actual configuration, in the fibre direction. Moreover, the squared value $\mathbf{a}^S\cdot\mathbf{a}^S$ of the fibre stretch can be expressed in terms of the fourth invariant J_{S4} as

$$\begin{aligned} \mathbf{a}^S\cdot\mathbf{a}^S &= \mathbf{F}_S\,\mathbf{a}_0^S\cdot\mathbf{F}_S\,\mathbf{a}_0^S = \mathbf{F}_S^T\,\mathbf{F}_S\,\mathbf{a}_0^S\cdot\mathbf{a}_0^S = (\mathbf{C}_S\,\mathbf{a}_0^S)\cdot\mathbf{a}_0^S \\ &= \mathbf{C}_S\cdot(\mathbf{a}_0^S\otimes\mathbf{a}_0^S) = \mathbf{C}_S\cdot\boldsymbol{\mathcal{M}}^S \equiv J_{S4}\,, \end{aligned} \tag{2.42}$$

where $\mathbf{C}_S$ is the right *Cauchy-Green* deformation in the solid reference configuration. A multiplicative split of J_{S4} into an elastic part $(J_{S4e})_n$ and inelastic part $(J_{S4i})_n$ yields

$$J_{S4} = (J_{S4e})_n\,(J_{S4i})_n\,. \tag{2.43}$$

Similar to the isotropic viscoelasticity, the additive split of $\mathbf{T}_{\text{ANI}}^S$ into the equilibrium contribution $\mathbf{T}_{\text{ANI}}^{\text{EQ}}$ and the non-equilibrium contribution $\mathbf{T}_{\text{ANI}}^{\text{NEQ}}$ is

$$\mathbf{T}_{\text{ANI}}^S = \mathbf{T}_{\text{ANI}}^{\text{EQ}} + \mathbf{T}_{\text{ANI}}^{\text{NEQ}}\,. \tag{2.44}$$

In particular, the equilibrium and non-equilibrium contributions are obtained from an *Ogden*-like strain-energy function (Karajan [138], Markert [174], Markert *et al.* [175]) as

$$\begin{aligned} \mathbf{T}_{\text{ANI}}^{\text{EQ}} &= \sum_{m=1}^{M_f}\frac{\widetilde{\mu}_m}{J_S}J_{S4}^{-1}(J_{S4}^{(\widetilde{\gamma}_m/2)}-1)\,\boldsymbol{\mathcal{N}}^S \quad \text{and} \\ \mathbf{T}_{\text{ANI}}^{\text{NEQ}} &= \sum_{n=1}^{N}\Big[\sum_{m=1}^{M_{fe}}\frac{(\widetilde{\mu}_m)_n}{J_S}J_{S4}^{-1}(J_{S4e}^{((\widetilde{\gamma}_m)_n/2)}-1)\Big]\,\boldsymbol{\mathcal{N}}^S\,. \end{aligned} \tag{2.45}$$

Regarding the equilibrium anisotropic contribution $\mathbf{T}^{\text{EQ}}_{\text{ANI}}$, $\widetilde{\mu}_m$ and $\widetilde{\gamma}_m$ are the anisotropic parameters, and M_f is the number of polynomial terms. The parameters $(\widetilde{\mu}_m)_n$, $(\widetilde{\gamma}_m)_n$ and M_{fe} of the $n = \{1, .., N\}$ *Maxwell* elements are likewise defined for the non-equilibrium anisotropic contribution $\mathbf{T}^{\text{NEQ}}_{\text{ANI}}$. To solve $(2.45)_2$, the evolution equation for the viscous counterpart J_{S4i} of the fourth invariant is obtained from its material time derivative $(J_{S4i})'_S$ as (Markert [174], Zinatbakhsh [267])

$$(J_{S4i})'_S = \frac{1}{\eta_f} \sum_{n=1}^{N} \sum_{m=1}^{M_{fe}} (\widetilde{\mu}_m)_n \, J_{S4}^{-1} \left[(J_{S4e})_n^{((\widetilde{\gamma}_m)_n/2)} - 1 \right]. \tag{2.46}$$

Herein, η_f is a parameter related to the fibre viscosity.
Note that $\mathbf{T}^S_{\text{ANI}}$ expressed in equation (2.45) is derived from the anisotropic strain-energy function W^S_{ANI}, yielding

$$\mathbf{T}^S_{\text{ANI}} = 2\, J_S^{-1}\, \mathbf{F}_S \, \frac{\partial W^S_{\text{ANI}}}{\partial \mathbf{C}_S} \, \mathbf{F}_S^T \,. \tag{2.47}$$

In particular, the additional split given in equation (2.44) leads to

$$\mathbf{T}^{\text{EQ}}_{\text{ANI}} + \mathbf{T}^{\text{NEQ}}_{\text{ANI}} = 2\, J_S^{-1}\, \mathbf{F}_S \left(\frac{\partial W^{\text{EQ}}_{\text{ANI}}}{\partial \mathbf{C}_S} + \frac{\partial W^{\text{NEQ}}_{\text{ANI}}}{\partial \mathbf{C}_S} \right) \mathbf{F}_S^T \,. \tag{2.48}$$

For more information about the derivation of the equilibrium part $W^{\text{EQ}}_{\text{ANI}}$ of the anisotropic strain-energy function, the interested reader is referred to the works of Karajan [138], Markert [174] and Zinatbakhsh [267]. The requirements for polyconvexity of the non-equilibrium part $W^{\text{NEQ}}_{\text{ANI}}$ of the anisotropic strain-energy function are verified in Appendix B.2.

2.3.4 Fibre-Matrix Shear Interaction

The fibre-matrix interaction is related to the interaction phenomena observed by Wagner & Lotz [250] between fibres and ECM, and amongst fibres within the same lamella. The collagen cross-links constrain the fibres from sliding past one another. Subsequently, the resistance to shear along fibres disposed in the same plane is directly related to collagen cross-linking. The fibre-matrix shear-interaction stresses can be quantified depending on the extent of along-fibre shear deformation. As a preliminary step in the description of shear deformation, the definition of the fifth invariant

$$J_{S5} \equiv \text{tr}\,(\mathbf{C}_S^2 \, \boldsymbol{\mathcal{M}}^S) = \mathbf{a}_0^S \cdot \mathbf{C}_S^2 \, \mathbf{a}_0^S \tag{2.49}$$

is required. This invariant has no physical meaning as a single entity. However, a combination of J_{S5} and J_{S4} is adapted for the mathematical expression of shear interactions. Shear interactions can be exemplary illustrated by cutting out a REV.

The chosen REV contains fibres embedded in a plane, which are formulated using a right-handed set of mutually orthogonal unit vectors $\boldsymbol{\xi}_1$, $\boldsymbol{\xi}_2$ and $\boldsymbol{\xi}_3$ in Figure 2.5. The local anisotropy is represented by the local unit fibre direction given by $\mathbf{a}_0^S$ of the form

$$\mathbf{a}_0^S = \sin\phi_0^S\,\boldsymbol{\xi}_1 + \cos\phi_0^S\,\boldsymbol{\xi}_2\,, \tag{2.50}$$

where ϕ_0^S is the fibre angle in the solid reference configuration. Considering the same orientation of $\boldsymbol{\xi}_i$ and the global orthogonal unit vectors $\mathbf{e}_i$, the structural tensor $\boldsymbol{\mathcal{M}}^S$ and the right *Cauchy-Green* tensor $\mathbf{C}_S$ can be expressed in the same orthogonal basis.

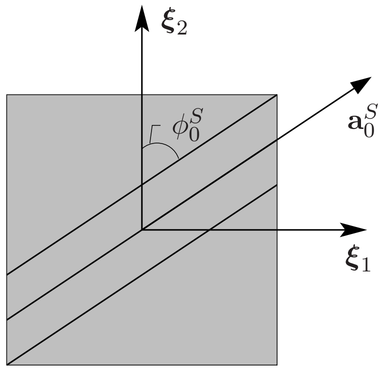

Figure 2.5: *In-plane embedded fibres of a REV.*

Then, after inserting (2.50) into (2.42) and (2.49) and assuming pure stretch deformations in the direction of $\boldsymbol{\xi}_2$, one obtains for a plane-strain state:

$$J_{S4} = C_{11}\sin^2\phi_0^S + C_{22}\cos^2\phi_0^S \quad \text{and} \quad J_{S5} = C_{11}^2\sin^2\phi_0^S + C_{22}^2\cos^2\phi_0^S\,. \tag{2.51}$$

Therein, C_{11} and C_{22} are the diagonal components of the right *Cauchy-Green* tensor $\mathbf{C}_S$ in the solid reference configuration and are related to the principal strains $E_{11} = \frac{1}{2}\,(C_{11} - 1)$ and $E_{22} = \frac{1}{2}\,(C_{22} - 1)$ by the definition of the *Green-Lagrange*an solid strain $\mathbf{E}_S$ in (2.15). In particular, the shear strain γ_a along the fibre direction $\mathbf{a}_0^S$ can be expressed as a function of the principal strains after a *Mohr*'s circle analysis yielding

$$\begin{aligned} \gamma_a &= \frac{1}{2}\,(E_{11} - E_{22})\sin(2\phi_0^S) \\ &= \frac{1}{4}\,(C_{11} - C_{22})\sin(2\phi_0^S)\,. \end{aligned} \tag{2.52}$$

To represent the fibre-matrix interaction by an even function of both positive and negative shear strains, the squared value γ_a^2 of the shear strain is determined based on trigonometrical relations as

$$\begin{aligned} \gamma_a^2 &= \frac{1}{16}\,(C_{11} - C_{22})^2\sin^2(2\phi_0^S) \\ &= \frac{1}{4}\,(C_{11}^2\sin^2\phi_0^S\cos^2\phi_0^S - 2\,C_{11}\,C_{22}\sin^2\phi_0^S\cos^2\phi_0^S + C_{22}^2\sin^2\phi_0^S\cos^2\phi_0^S) \\ &= \frac{1}{4}\,[\,C_{11}^2\sin^2\phi_0^S\,(1-\sin^2\phi_0^S) - 2\,C_{11}\,C_{22}\sin^2\phi_0^S\cos^2\phi_0^S + C_{22}^2\cos^2\phi_0^S\,(1-\cos^2\phi_0^S)] \\ &= \frac{1}{4}\,[\,\underbrace{C_{11}^2\sin^2\phi_0^S + C_{22}^2\cos^2\phi_0^S}_{J_{S5}} - \underbrace{(C_{11}\sin^2\phi_0^S + C_{22}\cos^2\phi_0^S)^2}_{J_{S4}^2}\,]\,, \end{aligned} \tag{2.53}$$

which recovers the expressions of J_{S4} and J_{S5} given in (2.51). Other authors such as Guo *et al.* [104, 105, 106] and Wagner & Lotz [250] also interpreted $J_{S5} - J_{S4}^2$ as the extent of along-fibre shear deformation.

Following this, the stress contribution $\mathbf{T}^S_{\text{INT}}$ is derived from a fibre-matrix interaction strain-energy function W^S_{INT} yielding

$$\begin{aligned}\mathbf{T}^S_{\text{INT}} &= 2\,J_S^{-1}\,\mathbf{F}_S\,\frac{\partial W^S_{\text{INT}}}{\partial \mathbf{C}_S}\,\mathbf{F}_S^T \\ &= \mu_{\text{int}}\,\alpha_{\text{int}}\,J_S^{-1}\,(J_{S5}-J_{S4}^2)^{(\alpha_{\text{int}}-1)}\mathbf{F}_S\,(\,2\,J_{S4}\,\boldsymbol{\mathcal{M}}^S+\mathbf{C}_S\,\boldsymbol{\mathcal{M}}^S+\boldsymbol{\mathcal{M}}^S\,\mathbf{C}_S\,)\,\mathbf{F}_S^T\,,\end{aligned} \tag{2.54}$$

where μ_{int} and α_{int} are material parameters. In the particular case of no shear along the fibres, i. e., $J_{S5}-J_{S4}^2=0$, the fibre-matrix interaction stresses vanish, i. e., $\mathbf{T}^S_{\text{INT}}=\mathbf{0}$. For more information about the function W^S_{INT}, the interested reader is referred to Appendix B.3. Therein, the requirement for polyconvexity of W^S_{INT} and the detailed calculation of $\mathbf{T}^S_{\text{INT}}$ are also presented.

Note that the fibre-matrix shear interaction is generally neglected due to the much higher fibre stiffness than the stiffness of the ECM. However, neglecting this term often leads to excessive rotation of the fibres in the ECM, called strongly directional behaviour (SDB) (Duong *et al.* [58], Gasser *et al.* [95]) (see Appendix C).

2.3.5 Interstitial Pore-Fluid Flow

Empirical evidence of Forcheimer [91] and Maroudas [178] showed the restrictions of *Darcy*'s filter law

$$n^F\,\mathbf{w}_F = -K^F\,\text{grad}\,\mathcal{P}\,, \tag{2.55}$$

to lingering fluid flows. In equation (2.55), the specific permeability K^F (in mm^4/N s) is related to the *Darcy* flow coefficient (hydraulic conductivity) k^F (in mm/s) by

$$k^F = \gamma^{FR}\,K^F\,, \tag{2.56}$$

where $\gamma^{FR}=\rho^{FR}\,g$ is the effective fluid weight, ρ^{FR} is the effective fluid density and $g=|\mathbf{g}|$ is the vectorial norm of the gravitation $\mathbf{g}$. In particular, the linearity between the seepage velocity $\mathbf{w}_F$ and the pressure gradient grad $\mathcal{P}$ breaks down due to turbulences in the seepage flow, created by the tortuosity of the pore structure (Mow & Mansour [193]). The nonlinear influence of the pressure gradient on the seepage velocity is constitutively described by the *Forchheimer* equation (Forcheimer [91]) and extended by Hassanizadeh & Gray [108] as

$$-\text{grad}\,\mathcal{P} = (\frac{1}{K^F}+\frac{\rho^{FR}}{B^S}\,|\mathbf{w}_F|)\,\mathbf{w}_F\,, \tag{2.57}$$

where B^S is the tortuosity parameter.

Equation (2.57) can be rewritten as

$$\mathbf{w}_F = -\underbrace{(\frac{1}{K^F}+\frac{\rho^{FR}}{B^S}\,|\mathbf{w}_F|)^{-1}}_{K^F_F}\,\text{grad}\,\mathcal{P}\,, \tag{2.58}$$

where K^F_F is the nonlinear permeability. After taking the norm of (2.57), solving the obtained quadratic equation for$|\mathbf{w}_F|$ and inserting $|\mathbf{w}_F|$ into (2.58), the dependency of

K_F^F on the seepage velocity is substitued to the pressure-gradient dependence yielding (Knupp & Lage [146], Markert [172])

$$K_F^F = K^F \left(\frac{1}{2} + \sqrt{\frac{1}{4} + \frac{\rho^{FR}}{B^S} (K^F)^2 \, |\mathrm{grad}\, \mathcal{P}|} \right)^{-1} . \tag{2.59}$$

Herein, the influence of the deformation state on the specific permeability K^F and the tortuosity B^S takes the form (Markert [173])

$$K^F = K_{0S}^F \, (\frac{n^F}{n_{0S}^F} \frac{n_{0S}^S}{n^S})^\kappa, \; \kappa \geq 0 \quad \text{and} \quad B^S = B_{0S}^S \, (\frac{n^F}{n_{0S}^F} \frac{n_{0S}^S}{n^S})^\beta, \; \beta \geq 0 \, , \tag{2.60}$$

where K_{0S}^F and B_{0S}^S are the initial values in the solid reference configuration, and κ and β are the factors governing the nonlinear deformation dependence.

Further investigations on fibre-reinforced porous materials by Federico & Herzog [86] revealed a strong correlation between pore-fluid flow directions and collagen fibre orientation. The preferred pore-fluid flow directions along the collagen fibres are captured by means of the permeability tensor (Eipper [80])

$$\boldsymbol{\mathcal{H}}^S = \boldsymbol{\mathcal{H}}_{0S}^S \, \boldsymbol{\mathcal{K}}^S \, . \tag{2.61}$$

Herein, the natural hydraulic anisotropy $\boldsymbol{\mathcal{H}}_{0S}^S$ is the constant part of the permeability tensor $\boldsymbol{\mathcal{H}}^S$ and is expressed analogously to the additive split of the stresses in (2.32) by Federico & Herzog [86] and Ricken & Bluhm [217] as

$$\boldsymbol{\mathcal{H}}_{0S}^S = (1 - \frac{n_{\mathrm{coll}}^S}{n^S}) \, \mathbf{I} + \frac{n_{\mathrm{coll}}^S}{n^S} \, \boldsymbol{\mathcal{M}}^S \, . \tag{2.62}$$

Besides, the deformation-dependent part $\boldsymbol{\mathcal{K}}^S$ of the permeability tensor $\boldsymbol{\mathcal{H}}^S$ expressed in (2.61) is related to the development of preferred flow paths under finite deformation of the solid skeleton and is described by Eipper [80] as

$$\boldsymbol{\mathcal{K}}^S = \frac{1}{2} \sum_{\substack{k=1 \\ j \neq l \neq k \neq j}}^{3} [\lambda_{S(j)} \lambda_{S(l)}]^\theta \, \mathbf{N}_{S(k)} \equiv (\mathrm{cof}\, \mathbf{B}_S)^\theta \quad \text{with} \quad \theta \geq 0 \, , \tag{2.63}$$

where $\lambda_{S(j)} \lambda_{S(l)}$ $(j \neq l)$ represents the eigenvalues of the cofactor of $\mathbf{B}_S$, and θ is the real-valued power governing the nonlinearity. If $\theta = 0$, the deformation-induced anisotropy is not considered, i. e., $\boldsymbol{\mathcal{K}}^S = \mathbf{I}$.

The expressions obtained in (2.59), (2.61), (2.62) and (2.63) are finally introduced into the generalised 3-d filter law for the incompressible pore-fluid flow, yielding

$$n^F \, \mathbf{w}_F = -\mathbf{K}^F \, \mathrm{grad}\, \mathcal{P} \quad \text{with} \quad \mathbf{K}^F = K_F^F \, \boldsymbol{\mathcal{H}}^S \, , \tag{2.64}$$

where $\mathbf{K}^F$ is the generalised permeability tensor.

Chapter 3: Numerical Treatment

A short overview of the numerical techniques involved in the computation of the proposed model is provided in the present section. After establishing the governing and constitutive equations and choosing primary variables as well as boundary and initial conditions, an initial-boundary-value problem (IBVP) can be defined.

The set of coupled partial differential equations (PDE) given in Chapter 2 is rearranged to suit a numerical solution scheme such as the finite-element method (FEM) involved in the finite-element (FE) software PANDAS (Porous Media Adaptive Nonlinear Finite Element Solver based on Differential Algebraic Systems). In this regard, weak formulations are derived from the governing equations. Thereafter, the spatial discretisation is performed using the FE scheme, whereas the temporal discretisation is carried out by means of the finite-difference method.

3.1 Finite-Element Method

The obtained PDE are solved within the framework of the FEM. Herein, weak forms are obtained by multiplying the governing equations by test functions and integrating over the spatial domain. Then, the overall domain is discretised in space by means of FE. In a further step, the time discretisation based on the implicit *Euler* scheme is performed before briefly introducing the numerical solution procedure of the *Newton* method. The interested reader is referred to the works of Bathe [19], Braess [37] and Schwarz [228] for further general information about the FEM. Further works of Ammann [6] and Ellsiepen [83] include porous materials in the framework of the FEM.

3.1.1 Weak Formulation

The governing equations of the coupled solid-fluid problem are solved within a numerical solution procedure by the FEM. However, solving the equations given in their strong forms is generally not possible for a numerical solution strategy. Therefore, the governing equations are transformed into their weak counterparts. Consequently, the validity of the obtained equations is guaranteed for the overall domain in an integral manner but not for each single spatial point.

As established in Chapter 2, the strong formulation of the coupled solid-fluid problem comprises the following:

- Saturation condition:
  $n^S + n^F \; = \; 1$
- Overall volume balance:
  $0 = \operatorname{div} [\, (\mathbf{u}_S)'_S + n^F \mathbf{w}_F \,]$
- Solidity:
  $n^S \; = \; n^S_{0S} \, J_S^{-1}$
- Overall momentum balance:
  $\mathbf{0} = \operatorname{div} \; \mathbf{T}$
- Overall stress:
  $\mathbf{T} = \mathbf{T}^S_E - \mathcal{P} \, \mathbf{I}$
- Generalised filter law:
  $n^F \mathbf{w}_F = -\mathbf{K}^F \operatorname{grad} \mathcal{P}$

In this connection, the primary variables are defined as the solid displacement $\mathbf{u}_S$ and the hydraulic pore-fluid pressure $\mathcal{P}$. The choice of the hydraulic pore-fluid pressure $\mathcal{P}$ is motivated by its constant value over the domain boundary. Choosing the overall pressure p as the primary variable would easily lead to unstable numerical solutions with oscillations (Ehlers & Acartürk [70], Karajan [138], Snijders *et al.* [235]).

Furthermore, the set of trial functions yields

$$\begin{aligned} \mathbf{S}_{\mathbf{u}_S}(t) \; &= \; \{ \;\; \mathbf{u}_S \;\; \in \;\; H^1\,(\Omega)^d \;\; : \;\; \mathbf{u}_S(\mathbf{x}) \;\; = \;\; \bar{\mathbf{u}}_S(\mathbf{x}, t) \;\; \text{on} \;\; \Gamma_{\mathbf{u}_S} \;\; \}, \text{ and} \\ \mathbf{S}_{\mathcal{P}}(t) \; &= \; \{ \;\; \mathcal{P} \;\; \in \;\; H^1\,(\Omega) \;\; : \;\; \mathcal{P}(\mathbf{x}) \;\; = \;\; \bar{\mathcal{P}}(\mathbf{x}, t) \;\; \text{on} \;\; \Gamma_{\mathcal{P}} \;\; \}, \end{aligned} \tag{3.1}$$

where $H^1\,(\Omega)$ is the *Sobolev* space corresponding to functions, which first derivatives are square integrable within the spatial domain Ω, and $d \in \{1, 2, 3\}$ relates to the space dimension of the problem. Herein, $\Gamma_{\mathbf{u}_S}$ and $\Gamma_{\mathcal{P}}$ are the domain boundaries on which the *Dirichlet* boundary conditions $\{\bar{\mathbf{u}}_S, \, \bar{\mathcal{P}}\}$ are described for the set $\{\mathbf{u}_S, \, \mathcal{P}\}$ of primary variables. Furthermore, the *Neumann* or natural boundary conditions $\{\bar{\mathbf{t}}, \, \bar{q}\}$ are defined on the boundaries $\Gamma_{\mathbf{t}}$ and Γ_q.

In summary, every PDE can mathematically be split over the overall domain surface Γ as

$$\begin{aligned} \Gamma \;\; &= \;\; \Gamma_{\mathbf{u}_S} \;\; \cup \;\; \Gamma_{\mathbf{t}} \quad \text{with} \quad \Gamma_{\mathbf{u}_S} \;\; \cap \;\; \Gamma_{\mathbf{t}} \;\; = \;\; \emptyset \,, \text{ and} \\ \Gamma \;\; &= \;\; \Gamma_{\mathcal{P}} \;\; \cup \;\; \Gamma_q \quad \text{with} \quad \Gamma_{\mathcal{P}} \;\; \cap \;\; \Gamma_q \;\; = \;\; \emptyset \,. \end{aligned} \tag{3.2}$$

Similar to equations (3.1), arbitrary test functions $\delta\mathbf{u}_S$ and $\delta\mathcal{P}$ of the corresponding primary variables are defined as

$$\begin{aligned} \mathbf{T}_{\mathbf{u}_S}(t) \;\; &= \;\; \{ \;\; \delta\mathbf{u}_S \;\; \in \;\; H^1\,(\Omega)^d \;\; : \;\; \delta\mathbf{u}_S(\mathbf{x}) \;\; = \;\; \mathbf{0} \;\; \text{on} \;\; \Gamma_{\mathbf{u}_S} \;\; \}, \text{ and} \\ \mathbf{T}_{\mathcal{P}}(t) \;\; &= \;\; \{ \;\; \delta\mathcal{P} \;\; \in \;\; H^1\,(\Omega) \;\; : \;\; \delta\mathcal{P}(\mathbf{x}) \;\; = \;\; 0 \;\; \text{on} \;\; \Gamma_{\mathcal{P}} \;\; \}\,. \end{aligned} \tag{3.3}$$

Then, the weak counterparts of the given set of strong balance equations are defined after multiplication of the balance relations with the test functions and integration over the domain Ω. After this, *Gauß*ian divergence theorem is applied to specify the boundary integrals. In particular, the weak form of the overall momentum balance is

$$\mathcal{G}_{\mathbf{u}_S}(\, \delta\mathbf{u}_S, \mathbf{u}_S, \mathcal{P} \,) \equiv \int_\Omega (\mathbf{T}^S_E - \mathcal{P}\;\mathbf{I}) \cdot \operatorname{grad} \delta\mathbf{u}_S \; \mathrm{d}v \; - \int_{\Gamma_{\mathbf{t}}} \bar{\mathbf{t}} \cdot \delta\mathbf{u}_S \; \mathrm{d}a \; = \mathbf{0} \,, \tag{3.4}$$

where $\overline{\mathbf{t}} = (\mathbf{T}_E^S - \mathcal{P}\,\mathbf{I})\mathbf{n}$ is the external load vector acting on the boundary of the entire aggregate. Herein, $\mathbf{n}$ is the outward-oriented surface normal unit vector.

Furthermore, the weak form of the overall volume balance is given as

$$\begin{aligned} \mathcal{G}_{\mathcal{P}}(\delta\mathcal{P}, \mathbf{u}_S, \mathcal{P}) \equiv & \int_\Omega \operatorname{div}(\mathbf{u}_S)'_S\, \delta\mathcal{P}\, \mathrm{d}v \;+\; \int_\Omega n^F \mathbf{w}_F \cdot \operatorname{grad}\delta\mathcal{P}\, \mathrm{d}v \;+ \\ & + \int_{\Gamma_q} \bar{q}\, \delta\mathcal{P}\, \mathrm{d}a \;=\; 0\,, \end{aligned} \tag{3.5}$$

where $\bar{q} = n^F \mathbf{w}_F \cdot \mathbf{n}$ represents the outward-directed fluid flow.

3.1.2 Initial Conditions

Starting from the natural initial conditions $\mathbf{u}_S = 0$ and $\mathcal{P} = 0$, it is worth mentioning that the model does not present a stress-free reference configuration. The system always develops an initial osmotic pressure (Karajan [138])

$$\Delta\pi_{0S} \;=\; R\,\Theta\left(\sqrt{4\,\bar{c}_m^2 + (c_{m,0S}^{fc})^2} - 2\,\bar{c}_m\right), \tag{3.6}$$

which generates initial values of the *Cauchy* stress tensor $\mathbf{T}_{0S}$ different from $\mathbf{0}$. In order to solve this problem, the solid matrix is pre-stressed without any deformation when adding the initial osmotic part $\Delta\pi_{0S}\,\mathbf{I}$ to the extra mechanical solid stress $\mathbf{T}^S_{\text{mech}}$, i. e., $\mathbf{T}^S_{0S,\text{mech}} = \Delta\pi_{0S}\,\mathbf{I}$. For more details, the interested reader is referred to Karajan [138].

3.1.3 Space Discretisation with Mixed Finite Elements

In this section, an IBVP has to be solved within the spatial domain $\mathbf{x} \in \Omega$ and the time domain $t \in [0, T]$ by means of a numerical procedure. Therefore, the spatial domain Ω is fragmented into several finite subdomains Ω_e and leads to the approximated domain Ω^h, yielding

$$\Omega \approx \Omega^h = \bigcup_{e=1}^{N_e} \Omega_e\,, \tag{3.7}$$

where the number N_e of subdomains or FE, characterised by N_n nodes, assembles the FE mesh Ω^h.

In a further step, the discrete counterparts $\mathbf{S}^h_{\mathbf{u}_S}$ and $\mathbf{S}^h_{\mathcal{P}}$ of the spatially continuous, infinite dimensional trial and test spaces $\mathbf{S}_{\mathbf{u}_S}$ and $\mathbf{S}_{\mathcal{P}}$ given in equations (3.1) and (3.3) are obtained as

$$
\begin{array}{lclclcll}
\mathbf{u}_S\,(\mathbf{x},t) & \approx & \mathbf{u}_S^h(\mathbf{x},t) & = & \bar{\mathbf{u}}_S^h(\mathbf{x},t) & + & \displaystyle\sum_{j=1}^{N_{\mathbf{u}_S}} \phi_{\mathbf{u}_S}^j(\mathbf{x})\mathbf{u}_S^j(t) & \in\ \mathbf{S}_{\mathbf{u}_S}^h(t)\,, \\
\mathcal{P}\,(\mathbf{x},t) & \approx & \mathcal{P}^h(\mathbf{x},t) & = & \bar{\mathcal{P}}^h(\mathbf{x},t) & + & \displaystyle\sum_{j=1}^{N_{\mathcal{P}}} \phi_{\mathcal{P}}^j(\mathbf{x})\mathcal{P}^j(t) & \in\ \mathbf{S}_{\mathcal{P}}^h(t)\,, \\
\delta\mathbf{u}_S\,(\mathbf{x}) & \approx & \delta\mathbf{u}_S^h(\mathbf{x}) & = & & & \displaystyle\sum_{j=1}^{N_{\mathbf{u}_S}} \phi_{\mathbf{u}_S}^j(\mathbf{x})\delta\mathbf{u}_S^j & \in\ \mathbf{T}_{\mathbf{u}_S}^h(t)\,, \\
\mathcal{P}\,(\mathbf{x},t) & \approx & \delta\mathcal{P}^h(\mathbf{x}) & = & & & \displaystyle\sum_{j=1}^{N_{\mathcal{P}}} \phi_{\mathcal{P}}^j(\mathbf{x})\delta\mathcal{P}^j & \in\ \mathbf{T}_{\mathcal{P}}^h(t)\,.
\end{array}
\tag{3.8}
$$

Herein, $\bar{\mathbf{u}}_S^h(\mathbf{x},t)$ and $\bar{\mathcal{P}}^h(\mathbf{x},t)$ are the *Dirichlet* boundary conditions. Moreover, $\mathbf{u}_S^j(t)$ and $\mathcal{P}^j(t)$ are the time-dependent values at the N_n nodes of the FE mesh, where $\{N_{\mathbf{u}_S},\, N_{\mathcal{P}}\} \leq N_n$ depends on the approximation accuracy. Besides, $\phi_{\mathbf{u}_S}^j = \{\phi_{\mathbf{u}_S}^1, ..., \phi_{\mathbf{u}_S}^d\}$ and $\phi_{\mathcal{P}}^j = \{\phi_{\mathcal{P}}^1, ..., \phi_{\mathcal{P}}^d\}$ are the space-dependent global basis functions for the trial and test functions. In this context, the *Bubnov-Galerkin* method justifies the coincidence between the basis functions for the trial and test functions. Consequently, homogeneous *Dirichlet* boundary conditions are obtained at the *Dirichlet* boundaries, i. e., the test functions $\delta\mathbf{u}_S$ and $\delta\mathcal{P}$ vanish at $\Gamma_{\mathbf{u}_S}$ and $\Gamma_{\mathcal{P}}$. In particular, the obtained discrete version $\mathcal{G}_{\mathbf{u}_S}^h$ and $\mathcal{G}_{\mathcal{P}}^h$ of the weak forms is expressed by a system of $d \cdot N_{\mathbf{u}_S} + N_{\mathcal{P}}$ linearly independent equations (Ammann [6], Ellsiepen [83]).

In the framework of a strongly coupled solid-fluid problem, an adapted, mixed FE formulation is used. The primary variables $\{\mathbf{u}_S,\, \mathcal{P}\}$ appear simultaneously in the weak forms of the overall volume and momentum balances. To achieve an equal-order approximation for the solid extra stresses $\mathbf{T}_E^S$ and the hydraulic pressure $\mathcal{P}$ in (3.4), the choice of *Taylor-Hood* elements formulated by means of quadratic approximation for the solid displacement $\mathbf{u}_S$ and linear approximation for the hydraulic pore-fluid pressure $\mathcal{P}$ comes up naturally. In particular, the 2-d rectangular and 3-d hexahedral *Taylor-Hood* elements are depicted in Figure 3.1.

From a mathematical point of view, this choice of *Taylor-Hood* elements fulfils the requirements of stability and accuracy expressed by the *Ladyzhenskaya-Babuška-Brezzi* (LBB) condition (Braess [37], Brezzi & Fortin [39]) and the patch test for mixed formulations (Zienkiewicz *et al.* [265]). Considering the aforementioned conditions, oscillations in the numerical solution can be avoided.

Next, an adapted numerical integration of the weak form of the set of equations is performed by means of the *Gauß* quadrature (Zienkiewicz & Taylor [266]). As given in equation (3.7), the continuous integral over the domain Ω is approximated on the discrete domain Ω^h consisting of the summation over its subdomains Ω_e^h. Then the global coordinates $\mathbf{x}$ are reformulated in the local element coordinates ξ via the *Jacobi*an J_e. In this regard, the geometrical transformation is performed using an isoparametric concept, i. e., the same basis functions are chosen for the geometry and the displacements. Then the numerical integration is carried out after the approximation of its continuous coun-

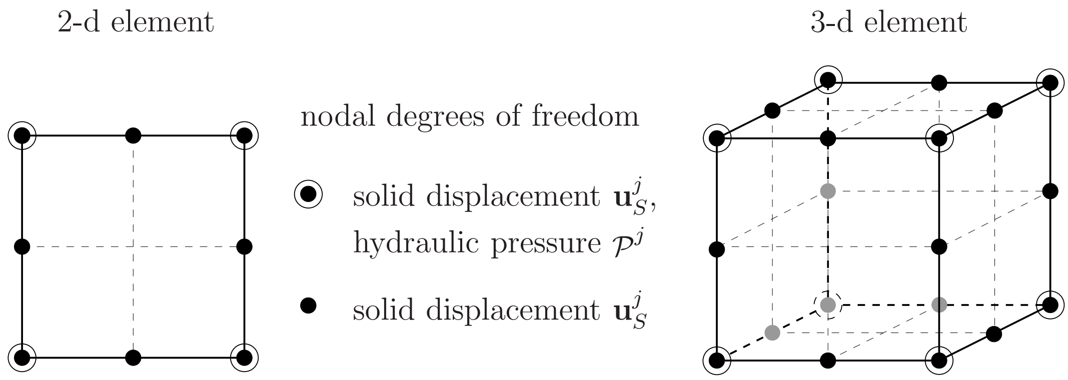

Figure 3.1: *2-d rectangular and 3-d hexahedral Taylor-Hood elements.*

terpart at K_g discrete *Gauß* points ξ_k and the definition of weight factors w_k (Ellsiepen [83], Zienkiewicz & Taylor [266]). The whole procedure is as follows:

$$\int_\Omega f(\mathbf{x})\,\mathrm{d}\mathbf{x} \approx \int_{\Omega^h} f(\mathbf{x})\,\mathrm{d}\mathbf{x} = \sum_{e=1}^{N_e} \int_{\Omega_e^h} f(\mathbf{x})\,\mathrm{d}\mathbf{x} \approx \sum_{e=1}^{N_e} \sum_{k=1}^{K_g} f(\xi_k)\, J_e(\xi_k)\, w_k\,. \tag{3.9}$$

3.1.4 Semi-Discrete Initial-Value Problem

Before introducing the time discretisation, the aforementioned considerations can be summarised within the framework of a semi-discrete initial-value problem based on Ehlers & Ellsiepen [71] and Ellsiepen [83]. In particular, only the spatial domain is so far discretised, whereas the time domain is still continuous. Next, the space-discrete values of the $N_{\mathbf{u}_S}$ displacement nodes and the $N_\mathcal{P}$ hydraulic pressure nodes are collected in the vector of unknowns $\mathbf{u}$ which consists of all degrees of freedom (DOF) as

$$\mathbf{u} \;=\; \Big[(\mathbf{u}_S^1, \mathcal{P}^1), ..., (\mathbf{u}_S^{N_\mathcal{P}}, \mathcal{P}^{N_\mathcal{P}}), ..., (\mathbf{u}_S^{N_{\mathbf{u}_S}})\Big]^T\,. \tag{3.10}$$

Furthermore, the internal (or history) variables related to the isotropic and anisotropic viscoelasticity are contained in the vectors $\mathbf{q}_{\mathrm{ISO}}$ (cf. Karajan [138], Markert [172]) and $\mathbf{q}_{\mathrm{ANI}}$ at the Q quadrature points and for the N *Maxwell* elements, yielding

$$\left.\begin{aligned} \mathbf{q}_{\mathrm{ISO}} &= \Big[(\mathbf{C}_{Si})_1^1, ..., (\mathbf{C}_{Si})_N^1, ..., (\mathbf{C}_{Si})_1^Q, ..., (\mathbf{C}_{Si})_N^Q\Big]^T \\ \mathbf{q}_{\mathrm{ANI}} &= \Big[(J_{S4i})_1, ..., (J_{S4i})_N\Big]^T \end{aligned}\right\} \quad \mathbf{q} = (\mathbf{q}_{\mathrm{ISO}}^T, \mathbf{q}_{\mathrm{ANI}}^T)^T\,. \tag{3.11}$$

Herein, the vector $\mathbf{q}$ is defined as the combination of $\mathbf{q}_{\mathrm{ISO}}$ and $\mathbf{q}_{\mathrm{ANI}}$. Besides, a local vector $\mathbf{L}$ is introduced containing the $N\cdot(Q+1)$ evolution equations of the $N\cdot Q$ tensorial history variables resulting from the viscous ECM behaviour and the N scalar history variables due to the viscous anisotropic setting. In particular, $\mathbf{L}$ belongs to the class of systems of ordinary differential equations (ODE) of first order in time. In a similar way, the global equations are gathered in the space-discrete function vector $\mathbf{G} = [\mathcal{G}_{\mathbf{u}_S}^h, \mathcal{G}_\mathcal{P}^h]^T$ corresponding to a system of differential-algebraic equations (DAE) of first order in time (Ellsiepen [83]).

After combining the vectors $\mathbf{u}$ and $\mathbf{q}$ in the general vector of unknowns $\mathbf{y} = (\mathbf{u}^T, \mathbf{q}^T)^T$, the implicit initial-value problem is formulated by the space-discrete vector $\mathbf{F}$ as

$$\mathbf{F}(t, \mathbf{y}, \mathbf{y}') = \begin{bmatrix} \mathbf{G}(t, \mathbf{u}, \mathbf{u}', \mathbf{q}) \\ \mathbf{L}(t, \mathbf{q}, \mathbf{q}', \mathbf{u}) \end{bmatrix} = \begin{bmatrix} \mathbf{M}\,\mathbf{u}' + \mathbf{k}(\mathbf{u}, \mathbf{q}) - \mathbf{f} \\ \mathbf{A}\,\mathbf{q}' - \mathbf{r}(\mathbf{q}, \mathbf{u}) \end{bmatrix} \stackrel{!}{=} \mathbf{0}\,, \tag{3.12}$$

where $\mathbf{y}'$, $\mathbf{u}'$ and $\mathbf{q}'$ are the time derivatives with respect to the solid motion. Moreover, $\mathbf{M}$ is the generalised mass matrix, and $\mathbf{k}$ corresponds to the generalised stiffness vector. Furthermore, $\mathbf{f}$ is the generalised external force vector containing the *Neumann* boundary conditions, and $\mathbf{A}$ is a regular identity matrix (Acartürk [2], Ammann [6], Karajan [138]).

3.1.5 Temporal Discretisation

In the next step, the time discretisation of the semi-discrete initial-value problem is performed. In this context, the *Runge-Kutta* methods deal with the numerical time integration of differential equations of first order in time such as the equations contained in the vectors $\mathbf{G}$ and $\mathbf{L}$. In particular, a stiffly accurate, s-stage diagonally implicit *Runge-Kutta* (DIRK) method together with mixed-order FEM provides unconditionnally stable numerical solutions for the given problem. If instead, an explicit time integration scheme is applied, special stabilisation techniques have to be used, since explicit schemes are conditionally stable (Diebels *et al.* [56], Ellsiepen [83], Heider [111]). Amongst the existing DIRK methods, the implicit (backward) *Euler* method is the present concern. Herein, the time derivatives $\mathbf{y}'_n$, $\mathbf{u}'_n$ and $\mathbf{q}'_n$ of the vectors of unknowns $\mathbf{y}$, $\mathbf{u}$ and $\mathbf{q}$ at the n-th time step are approximated respectively as

$$\begin{aligned} \mathbf{y}'_n &= \frac{\mathbf{y}_n - \mathbf{y}_{n-1}}{\Delta t} = \frac{\Delta \mathbf{y}_n}{\Delta t} \quad \text{with} \quad \mathbf{y}_n = \mathbf{y}_{n-1} + \Delta \mathbf{y}_n\,, \\ \mathbf{u}'_n &= \frac{\mathbf{u}_n - \mathbf{u}_{n-1}}{\Delta t} = \frac{\Delta \mathbf{u}_n}{\Delta t} \quad \text{with} \quad \mathbf{u}_n = \mathbf{u}_{n-1} + \Delta \mathbf{u}_n\,, \\ \mathbf{q}'_n &= \frac{\mathbf{q}_n - \mathbf{q}_{n-1}}{\Delta t} = \frac{\Delta \mathbf{q}_n}{\Delta t} \quad \text{with} \quad \mathbf{q}_n = \mathbf{q}_{n-1} + \Delta \mathbf{q}_n\,, \end{aligned} \tag{3.13}$$

where Δt is the time increment, and $\mathbf{y}_{n-1}$, $\mathbf{u}_{n-1}$ and $\mathbf{q}_{n-1}$ represent the vectors of unknowns at the $(n-1)$-th time step.

In order to conclude the time discretisation procedure, equation (3.13) is inserted into the global and local systems of equations given in (3.12), yielding

$$\begin{aligned} \mathbf{F}_n(t_n, \mathbf{y}_n, \frac{\Delta \mathbf{y}_n}{\Delta t}) &= \begin{bmatrix} \mathbf{G}_n(t_n, \mathbf{u}_n, \dfrac{\Delta \mathbf{u}_n}{\Delta t}, \mathbf{q}_n) \\ \mathbf{L}_n(t_n, \mathbf{q}_n, \dfrac{\Delta \mathbf{q}_n}{\Delta t}, \mathbf{u}_n) \end{bmatrix} = \begin{bmatrix} \mathbf{M}\,\dfrac{\Delta \mathbf{u}_n}{\Delta t} + \mathbf{k}(\mathbf{u}_n, \mathbf{q}_n) - \mathbf{f} \\ \mathbf{A}\,\dfrac{\Delta \mathbf{q}_n}{\Delta t} - \mathbf{r}(\mathbf{q}_n, \mathbf{u}_n) \end{bmatrix} \\ &= \mathbf{R}_n(\Delta \mathbf{y}_n) \stackrel{!}{=} \mathbf{0}\,. \end{aligned} \tag{3.14}$$

Herein, the nonlinear functional $\mathbf{R}_n(\Delta \mathbf{y}_n)$ has to vanish after solving the nonlinear equation system with respect to the unknown increment $\Delta \mathbf{y}_n$.

3.2 Numerical Solution Procedure

A convenient way to solve the nonlinear system formulated in (3.14) is proposed by the *Newton-Raphson* method. In particular, the *Jacobi*an (tangent) matrix $\mathbf{J}_n = \dfrac{\mathrm{d}\mathbf{R}_n}{\mathrm{d}\Delta\mathbf{y}_n}$ of the system has a block-structured nature (Karajan [138], Markert [172]). For this purpose, the use of the generalised Block *Gauß-Seidel-Newton* method, also called the multi-level or two-stage *Newton* procedure, is appropriate. More information about the solution procedure is given in Ellsiepen [83] and Diebels *et al.* [56]. In this regard, a local *Newton-Raphson* scheme is applied for each substep of the global *Newton* iteration. In particular, the local system containing the nonlinear evolution equations $\mathbf{L}_n$ is first solved for the local increments $\Delta\mathbf{q}_n$ of the internal variables. Regarding the history variables $\Delta\mathbf{q}_{n,ISO}$ related to the intrinsic viscoelasticity of the ECM, a local *Newton-Raphson* procedure with given increments of $\Delta\mathbf{u}_n$ provides a local solution at each integration point Q and for each *Maxwell* element N.

In terms of the internal variables $\Delta\mathbf{q}_{n,\mathrm{ANI}} = [(J_{S4i})_1, ..., (J_{S4i})_N]^T$ referring to the viscous behaviour of the anisotropic structure, the numerical implementation is treated as follows. For clarity reasons, the evolution equation (2.46) of the inelastic counterpart of the fibre stretch is expressed for one *Maxwell* element ($N = 1$) as

$$(J_{S4i})'_S = J_{S4}^{-1}\,\frac{1}{\eta_f}\sum_{m=1}^{M_{fe}}(\widetilde{\mu}_m)_1\,(J_{S4e}^{((\widetilde{\gamma}_m)_1/2)} - 1)\,. \tag{3.15}$$

Equation (3.15) is discretised in time by means of an implicit *Euler*ian scheme as

$$(J_{S4i})'_S = \frac{J_{S4i,n} - J_{S4i,n-1}}{\Delta t}\,, \tag{3.16}$$

where $J_{S4i,n}$ is the unknown viscous counterpart of the fibre stretch at the n-th time step, and $J_{S4i,n-1}$ is the preceding value of the viscous counterpart of the fibre stretch at the $(n-1)$-th time step. A local residuum r_n of the form

$$r_n = J^k_{S4i,n} - J_{S4i,n-1} - J_{S4}^{-1}\,\frac{\Delta t}{\eta_f}\sum_{m=1}^{M_{fe}}(\widetilde{\mu}_m)_1\,\Big[\Big(\frac{J_{S4}}{J^k_{S4i,n}}\Big)^{((\widetilde{\gamma}_m)_1/2)} - 1\Big] \overset{!}{=} 0 \tag{3.17}$$

is evaluated and numerically solved using a *Newton-Raphson* iteration process to meet the requirement $||r_n|| < \varepsilon_{loc}$, where ε_{loc} is a given tolerance. Herein, $J^k_{S4i,n}$ is the viscous counterpart of the fibre stretch at the n-th time step after the k-th local *Newton* iteration. For instance, the $(k+1)$-th *Newton* iteration delivers the value $J^{(k+1)}_{S4i,n}$ at the n-th time iteration, yielding

$$J^{(k+1)}_{S4i,n} = J^k_{S4i,n} - r_n\,\Big(\frac{\mathrm{d}r_n}{\mathrm{d}J^k_{S4i,n}}\Big)^{-1}\,. \tag{3.18}$$

In this context, $\dfrac{\mathrm{d}r_n}{\mathrm{d}J^k_{S4i,n}}$ is the derivative of r_n calculated as

$$\frac{\mathrm{d}r_n}{\mathrm{d}J^k_{S4i,n}} = 1 + \frac{\Delta t}{2\,\eta_f}\sum_{m=1}^{M_{fe}}(\widetilde{\mu}_m)_1\,(\widetilde{\gamma}_m)_1\,\frac{J_{S4}^{((\widetilde{\gamma}_m)_1/2-1)}}{(J^k_{S4i,n})^{((\widetilde{\gamma}_m)_1/2+1)}}\,. \tag{3.19}$$

After updating sequentially the isotropic and anisotropic contributions of the internal variables, the overall new vector $\mathbf{q}_n^{m,k+1}$ of the internal variables at the $(k+1)$-th local *Newton-Raphson* iteration is

$$\mathbf{q}_n^{m,k+1} = \mathbf{q}_n^{m,k} + \Delta\mathbf{q}_n^{m,k} \,. \tag{3.20}$$

Following this, the consistent global *Jacobi*an (tangent) matrix $\mathbf{J}_{\mathbf{G}_n} = \dfrac{\mathrm{d}\mathbf{G}_n}{\mathrm{d}\Delta\mathbf{u}_n}$, which indirectly depends on $\Delta\mathbf{q}_n$, can be computed.

As a next step, the global system $\mathbf{G}_n$ is solved for the *Newton* increment $\Delta\mathbf{u}_n^m$ by means of the iterative method of the generalised minimal residual (GMRES) (Saad & Schultz [220], Wieners *et al.* [252]). This method is faster and less memory consuming than direct solvers for large DAE systems. In this case, the simplified *Newton* method is applied in order to avoid a multiple calculation of the *Jacobi*an matrix for each *Newton* step, in contrast to the standard *Newton* method.

After solving the system, the global vector $\mathbf{u}_m$ at the m-th global *Newton-Raphson* iteration is updated as

$$\mathbf{u}_n^{m+1} = \mathbf{u}_n^m + \Delta\mathbf{u}_n^m \,. \tag{3.21}$$

Here again, the iteration process is performed until the condition on the L_2-norm of the function vector $\mathbf{G}_n$ is fulfilled, i. e., $||\mathbf{G}_n|| < \varepsilon_{glob}$, where ε_{glob} is a given tolerance.

Chapter 4: Model Refinement

In this chapter, the constitutive model presented in Chapter 2 is refined to make it possible to describe the behaviour of multiphasic, anisotropic, viscoelastic materials such as articular cartilage and skin tissue. The aim is to extend the existing model with required additional features such as anisotropy or heterogeneity. In particular, sections 4.1 and 4.2 are related to specific properties observed in articular cartilage. The modelling of these specifications in the proposed model is thorougly explained. In sections 4.3 and 4.4, further properties such as anisotropic viscoelasticity and fibre-matrix shear interaction are investigated. The presented numerical simulations introduce the central topics of model calibration and sensitivity analysis addressed in Chapter 5. Finally, section 4.5 proposes a first reduction of the computational model.

4.1 Main Features of Articular Cartilage

4.1.1 Description of Cartilage

Within the human body, there are three different types of cartilage with slightly varying structures and functions, i. e., elastic cartilage, fibrocartilage and hyaline or articular cartilage (see Figure 4.1). Articular cartilage is the most abundant type.

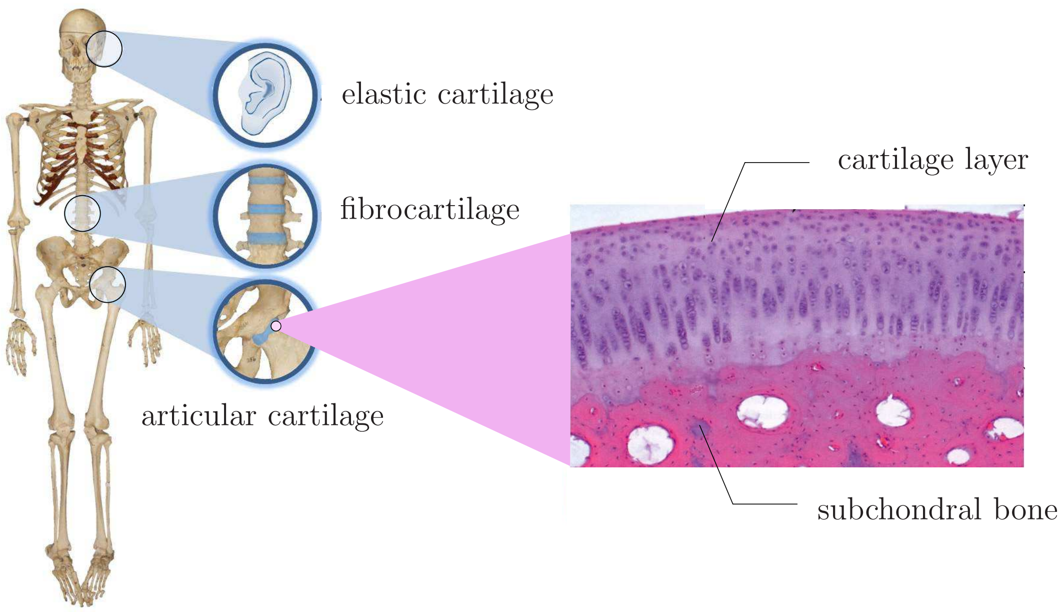

Figure 4.1: *Cartilage types in the human body (left) [http://lyceum.algonquincollege.com] and section through cartilage layer and subchondral bone (right) [http://www.vetmed.vt.edu].*

Along with the synovial fluid, articular cartilage enables smooth motion within synovial joints and acts as a shock absorber. Furthermore, it contributes to an even distribution of the loads between the femoral head and the acetabular cup in a synovial joint.

In its healthy state, articular cartilage is an aneural and avascular, soft biological tissue consisting of a bluish-white, smooth and shiny ground elastic material into which collagen fibrils and cartilage cells are embedded. In this context, cartilage can be regarded as a multiphase material. Approximately 70 to 85% of the weight of the whole tissue comprises interstitial water. The remainder of the tissue is composed primarily of proteoglycans (PG) and collagen (Maroudas [178], Mow *et al.* [191]). PG consist of a protein core to which glycosaminoglycans (chondroitin sulfate and keratan sulfate) are connected to each other, forming a bottlebrush-like structure. Approximately 30% of the dry weight of articular cartilage is composed of PG, while collagen makes up the remaining 60 to 70%. Collagen type II is predominant in articular cartilage, although other types are present in smaller amounts.

4.1.2 Arcade-Like Collagen Structure

In early 1925, Benninghoff [22] suggested a simplified arcade-like form of the collagen structure related to the cartilage layer of the femoral head (see Figure 4.2, left). Later, the exact ultrastructure of articular cartilage could be visualised by means of light and electron microscopes (Broom & Myers [42]) and also magnetic resonance imaging (MRI) techniques (Azuma *et al.* [12], Gründer [100]). The arrangement of collagen fibres can be divided into three distinct zones between the surface of articular cartilage and the subchondral bone (see Figure 4.2, right). Directly underneath the articular surface is the superficial zone, where the collagen fibres are tangentially oriented to the articular surface. This zone neighbours the middle zone, where the fibrils are randomly oriented. In the deep zone connecting to the subchondral bone, they are perpendicularly aligned to the bone surface and anchored into the subchondral bone.

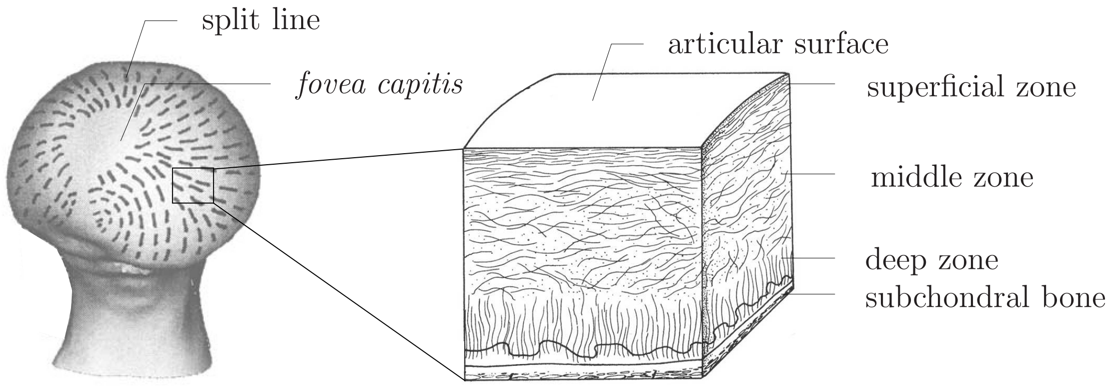

Figure 4.2: *Top view of the femoral head with split-line contours (left) (Lieser [160]) and schematic representation of a section through the cartilage layer with fibre orientation (right) [http://www.jaaos.org].*

From a mathematical point of view, the arcade-like fibre alignment is represented by the fibre vector $\mathbf{a}_0^S$ in the reference configuration. The angular variation ϕ_0^S of the direction of $\mathbf{a}_0^S$ with respect to the normal direction $\mathbf{n}$ to the articular surface is calculated at each *Gauß* point (GP) using a function of the normalised depth $\tilde{z} = z/h$, starting from the articular surface (see Figure 4.3).

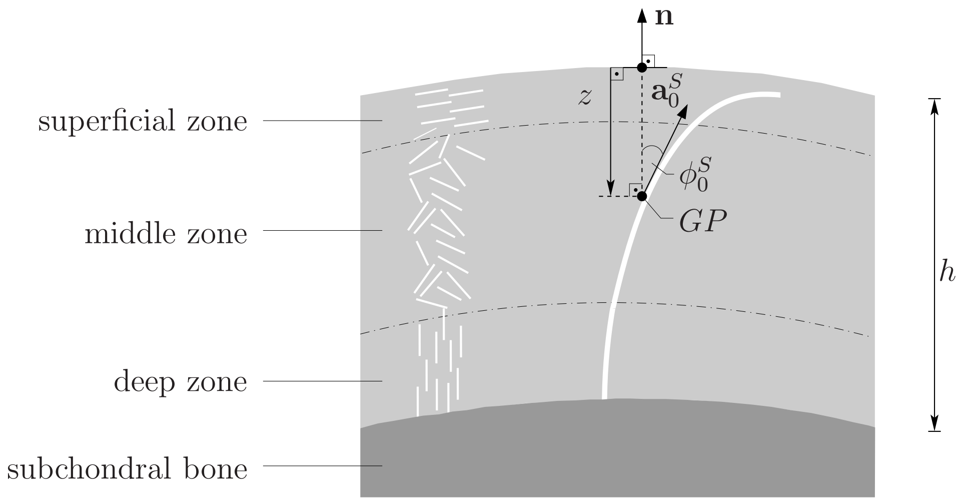

Figure 4.3: *Angular fibre variation ϕ_0^S as a function of the normalised depth $\tilde{z} = z/h$.*

In particular, the angle ϕ_0^S (in radians) is approximated by the function

$$\phi_0^S = \frac{\pi}{2} (\tilde{z} - 1)^2 . \tag{4.1}$$

If $\tilde{z} = 0$, the fibres are parallel to the articular surface, i. e., $\phi_0^S = \pi/2$ while they are oriented perpendicularly to the cartilage-bone interface, i. e., $\phi_0^S = 0$, if $\tilde{z} = 1$.

Then, the components of $\mathbf{a}_0^S$ are stored at each GP of the spatial domain as internal (history) variables. The same procedure is used for the depth-dependent heterogeneities of cartilage addressed in section 4.2.1. Further information about FE modelling of inhomogeneities related to intervertebral discs is given by Karajan [138].

4.1.3 Split-Line Contours

Figure 4.2 (left) also shows preferred orientations of the collagen network structure at the cartilage surface of the femoral head, which can be revealed by means of the split lines. Split lines are observed after puncturing the cartilage surface at multiple sites with a circular awl. The resulting holes are not circular but elliptical. The long axes of the ellipses are aligned in a so-called split-line direction. The direction of the split lines matches that of the highest tensile stresses within the cartilage (Bae *et al.* [15], Lieser [160]).

In the modelling, the split lines are assumed to be radial to the *fovea capitis*, the pit on the femoral head, where the ligament inserts, and oriented in the direction of the beeline between the cartilage margins. Here, the zones of circular distribution of the split lines (Lieser [160]) are neglected.

4.2 Further Properties of Cartilage

4.2.1 Depth-Dependent Heterogeneities

The inhomogeneous distribution of the collagen structure within the cartilage layer leads to inhomogeneous features of articular cartilage (Lipshitz *et al.* [165], Mow *et al.* [192]). The distribution $\dfrac{n^S_{\text{coll}}}{n^S}$ of the collagen fibres with respect to the solid constituent is depicted in Figure 4.4 (left) based on Wilson *et al.* [255]. This distribution is approximated by a quadratic function of the normalised depth $\tilde{z}$ of the form (Wilson *et al.* [255])

$$\frac{n^S_{\text{coll}}}{n^S} = 1.4\,\tilde{z}^2 - 1.1\,\tilde{z} + 0.59\,. \tag{4.2}$$

The expression in (4.2) is then inserted into the calculation of the extra mechanical stresses $\mathbf{T}^S_{E,mech}$ formulated in (2.32).

Note that recent studies of Lilledahl *et al.* [162] involved a detailed characterisation of the anisotropy using an imaging process. Therein, $\dfrac{n^S_{\text{coll}}}{n^S}$ was associated to the dispersion parameter of the collagen fibres over the depth of the cartilage layer.

Next, observations of Maroudas [178] about the variation of the specific permeability K^F_{0S} over the cartilage layer are depicted in Figure 4.4 (right). The variation of K^F_{0S} is approximated by means of a quadratic function of the normalised depth $\tilde{z}$ reading

$$K^F_{0S} = (-2.14\,\tilde{z}^2 + 1.67\,\tilde{z} + 0.88)\,\bar{K}^F_{0S} \quad [\text{mm}^4/\text{N s}]\,, \tag{4.3}$$

where $\bar{K}^F_{0S}$ is the mean value over the cartilage domain.

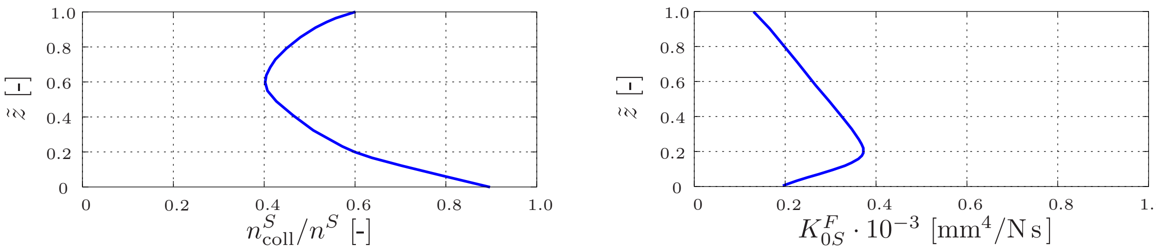

Figure 4.4: *Distribution of the collagen fibres [255] (left) and measured specific permeability [178] (right).*

The porosity also displays a heterogeneous distribution throughout the cartilage (Lipshitz *et al.* [165], Wilson *et al.* [255]), as depicted in Figure 4.5 (left). This distribution is inspired from Wilson *et al.* [255], yielding

$$n^F_{0S} = (1.13\,-\,0.26\,\tilde{z})\,\bar{n}^F_{0S}\,, \tag{4.4}$$

where $\bar{n}^F_{0S}$ is the mean initial porosity.

Another heterogeneity is caused by the unequal distribution of the fixed charge's density over the cartilage layer's thickness, as depicted in Figure 4.5 (right) (Wilson *et al.* [255]).

The distribution of the concentration of the fixed charges is defined by a quadratic function of the normalised depth. After modification of Wilson *et al.* [255] using the mean value $\bar{c}^{fc}_{m,0S}$ of the initial concentration of the fixed charges over the cartilage domain, it reads

$$c^{fc}_{m,0S} = (-0.82\,\tilde{z}^2 + 1.97\,\tilde{z} + 0.29)\,\bar{c}^{fc}_{m,0S} \quad [\text{mol/l}]\,. \tag{4.5}$$

The concentration of the fixed charges is also influenced by another phenomenon whose mechanical significance has been advocated by Maroudas & Bannon [180], Maroudas *et al.* [181] and Urban & McMullin [246]. A part of the interstitial pore fluid is attached to the collagen fibres and hence, is chemically inactive (Lipshitz *et al.* [165]). Therefore, the effective concentration $c^{fc}_{m,\text{eff}}$ of the fixed charges is defined as the freely movable extrafibrillar part of the initial concentration $c^{fc}_{m,0S}$ of the fixed charges, yielding (Wilson *et al.* [255])

$$c^{fc}_{m,\text{eff}} = c^{fc}_{m,0S}\,\frac{n^F_{0S}}{n^F_{\text{free},0S}}\,, \tag{4.6}$$

where $n^F_{\text{free},0S}$ represents the initial volume ratio of the freely movable, interstitial pore fluid as follows (Wilson *et al.* [255]):

$$n^F_{\text{free},0S} = (-1.96\,\tilde{z}^2 + 0.01\,\tilde{z} + 3.2)\,\bar{n}^F_{0S}\,. \tag{4.7}$$

The effective concentration $c^{fc}_{m,\text{eff}}$ formulated in (4.6) is then substituted to $c^{fc}_{m,0S}$ in the calculation of the concentration of the fixed charges given in (2.27).

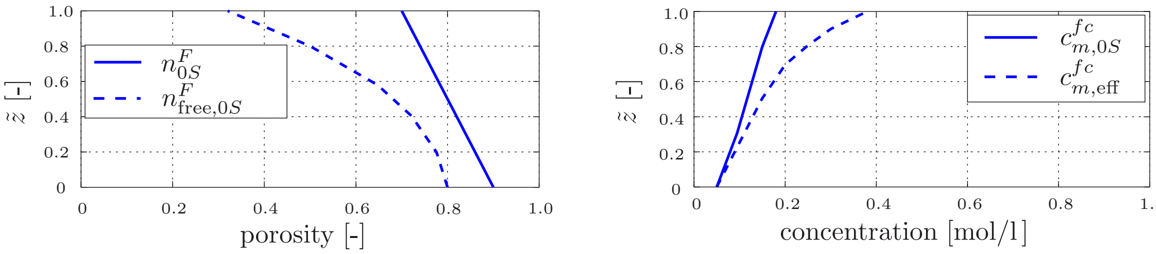

Figure 4.5: *Distribution of porosity [255] (left) and fixed charge's concentration [255] (right).*

4.2.2 Deformation- and Flow-Dependent Properties

Regarding the properties describing the interstitial pore-fluid flow, it can be observed that permeability depends on the deformation state (Maroudas [178]) and the pressure gradient, as depicted in Figure 4.6. Figure 4.6 (left) clearly represents to what extent the applied pressure gradient modifies the measured permeability. The linear dependence between the interstitial fluid flow and the hydraulic gradient breaks down. In other words, a traditional *Darcy* law for lingering flows driven by slight pressure gradients does not hold in the present case.

Furthermore, experimental observations suggest different permeability properties for the radial and axial directions (Quinn *et al.* [211], Reynaud & Quinn [216]). Figure 4.6 (right) depicts the variation of the ratio between measured radial and axial permeabilities with respect to the compressive strain at different stress states. Further investigations reveal the significant influence of the collagen fibres' disposition on the pore-fluid flow (Federico & Herzog [86], Reynaud & Quinn [216]).

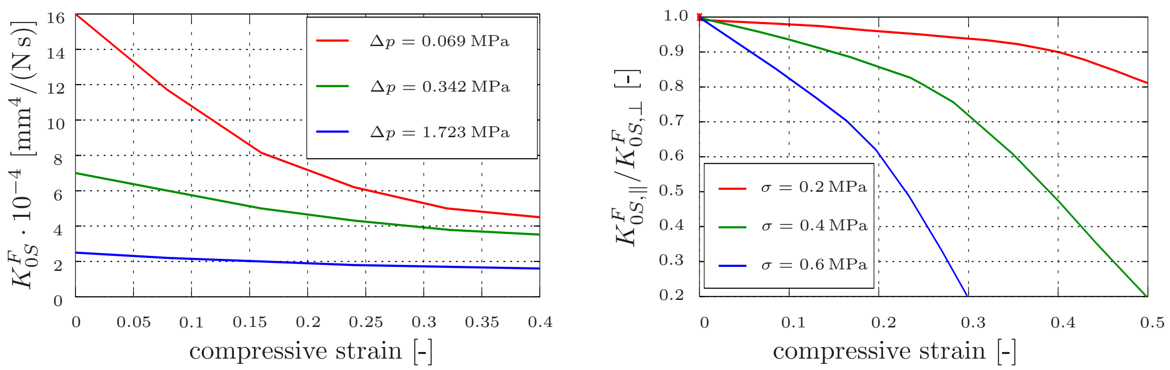

Figure 4.6: *Permeability at different strain states and applied pressure differences [178] (left) and anisotropic permeability at different stress states [211] (right).*

4.3 Application to Anisotropic Viscoelasticity

This section is devoted to the extension and application of the constitutive viscoelastic formulation presented in Chapter 2. The viscoelastic properties of the collagen fibres are investigated in order to isolate the important anisotropic features of collagen from the influences of the ECM. The focus lies on numerical investigations of the fibre viscoelasticity and on its evaluation by means of academic numerical examples.

4.3.1 Tensile Test

First, the results obtained using the presented model are compared with tensile tests on anisotropic materials. The experimental data for relaxation are adopted from Sanjeevi *et al.* [225]. The experiments concern the stress relaxation of dry collagen fibres ($l =$ 10 mm) of rat tail tendons after a displacement jump is applied. The simulation is carried out over 400 s on a geometry, which is discretised using 20 horizontally aligned, 20-noded hexahedral $Taylor$-$Hood$ elements, yielding 828 DOF. To express the pressure boundary conditions, the excess pressure $\bar{\mathcal{P}} = \mathcal{P} - \mathcal{P}_0$ is defined with respect to the atmospheric pressure $\mathcal{P}_0$. In the present case, all boundary surfaces are perfectly drained, i. e., $\bar{\mathcal{P}} = 0$, in order to concentrate only on the effects from the viscoelastic fibres. Besides, the permeability and the solidity are artificially raised, and the stiffness of the matrix is extremely decreased. The boundary surfaces of the geometry are fixed in the out-plane direction, to mimic the one-dimensional behaviour of collagen fibres, except the lateral surface on the right-hand side, which undergoes a horizontal displacement $\bar{\mathbf{u}}_S(t)$, as shown in the IBVP in Figure 4.7.

In the first step, a horizontal displacement of $|\bar{\mathbf{u}}_S(t)| = 1$ mm is applied as a step function in the fibre direction. The experimental and numerical results obtained with PANDAS are compared in Figure 4.8 after a short manual calibration. The stress response, i. e., the average stress related to the reaction force in the direction of the applied displacement, is represented over the simulation time. The blue curve with cross points refers to the results obtained from the experiment, and the red line indicates the simulation results.

It appears that the presented model with the optimised parameter set given in Table 4.1, using one polynomial term ($M_f = 1$) for the equilibrium part and one *Maxwell* element ($N = 1$) with one polynomial term ($M_{fe} = 1$) for the non-equilibrium part, leads to an excellent approximation of the experimental results.

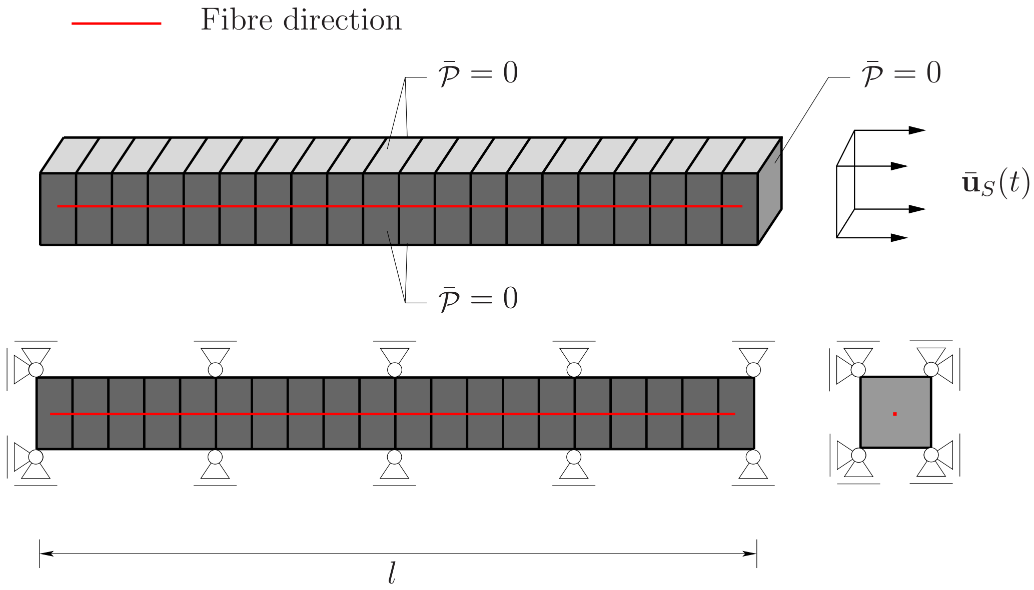

Figure 4.7: *IBVP of the stress relaxation experiment and dimension of meshed geometry (length $l = 10\,\mathrm{mm}$) (top), side view (bottom, right) and plan view (bottom, left).*

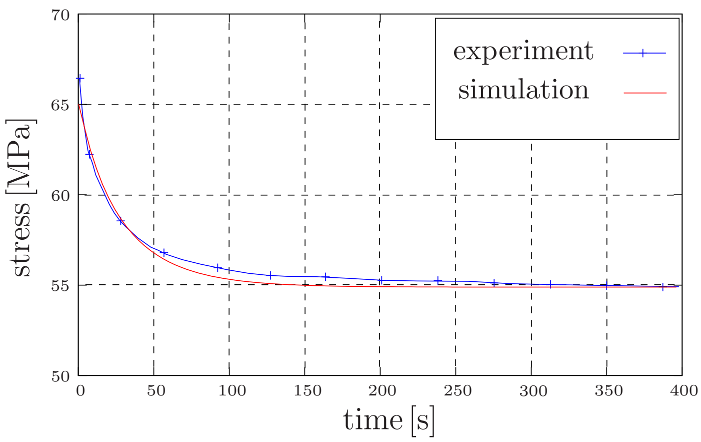

Figure 4.8: *Stress relaxation of a dry collagen fibre.*

Properties of	Type	Notation	Range	Unit
matrix and fibres	matrix elasticity	μ_0^S	$0.3 \cdot 10^{-4}$	MPa
		λ_0^S	$0.1 \cdot 10^{-4}$	MPa
		γ_0^S	1.0	-
	fibre elasticity	$\widetilde{\mu}_1$	287.52	MPa
		$\widetilde{\gamma}_1$	2.0	-
	fibre viscoelasticity	$(\widetilde{\mu}_1)_1$	54.32	MPa
		$(\widetilde{\gamma}_1)_1$	2.0	-
		η_f	1228.68	MPa s
pore-fluid flow	porosity	n_{0S}^F	0.01	-
	effective fluid density	ρ^{FR}	10^{-6}	kg/mm^3
	permeability	K_{0S}^F	6.9	mm^4/N s

Table 4.1: *Optimised constitutive parameters.*

4.3.2 Loading-Holding Experiment

In the next step, the numerical model is calibrated with the experimental data presented by Sanjeevi [224]. The same geometrical arrangement as depicted in Figure 4.8 is used. Figure 4.9 presents the stress response when the specimen experiences a displacement $\bar{\mathbf{u}}_S(t)$ with a rate of $|(\mathbf{u}_S)'_S| = 0.012\,\text{mm/s}$. The calculated non-equilibrium and equilibrium contributions of the stress response are shown separately by means of the blue and red curves, respectively. The curves with crossed points are the experimental equivalents. Furthermore, the stress decay at small intervals of strain due to the loading-holding imposition is indicated by the red dashed line.

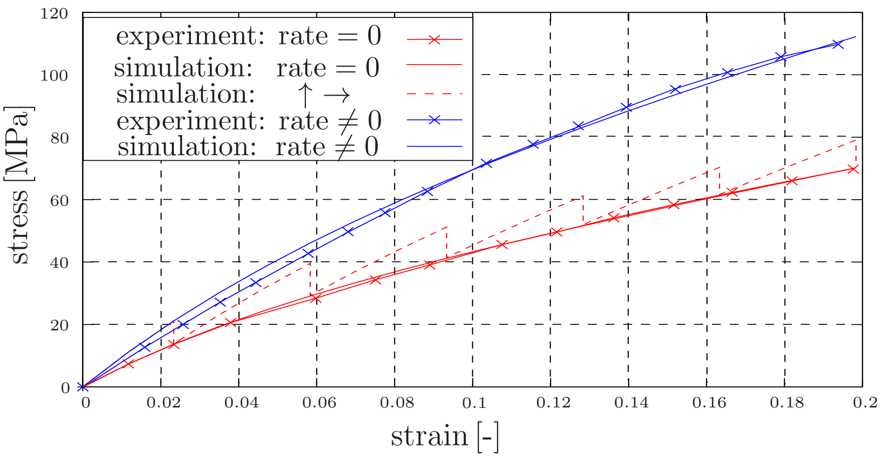

Figure 4.9: *Stress-strain diagram for tension test on dry collagen fibres.*

The material parameters with two polynomial terms ($M_f = 2$) for the equilibrium part and two *Maxwell* elements ($N = 2$) with one polynomial term ($M_{fe} = 1$) for the non-equilibrium part lead to the presented numerical results after a short parameter optimisation by hand. The material parameters are summarised in Table 4.2.

Properties of	Type	Notation	Range	Unit
matrix and fibres	matrix elasticity	μ_0^S	$0.3 \cdot 10^{-4}$	MPa
		λ_0^S	$0.1 \cdot 10^{-4}$	MPa
		γ_0^S	1.0	-
	fibre elasticity	$\widetilde{\mu}_1$	110.74	MPa
		$\widetilde{\gamma}_1$	2.5	-
		$\widetilde{\mu}_2$	-21.56	MPa
		$\widetilde{\gamma}_2$	-18.4	-
	fibre viscoelasticity	$(\widetilde{\mu}_1)_1$	350.84	MPa
		$(\widetilde{\gamma}_1)_1$	2.0	-
		$(\widetilde{\mu}_1)_2$	-177.38	MPa
		$(\widetilde{\gamma}_1)_2$	2.0	-
		η_f	3430.0	MPa s
pore-fluid flow	porosity	n_{0S}^F	0.01	-
	effective fluid density	ρ^{FR}	10^{-6}	kg/mm^3
	permeability	K_{0S}^F	6.9	mm^4/N s

Table 4.2: *Optimised constitutive parameters.*

4.4 Application to Fibre-Matrix Shear Interaction

After investigating the intrinsic viscoelasticity of fibres, the next focus is on the shear interactions between the fibres and the surrounding ground matrix. Parameter studies are performed on a homogeneous, poroelastic, anisotropic material roughly related to the human skin, for the following reasons. First, the computational effort when using the complex model instead of a simplified one bears no relation to the gained information. Second, the application of the complex constitutive model of cartilage would require calibration strategies which go beyond the scope of this section (see Chapter 5). The aim of the simplistic modelling in this section is obviously not to capture the features of complex multi-layered structures such as skin tissues (Groves *et al.* [99], Naresh *et al.* [200], Pailler-Mattei *et al.* [206], Ridge & Wright [218]). Instead, general considerations of an academic case for the purpose of numerical investigations on shear interactions are addressed here.

4.4.1 Concept of Tensile Tests on Notched Specimens

A concept of experimental procedure is proposed for identifying the material parameters μ_{int} and α_{int} related to the shear interaction between fibres and matrix. To "activate" the shear interaction phenomena, a tensile test on notched specimens is proposed. Two different configurations ($L = 20\,\text{mm}$, $h = 1\,\text{mm}$) are compared and evaluated with respect to their ability to model shear interaction phenomena. In configuration 1 (Figure 4.10, top), a notch (length l_1) is cut at mid-length of the specimen, which spans between two loading clamps. In configuration 2 (Figure 4.10, bottom), two notches are modelled. For both configurations, a notch length ratio $e = l_1/L = (l_1 + l_1)/2L$ is defined. A horizontal displacement $|\bar{\mathbf{u}}_S(t)| = 4\,\text{mm}$ is applied as a step function in the fibre direction, and the resulting reaction force is calculated numerically. All surfaces are perfectly drained ($\bar{\mathcal{P}} = 0$). Due to symmetry conditions, the simulation is performed on a half (for configuration 1) or a quarter (for configuration 2) of the geometry. The domain is discretised using 968 20-noded, hexaedral *Taylor-Hood* elements, yielding 18 630 DOF.

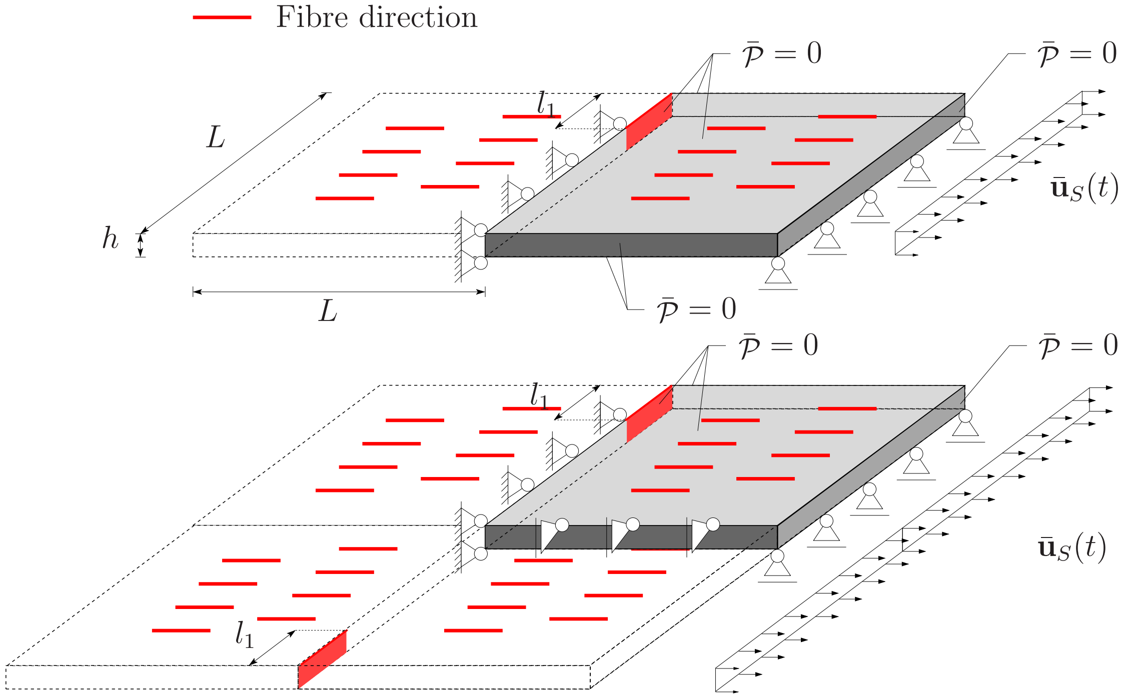

Figure 4.10: *IBVP of configuration 1 (top) and 2 (bottom) and dimensions of geometry (length $L = 20\,\text{mm}$, thickness $h = 1\,\text{mm}$, notch length l_1).*

4.4.2 Influence of the Involved Parameters

In order to determine the value of the material parameters experimentally, the sensitivity of the calculated reaction force to the interaction parameters is first evaluated. The specimen under consideration is modelled as a skin tissue, where the fibres are oriented parallel to *Langer*'s lines in the direction of the applied displacement. *Langer*'s lines correspond to the natural orientation of the collagen fibres in the skin (Gallagher *et al.* [93]). The material parameters for the matrix and the fibres are obtained from the literature (Gallagher *et al.* [93], Groves *et al.* [99], Pailler-Mattei *et al.* [206], Silver *et al.* [232]). Experimental data regarding fibre-matrix interaction in articular cartilage are lacking. For the sake of clarity, only the interaction parameter μ_{int} is varied between 0.005 and 0.025 MPa, while the other interaction parameter α_{int} is kept constant. The complete set of material parameters used for the computations is given in Table 4.3.

The results are summarised in Figure 4.11. All graphs show the stress response of the material to the applied stretch (displacement) over strain. The difference between the figures is the notch length ratio e. For the four notch-length-ratio values and the high and low values of the interaction parameter, configurations 1 and 2 have been computed. The

Properties of	Type	Notation	Value/Range	Unit
matrix and fibres	matrix elasticity	μ_0^S	0.288	MPa
		λ_0^S	0.431	MPa
		γ_0^S	1.0	-
	fibre elasticity	$\widetilde{\mu}_1$	0.006	MPa
		$\widetilde{\gamma}_1$	2000	-
	matrix-fibre interaction	μ_{int}	[0.005-0.025]	MPa
		α_{int}	500	-
pore-fluid flow	porosity	n_{0S}^F	0.01	-
	effective fluid density	ρ^{FR}	10^{-6}	kg/mm^3
	permeability	K_{0S}^F	6.9	$\text{mm}^4/\text{N s}$

Table 4.3: *Chosen constitutive parameters.*

red curves relate to the calculated stress in configuration 1. Configuration 2 is presented by the green curve. The cases of low and high μ_{int}-values are described by simple curves and curves with colored dots, respectively.

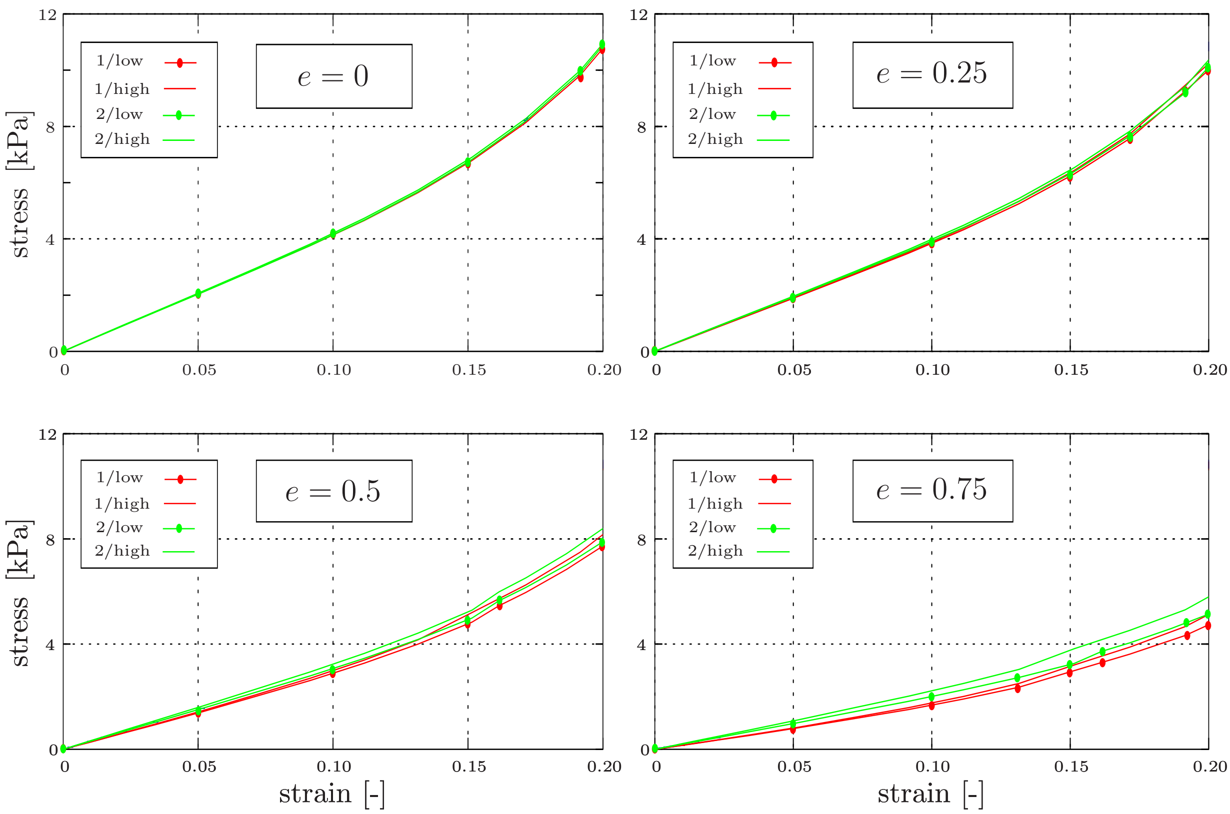

Figure 4.11: *Stress-strain diagrams for different notch length ratios e, configurations 1 and 2 and low and high values of the interaction parameter μ_{int}.*

It appears that not only the notch length ratios e but also the configuration type have an influence on the variation of the calculated stress. This observation is more noticeable in Figure 4.12. Therein, configurations 1 and 2 are compared with respect to the percentaged sensitivity $S = \dfrac{\Delta\sigma}{\Delta\mu_{\text{int}}} 100\,[\%]$ of the variation $\Delta\sigma$ of stress to the variation $\Delta\mu_{\text{int}}$ of the interaction parameter for different notch length ratios e. The crossed red curve and the crossed green curve describe the sensitivity calculated in configurations 1 and 2, respectively.

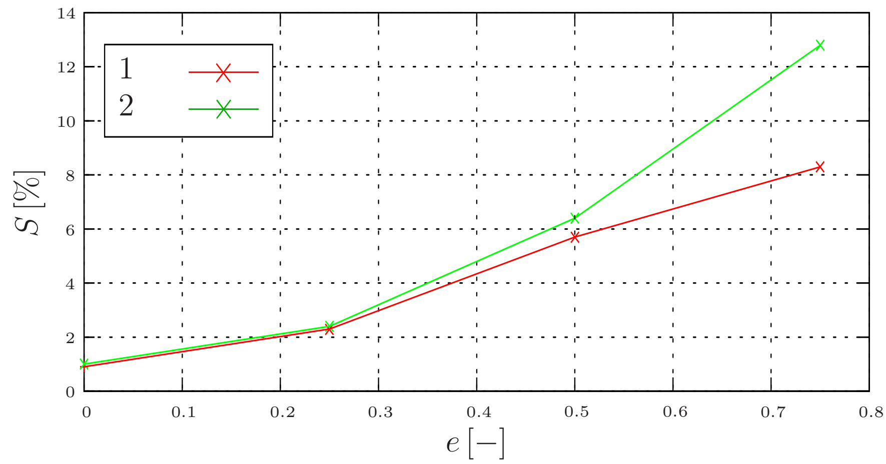

Figure 4.12: *Sensitivity S as a function of the notch length ratio e for configurations* 1 *and* 2.

Figure 4.13 clearly shows that configuration 2 with high values of e leads to an easier identification of the interaction parameter μ_{int} for the same applied displacement. In other words, for the same value of e, one observes a more widespread distribution of the overall in-plane shear stresses τ in configuration 2 than in configuration 1.

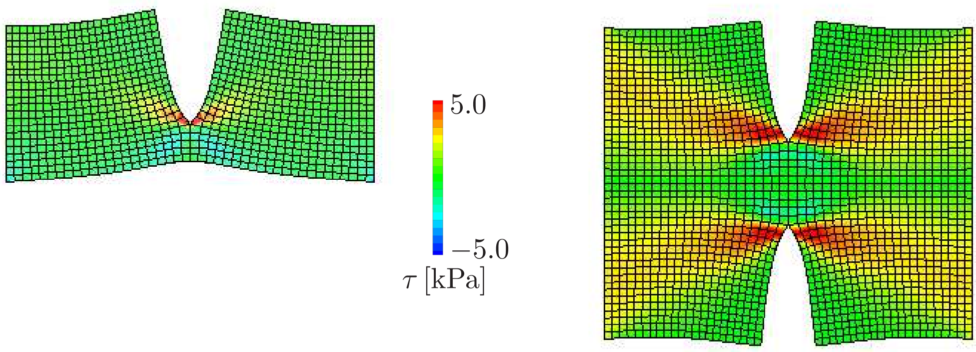

Figure 4.13: *Shear stress contours and mesh deformation in configuration* 1 *(left) and configuration* 2 *(right).*

A difference can also be observed in the deformation characteristics due to the consideration of the fibre-matrix shear component. Figure 4.14 represents the deformation contours with and without the influence of the fibre-ground-matrix shear interaction for configuration 2. More generally, the absence of the fibre-matrix shear interaction is a source of errors, when the deformation characteristics of the soft tissues are relevant (Gasser *et al.* [95], Peng *et al.* [208]). The origin of the incorrect deformation prediction is mostly related to the neglect of the increase of the matrix stiffness when the fibres are stretched. With a smaller matrix stiffness, the fibres rotate more easily in the matrix ground substance and match their direction to carry the loads. Subsequently, this excessive rotation leads to larger transverse deformations than the deformations observed through experimental data.

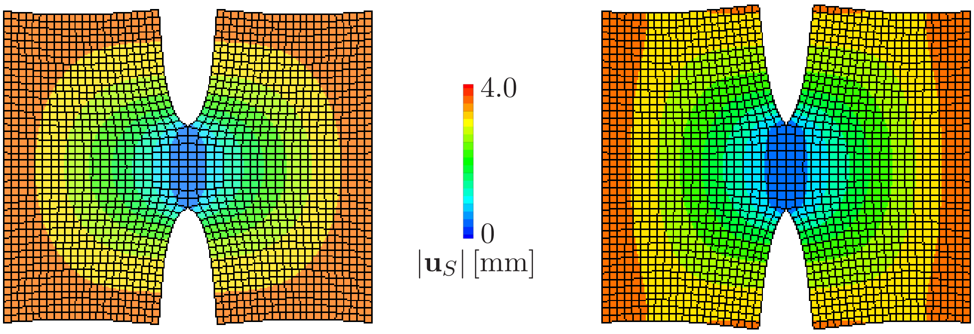

Figure 4.14: *Displacement contours and mesh deformation in configuration 2 without (left) and with (right) fibre-matrix shear interaction.*

4.5 First Model Reduction

After tackling the complexity of cartilage modelling in detail throughout this chapter, a first model reduction is performed.

The discussed interaction mechanisms between the ECM and the collagen fibres will not be further considered in the numerical model. Strong effects due to fibre-matrix shear interactions were only observable for large deformations (applied strain $> 20\%$), which do not occur in the investigated experiments related to articular cartilage. Subsequently, those effects are not part of the calibration strategy of Chapter 5.

Regarding the mechanical behaviour of the collagen fibres, the anisotropic viscoelasticity in articular cartilage is generally investigated using tensile tests. However, cartilage is a soft biological tissue mainly "designed" to resist compressive loads. In this regard, various studies prove that even though tensile stresses exist within cartilage, their values are relatively low (Eberhardt *et al.* [60, 61, 62]). From these considerations, the anisotropic viscoelastic effects resulting from the fibres are not treated in the already complex cartilage model.

Chapter 5: Strategy for Cartilage Model Calibration

As already mentioned in sections 4.3 and 4.4, the validity of a given numerical model cannot be investigated without addressing the central notion of model calibration, i. e., parameter identification and sensitivity analysis. Herein, these operations were mainly manageable due to the model's relative simplicity.

When considering the more complex case of articular cartilage described as a heterogeneous, anisotropic and osmotically swelling, poroviscoelastic solid, saturated by a fluid, as summarised in section 4.5, a consistent strategy has to be proposed. A consequence of the model complexity is the difficulty to estimate each constitutive parameter without utilising advanced numerical tools. Furthermore, some parameters might be coupled or cannot be identified accurately due to the lack of experimental data or technical literature. Moreover, a small error in the initial simulation may exponentially increase the model output when dealing with particularly "sensitive" parameters (Helton *et al.* [114], Iman *et al.* [126]). This chapter introduces a model calibration strategy in which different aspects, such as parameter identification and sensitivity analysis related to strongly coupled solid-fluid problems, are thoroughly discussed.

5.1 Method for Parameter Identification

Identifying parameters is an extremely delicate task when dealing with soft biological tissues such as articular cartilage. Many disruptive factors complexify an easy identification of parameters. In addition to difficult interpretable parameters related to the strongly coupled solid-fluid problem, other sources of errors have to be considered. Particularly, the storage conditions of the specimens, as well as the procedure chosen by the experimenter to test such tissues, are of great importance. Articular cartilage is also highly patient-specific, i. e., depends on various factors such as age and overall state of health. Hence, an adapted stepwise identification for multiple tests, combined with an individual parameter identification technique for each given test, shall be considered.

5.1.1 Stepwise Identification for Multiple Testing

In order to identify material-specific and unknown parameters correlated with the experimental data and given in the constitutive equations, a parameter optimisation strategy is proposed. First, the material parameters governing solid elasticity are estimated simultaneously for a given set of experimental tests. Then, the remaining parameters governing fluid viscosity and solid viscoelasticity are evaluated. In this context, an optimisation problem is solved, which implies the minimisation of a least-squares functional $f(\mathbf{s})$ subjected to a certain number of inequality constraints. At the end of the parameter identification process, a new variable vector of parameters generated from function values is obtained.

5.1.2 Constraint Optimisation by Linear Approximation

In this work, a trust-region method is chosen out of the available gradient-free methods for identifying the material parameters. This method rests upon a constraint optimisation by linear approximation (COBYLA) (Powell [210]). Its advantage lies in the individual treatment of the inequality constraints during the iterative optimisation procedure, instead of bringing together all constraints into a single penalty function. This method is also used because it allows black box computations with no direct access to material routines. In particular, a merit function compares the quality of different variable vectors with respect to the greatest constraint violation.

The objective function to minimise is

$$f(\mathbf{s}) = \sum_{n=1}^{N} w_n \, [\, \phi_n(\mathbf{s}) - \tilde{\phi}_n \,]^2 \,, \tag{5.1}$$

depending on the vector $\mathbf{s}$ of constitutive parameters and subjected to N_{inq} inequality constraints

$$g(\mathbf{s}) = g_k\,(\mathbf{s}) \geq 0 \,, \; k = 1, ..., N_{inq} \,. \tag{5.2}$$

Herein, $\tilde{\phi}_n$ is the experimental output, and $\phi_n(\mathbf{s})$ is the output of the simulation. Besides, w_n and N are the weighting factors and the number of data points, respectively.

5.2 Method for Sensitivity Analysis

One important approach in the identification of uncertainty is sensitivity analysis. Sensitivity analysis estimates how variations in the model output can be deduced from variations in model parameters (Crosetto *et al.* [52]).

A broad spectrum of sensitivity-analysis techniques is currently available (Crosetto *et al.* [52], Helton [113]). In the following section, a local sensitivity analysis is conducted for the sake of computational simplicity. A more comprehensive overview of the theoretical background is provided by Ehlers & Scholz [79].

5.2.1 Definition of Sensitivity Vectors

The sensitivity vectors $\dfrac{\mathrm{d}\phi_n}{\mathrm{d}\mathbf{s}}$ are contained in the objective function derivative in the form of

$$\frac{\mathrm{d}f(\mathbf{s})}{\mathrm{d}\mathbf{s}} = 2 \sum_{n=1}^{N} w_n \, \frac{\mathrm{d}\phi_n}{\mathrm{d}\mathbf{s}} \, [\, \phi_n(\mathbf{s}) - \tilde{\phi}_n \,] \,. \tag{5.3}$$

In particular, the i-th component of the sensitivity vector is numerically calculated by means of the forward difference method as

$$\left.\frac{\mathrm{d}\phi_n}{\mathrm{ds}}\right|_{\hat{s}_i} \approx \frac{\phi_n(\hat{s}_i + \Delta\, s_i) - \phi_n(\hat{s}_i)}{\Delta\, s_i}\,, \tag{5.4}$$

where $\hat{s}_i$ is the i-th entry in the set of parameters, and the increment $\Delta\, s_i$ is chosen to avoid truncation and round-off errors.

5.2.2 Derivation of Correlation Matrices

Next, the conjoint effects of the change of two material parameters $\hat{s}_i$ and $\hat{s}_j$ on the material response $\tilde{\phi}_n$, i. e., the covariances k_{ij} (with $i \neq j$), are gathered in the covariance matrix $\mathbf{K}$, yielding

$$\mathbf{K} = \Big[\sum_{n=1}^{N} \frac{\mathrm{d}\phi_n}{\mathrm{ds}} \Big(\frac{\mathrm{d}\phi_n}{\mathrm{ds}}\Big)^T\Big]^{-1}. \tag{5.5}$$

The correlation coefficients r_{ij} are obtained after normalisation of the covariances as

$$r_{ij} = \frac{k_{ij}}{\sqrt{k_{ii}\, k_{jj}}} \tag{5.6}$$

and gathered in the correlation matrix, which is *per se* symmetric. The values of the correlation matrix entries vary between -1 and 1. A strong correlation between material parameters is indicated by $|r_{ij}| \approx 1$. In this case, the origin of an observed phenomenon cannot be precisely assigned to one or another parameter, which handicaps a unique parameter identification. Furthermore, if incertitude exists on the measurement of this parameter, a rigorous parameter finding is almost impossible for a given set of experiments.

Note in passing that the correlation matrix only offers valuable clues to the sensitivity analysis. Contrary to the uncertainty analysis, where the parameter importance is investigated, only the parameter sensitivity is examined. In this regard, an important parameter is always sensitive with respect to the output. However, a sensitive parameter is not necessarily important and thus might have only a slight influence on the output.

5.3 Cartilage Model Calibration Strategy

Before addressing experimental testing of cartilage, the model calibration strategy exposed in the previous sections is recapitulated in Figure 5.1. At the beginning ("Start"), an IBVP is carefully derived from a given experimental set-up. This first step requires a close collaboration between the "simulator" and the "experimenter". A well-thought-out IBVP confronted with the technical possibilities of the laboratory facilities is the necessary fundament of a valid model calibration. Subsequently, experiments and simulations based on the elaborated computational model are performed, and the output from the experiment is compared with the numerical results. Next, material parameters are iteratively identified by means of an optimisation procedure until the objective function

$f(\mathbf{s})$ is smaller than a chosen tolerance value. Then, a sensitivity analysis is performed to evaluate the coupling pattern and the interdependency amongst the parameters. If parameters appear to be fully decoupled, i. e., the variation of the output can be clearly assigned to a single parameter, a model reduction can be eventually performed. In this case, the reduced set of parameters should ideally be identified again. In the monograph, this step is intentionally omitted to avoid a laborious presentation of multiple correlation matrices related to the same IBVP, and the end of the calibration process is assumed ("End"). If parameters are displaying high correlation, a unique parameter identification is not guaranteed. In other words, the chosen IBVP is not adapted to calibrate the model. Therefore, a new IBVP has to be elaborated, leading to a repeat of the same process from the beginning ("Start").

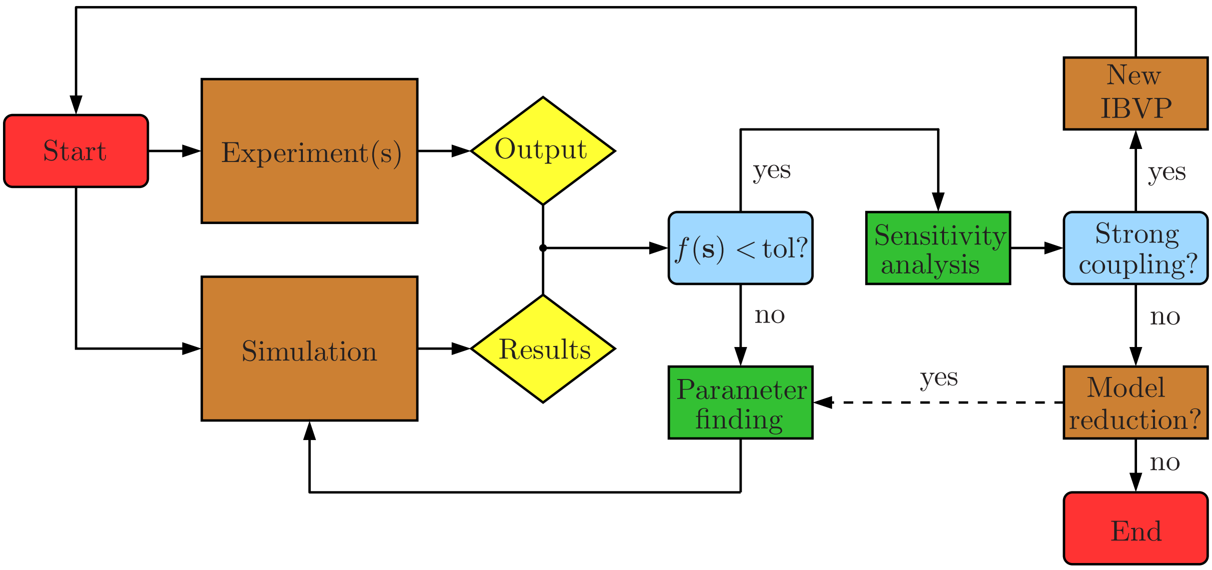

Figure 5.1: *Flowchart of cartilage model calibration.*

In the following sections, the flowchart of the model calibration is applied to real experimental set-ups such as multiple indentation testing of cartilage (see section 5.4) and multi-directional shear loading of cartilage (see section 5.5).

5.4 Application to Indentation Testing of Cartilage

A classic way to calibrate cartilage models is to perform indentation tests. Indentation testing has been broadly used to measure the penetration depth and to obtain the properties of various materials (Hayes & Mockros [110], Kang *et al.* [137]). In this regard, the most commonly used indenters are the flat-ended cylindrical, spherical, conical and *Berkovich* types (Khrushchov & Berkovich [144]). Depending on their configuration (quantified as the projected area on the material loaded surface) and on the applied indentation force, different displacement ranges are observed. For example, a *Berkovich* indenter displaces more volume than a conical one and creates higher local stresses. Other effects related to the indenter geometry, such as friction, sharpness of the indenter tip and size may also have a large influence on the experimental testing and, of course, on the FE modelling.

In the framework of single-phase, isotropic and homogeneous materials loaded by flat-ended cylindrical and spherical indenters, Hayes *et al.* [109] proposed an analytical solution to determine the *Young*'s modulus and *Poisson*'s ratio. The mechanical response was found to be dependent on a scaling factor called the aspect ratio, defined as the ratio between the indenter radius and the material thickness. Jin & Lewis [128] proposed the use of a dual indenter system to determine the unknown material parameters at equilibrium.

In the case of soft biological tissues such as cartilage, indentation testing is commonly the first choice for finding the mechanical properties (Kempson *et al.* [143], Li & Herzog [157], Mak *et al.* [170], Mow *et al.* [190]). In particular, spherical and cylindrical indenters present advantages and drawbacks, which should be briefly mentioned. On the one hand, using a spherical indenter will achieve a more uniform deformation state. Besides, lower deformation gradients in the tissue are observed for the same compression amount when using a spherical cylinder. On the other hand, non-uniform stresses will appear at the sharp edges of cylindrical indenters. This can naturally lead to tissue damage, which can be avoided by choosing a cylindrical indenter with a fillet of sufficiently large radius. From the experimental point of view, cylindrical indenters are preferred over their spherical counterparts, because they do not slip so easily. From the numerical point of view, the use of spherical indenters requires the modelling of more complex contact conditions.

For these reasons, flat-ended cylindrical indenters with radii ranging between 0.4 mm (Korhonen *et al.* [149]) and 0.75 mm (Mow *et al.* [190]) are chosen. However, performing single-indentation tests in order to obtain a unique parameter identification is not feasible when dealing with solid-fluid coupled problems. Particularly, it is not easy to distinguish the intrinsic viscoelasticity of the solid phase from the viscous drag resulting from the pore-fluid flow due to the strong coupling between the solid and the fluid phases. One way to quantify the contributions of the fluid percolation and the solid viscoelasticity to the overall creep behaviour is to carry out a set of indentation tests that only differ in the indenter size. A sensible suggestion would be that the viscous pore-fluid drag through the cartilage layer plays a more relevant role when a larger indenter is used. Accordingly, the influence of the pore-fluid contribution can be investigated more precisely and depending on the indenter size, should lead to an easier identification of the parameters related to the pore-fluid flow properties.

5.4.1 Multiple-Indentation Tests

Multiple-indentation tests on stifle joints of bovine origin collected from a local slaughterhouse were performed at the Medical School of Hannover. Osteochondral cylinders (diameter $D = 6\,\text{mm}$, thickness $h = 1.98\,\text{mm}$) were harvested from the load bearing area of the femoral condyles immediately after the animals were sacrificed. Specimens were then sorted out for uniform cartilage thickness. The specimens were preserved at 253 K in cryotubes containing phosphate buffered saline (PBS), a buffer solution commonly used in biological research, and inhibitors, prior to thawing for 30 minutes and stabilising for an extra 30 minutes at 310 K. The centre points of the specimens were marked using a 0.5 mm Edding marker to assure the creep measurement at the same point while performing multiple creep tests. Creep tests were performed at 310 K under atmospheric pressure conditions, and the specimens were kept in 0.15 mol/l of PBS, with proteases inhibitors (0.001 mol/l of PMSF (P7626); 0.001 mol/l of iodoacetimide (I6125); 5 g/l of pepstatin A (PP4265); 0.001 mol/l of EDTA (ED4SS), all from Sigma) (Langelier & Buschmann [153]). A total number of three specimens were measured under creep indentation by means of three different indenter sizes. A custom-built creep-indentation testing machine (Medical School of Hannover, central research workshop), featuring flat-end cylindrical indenters of radii 0.4, 0.5, and 0.75 mm, was used to apply an equivalent load vector $\bar{\mathbf{t}}$ corresponding to a maximal load of 0.1 N as a step function, which was kept constant until achievement of a steady-state indentation depth (see Figure 5.2, left). After each creep test, the specimens were given two hours of swelling time. Then, a needle-probe thickness measurement was performed at 310 K. The thickness of the cartilage layer at five locations including the CI measurement points in accordance with a location pattern was measured using the needle-probe method (Jurvelin *et al.* [134]).

As depicted in Figure 5.2 (right), the axial-symmetric IBVP of the indentation test with the arcade-like collagen structure in cartilage (Han *et al.* [107], Saarakkala *et al.* [222]) is carried out on a half of the geometry, which is discretised using 385 8-noded, rectangular *Taylor-Hood* elements yielding 2 903 DOF. The upper surface and the lateral border of the cartilage are perfectly drained ($\bar{\mathcal{P}} = 0$). The bottom surface is fixed and impermeable due to its direct connection to the subchondral bone.

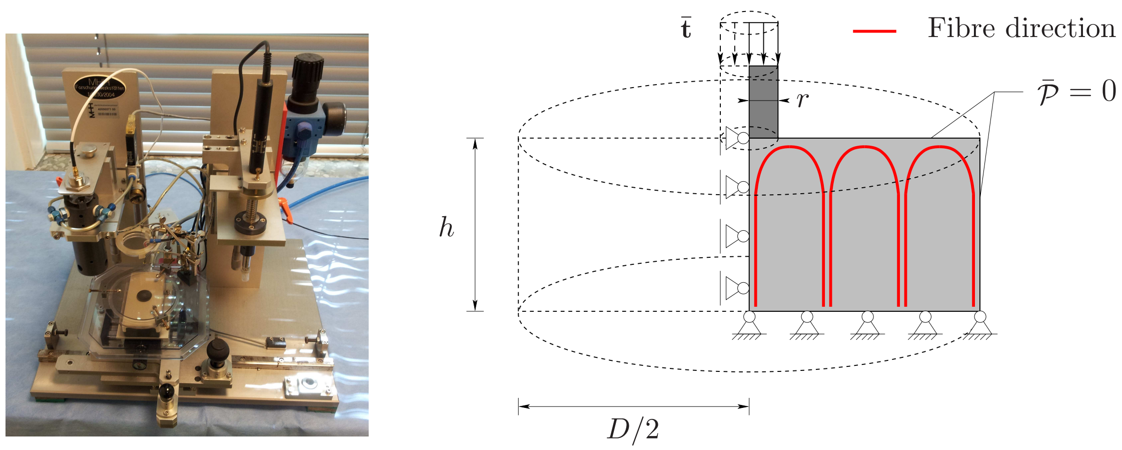

Figure 5.2: *Experimental set-up for multiple-indentation tests at the Medical School of Hannover (left) and IBVP of the indentation test with variable indenter radius r and average dimensions of cartilage specimen (diameter $D = 6$ mm, thickness $h = 1.98$ mm) (right).*

5.4.2 Parameter Identification

The first step in parameter identification consists of the specification of the parameter ranges or increments. These physiological ranges are always related to models, which might differ to some extent from the presented model. Therefore, an unknown uncertainty still involves the choice of parameter ranges. Nevertheless, physiological ranges are cautiously estimated according to the literature (Li & Herzog [156], Ratcliffe & Mow [215], Wilson *et al.* [255]). In Table 5.1, the parameters which are not addressed with $(\,\cdot\,)^*$ are varied within the physiological range.

Properties of	Type	Notation	Range	Unit
matrix and fibres	matrix elasticity	μ_0^S	$[\,0-1\,]$	MPa
		λ_0^S	$[\,0-1\,]$	MPa
		γ_0^{S*}	30.0	-
	matrix viscoelasticity	μ_1^S	?	MPa
		λ_1^S	?	MPa
		η_1^S	?	MPa s
		ζ_1^S	?	MPa s
		γ_1^{S*}	12.0	-
		μ_2^S	?	MPa
		λ_2^S	?	MPa
		η_2^S	?	MPa s
		ζ_2^S	?	MPa s
		γ_2^{S*}	12.0	-
	fibre elasticity	$\widetilde{\mu}_1$	$[\,1-10\,]$	MPa
		$\widetilde{\gamma}_1$	$[\,1-10\,]$	MPa
	osmosis	$\bar{c}_{m,0S}^{fc\,*}$	0.2	mol/l
		$\bar{c}_m^*$	0.15	mol/l
		$R\,\Theta^*$	2477721	N mm/mol
pore-fluid flow	porosity	$\bar{n}_{0S}^{F\,*}$	0.75	-
	effective fluid density	ρ^{FR*}	10^{-6}	$\mathrm{kg/mm^3}$
	def.-dep. permeability	K_{0S}^F	$[\,10^{-4}$ - $10^{-2}\,]$	$\mathrm{mm^4/N\,s}$
		κ	$[\,1$ - $20\,]$	-
	tortuosity	B_{0S}^S	$[\,0$ - $10^{-16}\,]$	mm
		β	$[\,1$ - $20\,]$	-
	anisotropic permeability	θ	$[\,1$ - $20\,]$	-

Table 5.1: *Constitutive parameters needed for the presented model.*

Regarding the values of the volumetric extension terms γ_0^S, γ_1^S and γ_2^S inspired by Karajan [138], they are chosen in order to reflect the characteristics of the ECM, such as the osmotically swelling features and the stiffening effect during dilatation. As indicated by the symbol "?", information was lacking for the starting values and the variation ranges of the parameters μ_1^S, λ_1^S, η_1^S, ζ_1^S and μ_2^S, λ_2^S, η_2^S, ζ_2^S describing the intrinsic viscoelastic behaviour by means of two *Maxwell* elements ($N = 2$). Furthermore, no information on the variation ranges of the deformation-dependent factors β and θ could be gathered. Hence, the same admissible range as for the exponent κ, governing the nonlinear dependency of the permeability on the deformation rate, is assumed. For the determination of the initial tortuosity parameter B_{0S}^S, no precise data are available. However, to potentially decrease the specific permeability K_{0S}^F of one order of magnitude, as illustrated in

Figure 4.6 (left), an extremal value of 10^{-16} mm for the parameter B^S_{0S} is estimated by means of equation (2.59). During the parameter identification procedure, the material properties of the chosen reference state are provided by the central values of the given physiological ranges. Furthermore, the material parameters to be identified are subjected to the following inequality constraints

$$\begin{array}{lcl|lcl} \mu^S_0,\, \lambda^S_0 & > & 0 & \widetilde{\gamma}_1 & \geq & 2 \\ \mu^S_1,\, \lambda^S_1 & > & 0 & K^F_{0S} & > & 0 \\ \eta^S_1,\, \zeta^S_1 & > & 0 & B^S_{0S} & > & 0 \\ \mu^S_2,\, \lambda^S_2 & > & 0 & \kappa & \geq & 0 \\ \eta^S_2,\, \zeta^S_2 & > & 0 & \beta & \geq & 0 \\ \widetilde{\mu}_1 & \geq & 0 & \theta & \geq & 0\,. \end{array} \tag{5.7}$$

The elaborated model calibration strategy of Figure 5.1 leads to the set of optimised parameters given in Table 5.2.

Material parameters								
μ^S_0	$= 0.58$	[MPa]	λ^S_0	$= 0.02$	[MPa]	μ^S_1	$= 0.10$	[MPa]
λ^S_1	$= 0.16$	[MPa]	η^S_1	$= 10.0$	[MPa s]	ζ^S_1	$= 10.64$	[MPa s]
μ^S_2	$= 10.0$	[MPa]	λ^S_2	$= 9.4$	[MPa s]	η^S_2	$= 2.5$	[MPa s]
ζ^S_2	$= 3.0$	[MPa s]	$\widetilde{\mu}_1$	$= 1.0$	[MPa]	$\widetilde{\gamma}_1$	$= 2.0$	[–]
K^F_{0S}	$= 0.7 \cdot 10^{-3}$	[mm^4/N s]	κ	$= 11.0$	[–]	β	$= 10.5$	[–]
B^S_{0S}	$= 10^{-19}$	[mm]	θ	$= 3.0$	[–]			

Table 5.2: *Optimised material parameters after model calibration strategy.*

After model calibration for the different indenter geometries, the experimental and numerical results are depicted over the simulation time t in Figure 5.3. In the upper diagram, the raw experimental data (denoted by "exp") are depicted by the light red, green and blue curves with dots for the small ($r = 0.4$ mm), medium ($r = 0.5$ mm) and large ($r = 0.75$ mm) indenters, respectively. These curves are approximated by the logarithm functions f_1, f_2 and f_3 (denoted by "fit") via

$$\begin{aligned} f_1 &= 20.531 \log t - 0.0231\, t + 49.889\, [\text{mm}]\,, \\ f_2 &= 13.836 \log t - 0.003\, t + 29.427\, [\text{mm}]\,, \\ f_2 &= 7.666 \log t - 0.007\, t + 35.2731\, [\text{mm}] \end{aligned} \tag{5.8}$$

for the small, medium and large indenters. These functions are represented by the dark red, green and blue dashed lines, respectively. Then, the aforementioned parameter identification technique is performed, in which f_1, f_2 and f_3 are inserted in the objective function $f(\mathbf{s})$. After parameter identification, the model calibration delivers the results presented by the curves denoted by "sim" in the lower diagram of Figure 5.3. The light red curve refers to the numerical results of the simulation when using an indenter of radius $r = 0.4$ mm. When using an indenter of radius $r = 0.5$ mm, the light green curve is obtained from the simulation. A large indenter of radius $r = 0.75\,\mathrm{mm}$ leads to the light blue curve, obtained from the simulation. It appears that the presented model leads to

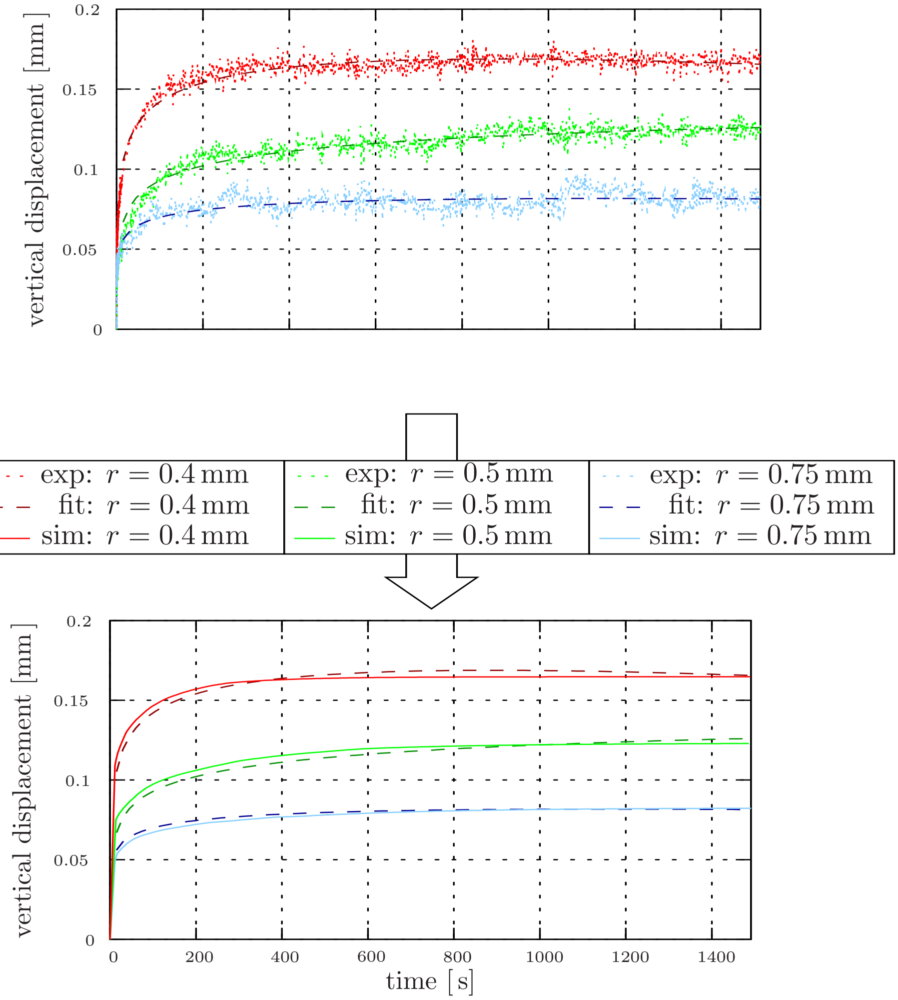

Figure 5.3: *History plot of indenter displacement of experiments and simulations for different indenter geometries.*

a good match to the experimental results with the same parameter set for the different indenter geometries. A slight mismatch between the experimental and the numerical results related to the indenters of radii $r = 0.4$, $r = 0.5\,\mathrm{mm}$ and $r = 0.75\,\mathrm{mm}$ is most likely due to the appearance of "noise" in the experimental data when measuring the indenter displacements.

5.4.3 Sensitivity Analysis

In this section, a detailed sensitivity analysis of the multiple-indentation IBVP introduced in Figure 5.2 (right) is performed. With regard to a clear and concise representation of the already complex coupled phenomena, articular cartilage is first considered as an isotropic, homogeneous and poroelastic material. In this framework, the considerations are split between low and high permeability values in the physiological range, because the permeability value is a good indicator for evaluating the solid-fluid "coupling strength". In the following, low permeability of articular cartilage is described by values of $K_{0S}^F = 10^{-4}\,\mathrm{mm}^4/\mathrm{N\,s}$ (equivalent to $k^F = 10^{-12}\,\mathrm{m/s}$) while high permeability is given by values of $K_{0S}^F = 10^{-2}\,\mathrm{mm}^4/\mathrm{N\,s}$ (equivalent to $k^F = 10^{-10}\,\mathrm{m/s}$). This distinction between low and high permeability is helpful to quantify the respective contributions of the pore-fluid effects and the intrinsic viscoelasticity to the overall creep response of cartilage. In this regard, Setton *et al.* [230] showed that for articular cartilage, the effects of drag forces caused by fluid flow were more dominant for the time-dependent phenomena compared to the intrinsic viscoelasticity, if the specific permeability K_{0S}^F was smaller than $10^{-2}\,\mathrm{mm}^4/\mathrm{N\,s}$. This value corresponds to the chosen limit of the permeability range. One goal of this paragraph is to verify qualitatively and quantitatively the validity of this statement and to extend it to small ($r = 0.4\,\mathrm{mm}$) and large ($r = 0.75\,\mathrm{mm}$) indenters.

In order to investigate the influence of a permeability change on the indentation testing of cartilage under a vertical load of 0.1 N, the first concern is the fluid flow, characterised by the seepage velocity vectors $\mathbf{w}_F$ whose directions are instantaneously tangential to the stream lines. The stream lines are represented by the white lines in Figure 5.4 at a low permeability regime ($K_{0S}^F = 10^{-4}\,\mathrm{mm}^4/\mathrm{N\,s}$). Figure 5.4 also shows the contours of the overall pore-fluid pressure p on snapshots for different time steps throughout the simulation for the small (Figure 5.4, top) and the large indenter (Figure 5.4, bottom). On the one hand, one observes a slightly deeper fluid flow when the cartilage is loaded by a small indenter. Due to the more local loading with a small indenter, the peak of pore-fluid pressure is more localised in the neighbourhood of the indenter. Therefore, the fluid pressure below the small indenter has to be higher than that for the large indenter. On the other hand, when loaded by a large indenter, high values of the pressure spread throughout the cartilage layer under the indenter position. Nevertheless, the fluid flows for both configurations at a low permeability regime look rather similar.

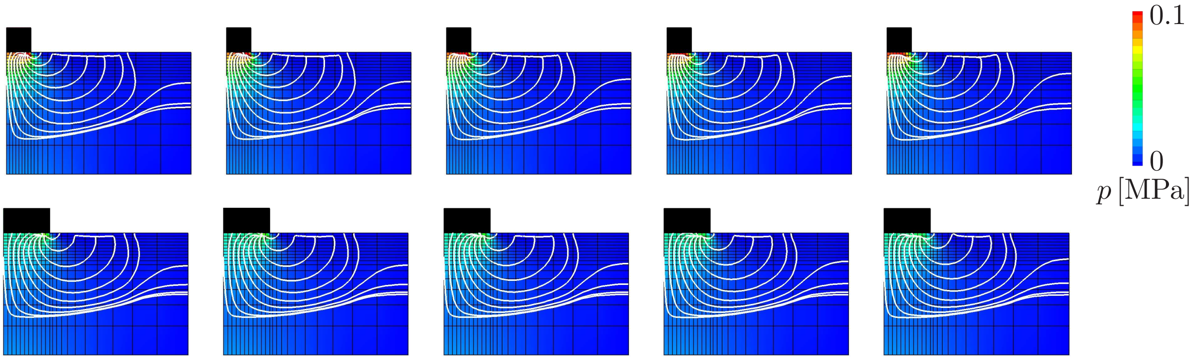

(a) $t = 150\,\mathrm{s}$ (b) $t = 250\,\mathrm{s}$ (c) $t = 500\,\mathrm{s}$ (d) $t = 1000\,\mathrm{s}$ (e) $t = 1500\,\mathrm{s}$

Figure 5.4: *Pore-fluid pressure contours and stream lines for small (top) and large (bottom) indenters at low permeability regime for different time steps.*

Figure 5.5 represents the same pattern at a high permeability regime ($K_{0S}^F = 10^{-2}\,\mathrm{mm}^4/\mathrm{N\,s}$). As expected, the permeability increase leads to a quicker fluid flow through the cartilage. Here again, similar fluid flows can be observed for both configurations by means of a set of chosen time steps. In this case, the stream lines under the small indenter concentrate earlier than those for large indenters.

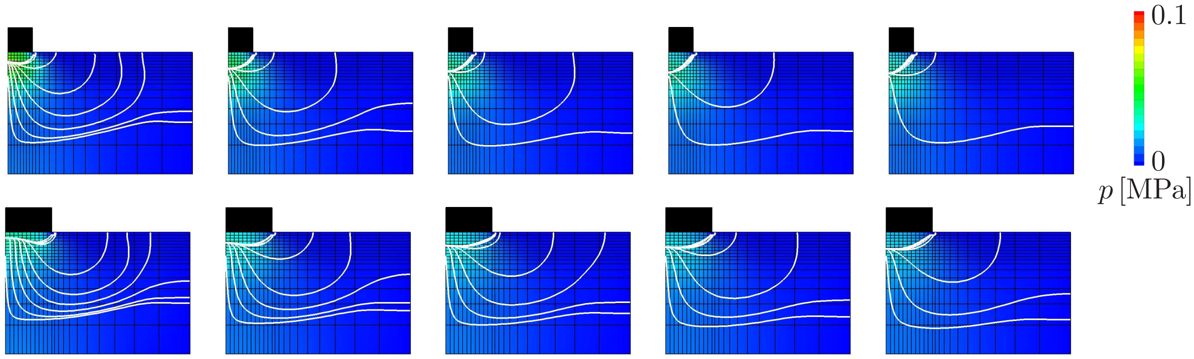

(a) $t = 150\,\mathrm{s}$ (b) $t = 250\,\mathrm{s}$ (c) $t = 400\,\mathrm{s}$ (d) $t = 450\,\mathrm{s}$ (e) $t = 500\,\mathrm{s}$

Figure 5.5: *Pore-fluid pressure contours and stream lines for small (top) and large (bottom) indenters at high permeability regime for different time steps.*

A closer look at the domain in the neighbourhood of the indenter at the same time $t = 150\,\mathrm{s}$ leads to Figures 5.6 and 5.7. Figure 5.6 depicts the contours of the pressure lens, as well as the uniformly scaled seepage velocity vectors, which are shown by red arrows. The pressure lens is obtained after cutting off the pressure contours below a given level.

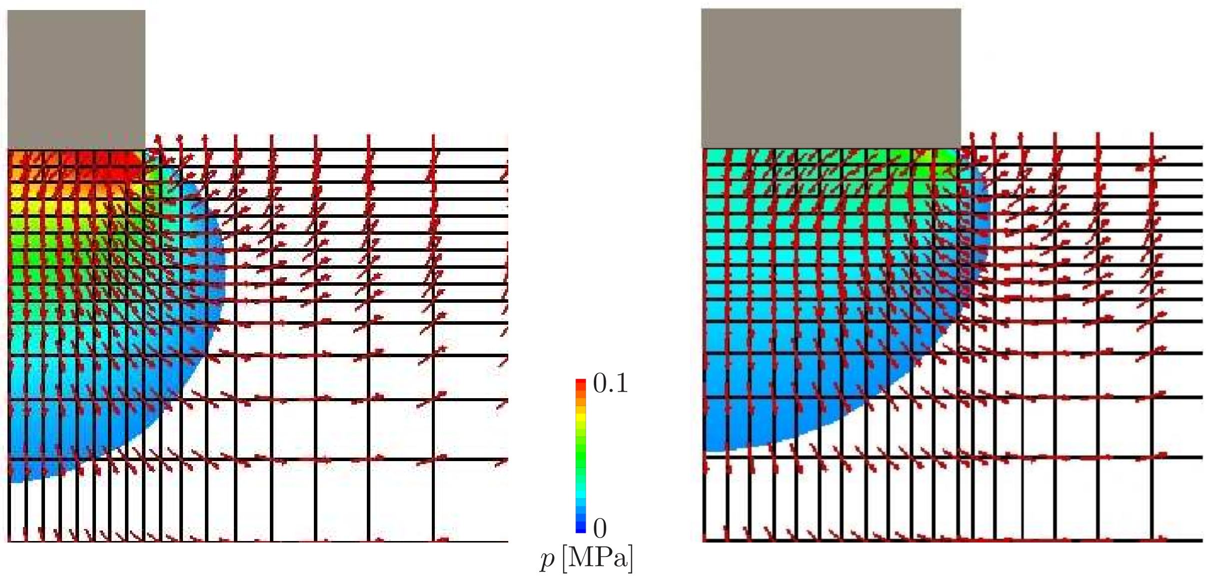

Figure 5.6: *Pressure lense and uniformly scaled seepage velocity vectors (depicted by red stripes) for small (left) and large (right) indenters at a low permeability regime at $t = 150\,\mathrm{s}$ (enlarged view).*

A significant difference appears between the small and the large indenter configurations at a low permeability regime. The pore fluid does not only flow deeper within the cartilage domain, but a different form of the pressure lens can also be pinpointed. A large belly

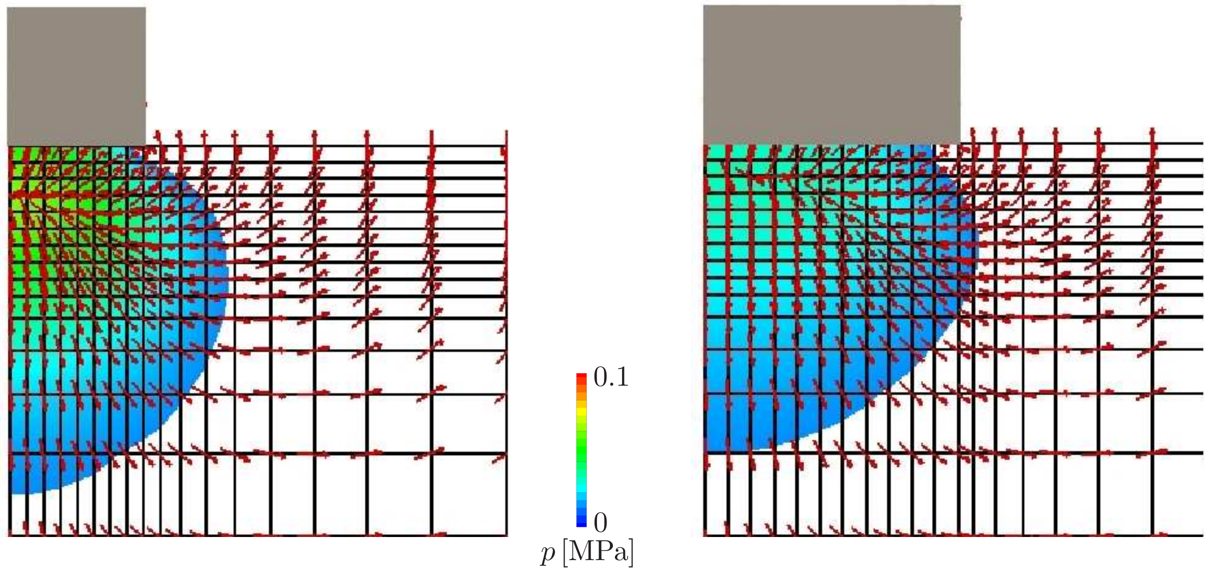

Figure 5.7: *Pressure lens and uniformly scaled seepage velocity vectors (depicted by red arrows) for small (left) and large (right) indenters at a high permeability regime at $t = 150\,\mathrm{s}$ (enlarged view).*

shape appears under the small indenter, in contrast to the large indenter. Additionally, the more local pore-fluid pressure distribution under a small indenter is diverging from a rather equally distributed pressure in the large indenter case. Consequently, an almost impermeable cartilage layer loaded by a small indenter generates a mostly local pressure peak under the indenter. A reasonable statement would be that using a small indenter, a small variation of the cartilage permeability around a given permeability state mostly influences the measured response locally, as opposed to the case of a large indenter.

The same comparison can be made in Figure 5.7 for cartilage tissues at a high permeability regime. For both indenter configurations, a more homogeneous pressure distribution can be observed in contrast to the case in Figure 5.6. Therefore, a small permeability variation around the given low permeability value might cause a similar perturbation of the measured response.

To verify these observations quantitatively and to compare the pore-fluid flow between small and large indenters, a normalised pressure $\tilde{p} = p/p_{\max}$ is defined, where $p_{\max}$ is the maximal pore-fluid pressure depicted in Figures 5.6 and 5.7 directly beneath the centre of the indenter. Similar to the definition of the normalised depth $\tilde{z}$ introduced in section 4.1.2, the normalised position $\tilde{x} = x_r/r$ below the indenter on the cartilage side is given by the radial distance x_r from the vertical symmetry axis, depicted in Figure 5.2 (right), referred to the indenter radius r. The normalised pressure distribution $\tilde{p}$ is depicted in Figures 5.8 and 5.9 at time $t = 150\,s$ by the red curve with red dots, at time $t = 700\,s$ by the crossed red curve and at the end of the simulation at time $t = 1\,500\,s$ by the red line. in Figure 5.8 (left), $\tilde{p}$ is depicted as a function of the normalised position $\tilde{x}$ for cartilage loaded by a small indenter at high and low permeability regimes. The case of a large indenter is represented in Figure 5.8 (right). A quicker diminution of the pore-fluid pressure over time can be clearly observed for the small indenter. Negligible pressure values are obtained at a high permeability regime with the small indenter. Moreover, a different pressure-distribution pattern occurs depending on the chosen indenter size.

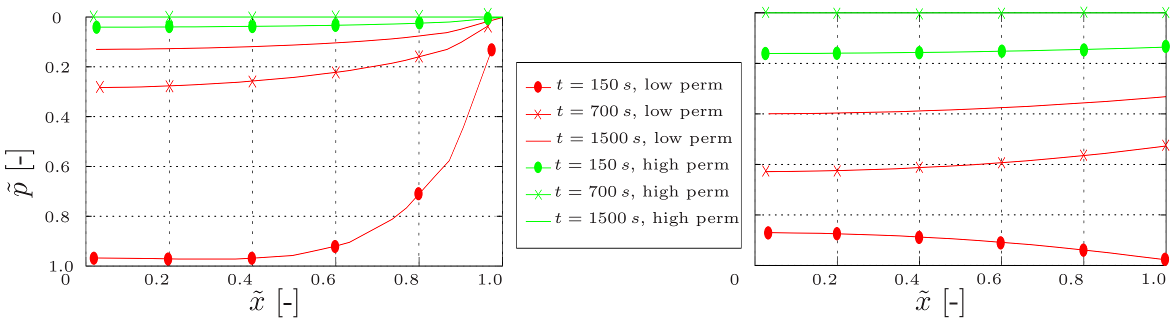

Figure 5.8: *Normalised pore-fluid pressure underneath the indenter for small (left) and large (right) indenters throughout the simulation.*

In Figure 5.9, the normalised pore-fluid pressure $\tilde{p}$ is depicted along the vertical symmetry axis below the indenter as a function of the normalised depth $\tilde{z}$. It appears that the high pressure peaks located in the direct neighbourhood of the small indenter diminish rapidly over the cartilage depth. This leads to high vertical pressure gradients responsible for a deeper fluid flow within the cartilage tissue. Nonetheless, the time-dependent behaviour of the pressure distribution reveals again that, by using the small indenter, the pressure decreases more quickly than in the case with the large indenter.

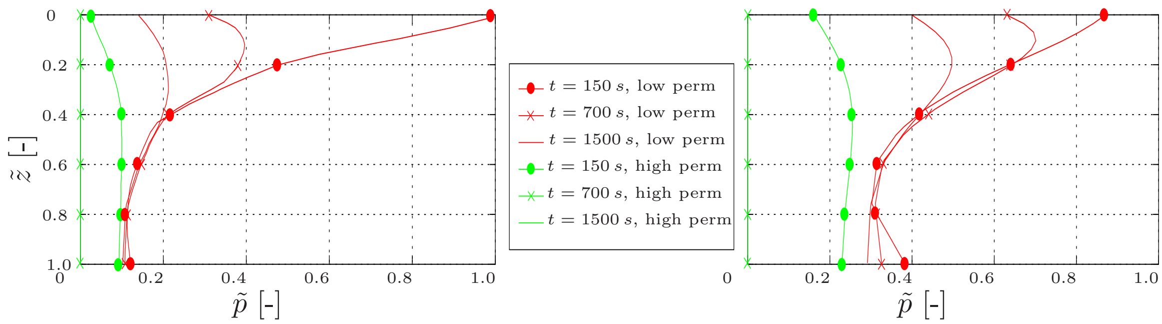

Figure 5.9: *Normalised pore-fluid pressure along the vertical symmetry axis for small (left) and large (right) indenters throughout the simulation.*

Based on the aforementioned considerations on an isotropic, homogeneous material, a complete sensitivity analysis of the sophisticated cartilage model is performed using the same split in two permeability regimes. In this regard, the sensitivity vector $\dfrac{\mathrm{d}\phi_n}{\mathrm{d}s}$ related to a given material parameter is calculated when varying a given material parameter and holding other parameters at central value as defined in equation (5.4). In the context of the creep-indentation test, the measured response $\tilde{\phi}_n$ is represented by the vertical displacement of the indenter. Then, the sensibility vectors are added as a column to a matrix arranged in a data set. The correlation coefficients r_{ij} of equation (5.6) gathered in the correlation matrix are automatically computed by utilising the commercial computer algebra system Maple.

In the first step, the focus lies on the time-independent material parameters, i. e., the material parameters governing the matrix (μ_0^S and λ_0^S) and the collagen fibre elasticity

($\widetilde{\mu}_1$ and $\widetilde{\gamma}_1$). The vertical displacement obtained at the end of the simulation is chosen as the index for the output of the computational model. For cartilage tissues at a high permeability regime, the correlation-matrix entries of the time-independent parameters relative to the small indenter (Table 5.3, left) are slightly smaller than in the case of a large indenter (Table 5.3, right). However, no significant difference could be observed in order to give a more proper statement. It just appears that the values are generally much smaller than 1, which means that a unique identification of each parameter should be possible. The same observations are presented for cartilage at a low permeability regime in Table 5.4.

r_{ij}	μ_0^S	λ_0^S	$\widetilde{\mu}_1$	$\widetilde{\gamma}_1$
μ_0^S	1.00	−0.062	−0.027	−0.041
λ_0^S		1.00	−0.224	−0.230
$\widetilde{\mu}_1$			1.00	−0.213
$\widetilde{\gamma}_1$				1.00

r_{ij}	μ_0^S	λ_0^S	$\widetilde{\mu}_1$	$\widetilde{\gamma}_1$
μ_0^S	1.00	−0.114	−0.088	−0.086
λ_0^S		1.00	−0.236	−0.235
$\widetilde{\mu}_1$			1.00	−0.221
$\widetilde{\gamma}_1$				1.00

Table 5.3: *Complete correlation matrix for the parameters governing the time-independent behaviour for* $r = 0.4$ mm *(left) and* $r = 0.75$ mm *(right) for* $K_{0S}^F = 10^{-4}\,\text{mm}^4/\text{N s}$.

r_{ij}	μ_0^S	λ_0^S	$\widetilde{\mu}_1$	$\widetilde{\gamma}_1$
μ_0^S	1.00	0.067	0.032	0.031
λ_0^S		1.00	−0.178	−0.179
$\widetilde{\mu}_1$			1.00	−0.198
$\widetilde{\gamma}_1$				1.00

r_{ij}	μ_0^S	λ_0^S	$\widetilde{\mu}_1$	$\widetilde{\gamma}_1$
μ_0^S	1.00	0.047	0.040	0.095
λ_0^S		1.00	−0.242	−0.220
$\widetilde{\mu}_1$			1.00	−0.223
$\widetilde{\gamma}_1$				1.00

Table 5.4: *Complete correlation matrix for the parameters governing the time-independent behaviour for* $r = 0.4$ mm *(left) and* $r = 0.75$ mm *(right) for* $K_{0S}^F = 10^{-2}\,\text{mm}^4/\text{N s}$.

In the second step, the sensitivity of each specific, time-dependent parameter to the measured output is investigated throughout the simulation. In this regard, the time dependency is carried out by means of a pseudo-analytical method, which calculates the vertical displacement of the indenter accumulated over the simulation time. This method for time-dependent phenomena is also used and extended by den Camp *et al.* [47] for multiple measurement points within a heterogeneous domain in the framework of a sensitivity analysis on soft biological tissues.

Tables 5.5 and 5.6 represent the complete correlation matrix for the parameters governing the time-dependent behaviour for small and large indenters at the low permeability regime. For the sake of simplicity, the matrice entries related to the parameters of the second *Maxwell* element ($N = 2$) are omitted. The cells highlighted in dark grey in the matrices are of special interest. They clearly show, at the low permeability regime, the correlation between the specific permeability K_{0S}^F and the specific parameters governing the solid viscoelasticity (μ_1^S, λ_1^S, η_1^S and ζ_1^S). The values of the matrice entries displayed in dark grey for the large indenter are higher than those of the small indenter case. In other words, none of these parameters can be identified separately, when using a single indentation test with a large indenter. It is reasonable to think that the influence of the pore-fluid flow is smaller for almost impermeable tissues loaded by a small indenter due to a local concentration of the pore-fluid pressure below the indenter. The remaining entries of the matrices do not reveal any strong coupling due to their lower values, except for the cells of the first four rows directly related to the intrinsic solid viscoelasticity.

r_{ij}	μ_1^S	λ_1^S	η_1^S	ζ_1^S	K_{0S}^F	κ	B_{0S}^S	β	θ
μ_1^S	1.00	0.968	0.999	−0.999	−0.369	0.110	0.108	0.109	0.090
λ_1^S		1.00	0.968	−0.969	−0.386	0.078	0.074	0.076	0.057
η_1^S			1.00	−0.999	−0.369	0.111	0.108	0.110	0.091
ζ_1^S				1.00	0.365	−0.115	−0.112	−0.114	−0.095
K_{0S}^F					1.00	−0.156	−0.155	−0.156	−0.149
κ						1.00	−0.111	−0.111	−0.114
B_{0S}^S							1.00	−0.112	−0.114
β								1.00	−0.114
θ									1.00

Table 5.5: *Complete correlation matrix for the parameters governing the time-dependent behaviour for* $r = 0.4$ mm *and* $K_{0S}^F = 10^{-4}\,\mathrm{mm}^4/\mathrm{N\,s}$.

r_{ij}	μ_1^S	λ_1^S	η_1^S	ζ_1^S	K_{0S}^F	κ	B_{0S}^S	β	θ
μ_1^S	1.00	0.977	0.999	−0.999	−0.998	0.110	0.110	0.110	0.184
λ_1^S		1.00	0.977	−0.977	−0.977	0.082	0.082	0.082	0.155
η_1^S			1.00	−0.999	−0.998	0.110	0.110	0.110	0.184
ζ_1^S				1.00	0.998	−0.114	−0.114	−0.113	−0.188
K_{0S}^F					1.00	−0.118	−0.118	−0.117	−0.191
κ						1.00	−0.111	−0.111	−0.102
B_{0S}^S							1.00	−0.111	−0.102
β								1.00	−0.102
θ									1.00

Table 5.6: *Complete correlation matrix for the parameters governing the time-dependent behaviour for* $r = 0.75$ mm *and* $K_{0S}^F = 10^{-4}\,\mathrm{mm}^4/\mathrm{N\,s}$.

Regarding cartilage at the high permeable regime, Tables 5.7 and 5.8 represent the same correlation between permeability, which refers to the viscosity due to the pore-fluid flow through the cartilage, and intrinsic viscoelasticity, as shown by the dark grey displayed entries. The next row of entries, also highlighted in dark grey, shows the correlation of the deformation dependency of the permeability with the solid viscoelasticity. Moreover, the entries displayed in medium dark grey reveal the significant influence of the parameters B_{0S}^S and β governing the tortuosity effects on the parameters governing the time-dependent phenomena. These effects appear for higher seepage velocity values at the high permeability regime. Finally, the matrix elements displayed in light grey represent the strong correlation between the the parameter θ governing the deformation-induced anisotropy and the solid viscoelasticity parameters.

r_{ij}	μ_1^S	λ_1^S	η_1^S	ζ_1^S	K_{0S}^F	κ	B_{0S}^S	β	θ
μ_1^S	1.00	0.999	0.999	−0.999	−0.998	0.452	0.620	0.843	0.696
λ_1^S		1.00	0.999	−0.999	−0.998	0.452	0.612	0.843	0.696
η_1^S			1.00	−0.999	−0.998	0.453	0.623	0.843	0.696
ζ_1^S				1.00	0.998	−0.453	−0.624	−0.843	−0.696
K_{0S}^F					1.00	−0.458	−0.681	−0.845	−0.699
κ						1.00	−0.083	−0.322	−0.235
B_{0S}^S							1.00	−0.015	−0.046
β								1.00	−0.539
θ									1.00

Table 5.7: *Complete correlation matrix for the parameters governing the time-dependent behaviour for* $r = 0.4$ mm *and* $K_{0S}^F = 10^{-2}\,\mathrm{mm^4/N\,s}$.

r_{ij}	μ_1^S	λ_1^S	η_1^S	ζ_1^S	K_{0S}^F	κ	B_{0S}^S	β	θ
μ_1^S	1.00	0.999	0.999	−0.999	−0.995	0.651	0.992	0.994	0.993
λ_1^S		1.00	0.999	−0.999	−0.999	0.650	0.992	0.994	0.993
η_1^S			1.00	−0.999	−0.995	0.650	0.992	0.994	0.993
ζ_1^S				1.00	0.995	−0.651	−0.992	−0.994	−0.993
K_{0S}^F					1.00	−0.638	−0.989	−0.990	−0.989
κ						1.00	−0.657	−0.657	−0.657
B_{0S}^S							1.00	−0.985	−0.984
β								1.00	−0.985
θ									1.00

Table 5.8: *Complete correlation matrix for the parameters governing the time-dependent behaviour for* $r = 0.75$ mm *and* $K_{0S}^F = 10^{-2}\,\mathrm{mm^4/N\,s}$.

5.4.4 Influence of Heterogeneities

The influence of each heterogeneity type on the macroscopic response is the concern of this section. The normalised displacement $\tilde{u} = |\bar{\mathbf{u}}_S\,(t)|/|\bar{\mathbf{u}}_S\,(t = 1\,500\,\mathrm{s})|$ is defined as the ratio between the vertical indenter displacement $|\bar{\mathbf{u}}_S\,(t)|$ over the simulation time and the vertical indenter displacement $|\bar{\mathbf{u}}_S\,(t = 1\,500\,\mathrm{s})|$ at the end of the simulation in the full heterogeneous case. In Figures 5.10 and 5.11, $\tilde{u}$ is represented over the simulation time for small (top) and large (bottom) indenters. Figure 5.10 refers to the low permeability regime and Figure 5.11 to the high permeability regime.

The role of each single heterogeneity is investigated by reducing the heterogeneous distribution of the listed material features to its average value. By doing so, the distributions of the remaining heterogeneities are not modified. For instance, the pink curve described by "homogeneous porosity distribution" only considers the numerical results obtained using a poroviscoelastic, anisotropic, osmotically swelling and heterogeneous model, in which only the porosity is homogeneously distributed over the cartilage layer. In this context, it appears that a fully heterogeneous model mostly leads to a physiological load support in cartilage due to a reduction of its deformation, as depicted by the red curve. This means

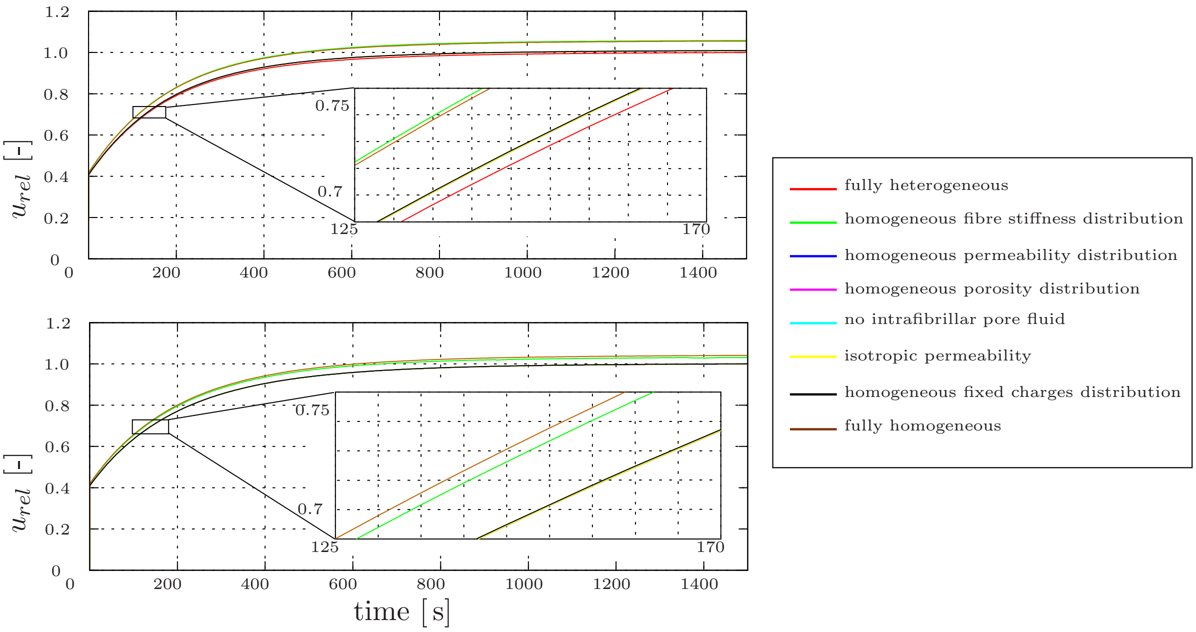

Figure 5.10: *Influence of heterogeneities for small (top) and large (bottom) indenters throughout the simulation at the low permeability regime.*

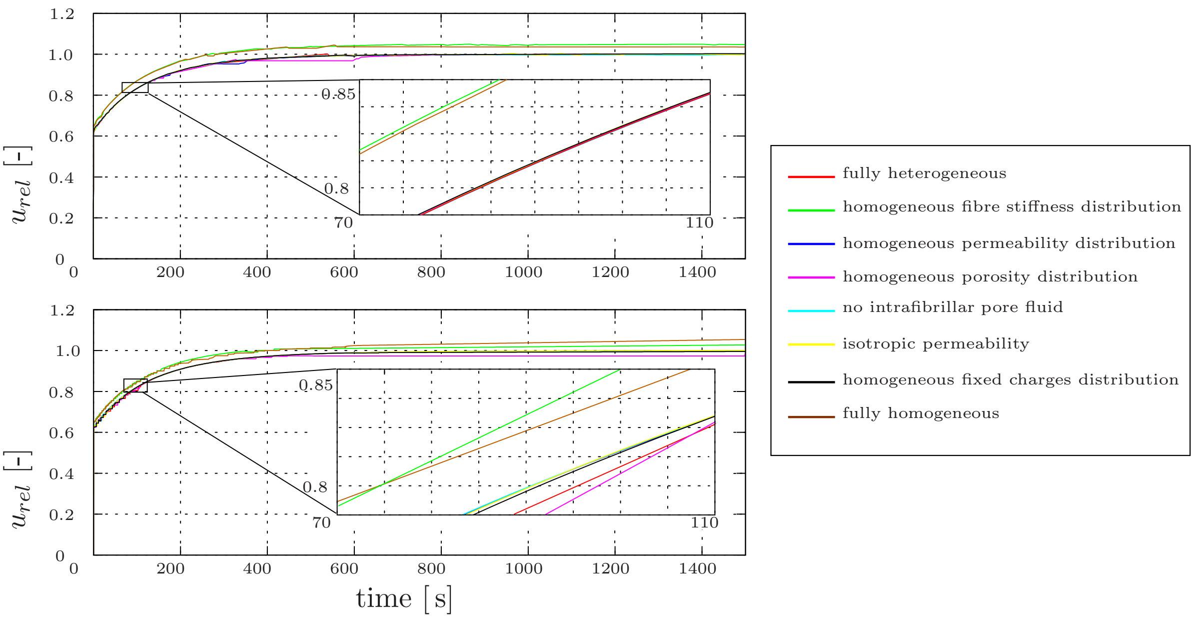

Figure 5.11: *Influence of heterogeneities for small (top) and large (bottom) indenters throughout the simulation at the high permeability regime.*

that the introduction of heterogeneities in the cartilage model generates smaller displacement values than the displacement values calculated by means of a fully homogeneous model, depicted by the brown curve. In particular, a homogeneous distribution of fibres over the cartilage thickness provides lower overall cartilage stiffness, as shown by the green curve. A fraction of the vertical load in creep testing is carried by the tangential fibres in the superficial zone. In this cartilage region, the higher fibre stiffness, represented in Figure 4.4 (left), will be more adapted to withstand deformations of the cartilage surface.

In the following, cartilage heterogeneities are not further considered in the modelling due to their minor influence on the numerical response.

5.5 Application to Shear Loading of Cartilage

A multiple-indentation testing with different indenter sizes was not fully capable of distinguishing the transient effects caused by the interstitial fluid from the effects of the solid phase due to the strong coupling between material parameters. In this connection, an alternative method for identifying material parameters is proposed by means of a novel concept of experimental set-up.

The second objective of this section is to determine experimentally the spatial orientation of the collagen fibres, a key factor for investigating the functionality and load-bearing mechanisms of soft tissues. In this regard, a few existing experimental techniques for determining the fibre architecture are briefly summarised. The usual investigation methods are the T2-weighted MRI (Smith & Mosh [234]) or the diffusion tensor MRI (DT-MRI) (de Visser *et al.* [249]) on intact tissues. Other methods relying on tomography are also used, such as optical coherence tomography (OCT) and polarisation-sensitive OCT (Ugryumova *et al.* [243]). The X-ray diffraction method (Mollenhauer *et al.* [187], Muehleman *et al.* [197]) is mostly limited to thin tissue sections. By means of a *Fourier* transformation imaging and micro-spectroscopy (Boskey & Camacho [33]), the zonal fibre orientation is clearly observable. Further methods based on microscopy are available, such as differential interference contrast microscopy (Broom & Flachsmann [41]) or laser scanning confocal microscopy (Wu *et al.* [259]). A standard technique is given by polarised light microscopy (PLM) (Xia *et al.* [261]). To investigate small tissue regions, the scanning electron microscopy (SEM) (Kaab *et al.* [136]) is appropriate but leads to a dehydration of cartilage specimens. Recently, multi-photon microscopes (MPM) (Lilledahl *et al.* [162], Zipfel *et al.* [268]) have been used in *in-vivo* experiments for 3-d imaging of collagen fibre architectures. However, due to its limited penetration depth, only the superficial layer could be viewed, which requires tissue sectioning. In order to determine the collagen fibre orientation of the articular cartilage's superficial layer, simple destructive methods such as the split-line technique (see section 4.1.3) can also be used. Alternatively, a new experimental set-up is explored that combines a simultaneous determination of fibre orientation with a mechanical shear loading of the cartilage.

5.5.1 Concept of Multi-Directional Shear Experiment

Classic indentation tests turned out not to be sufficient to distinguish the transient effects influenced by a "volumetric" deformation, i. e., a change in the tissue's overall volume, from the effects caused by shear deformations. Therefore, an adapted loading configuration is built up, in which shear is the dominant loading mode. In this framework, a concept of experimental set-up of indentation testing is proposed.

Figure 5.12 (left) shows how the set-up of an indentation testing machine, as used by the associated research partner PD Hurschler at the Medical School of Hannover, could be modified. The flat tip of a steel indenter of radius 4 mm is equipped with freely retractile needles, which can be fixed at the cartilage sample surface. Furthermore, a control mechanism allows the "experimenter" to apply a shear movement to the rotatably mounted indenter in different directions, as depicted by the white crossed arrows. The reason for applying an orientation change during shear loading is to reveal the 3-d anisotropic behaviour of cartilage. This behaviour is investigated on a cylindrical cartilage sample with the same dimensions as in the previous multiple-indenter testing (see Figure 5.2). The cartilage domain is discretised using 14 735 20-noded, hexahedral *Taylor-Hood* elements, yielding 48 055 DOF. The time-dependent boundary conditions of the applied displacement $\bar{\mathbf{u}}_S$ are depicted on the IBVP in Figure 5.12 (right). The sample is fixed at its bottom surface, and all the boundaries are perfectly drained ($\bar{\mathcal{P}} = 0$), except for the surface in contact with the indenter and the bottom surface. Furthermore, the searched direction of the superficial fibres is given by the red stripes on the cartilage surface.

The detailed test procedure is as follows:

- 1. Apply a vertical displacement of 0.01 mm for the indenter to be in contact with the cartilage surface.
- 2. Wait for 5 800 s until the fluid outflow at the cartilage surface is negligible.
- 3. The retractile needles are pushed out of the indenter to create a grip on the cartilage surface.
- 4. The indenter undergoes a single back-and-forth shear displacement of 0.1 mm within 3 s in a chosen direction at the cartilage surface.
- 5. The needles are pulled back into the indenter cavity, and the indenter is rotated clockwise by an angle $\alpha = 10°$ from the previous direction.
- 6. Repeat the experiment starting from step 4 and increase regularly the applied shear angle α in step 5 until 180° is reached.

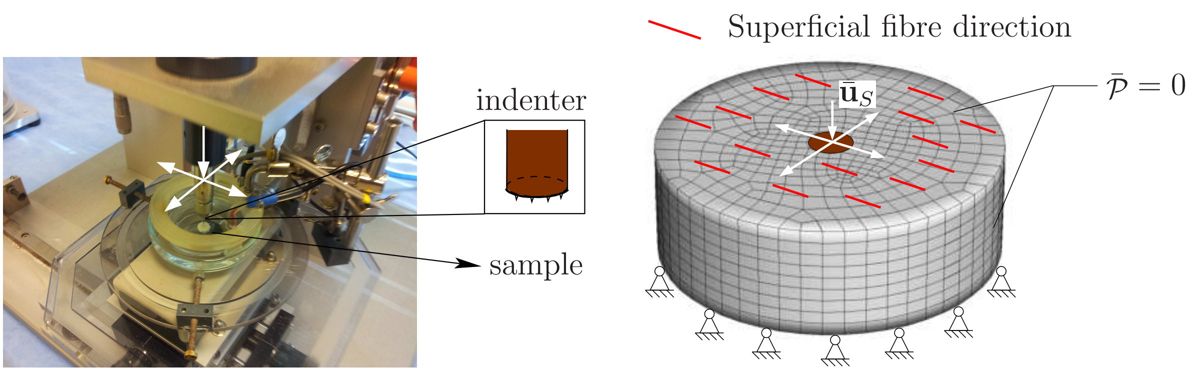

Figure 5.12: *Novel experimental set-up inspired from the laboratory installations at the Medical School of Hannover (left) and IBVP with meshed geometry and superficial fibre direction (right).*

5.5.2 Sensitivity Analysis

The chosen material parameters of the cartilage tissue are taken from the previous parameter identification in Tables 5.1 and 5.2. Regarding the specific permeability K_{0S}^F, a cartilage tissue sample at the low permeability regime is assumed. Table 5.9 represents the correlation matrix for the parameters governing the time-dependent behaviour of the IBVP depicted in Figure 5.12 (right). The entries of the matrix highlighted in dark grey are first considered. They clearly show the low correlation between the permeability K_{0S}^F and the constitutive parameters μ_1^S and η_1^S governing the deviatoric contribution to the intrinsic solid viscoelasticity. Similarly, the negligible influence of the volumetric contribution ζ_1^S to the intrinsic viscoelasticity is shown by the cells highlighted in light grey. As expected, an uncertainty on the parameters relative to the volumetric time-dependent properties of cartilage would still lead to an acceptable model calibration with experimental data and would guarantee a unique identification of the remaining parameters. The other entries of the matrix do not reveal any strong coupling due to their lower values, except for the cells of the second row. These cells contain the combined correlation values of volumetric-dependent parameters. Due to the weak dependence of the output on a change in the volumetric properties of cartilage, the combined influence of these parameters can be neglected.

r_{ij}	μ_1^S	λ_1^S	η_1^S	ζ_1^S	K_{0S}^F	κ
μ_1^S	1.00	−0.007	0.969	0.005	−0.011	−0.012
λ_1^S		1.00	0.236	0.998	0.999	0.999
η_1^S			1.00	0.247	0.232	0.231
ζ_1^S				1.00	0.998	0.997
K_{0S}^F					1.00	0.999
κ						1.00

Table 5.9: *Correlation matrix for the parameters governing the time-dependent behaviour.*

5.5.3 Determination of Fibre Orientation

To investigate ductile materials such as articular cartilage subjected to complex 3-d loading conditions (see Figure 5.12), the use of *von-Mises* stresses is of advantage. The *von-Mises* stresses σ_v calculated from the overall *Cauchy* stress tensor $\mathbf{T}$ reduce the complex stress state to one single scalar value, regardless of the mix of normal and shear stresses. The evolution of the *von-Mises* stresses σ_v during the test procedure of multi-directional shear loading described in section (5.5.1) is illustrated by a few snapshots in Figure 5.13. At time $t = 5\,803\,\text{s}$, cf. Figure 5.13 (a), the rotatably mounted indenter applies a shear loading in the starting direction given by the angle $\alpha_0 = 20°$ with respect to the superficial fibre direction captured in Figure 5.12 (right). At time $t = 5\,819\,\text{s}$, cf. Figure 5.13 (c), the shear loading takes place in the same direction as the superficial fibre orientation after rotating twice by the angle $\alpha = 10°$ from the starting direction α_0. At time $t = 5\,837\,\text{s}$, cf. Figure 5.13 (f), the shear loading is performed in the direction perpendicular to the fibre orientation after 9 rotations of the indenter. Higher values of the computed stresses are clearly observed during loading in the fibre direction (see Figure 5.13 (c)) than in the other directions, as depicted by the contours of the *von-Mises* stresses σ_v.

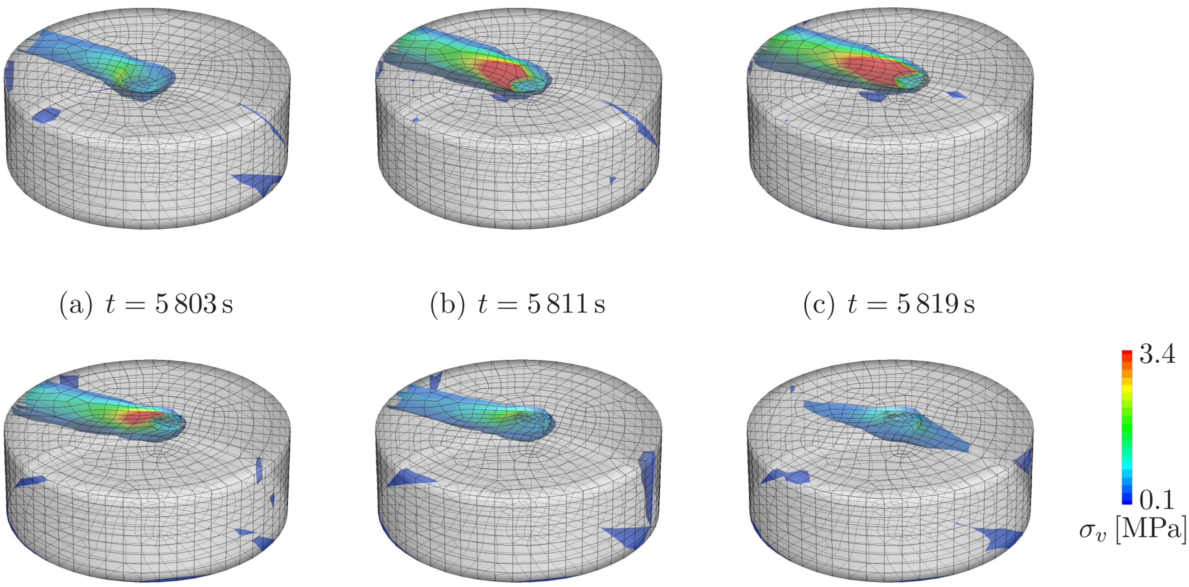

(a) $t = 5\,803\,\mathrm{s}$ (b) $t = 5\,811\,\mathrm{s}$ (c) $t = 5\,819\,\mathrm{s}$

(d) $t = 5\,831\,\mathrm{s}$ (e) $t = 5\,835\,\mathrm{s}$ (f) $t = 5\,837\,\mathrm{s}$

Figure 5.13: *Evolution of the von-Mises stresses σ_v during multi-directional shear loading.*

An alternative to this qualitative evaluation of the fibre orientation is to report every registered stress value in each simulated direction in the form of a diagram. In this regard, the *von-Mises* stress values measured under the indenter surface are depicted using a polar description, yielding

$$\left\{ \begin{aligned} \sigma_{v,\parallel} &= \sigma_v \cos\Omega \\ \sigma_{v,\perp} &= \sigma_v \sin\Omega \end{aligned} \right. \quad \text{with} \quad \Omega = b\,\alpha\,, \tag{5.9}$$

where b is the number of indenter rotations, and Ω is the angle of the actual position. The *von-Mises* stresses $\sigma_{v,\parallel}$ and $\sigma_{v,\perp}$ are the computed stresses parallel and perpendicular to the fibre direction, respectively. These stress values can be interpreted as the major and minor axes of an idealised ellipse, as depicted in Figure 5.14.

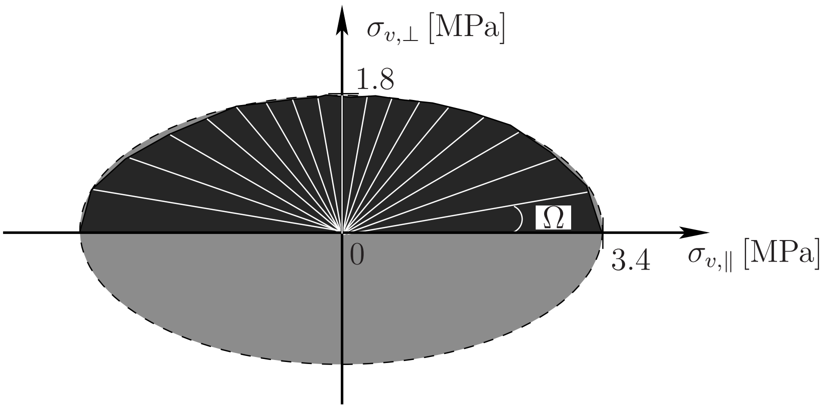

Figure 5.14: *Determination of the fibre direction using a polar description.*

5.6 Further Model Reduction

From these investigations, the model addressed in section 4.5 can be further reduced. Some material parameters related to cartilage properties revealed lower relevance than other central features, such as low-permeability characteristics, matrix viscoelasticity and anisotropic behaviour. When considering articular cartilage at the low permeability regime, anisotropic permeability, deformation-induced hydraulic anisotropy, deformation- and tortuosity-dependent permeability seemed not to play an important role, as is seen from the angle of the introduced IBVP. For the sake of computational efficiency, these features are removed from the proposed model in the following numerical applications. Note in passing that the reason why these properties are negligible lies within the almost impermeable character of the ECM. This assumption holds for healthy cartilage tissues; however, it will also be assumed in Chapter 6, when dealing with degenerative cartilage tissue properties.

Chapter 6: Application to Walking Processes

After the calibration strategy executed in the previous chapter, this chapter focuses on relevant applications of the computational model. In this regard, walking is an important pattern in the analysis of the loading conditions of articular cartilage, since it is the dominant cyclic activity of daily living. Moreover, walking processes are of interest for understanding pathomechanics of osteoarthritis (OA). In this context, the modelling of a complex hip-joint geometry is the first concern in order to investigate these processes. Loads are first applied on full hip-joint geometries to consider the contact of cartilage with synovial fluid by means of a continuum-mechanical treatment. Following this, simplified considerations based on a reduced geometry and contact forces are adopted and extended for further numerical studies. The last part of the present chapter is concerned with the influence of the given mechanical environment on the cartilage cells, the chondrocytes.

6.1 Compression and Shear Loads on a Hip Joint

A first attempt to understand the coupled mechanisms within hip joints is addressed in this section. A holistic biomechanical hip-joint model is elaborated, and first test calculations are performed. In particular, a combination of compression and shear loading (Radin *et al.* [212]) is applied on the designed biological structures.

6.1.1 Geometry and Finite-Element Mesh

In order to visualise the patient-specific, 3-d hip joint anatomy, MRI scans (Figure 6.1, left) are acquired from the associated research partner Prof. Schick (University Hospital of Tübingen). This non-invasive method is well suited for soft biological tissues filled with large amounts of interstitial fluid, such as articular cartilage. In this regard, a 3-d geometry obtained from the image processing software ScanIP is established by the associated research partner Dr. Jäger (University of Stuttgart). This step involves the identification of joint components (femur, ligament, cartilage layers, labrum, fluid gap and pelvis) (Figure 6.1, bottom) and their geometrical representation by spline surfaces (Figure 6.1, centre). The structures that are not directly related to the joint, such as muscles, are neglected. Then, the femur and pelvis bones are truncated to minimise the number of required finite elements and concentrate on the femoral head and the acetabular cup, respectively. This procedure results in a spherical section of the pelvis bone and a straightly cut femur.

Next, the meshing of each single component using 27 140 20-noded, hexaedral *Taylor-Hood* elements and resulting in 366 145 DOF is performed by means of the software ScanFE and CUBIT, as depicted in Figure 6.1 (right).

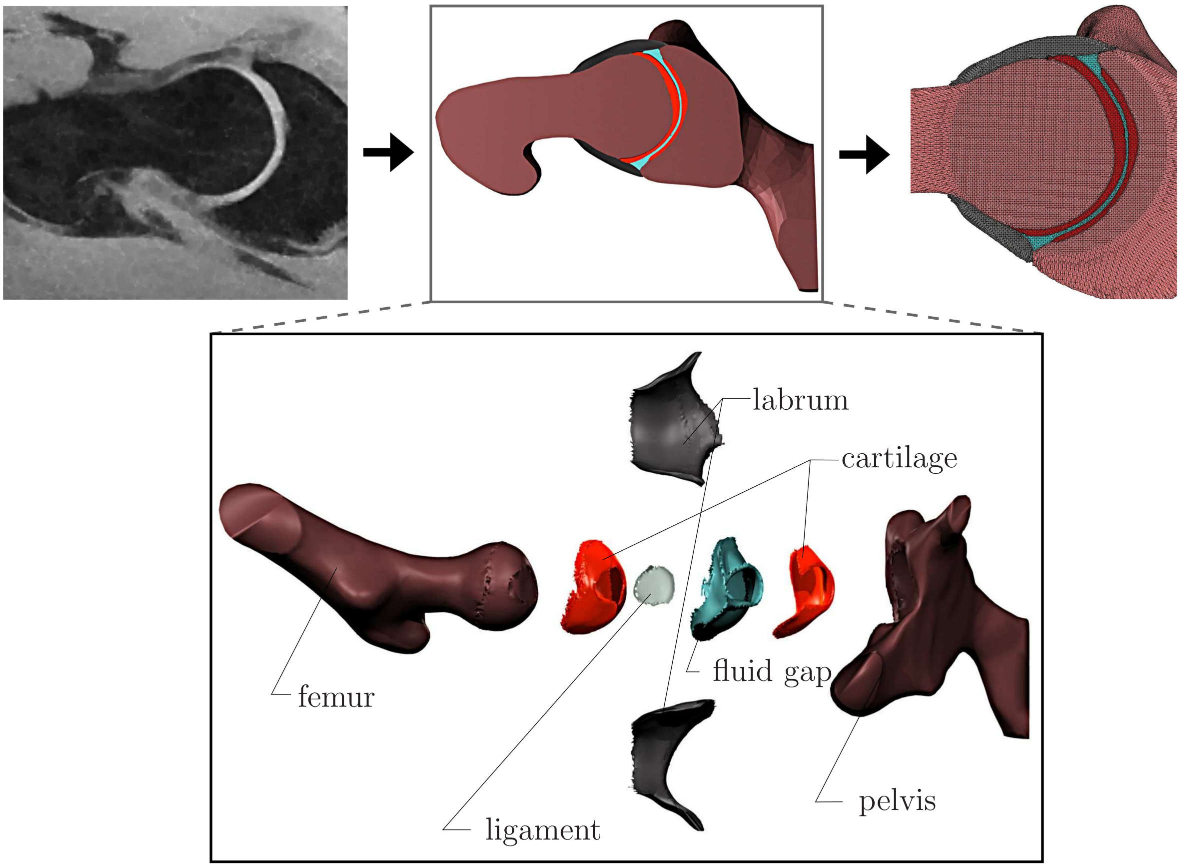

Figure 6.1: *MRI scan of hip joint (left), segmentation of geometry (centre), finite-element mesh (right) and decomposed representation (bottom).*

6.1.2 Visualisation of Stresses in the Hip Joint

After discretisation of the obtained geometry, the outer nodes of the acetabular cup are fixed in space, and all free surfaces are perfectly drained ($\bar{\mathcal{P}} = 0$), as depicted in Figure 6.2. Moreover, test load vectors $\bar{\mathbf{t}}_v$, $\bar{\mathbf{t}}_h$ are applied as a step function, perpendicular and parallel to the section of the femoral bone, respectively. A further load vector $\bar{\mathbf{t}}_n$ is applied perpendicular to the external labrum surface to replicate the "constraint" due to the joint capsule (Hoffmann & Grigg [120], Wingstrand & Wingstrand [257]).

Next, the femoral head, the acetabular cup, the ligament and the labrum are modelled by means of an isotropic poroelastic material (Ehlers [65, 68], Markert [172]) with parameters taken from the literature (Carter & Spengler [48], Ferguson *et al.* [87], Henak *et al.* [115], Hewitt *et al.* [116], Juszczyk *et al.* [135], Malo *et al.* [171], Yosibash *et al.* [263]). The simplified properties of the mentioned biological constituents are summarised in Table 6.1. For a more realistic modelling of the heterogeneous bony structure of the hip-joint constituents, the interested reader is referred to the works of Ascenzi *et al.* [9] and Kardas & Nackenhorst [140] among others. Therein, the bone density distribution is estimated from computed tomography (CT) data which is mapped onto the finite-element mesh. Regarding the description of the cartilage layers of the femoral head and the acetabular

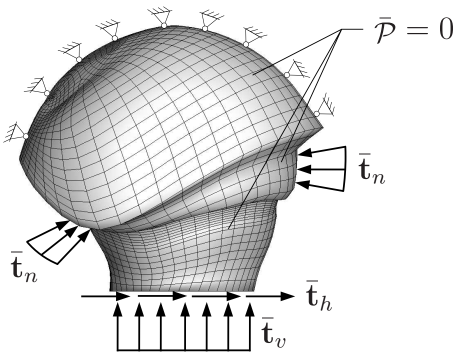

Figure 6.2: *IBVP of hip joint and meshed geometry.*

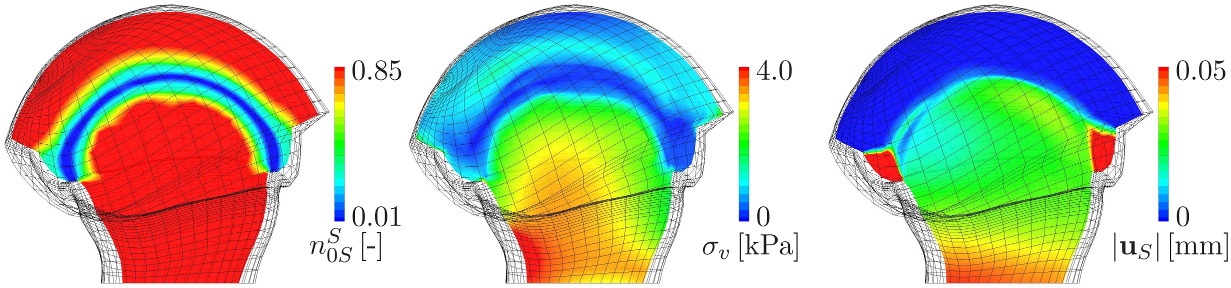

Figure 6.3: *Solidity (left), von-Mises stress (centre) and absolute displacement contours (right).*

cup, the complex bovine cartilage model of a stifle joint calibrated from the multiple-indenter testing in Chapter 5 is adopted. Although differences between material properties of bovine and human cartilage exist, bovine cartilage is often used as a model for human articular cartilage in the framework of pilot clinical studies (Athanasiou *et al.* [10], Nissi *et al.* [203]).

Bone		Ligament		Labrum	
μ_0^S =	$6.53 \cdot 10^3$ [MPa]	μ_0^S =	1.03 [MPa]	μ_0^S =	0.20 [MPa]
λ_0^S =	$9.81 \cdot 10^3$ [MPa]	λ_0^S =	4.66 [MPa]	λ_0^S =	0.10 [MPa]
γ_0^S =	1.0 [−]	γ_0^S =	1.0 [−]	γ_0^S =	1.0 [−]
ρ^{FR} =	10^{-6} [kg/mm^3]	ρ^{FR} =	10^{-6} [kg/mm^3]	ρ^{FR} =	10^{-6} [kg/mm^3]
n_{0S}^F =	0.15 [−]	n_{0S}^F =	0.5 [−]	n_{0S}^F =	0.8 [−]
K_{0S}^F =	$0.21 \cdot 10^{-4}$ [mm^4/N s]	K_{0S}^F =	$0.21 \cdot 10^{-2}$ [mm^4/N s]	K_{0S}^F =	$7.5 \cdot 10^{-6}$ [mm^4/N s]

Table 6.1: *Material parameters of various hip-joint constituents [48, 87, 115, 116, 135, 171, 263]*

As to the synovial fluid, a continuum-mechanical description is chosen, i. e., the fluid is modelled as a linear poroelastic solid. In particular, the fluid behaviour is represented by low values of solidity ($n_{0S}^S = 0.01$) and very low values of permeability ($K_{0S}^F = 0.22 \cdot 10^{-6}$ [mm^4/N s]). The incompressibility of the fluid flow is approached by *Poisson*'s ratio equal to 0.499. Furthermore, the intrinsic incapability of a fluid to resist shear forces is captured by values of the shear modulus or the second *Lamé* constant μ_0^S, much smaller than the first *Lamé* constant λ_0^S, yielding $\mu_0^S << \lambda_0^S$, as presented in Table 6.2. In Figure

Synovial fluid		
μ_0^S	=	0.02 [MPa]
λ_0^S	=	7.0 [MPa]
γ_0^S	=	1.0 [−]
n_{0S}^F	=	0.99 [−]
ρ^{FR}	=	10^{-6} [kg/mm^3]
K_{0S}^F	=	$0.22 \cdot 10^{-6}$ [mm^4/N s]

Table 6.2: *Chosen material parameters for the synovial fluid.*

6.3 (left), the solidity contours are depicted by means of a slice through the components of a whole hip joint. The *von-Mises* stress distribution in Figure 6.3 (centre) does not reveal any strong discontinuities. In Figure 6.3 (right), relatively high absolute displacements are already observed at the junction between labrum and synovial fluid elements for non-physically small load vectors $\bar{\mathbf{t}}_v$, $\bar{\mathbf{t}}_h$ and $\bar{\mathbf{t}}_n$ leading to maximal loads of 8 N, 1 N and 1 N, respectively. This result is related to the quick distortion of the "fluid" elements under shear loading. Thus, numerical instabilities take place and do not render any further computation feasible. This behaviour is obviously due to the treatment of the synovial fluid as a porous material. In the next section, countermeasures are proposed in terms of the implementation of physiological loads directly applied on the femoral head.

6.2 Walking Loads on the Femoral Head

This section presents an easier way to investigate the stress evolution in hip joints during daily activities such as walking. Herein, only the cartilage layer and the underlying femoral bone are considered. Next, a method to transfer reaction forces calculated from multi-body systems (MBS) to external load vectors acting on the boundary of the entire aggregate is explained thoroughly. This method is applied to physiological and pathological walking loads. A further distinction between healthy and osteoarthritic (OA) mechanical responses is also investigated.

6.2.1 Geometry and Finite-Element Mesh

The outer cartilage surface of the real-scale femoral head and its underlying femoral bone are extracted from the previous hip-joint geometrical model. For convenience, the spatial discretisation of the femoral head geometry is conserved and consists of 11 224 20-noded, hexahedral *Taylor-Hood* elements, yielding a total of 157 062 DOF. Then the discretised structure is subjected to the boundary conditions depicted in Figure 6.4 (left). The nodes of the section of the femoral bone are fixed in space and a perfectly drained ($\bar{\mathcal{P}} = 0$) outer surface of the cartilage is assumed. Besides, the contact load vector $\bar{\mathbf{t}}_c$ and the load vector $\bar{\mathbf{t}}_t$ are applied perpendicular and tangential to the cartilage surface, respectively.

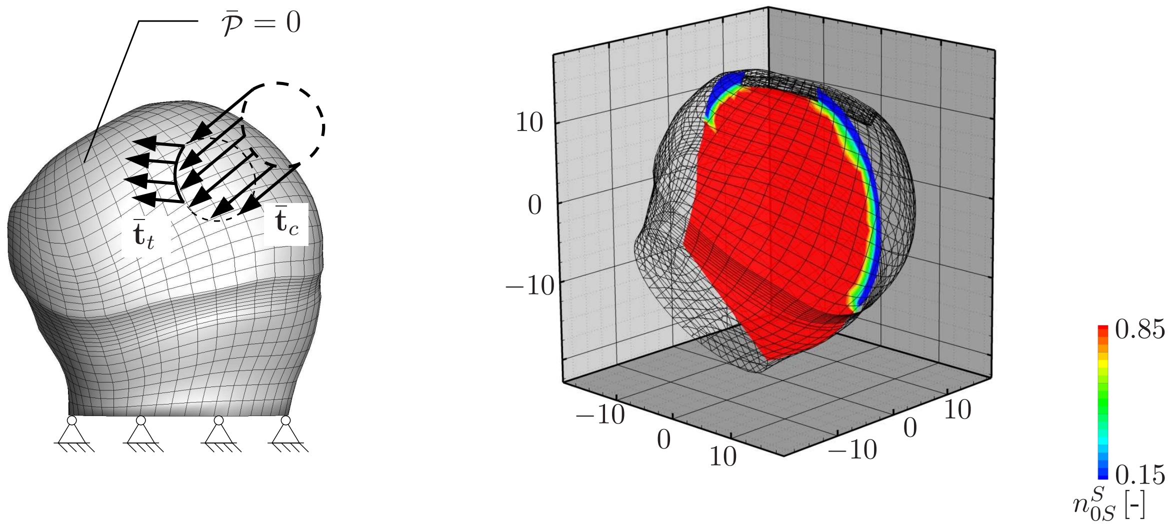

Figure 6.4: *IBVP of femoral head (left) and meshed femoral head geometry (expressed in mm) and solidity contours (right).*

These load vectors are related to walking processes and are therefore variable in space and time. The exact calculation of $\bar{\mathbf{t}}_c$ and its treatment as contact stresses σ_c is the concern of section 6.2.3. Additionally, $\bar{\mathbf{t}}_t$ is related to the low friction in healthy synovial joints, yielding

$$\bar{\mathbf{t}}_t = -\mu_k \, F_c \, \mathbf{s} \, . \tag{6.1}$$

Therein, $\mu_k \approx 0.01$ is the coefficient of friction (Caligaris & Ateshian [45], Linn [163], Mabuchi *et al.* [167], McCutchen [186], Unsworth *et al.* [244]), and F_c is the norm of $\bar{\mathbf{t}}_c$. Moreover, $\mathbf{s}$ is the unit vector in the motion direction of $\bar{\mathbf{t}}_c$ along the cartilage surface.

Figure 6.4 (right) shows the outline of the meshed geometry placed in a metered box. The solidity contours are represented by means of a slice through the cartilage layer and the underlying femoral bone. Furthermore, the geometrical model is oriented according to the joint coordinate system (JCS). To ensure simple comparability of results, this system is recommended for investigations of human joints ([258]).

6.2.2 Osteoarthritic Cartilage Modelling

After constructing the finite-element mesh of the femoral head, this section is concerned with cartilage degeneration and its implication for the presented model. A characterisation of the cartilage damage is generally performed by means of arthroscopy. In this regard, the International Cartilage Repair Society has established an arthroscopic grading system by which cartilage defects can be ranked as follows (Kellgren & Bier [141], Kellgren & Lawrence [142]):

- grade 0: healthy cartilage,
- grade 1: presence of soft spot or blisters at the cartilage surface,
- grade 2: small tears visible in the cartilage,

- grade 3: deep crevices due to lesions and
- grade 4: underlying (subchondral) bone exposed.

It is now well accepted that even small articular cartilage defects can progress to a degenerative state such as osteoarthritis (OA) (Wang *et al.* [251]). The most studied form of cartilage degeneration, OA, leads to a breakdown and eventual loss of the cartilage of one or more joints. The histology of normal and osteoarthritic cartilage layers is depicted in Figure 6.5. Healthy cartilage (Figure 6.5, top) has a smooth articular surface, while osteoarthritic cartilage (Figure 6.5, bottom) shows fibrillation, fissuring of articular surface and clustering of cells in the superficial zone.

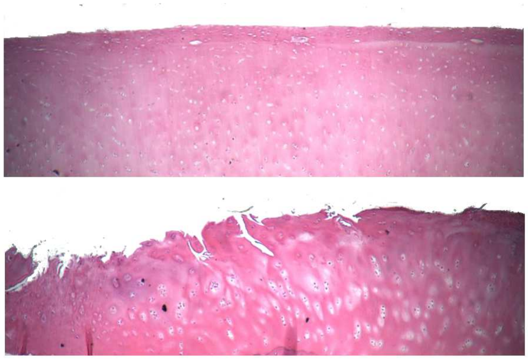

Figure 6.5: *Histology of cartilage in healthy (top) and OA (bottom) state [http://www.med.nyu.edu].*

Generally, OA affects the large weight-bearing joints, such as the knee and hip joints. This condition eventually leads to a complete loss of the cartilage cushion between the bones of the synovial joints. Irritation and inflammation of cartilage are the consequences of repetitive use of the worn joints over the years and cause joint pain due to friction, swelling and limitation of joint mobility (Neusch *et al.* [202]).

Regarding the origin of cartilage degeneration, primary and secondary OA are distinguished. Primary OA is mostly a result of the joint's natural ageing (Berenbaum [23]), when tiny crevasses are formed during cartilage degeneration.

Secondary OA is usually caused by disease, obesity, repeated trauma or surgical incidents, congenital abnormalities, gout and other hormonal disorders. Obesity is the most significant risk factor for secondary OA. Due to an increase of the mechanical stresses on the joint and therefore on the cartilage, an early development of OA is detected amongst overweight individuals and soccer players. Interestingly, studies did not find an increased risk of OA in long-distance runners. Moreover, uric acid and calcium pyrophosphate crystals due to gout or pseudogout condition can cause OA. A few individuals are also born with abnormally joint structures, since OA has a hereditary basis.

Many classifications of the OA degradation stages exist. From a clinical point of view, one empirically distinguishes amongst early, moderate and late stages (Matzat *et al.* [183]). The early stage occurs when cartilage starts to thin out. Cartilage has no nerves but as soon as friction starts to affect the underlying bone, the first symptoms of OA appear.

When cartilage wears down in the moderate stage, the underlying bone becomes thicker, and reactive tissues, called bony spurs, form along joint margins. At this stage, OA starts limiting physical activity, and muscles eventually become weaker, providing less support for the joints. At the later stages of OA, the joint structures are affected, and healthy lubricating synovial fluid is lost.

From a biomechanical point of view, the classifications of OA are based on the composition and structure of articular cartilage (Saarakkala *et al.* [221, 222], Seifzadeh *et al.* [229]). The different states of degradation regarding the collagen fibres, the PG and the cartilage cells are depicted in Figure 6.6. The healthy state of articular cartilage has already been addressed thoroughly in this work. The early OA stage describes superficial defects of cartilage due to the abrasion of the upper tangential fibre layer. During this period, the PG depletion leads to matrix degradation and thus, diminution of the concentration of fixed charges. At the advanced OA stage, deep defects are characterised by collagenase digestions, leading to a weakening of the overall collagen fibre structure. Additionally, the matrix stiffness is further reduced, as well as the concentration of fixed charges. Due to the dramatic PG depletion, the tissue permeability gradually increases.

Regarding the role of the cartilage cells, detailed information is provided in section 6.3.

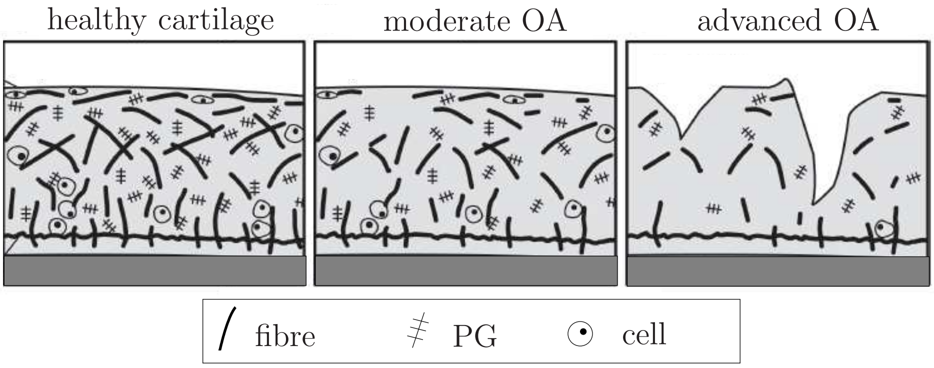

Figure 6.6: *Articular cartilage composition in healthy (left), moderate OA (centre) and advanced OA (right) state (Matzat et al. [183]).*

In this thesis, the cartilage modelling and the setting of constitutive parameters are based on the latter classification at the healthy and advanced OA stages.

The needed constitutive parameters are partially given in the literature (Saarakkala *et al.* [221, 222], Seifzadeh *et al.* [229], Wu *et al.* [260]). For the remaining parameters, no changes with respect to the healthy state, characterised by the parameters from the previous calibration strategy, are assumed. Table 6.3 summarises the structural changes of articular cartilage at the advanced OA stage.

OA state	Material parameter	Parameter change
Advanced OA	μ_0^S	decrease by 26 %
	$\bar{c}^{fc}_{m,0S}$	decrease by 34 %
	$\widetilde{\mu}_1$, $\widetilde{\gamma}_1$	decrease by 75 %
	K^F_{0S}	increase by 400 %
	tangential fibre layer	inexistent

Table 6.3: *Structural changes of articular cartilage in advanced OA state [221, 222, 229, 260].*

6.2.3 Multi-Body System Calculation of Walking

Depending on the grade of OA degeneration, normal or pathological walking processes are investigated. In this context, the use of MBS models in biomechanics and related fields arises from the limited possibilities to measure any kind of forces *in vivo*, although certain exceptions exist (Bergmann *et al.* [24, 25]). The general feasibility of such models could be shown previously (Heller *et al.* [112]). In the presented individual case study performed at the Medical School of Hannover, a 3-d inverse-dynamic MBS of the lower part of the human body consisting of 11 rigid body segments and 8 idealised joints as kinematic constraints was utilised (see left, top, front and right views in Figure 6.7).

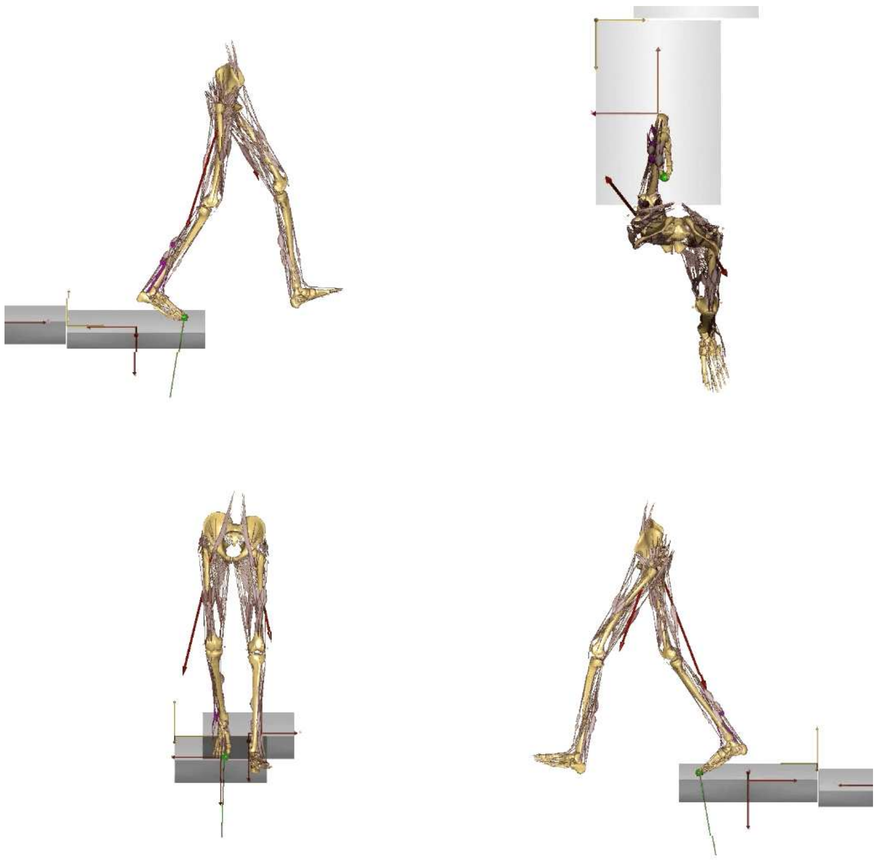

Figure 6.7: *Left (top left), top (top right), front (bottom left) and right (bottom right) views of the MBS walking model (Medical School of Hannover).*

The remaining degrees of freedom were controlled by drivers derived from motion capture data (Andersen *et al.* [7]). The physiological muscles were represented by a three-element *Hill*-type musculo-tendon actuator (Hill [117]). Reaction forces were calculated at the hip considering activation of muscles derived with the aid of a third-order polynomial optimisation criterion solved with a min-max approach (Rasmussen *et al.* [213], Vetterling & Press [247]). These reaction forces were related to physiological and pathological walking processes measured from two patients, who performed walking at a self-selected speed during one gait cycle. A gait cycle is represented by the period of time between the same repetitive events of walking, such as the contact of the same foot on the floor. The cycle is generally subdivided into a stance phase, in which the foot strikes the ground, and a swing phase, in which the foot is mostly in the air, as depicted in Figure 6.8.

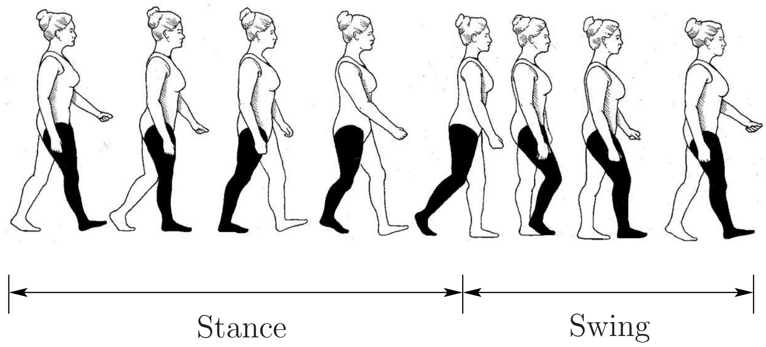

Figure 6.8: *Phases of gait cycle [http://www.jaaos.org].*

Data collection from the gait cycles were approved by the local ethics committee (Medical School of Hannover) and the patients provided written consent. Patient P1 (male, 46 years old, 80.2 kg, 1.71 m) did not show any signs of joint degeneration, while patient P2 (male, 45 years old, 76.2 kg, 1.75 m) displayed moderate OA (*Kellgren-Lawrence* grade 3) (Kellgren & Bier [141], Kellgren & Lawrence [142]) after examination with plain radiographs. The MBS model was scaled anthropometrically (Rasmussen *et al.* [214]) for an adjustment to the individual patient. The data related to the individual case study is summarised in Table 6.4.

Patient	Sex	Age	Body mass	Height	OA grade
P1	male	46 years	80.2 kg	1.71 m	0
P2	male	46 years	76.2 kg	1.75 m	3

Table 6.4: *Data of individual case study.*

6.2.4 Treatment of Contact Forces as Contact Stresses

The transfer of the contact forces $\mathbf{P}'_c$ in resulting contact areas and pressures is analysed in the framework of a contact problem. The solution for such a problem has been the concern over the last decades. Numerous contact force models have been developed, providing different ranges of application and accuracy, depending on the contact scenarios (Machado *et al.* [168]). Studies of contact problems were initially introduced by *Hertz*

The reaction forces $\mathbf{P}_c$ obtained from the MBS model were calculated at the origin O of the JCS. Assuming a perfectly spherical femoral head of radius $r_h = 25\,\text{mm}$, the position vector $\mathbf{x}_c$ of the intersection point C of $\mathbf{P}_c$ with the surface of the femoral head is expressed as

$$\mathbf{x}_c = \frac{r_h}{P_c}\,\mathbf{P}_c\,, \tag{6.2}$$

where $P_c = |\mathbf{P}_c|$ is the vectorial norm of the force $\mathbf{P}_c$. Then, the contact force $\mathbf{P}'_c$ is determined after translation of $\mathbf{P}_c$ along its line of action. A schematic 2-d representation of the idealised hip joint is given in Figure 6.9.

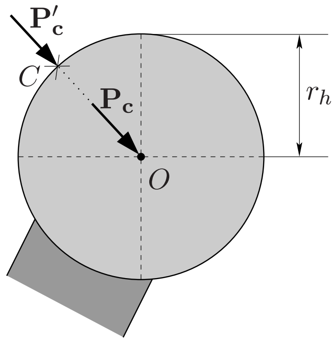

Figure 6.9: *Calculation of contact forces from reactions forces.*

(1881), who found an analytical form for the problem of the contact of two elastic spheres. *Hertz* made the following assumptions:

- the contact area is small compared to the areas of the contacting bodies and their relative radii of curvature,
- the body surfaces are smooth and have an ideal form,
- no friction is detected in the contact region and
- only linear elastic strains are measured in the contact zone.

Further studies showed that relaxing assumptions of the *Hertz*ian theory still lead to highly accurate results and that the stresses and deformations of inelastic bodies could be examined under certain conditions (Johnson [129]). In particular, the partial non-slip case, i. e., caused by friction, was addressed, and it was observed that even contact between non purely frictionless materials could be treated with the *Hertz*ian theory. The contact stresses could be rather well predicted, even with large contact areas (Zhupanska [264]). However, in the case of contacts at several points (Gonzalez-Perez *et al.* [97]) or for very large contact regions in connection with highly deformable contacting bodies (Ciavarella *et al.* [51]), the *Hertz*ian theory did not hold any more.

Besides, the anterior *Hertz*ian contact theory, based upon the linear elastic theory, does not comprehend the more recent framework of the TPM. Therefore, the parameters defined for a single-phasic deformable material described by the *Hertz*ian theory are regarded as estimations of material parameters deduced from the solid-fluid biphasic behaviour of articular cartilage. Articular cartilage acts almost as an incompressible material under rapid loading due to its very low permeability. Consequently, the overall *Poisson*'s ratio ν, required by the *Hertz*ian theory, is assumed to be equal to 0.5 in a geometric linear setting.

In contact studies, the hip joint is generally assimilated to a perfect ball-and-socket joint by means of a spherical femoral head (Genda *et al.* [96], Yoshida *et al.* [262]) where the cartilage layers of the ball (femoral head) and the socket (acetabular cup) have the same properties. A closer observation of the contact between cartilage layers reveals the similarity of the hip joint with a perfect ball-and-socket joint, as shown in MRI scans in Figure 6.1 (left). Nevertheless, it appears that a simplified contact study might eventually lead to inaccuracies in the predicted magnitude and distribution of cartilage contact pressures (Anderson *et al.* [8]). However, this assumption will be made in the simplified *Hertz*ian contact modelling of cartilage.

As illustrated in Figure 6.10, the repartition of the contact force $\mathbf{P}'_c$ is performed over the curved surface of a spherical cap of radius r_c reading (Sun & Hao [240])

$$r_c = \sqrt[3]{\frac{3\,P_c R}{2}\,\frac{1-\nu^2}{E^*}}\,, \tag{6.3}$$

where, $1/R = 1/r_h + 1/r_a$ is the sum of the curvatures of ball and socket, and $r_a = 28\,\text{mm}$ is the estimated radius of the acetabular cup. The height h of the spherical cap is easily calculated from *Pythagore*an theorem as

$$h = r_h - \sqrt{r_h^2 - r_c^2}\,. \tag{6.4}$$

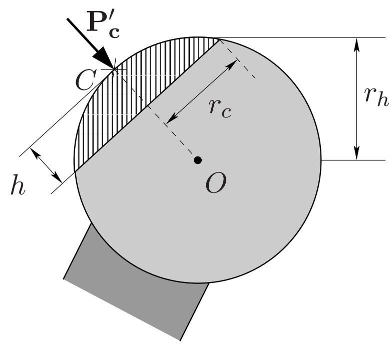

Figure 6.10: *Hertzian contact surface.*

In equation (6.3), the modulus $E^* \approx E\,(h_{\text{OK}}/h^*)$ (Hayes *et al.* [109], Wu *et al.* [260]) is inversely proportional to the cartilage thickness $h^* = \{h_{\text{OK}}, h_{\text{OA}}\}$ where h_{OK} and h_{OA} are the cartilage thickness in its healthy and OA states, respectively. At the OA advanced stage, the superficial fibre layer is abrased, i. e., $h_{\text{OA}} = 0.8\,h_{\text{OK}}$. The overall cartilage layer's modulus is evaluated as $E = 4.5\,\text{MPa}$, due to the limitation of the contact surface area $A_c = 2\,\pi\,r_h\,h$ to maximal values of $2\,450\,\text{mm}^2$ under physiological conditions (Daniel *et al.* [53]). As a consequence of equation (6.3), the following interdependencies hold for the evolution of the contact zone of radius r_c:

- the smaller the overall *Poisson*'s ratio ν, the greater the contact zone radius r_c,
- the smaller the overall stiffness E^*, the greater the contact zone radius r_c,
- the higher the contact force P_c, the greater the contact zone radius r_c.

The axial stresses σ_c obtained from this simplified *Hertz*ian contact model of cartilage in (6.5) are implemented as *Neumann* boundary conditions in the overall momentum balance of the aggregate and imported in PANDAS.

Following this, the contact force $\mathbf{P}'_\mathbf{c}$ is distributed over the contact surface by means of a paraboloidal repartition of the load vectors $\bar{\mathbf{t}}_c$ (see Figure 6.11), leading to axial stresses σ_c formulated as

$$\sigma_c = \sigma_{c,max} \sqrt{1 - \frac{r}{r_c}} \quad \text{with} \quad \sigma_{c,max} = \frac{3\,P_c}{2\,\pi\,r_c^2}\,, \tag{6.5}$$

where r is the distance between an arbitrary point X on the contact surface and the contact point C, and $\sigma_{c,max}$ is the maximal value of the axial contact stresses σ_c.

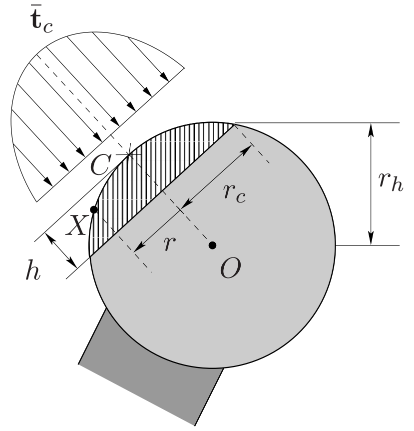

Figure 6.11: *Load distribution of Hertzian contact force.*

6.2.5 Visualisation of Stresses and Pressures in Cartilage

The visualisation of stresses and pressures in articular cartilage is subdivided in different cases summarised in Table 6.5 related to data of the individual case study in Table 6.4. Case I is related to healthy cartilage under physiological loading during the walking cycle of patient P1. Case II considers OA cartilage properties in its advanced stage for normal walking. Hereby, case II is a purely numerical case, in which the coexistence of OA cartilage and normal walking is assumed. Case III represents the pathological walking of OA cartilage related to patient P2.

Case	Cartilage state	Walking type	Patient
I	healthy	normal	P1
II	advanced OA	normal	/
III	advanced OA	pathologic	P2

Table 6.5: *Different cases of OA and walking.*

The *von-Mises* stress contours σ_v (expressed in MPa) related to the overall *Cauchy* stresses $\mathbf{T}$ at the cartilage surface (isolated from the underlying femoral bone) are represented for case I (top row), case II (centre row) and case III (bottom row), for different time steps in Figure 6.12.

In cases I to III, the mean contact stresses rise to about 1.9 MPa with peaks of 2.9 MPa. The mean values mainly range between 2.0 and 3.0 MPa, as obtained from *in-vitro* experiments (Day *et al.* [54]), though Hodge *et al.* [119] found maximum contact stresses of 4.0 MPa after *in-vivo* experiments during walking. A comparison of this study's results with those of Hodge *et al.* [119] reveals lower values obtained with the presented model. Multiple causes might be responsible for this discrepancy. One possible error source is the patient's unknown body weight, which plays an important role in the measured loads. Furthermore, the calculation of the contact area, which has a significant influence on the obtained contact stress values, may contain some imprecisions.

More recent numerical studies based on a discrete-element analysis (DEA) (Abraham *et al.*

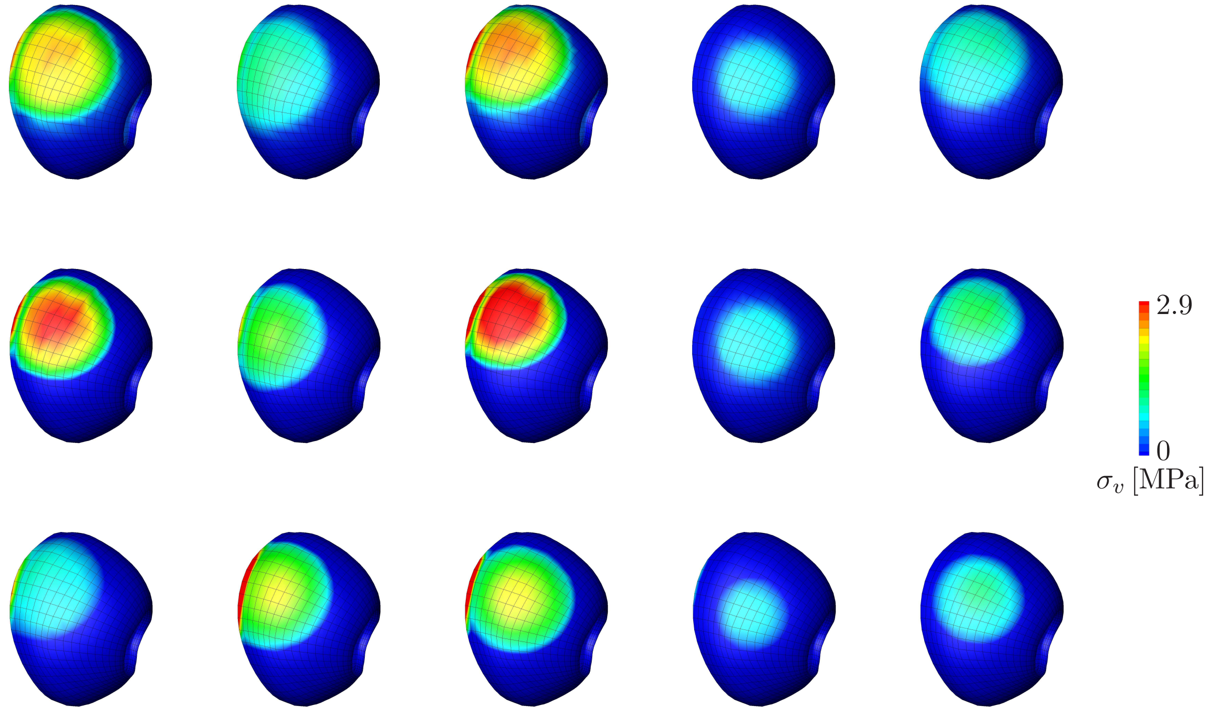

(a) $t = 0.1\,\mathrm{s}$ (b) $t = 0.3\,\mathrm{s}$ (c) $t = 0.5\,\mathrm{s}$ (d) $t = 0.7\,\mathrm{s}$ (e) $t = 1.0\,\mathrm{s}$

Figure 6.12: *von-Mises stress contours related to the overall Cauchy stresses* $\mathbf{T}$ *for case I (top row), case II (centre row) and case III (bottom row).*

[1], Genda *et al.* [96], Yoshida *et al.* [262]) systematically predict higher values than the contact stresses observed in the proposed model. In particular, due to an underestimation of the contact area discretised by compressed springs in the DEA, stiffer behaviour is expected. Comparisons of contact stresses predicted by both a finite-element analysis and a DEA show a mismatch for FE multiple-layer models (Abraham *et al.* [1]). In the context of a FE two-layer model, mean stress values between 2.0 and 2.5 MPa are obtained by Abraham *et al.* [1], whereas approximately 2.0 MPa is calculated by Anderson *et al.* [8]. These results mostly coincide with those obtained by the presented model.

Regarding case II, higher localised stress peaks and slightly smaller contact surfaces are observed. Even though the OA overall cartilage stiffness diminishes with respect to healthy cartilage, the predominant factor seems to be related to the combined effects of a reduction of the shear modulus as well as the removal of the superficial fibre layer. Consequently, smaller contact areas are obtained and thus, higher stresses are generated for the same external loading as in case I. As expected, the load support in OA cartilage diminishes and is more locally concentrated.

Another observation of the smaller contact areas in case II than those in case I is obtained from the contours of the overall pore-fluid pressure p at the cartilage-bone interface in Figure 6.13. Case II shows systematically smaller pressure surfaces at the cartilage-bone interface with more localised pressure distributions. One possible reason is that the load transfer is mostly redirected to the ECM. Subsequently, higher local stresses in the OA

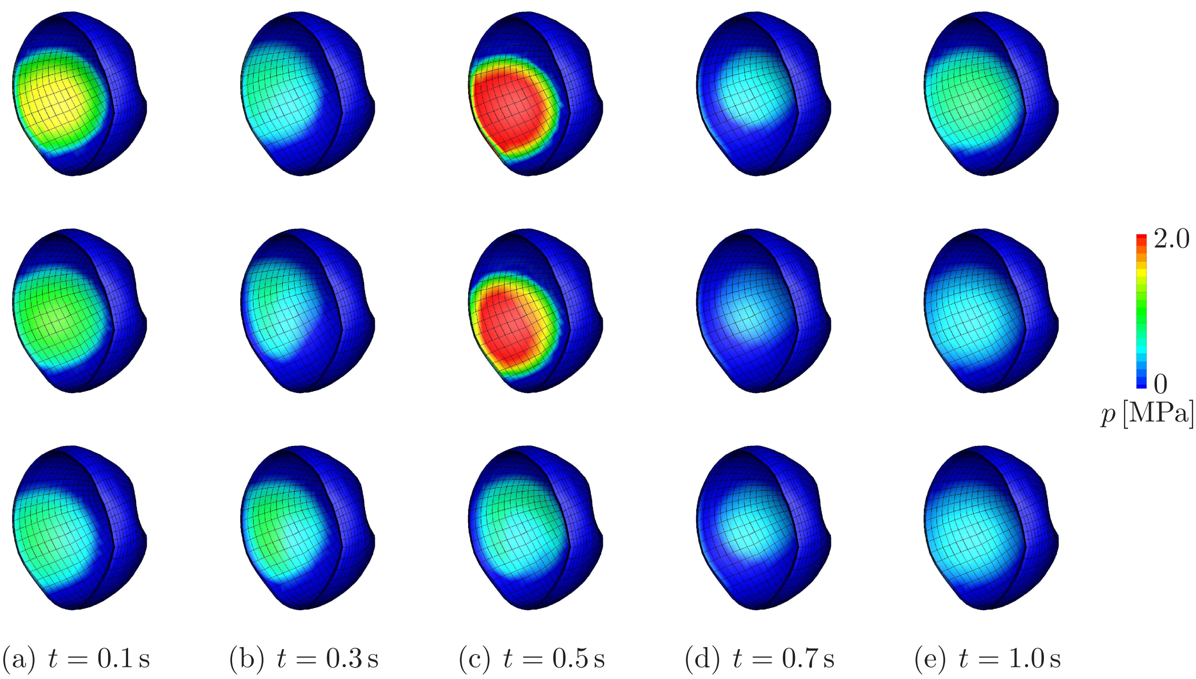

Figure 6.13: *Overall pressure contours for case I (top row), case II (centre row) and case III (bottom row).*

state than in the healthy state are calculated under the same loading conditions.

In case III (Figure 6.12, bottom row), the external loading is related to a pathological walking process combined with OA cartilage. In this context, the measured hip forces from the MBS are smaller and their orientations are different from the previous cases. It appears that in order to avoid pain, the patient suffering from OA modifies his walking pattern. As shown here, it leads to no significant high stress peaks and thus reduces the risk of further cartilage degradation. Note that the elongated red spots observed in Figure 6.12 for case II and III demarcate the end of the cartilage surface and are related to numerical inconsistencies due to accumulated boundary stresses at the bone interface.

6.2.6 Stereographic Projection of Stresses

After investigating the mechanical effects of OA on the cartilage layer, the objective of this section is to increase the practicability of the elaborated model for clinical purposes. In particular, 3-d views of variables, such as the *von-Mises* stresses σ_v or the overall pore-fluid pressure p, need to be presented in a concise way allowing for a comparison with other observations. Here, the processing of variables for visual representations using a simplified stereographic projection will be demonstrated.

The stereographic projection is *per se* a smooth and bijective mapping for projecting a sphere onto a plane with some inevitable compromises. The projection is defined on the entire sphere except at the projection point. It is conformal, i. e., the angles are preserved but neither isometric nor area preserving. Due to the intensive use of spheres and planes in many areas of mathematics, the applications of stereographic projection are numerous in various fields such as cristallography, cartography, geology and photography, amongst others. An upcoming field of application of projection techniques is the hip-joint and cartilage histology. In this regard, Kurrat & Oberländer [151] made use of conical and orthographic projections for deriving maps of distribution of cartilage thickness at the femoral head and acetabular cup of many subjects. More recent studies of Najjar *et al.* [199] investigated the excessive wear in prosthetic femoral heads due to clinical failures. In this connection, they depicted the deformations in acetabular cups based on stereographic projections of deviations between points located on the cup's internal surfaces and the points on an ideal hemisphere surface.

Similar to the globe, the femoral head geometry is divided into a system of meridians and latitudes. Furthermore, the "south pole" is chosen as the centre of the projection, as represented by the grid in Figure 6.14. Regarding the implementation procedure of

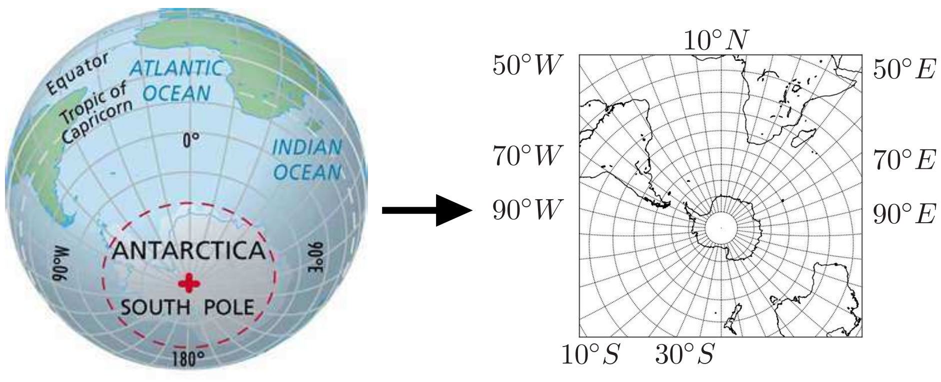

Figure 6.14: *Grid for stereographic projection of articular cartilage based on earth globe [http://www.travel-babel.com].*

stereographic mapping, two calculation steps are performed. First, the discrete nodal points at the cartilage surface are automatically extracted from the post-processor Tecplot using Matlab at each calculated time step, and the cartesian coordinates of the nodes are transformed into spherical coordinates. Then, the toolkit matplotlib basemap is used by the associated research partner Dr. Jäger as a library for plotting data on maps using the programming language Python. Particularly, this tool enables plotting of contours, images, vectors or points in the chosen transformed coordinates.

After simplifying the graphical representation of the results, a universal color code represented by the traffic lights, i. e., red, yellow and green, is adopted as a standardised legend for high, middle and low stress levels, respectively. In this regard, a unique estimation of the middle or normal stress level based on the literature seems not to be accepted overwhelmingly. Contact stresses fluctuate significantly, depending on the considered joint and the experimental conditions. In the particular case of contact stresses related to healthy hip joints under physiological loading, Brown & Shawn [43] evaluated the normal stress level at approximately 2.9 MPa. Brinckmann *et al.* [40] and Maxian *et al.* [185] suggested a normal stress level between 1.4 and 1.6 MPa and lower than 2 MPa, respectively. In this context, a range of stress values between 1 and 2.6 MPa is chosen.

The high or abnormal stress values found in the literature are mostly associated with clinical conditions of cartilage abnormalities. Experimental studies of Iglic *et al.* [125] and Hipp *et al.* [118] demonstrated an increase of contact stresses by two to five times, compared to normal stresses. Again, these reports show considerable variations, as well as overlaps with contact stress values under normal conditions. In this thesis, the high stress level is defined as the stresses exceeding 2.6 MPa, as introduced by Hipp *et al.* [118]. Subsequently, the lower domain of variation of the stresses in cartilage is given by stress values lower than 1 MPa. In summary, the distinction amongst the *von-Mises* stress contours across high, middle and low stress levels is presented in Figure 6.15.

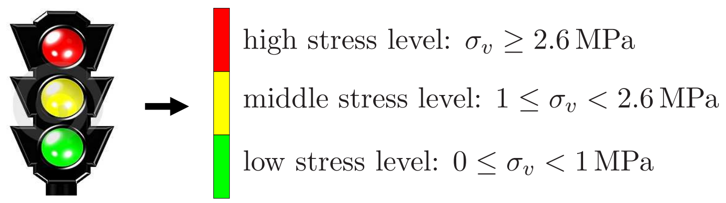

Figure 6.15: *Simplified legend for contact stress levels based on traffic lights [http:/www.radiokiepenkerl-online.de].*

Based on this, the application of the presented tool to the 3-d representation of the stress contours depicted in Figure 6.12 leads to Figure 6.16. Here, as well as for case I (healthy cartilage with normal walking) and case III (OA cartilage with pathological walking), the values of the *von-Mises* stresses are mainly observable in the low and middle ranges. Regarding case II (OA cartilage with normal walking), higher values of stresses are depicted at time $t = 0.1\,\mathrm{s}$ and $t = 0.5\,\mathrm{s}$. According to the chosen stress classification, a danger of further increase in OA can be established.

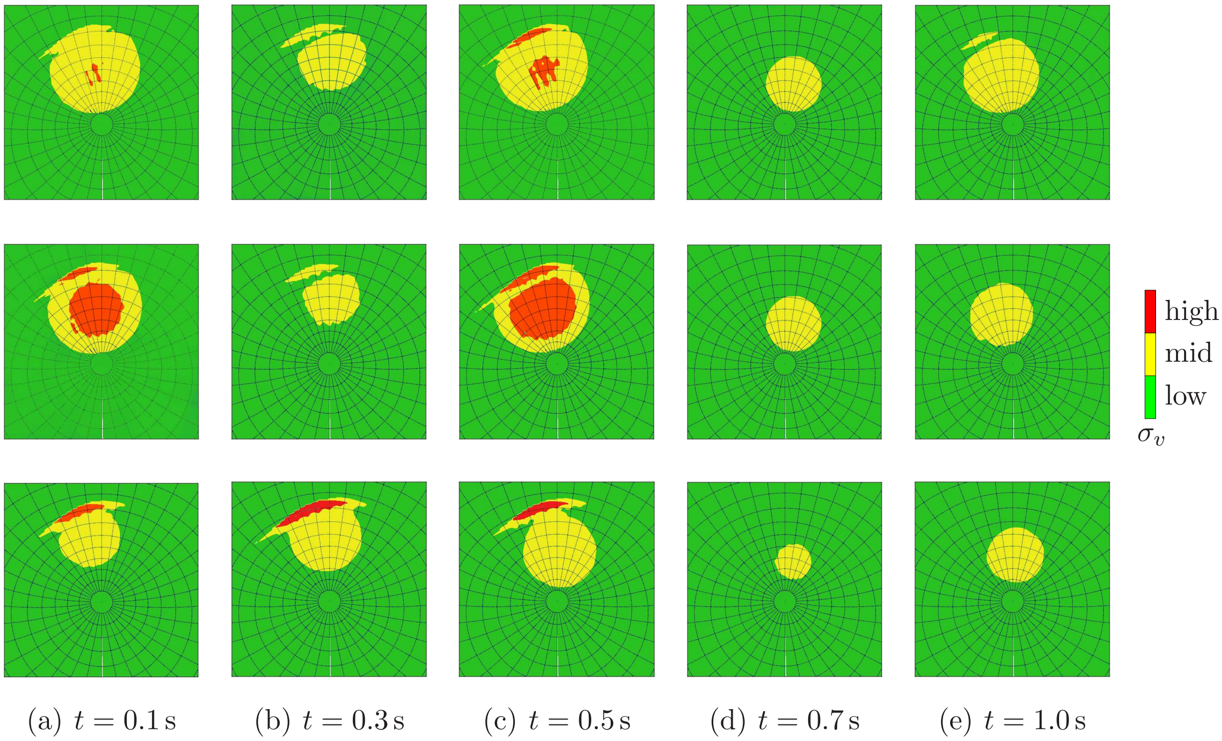

Figure 6.16: *Simplified stereographic projection of the von-Mises stresses for case I (top row), case II (centre row) and case III (bottom row).*

6.3 Aspects of Mechanobiology

Embedded within the ECM of articular cartilage are dispersed cells, the chondrocytes. The chondrocytes' role is to remodel the ECM when changes in loading history occur (Guilak *et al.* [103]). Their activity is mostly regulated by complex environmental influences and mechanical factors. In particular, the influence of the mechanical environment on the cells has been shown to be crucial (Guilak *et al.* [103], Stockwell [238]). A change in the mechanical environment is experienced through complex mechanisms of cell-matrix interaction and influences the metabolic and biosynthesic activities (Buschmann *et al.* [44], Kim *et al.* [145], Little & Ghosh [166], Sah *et al.* [223]). For instance, a specific visualisation tool in Figure 6.17 identifies cells in cartilage that are producing PG. These cells are represented by dark blue stains. When cartilage is not subjected to continuous passive motion (Figure 6.17, left), less PG are produced by chondrocytes than when the synovial joint is continuously moved (Figure 6.17, right).

Furthermore, cartilage degeneration such as OA will eventually lead to pathological changes in the mechanical signals perceived by the chondrocytes (Alexopoulos *et al.* [4], Guilak & Mow [101]). This section aims to investigate accurately the influence of the mechanical environment on the chondrocytes' response in healthy and OA cartilage during physiological and pathological walking processes.

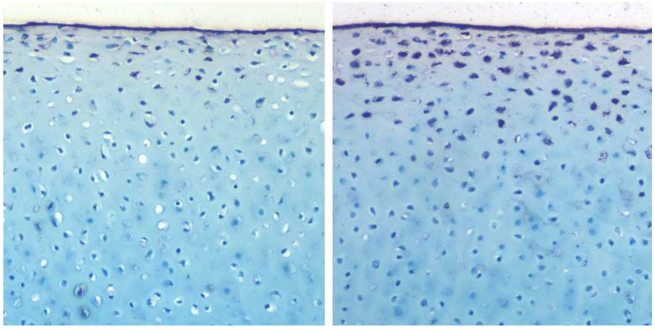

Figure 6.17: *Cell production state for low activity level (left) and for high activity level (right) [http://www.jacobsschool.ucsd.edu].*

6.3.1 Cells regarded as Weak Inclusions

Chondrocytes are further components of articular cartilage and occupy less than 10 % (Stockwell [237]) of the overall volume aggregate. They are composed of a solid phase consisting of cytoskeletal elements and other proteins, and a fluid phase containing water with dissolved proteins and ions. Previous studies show that chondrocytes change in shape across the thickness of the cartilage layer (Guilak *et al.* [102]) and display different material properties from the surrounding ECM (Jones *et al.* [131], Shin & Athanasiou [231]). Here, chondrocytes are considered as perfectly spherical (Eggli *et al.* [63]) and attached to the ECM through a narrow tissue region, the pericellular matrix (PCM). The PCM is primarily characterised by the presence of type VI collagen but also possesses a high concentration of PG. The PCM (2.5 μm thick) combined with the encapsuled cell (7.5 μm diameter) build the chondron, a functional unit in cartilage tissues.

In this framework, chondrons are regarded as spherical inclusions, embedded in the overall inhomogeneous tissue material of the ECM. The idea of using this concept for predicting the effective properties of an inhomogeneous continuum, such as composite materials, was originally introduced by Eshelby [84, 85]. Based on his theory, numerous models of elastic and elastoplastic materials with direct application to natural or manufactured multi-phase composites have been developed over the last three decades. Nevertheless, inadequacies were detected when the reinforcement in volume fraction or when the inhomogeneity of the inclusion and the matrix became important (Viéville & Lipinski [248]). In this approach, the inclusion modelling an inhomogeneity is smeared in a homogenised material, whose properties can be very different from those of the original matrix surrounding the inclusion. In Mori & Tanaka [188], the inclusion directly interacts with a uniform matrix, which is submitted to an external load or constraint. In the particular case of isotropic spherical inclusions embedded in a matrix, the effective specific parameters of the homogenised material for the effective compression modulus $\delta^S_{0,\text{eff}}$ and shear modulus $\mu^S_{0,\text{eff}}$ are:

$$\delta^S_{0,\text{eff}} = \delta^S_0 + n^C_0 \, \frac{(\delta^C_0 - \delta^S_0)\, \delta^S_0}{\delta^S_0 + \alpha_M \, (1 - n^C_0)(\delta^C_0 - \delta^S_0)} \tag{6.6}$$

and

$$\mu^S_{0,\text{eff}} = \mu^S_0 + n^C_0 \, \frac{(\mu^C_0 - \mu^S_0)\, \mu^S_0}{\mu^S_0 + \beta_M \, (1 - n^C_0)(\mu^C_0 - \mu^S_0)}\,, \tag{6.7}$$

where

$$\alpha_M = \frac{3\,\delta_0^S}{3\,\delta_0^S + 4\,\mu_0^S} \quad \text{and} \quad \beta_{\mathrm{M}} = \frac{6\,(\delta_0^{\mathrm{S}} + 2\,\mu_0^{\mathrm{S}})}{5\,(3\,\delta_0^{\mathrm{S}} + 4\,\mu_0^{\mathrm{S}})} \tag{6.8}$$

are scalar parameters. The parameters denoted by $(\,\cdot\,)_0^C$ are related to the chondrons, and the parameters characterised by $(\,\cdot\,)_0^S$ are related to the ECM. In particular, n_0^C is the inclusion concentration (also called the secondary porosity), i. e., the volume fraction of the chondron.

In the present case of a cell coated by the PCM and embedded inside the ECM, a generic way to handle coating is given by the multi-inclusion method of Nemat-Nasser & Hori [201]. Thereby, the PCM (coating) behaves as if it were a second inclusion in the ECM (matrix), additionally to the original cell (first inclusion), as depicted in Figure 6.18.

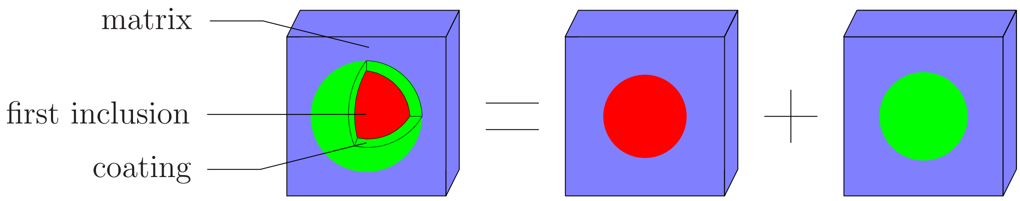

Figure 6.18: *Multi-inclusion concept of Nemat-Nasser & Hori.*

In this framework,

$$n_0^C = n_0^Z + n_0^P\,, \tag{6.9}$$

where n_0^Z and n_0^P are the volume fractions of the chondrocytes and the PCM, respectively. Based on the volume of a sphere expressed for the cell and chondron volumes and assuming $n_0^C = 0.1$ (Stockwell [237]),

$$\begin{aligned} n_0^Z &= \frac{\frac{1}{6}\,\pi\,D_Z^3}{\frac{1}{6}\,\pi\,D_C^3}\,n_0^C = 0.042 \quad \text{and} \\ n_0^P &= n_0^C - n_0^Z = 0.058\,, \end{aligned} \tag{6.10}$$

where D_Z and D_C are the diameters of a single chondrocyte and a chondron, respectively. Subsequently, equations (6.6) and (6.7) are extended as

$$\delta_{0,\text{eff}}^S = \delta_0^S + n_0^Z \frac{(\delta_0^Z - \delta_0^S)\,\delta_0^S}{\delta_0^S + \alpha_M\,(1 - n_0^Z)(\delta_0^Z - \delta_0^S)} + n_0^P \frac{(\delta_0^P - \delta_0^S)\,\delta_0^S}{\delta_0^S + \alpha_M\,(1 - n_0^P)(\delta_0^P - \delta_0^S)} \tag{6.11}$$

and

$$\mu_{0,\text{eff}}^S = \mu_0^S + n^Z \frac{(\mu_0^Z - \mu_0^S)\,\mu_0^S}{\mu_0^S + \beta_M\,(1 - n_0^Z)(\mu_0^Z - \mu_0^S)} + n_0^P \frac{(\mu_0^P - \mu_0^S)\,\mu_0^S}{\mu_0^S + \beta_M\,(1 - n_0^P)(\mu_0^P - \mu_0^S)}\,. \tag{6.12}$$

Therein, the parameters denoted by $(\,\cdot\,)_0^Z$ are related to the cells, and the parameters denoted by $(\,\cdot\,)_0^P$ refer to the PCM. From equations (6.11) and (6.12), the effective first *Lamé* constant $\lambda_{0,\text{eff}}^S$ is easily deduced.

Next, the effective permeability of tissue composed of the ECM and fluid-filled inclusions of finite size is obtained by using effective medium schemes such as differential effective medium, self-consistent or *Maxwell* methods or even more recent methods (Berryman & Berge [26], Markov *et al.* [177]). According to *Maxwell* formula, the effective permeability $K^S_{0S,\text{eff}}$ of the overall aggregate containing spherical inclusions is given by

$$K^F_{0S,\text{eff}} = K^F_{0S}\,\frac{1 + 2\,n^C_0\,\zeta_C}{1 - n^C_0\,\zeta_C} \quad \text{with} \quad \zeta_C = \frac{K^C_0 - K^F_{0S}}{K^C_0 + 2\,K^F_{0S}}\,. \tag{6.13}$$

Here, ζ_C is a scalar parameter, and the chondron permeability K^C_0 is postulated as the volumetric average of the permeability K^Z_0 of the cell and the permeability K^P_0 of the PCM, yielding

$$K^C_0 = \frac{n^Z_0}{n^C_0}\,K^Z_0 + \frac{n^P_0}{n^C_0}\,K^P_0\,. \tag{6.14}$$

In this regard, the chondrons are modelled by means of an isotropic, poroviscoelastic formulation (Markert [172]). For the sake of simplicity, the volumetric and deviatoric retardation time constants of chondrocytes and PCM are assumed to be equal to the time constants of the ECM. The above-mentioned homogenisation procedure can thus be extended to predict the behaviour of viscoelastic inclusions (Camacho *et al.* [46], Lielens [159], Pierard *et al.* [209]).

As the properties of the chondrons appear to be fairly uniform amongst the different zones of the tissue (Alexopoulos *et al.* [4, 5]), constant material parameters over the cartilage thickness are taken from the literature (Athanasiou *et al.* [11], Bachrach *et al.* [14], Chen & Lu [49], Guilak & Mow [101], Koay *et al.* [147], Korhonen *et al.* [148], Leipzig & Athanasiou [155], Likhitpanichkul *et al.* [161]). As explained in section 5.4.2, the parameters found in the literature have to be considered in a very differentiated and careful way for several reasons. First, these parameters are related to various models which might differ from the present model and are generally identified by means of model-dependent calibration strategies. Second, experimental tests performed on small entities such as cells are more easily prone to measurement errors than experiments on cartilage tissues. This difference becomes clear by examining closer the widespread range of parameters for cell and PCM given in the literature. Accordingly, the chosen parameters for the cells and PCM are summarised in Table 6.6.

Chondrocyte			PCM		
μ^Z_0	=	$1.4 \cdot 10^{-3}$ [MPa]	μ^P_0	=	$19.2 \cdot 10^{-3}$ [MPa]
λ^Z_0	=	$0.2 \cdot 10^{-3}$ [MPa]	λ^P_0	=	$1.7 \cdot 10^{-3}$ [MPa]
K^Z_0	=	$0.72 \cdot 10^{4}$ [mm^4/N s]	K^P_0	=	$0.71 \cdot 10^{-1}$ [mm^4/N s]

Table 6.6: *Material parameters of chondrocytes and PCM [11, 14, 49, 101, 147, 148, 155, 161].*

6.3.2 Local Stresses in Cells

This section intends to describe the simulation of a small number of cartilage cells at given positions. This description is based on the "re-creation" of the mechanical environment of the cells using the investigated walking processes. Furthermore, the calculated stress states of single cells obtained with the proposed cartilage model are confronted with the results from the extended cartilage model containing cells as weak inclusions.

In particular, three chosen cell locations, at the mid-depth of the articular cartilage layer, are represented by the white dots depicted on the femoral head geometry in Figure 6.19. For each single cell, the loading history during walking is represented by means of the *von-Mises* stresses σ_v for case I (left column), case II (centre column) and case III (right column). The red curves are related to the results obtained with the original cartilage model. The green curves refer to the results calculated with the extended cartilage-cell model. Almost no difference between both curves can be observed, except for one cell position, where the cartilage-cell model provides slightly smaller stress values. This result is likely due to the "weakening" of the ECM when considering cells as weak inclusions. However, this influence is mostly negligible because of the small cell volume fraction in the tissue (Stockwell [237]). The negligible influence of a small variation of the material parameters (represented by the inclusion of cells) on the model output proves implicitely the stability of the model calibration exposed in Chapter 5. In this regard, it seems reasonable to "lump" the cell volume as part of the solid phase within the framework of the cartilage biphasic modelling presented in Chapters 2 and 4.

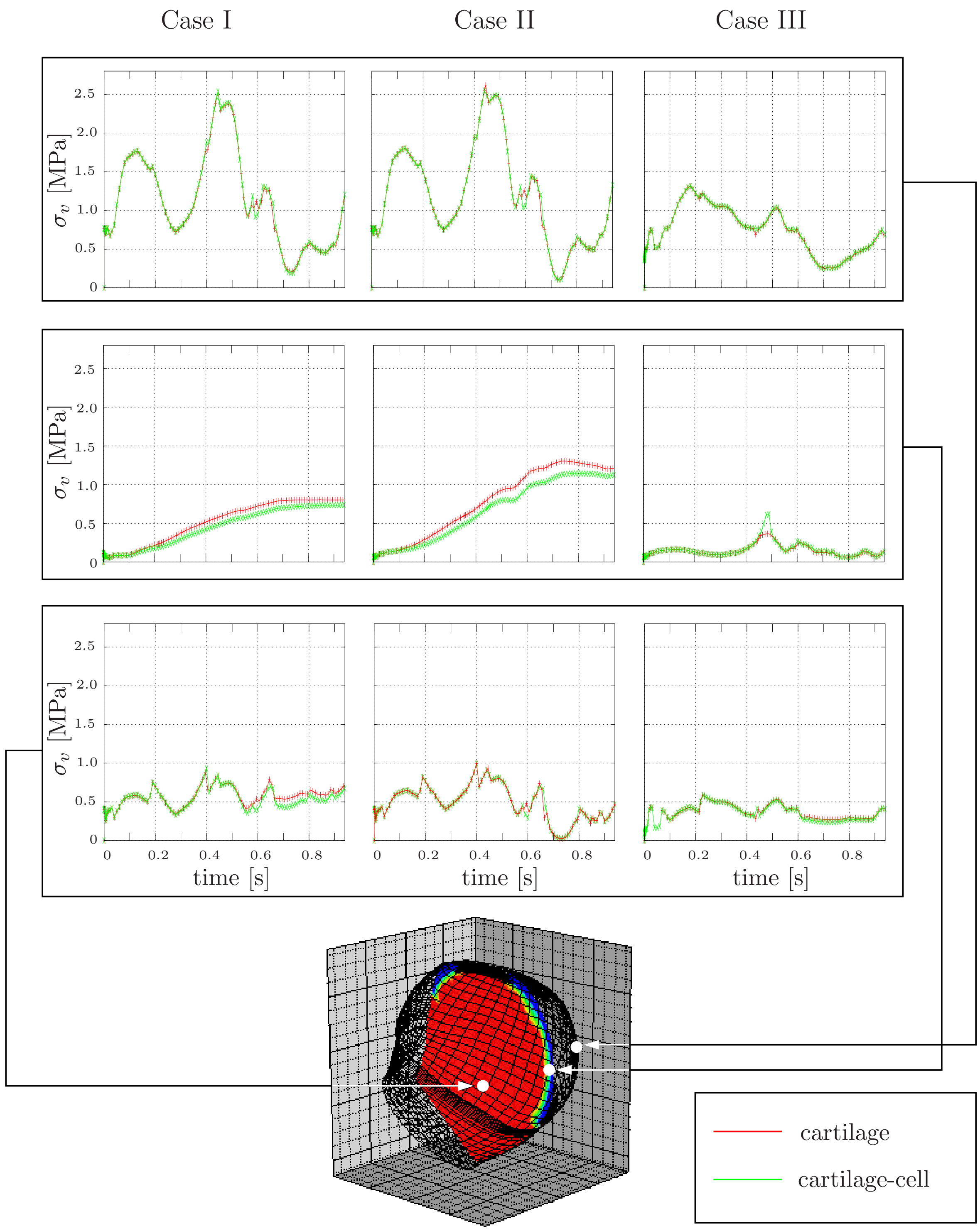

Figure 6.19: *Local stresses in cell positions for case I (left column), case II (centre column) and case III (right column) and comparison between model without (red curve) and with (green curve) chondrocytes.*

Chapter 7: Summary and Outlook

7.1 Summary

In the framework of this monograph, different solutions have been proposed in order to shed light on the intricacy related to the simulation of the inferences of walking processes in the human hip joint. In this context, the author went through different steps from the elaboration of a computational model to significant numerical applications, across the construction of a problem-specific model calibration.

7.1.1 Articular-Cartilage Modelling

The first goal of this contribution was to adapt a thermodynamically consistent model based on the Theory of Porous Media (TPM) of a soft biological tissue for the purpose of modelling articular cartilage. In particular, the main features of articular cartilage, such as arcade-like viscoelastic anisotropy, fibre-matrix shear interaction, anisotropic permeability and cartilage-specific heterogeneities, were included in already existing biphasic, anisotropic, poroviscoelastic and osmotic swelling models of a soft biological tissue. Next, a first subjective reduction of the complex model was adopted. Introductive studies showed a simplified model calibration related to the anisotropic viscoelasticity and the influence of the shear interactions between fibres and the extracellular matrix (ECM). In the discussion, the viscoelastic behaviour of the collagen fibres and the fibre-matrix shear effects were neglected due to their irrelevance to the studied phenomena of cartilage, mostly represented under compression for physiological loading states, and the lack of relevant experimental data and precise literature, amongst others.

An initial-boundary-value problem (IBVP) was then described after choosing the solid displacement and the hydraulic pore-fluid pressure as primary variables for the strong formulation of the balance relations including the set of constitutive equations and initial and boundary conditions. The proposed coupled problem had to be solved within a numerical solution procedure by the finite-element method (FEM). Therefore, the governing partial differential equations (PDE) were transformed into their weak counterparts. In particular, the spatial discretisation was performed using a mixed finite-element (FE) formulation based on 2-d, axial-symmetrical rectangular and 3-d, hexahedral *Taylor-Hood* elements with a quadratic formulation for the solid displacement and a linear formulation for the hydraulic pore-fluid pressure. Furthermore, an implicit monolithic strategy by means of an *Euler*ian time-integration scheme was used, which provided suitable numerical solutions for the given coupled solid-fluid problem.

7.1.2 Parameter Identification and Sensitivity Analysis

This work further aimed to propose a method to unambiguously find material parameters in soft biological tissues and to determine the optimal cartilage model's complexity relevant to numerical calculations. To this end, a concept of calibration strategy for the cartilage model was introduced. This concept was based on a stepwise identification of material parameters using a constraint optimisation scheme by linear approximation (COBYLA) and a local sensitivity analysis formulated from correlation matrices.

This calibration strategy was first implemented for a set of indentation tests with varying indenter sizes performed at the Hannover Medical School by the associated research group of PD Hurschler. After identifying the parameters in correlation with the experimental data, a sensitivity study was performed, which underlays the goodness-to-fit index for the parameter optimisation. It appeared that for cartilage tissues depicting low permeability values within the physiological domain, some parameters with lower influence on the measured output could be removed, such as tortuosity or anisotropic permeability. As expected, the influence of a permeability change was not predominant when dealing with small indenters. In this case, the creep behaviour of the solid-fluid aggregate could be mainly associated with the solid phase. This could lead to an efficient parameter identification for the solid viscoelasticity. In contrary, fluid-flow phenomena played a bigger role when dealing with larger indenters and considering higher values of the permeability. This did not lead to a unique identification of material parameters. Further investigations of the role of the heterogeneities in the vertical indenter displacement revealed a slight increase in cartilage stiffness, compared to that of fully homogeneous models.

However, only a few material parameters could be obtained by means of a set of indenter tests due to the lack of experimental data and the strong coupling amongst specific parameters. In order to identify the set of remaining unknown parameters such as those related to the deviatoric intrinsic viscoelasticity, a tailored sensitivity analysis was performed on a concept of multi-directional shear loading experiment. In this context, the superficial 3-d collagen fibre orientation could also be revealed, when changing direction of shear loading, by means of qualitative and quantitative methods. Based on these two numerical examples, a final model reduction could be performed.

7.1.3 Calculation of Stresses in Hip Joints and Mechanobiology

The capability of the computational model was tested to investigate complex phenomena such as walking processes in healthy and osteoarthritic (OA) hip joints. In this regard, a 3-d, patient-specific geometry was recreated from magnetic resonance imaging (MRI) scans created at the University Hospital of Tübingen by the associated research group of Prof. Schick. An introductive simulation was presented in which each component of the hip joint was modelled using a continuum-mechanical description. In this case, the calculation was aborted due to the rapid distortion of fluid elements under shear loading. An alternative solution consisted of inserting the contact forces during walking, obtained from multi-body systems (MBS) calculations performed by the associated research group of PD Hurschler, in the FE computational model of cartilage. For this purpose, a practical scheme was adopted for transferring the contact forces as readable boundary conditions in PANDAS. Furthermore, the cartilage model needed to be extended in order to gather the modified properties of degenerative cartilage tissue. Next, the study focused on the distinctions amongst normal walking and healthy cartilage, normal walking and degenerated cartilage, and pathological walking and degenerated cartilage. In particular, the influence of cartilage degeneration and pathological walking was investigated by means of the stress distribution at the cartilage surface and the pore-fluid pressure at the cartilage-bone interface. In OA cartilage tissues, higher contact stresses than those in the healthy state were detected for normal walking. Pathological walking reduced the risk of the appearance of high local stresses in already degenerated cartilage tissues. Finally, the study introduced the applicability of a new rendition technique to visualise simulation results based on a standardised stereographic projection of the stresses along the curved cartilage surface.

After confronting the results obtained with the calibrated cartilage model and a cartilage model extended with the presence of cells, a distinction between these two models could be neglected due to the low volume fraction of the cells within the ECM. This revealed that small perturbations of parameters due to the inclusion of cells did not change the output of the calibrated cartilage model.

7.2 Outlook

In this monograph, a thermodynamically consistent cartilage modelling has been elaborated for simulating relevant clinical processes in human hip joints. In this connection, an adapted calibration strategy has been thoroughly explained, which could be principally adopted for other complex biphasic solid-fluid models. In a next step, the synovial fluid-cartilage interaction mechanisms were introduced by means of simplified cartilage modelling. Furthermore, OA and pathological walking were better understood on the basis of the interpretation of the stress and pressure distributions for different cartilage states. This development could give birth to novel applications of the MBS related to FE models for a more realistic loading pattern. Based on the presented work, further improvements could be gained, as specified in the following paragraphs.

7.2.1 Full Completion of the Parameter Identification Based on Further Experimental Data

The full set of material parameters is still not fully obtained due to the lack of experimental data. Particularly, an adaptation of the concept of multi-directional shear loading to the given scope in laboratory installations would allow a final confrontation of the obtained parameters by means of alternative test protocols. Similarly, a deeper insight into the fibre-matrix shear interaction could be achieved when implementing the proposed IBVP as an experimental set-up. Further cartilage tests should be preconceived and constructed only after a controlling process given by the results of an introductive sensitivity analysis, as presented in this work.

7.2.2 Bone Material and Cartilage-Bone Interface Modelling

In contrast to the assumption made in this thesis, the subchondral bone structure is not exactly an isotropic and homogeneous material, except within the range of small applied loads. Moreover, the mechanical properties of the underlying subchondral bone exhibit a continuous variation from the deeper cartilage layers to the compact bone of the femur or the pelvis. An interface modelling would even out the actual high variations between cartilage and bone. Consequently, the stress distribution within hip joints would be represented more realistically, and the numerical solution would be more stable due to a decreased parameter jump at the interface. Further possible improvements of the cartilage-bone interactions would be to connect the complex cartilage model to bone remodelling formulations. By doing this, a more representative bone structure could be achieved due to the direct mechanical influence of the cartilage loading.

7.2.3 Towards a Macro-Meso Model for Cells

Regarding the influence of the mechanical environment on the cells, further numerical investigations could be performed in the formulation of multi-scale models. The applied loading obtained from the stress and strain states on the macro-scale could be addressed in meso-scale FE models related to a realistic cell representation. Only a "one-way" coupling would be needed due to the cells' low influence on the macroscopical behaviour, as discussed in this work. By doing this, key factors for cell evolution, such as local pore-fluid pressure, stress distribution and deformations in chondrocytes, could be studied and extended to the cases of OA degenerative cartilage and pathological walking pattern.

7.2.4 Multi-Body Systems for Full Hip-Joint Geometries

More realistic hip-joint simulations could be performed after applying the time- and location-dependent contact forces obtained from the MBS directly on the femoral bone in the same fashion than for the discussed half hip-joint geometry case. Practically, every new loading step imposed from the MBS would need an internal calculation loop for the solid-fluid system to "adapt" to the external loading.

7.2.5 Alternatives for Modelling Fluid-Cartilage Interaction

Different alternatives to the use of the MBS for dealing with synovial fluid-cartilage interaction have been developped by the associated research group of Prof. Nackenhorst at the Leibniz University of Hannover. One possibility to investigate interaction phenomena in hip joints is given by a contact-based approach adapted to a gap filled with an incompressible fluid. Another possibility relies on the solution of a fluid-structure interaction (FSI) problem using a staggered scheme. Both computational strategies are analysed and compared in Fietz [88] and Fietz & Nackenhorst [89, 90].

7.2.6 Variety of Joint-Lubrication Modes

In the framework of this monograph, the synovial fluid-cartilage interaction, based on a fluid-pressure contact, was considered as the only lubrication mode. However, sometimes nature does not want to typecast. Apparently, it prevails when considering the joint lubrication in synovial joints. The load-bearing system within joints is generally recognised as a combination of a fluid lubrication (at high loads and/or high velocity) and boundary lubrication (at low loads and/or low velocity) (see Baykal *et al.* [21], Linn & Radin [164], Roberts *et al.* [219], amongst others). Low-friction surfaces for joint movement can also be obtained without a fluid film, through a mechanism called boundary lubrication. At present, no exhaustive synovial joint model, which enables a switch between lubrication modes depending on the applied load magnitude, could be found in the literature.

Appendix A: Assumptions in the Modelling

A.1 Neglect of Gravitational Forces

Gravitational forces in soft biological tissues such as articular cartilage are neglected after comparing the weight $P_f \approx 1.0\,\mathrm{N}$ of the femoral head depicted in Figure 6.4 and the mean vertical loads acting on the hip joint during walking. The hip forces $\mathbf{P}_c$ were calculated by the associated research partner PD Hurschler at the Medical School of Hannover. In Figure A.1, the red curves represent the vertical components $P_{v,1}$ and $P_{v,2}$ of $\mathbf{P}_c$ and the green lines are their mean values $P_{\mathrm{mean},1}$ and $P_{\mathrm{mean},2}$ during one gait cycle for normal (see Figure A.1, left) and pathological walking (see Figure A.1, right). In Figure A.1 (left), an extremal value of $P_{v,1} = 3566\,\mathrm{N}$ is reached.

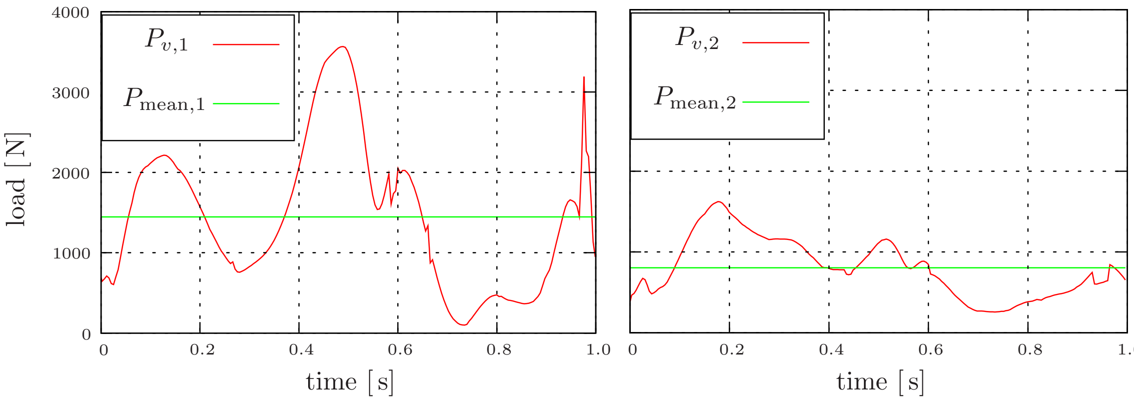

Figure A.1: *Evolution of the vertical components $P_{v,1}$ and $P_{v,2}$ of the hip forces and their mean value $P_{\mathrm{mean},1}$ and $P_{\mathrm{mean},2}$ during one normal (left) and pathological (right) gait cycle.*

Under consideration of the mean values $P_{\mathrm{mean},1} = 1446\,\mathrm{N}$ and $P_{\mathrm{mean},2} = 804\,\mathrm{N}$ given in Figure A.1, one calculates

$$|\rho\,\mathbf{g}| = P_f \approx 1.0\,\mathrm{N} \quad \text{and} \quad \min\,(P_{\mathrm{mean},1}; P_{\mathrm{mean},2}) = \min\,(1446\,\mathrm{N}, 804\,\mathrm{N}) = 804\,\mathrm{N}\,, \qquad \text{(A.1)}$$

where $\rho = \sum_\alpha \rho^\alpha$ is the overall density of the aggregate. Then, the ratio between the gravitational forces and the external vertical loads reads

$$\frac{P_f}{\min\,(P_{\mathrm{mean},1}; P_{\mathrm{mean},2})} \approx 1.2 \cdot 10^{-3}\,, \qquad \text{(A.2)}$$

which justifies the neglect of the term $\rho\,\mathbf{g}$ in the overall momentum balance.

The reason for high vertical forces in the hip joint, as observed in Figure A.1 (left), is briefly explained by the representation of the maximal hip force $\mathbf{P}_{v,\max}$ under purely static conditions in Figure A.2. Therein, the force $\mathbf{G}$ acting at the centre of gravity of the pelvis, represents the weight of the upperbody ($\approx 500\,\mathrm{N}$) and of one leg ($\approx 150\,\mathrm{N}$) for a male patient of 80 kg. Besides, the muscle force $\mathbf{M}$ activated by the abductors is attached at a distance a from the hip joint and at a distance $5\,a$ from the centre of the pelvis. The static equilibrium of the pelvis is then achieved if

$$\left.\begin{aligned} P_{v,\max} &= G + M \\ M \cdot a &= G \cdot 4\,a \end{aligned}\right| \rightarrow \quad \begin{aligned} P_{v,\max} &= G\,(1+4) \\ &= 3250\,\mathrm{N}\,, \end{aligned} \tag{A.3}$$

where $P_{v,\max}$, G and M are the vectorial norms of the forces $\mathbf{P}_{v,\max}$, $\mathbf{G}$ and $\mathbf{M}$, respectively.

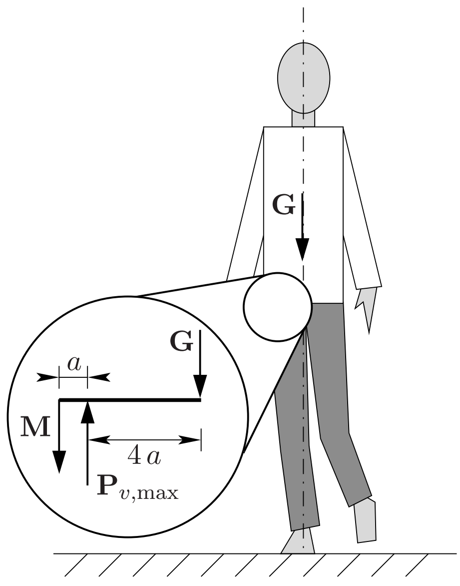

Figure A.2: *Schematic representation of equilibrium of forces in the pelvis.*

Note that the dynamic equilibrium of the femoral head due to the accelerating leg motion can be expressed after considering the *D'Alembert*'s inertial forces $\mathbf{t} = -\rho\,\ddot{\mathbf{x}}$ in addition to the external forces obtained from the overall momentum balance. Therein, $\ddot{\mathbf{x}}$ is the acceleration of the overall aggregate φ calculated as (de Boer & Ehlers [32])

$$\ddot{\mathbf{x}} = \sum_{\alpha} \left[\, \rho^\alpha \overset{\prime\prime}{\mathbf{x}}_\alpha - \operatorname{div}\left(\rho^\alpha\, \mathbf{d}_\alpha \otimes \mathbf{d}_\alpha\right) + \hat{\rho}^\alpha \overset{\prime}{\mathbf{x}}_\alpha \,\right], \tag{A.4}$$

where $\mathbf{d}_\alpha = \overset{\prime}{\mathbf{x}}_\alpha - \dot{\mathbf{x}}$ is the diffusion velocity of φ^α and $\dot{\mathbf{x}} = \dfrac{1}{\rho} \sum_{\alpha} \rho^\alpha \overset{\prime}{\mathbf{x}}_\alpha$ is the barycentric velocity of the aggregate φ. These inertial forces are already considered by the hip forces depicted in Figure A.1 which do not differ much from the forces calculated in (A.3) under purely static equilibrium. Hence, the influence of the dynamic effects on the system is not relevant in the case of walking at moderate speed.

A.2 Quasi-Static Conditions

Assuming quasi-static conditions implies to neglect the acceleration terms of the solid and fluid constituents, i. e., $\rho^\alpha \overset{\prime\prime}{\mathbf{x}}_\alpha \approx \mathbf{0}$.

Due to the very low permeability of the ECM, only slow deformations $\overset{\prime}{\mathbf{x}}_S$ of the solid skeleton are assumed under physiological loads. This leads to a negligible acceleration term $\rho^S \overset{\prime\prime}{\mathbf{x}}_S$, i. e.,

$$\overset{\prime\prime}{\mathbf{x}}_S \approx \mathbf{0}\,. \tag{A.5}$$

Furthermore, a lingering fluid flow through the porous matrix described by the *Darcy*'s equation (2.55) is assumed. In this case, the acceleration term $\rho^S \overset{\prime\prime}{\mathbf{x}}_F$ is neglected, i. e.,

$$\overset{\prime\prime}{\mathbf{x}}_F \approx \mathbf{0}\,. \tag{A.6}$$

Note that the sum $\mathbf{T}^S + \mathbf{T}^F$ in equation (2.28) cannot generally be associated to the overall *Cauchy* stress $\mathbf{T}$ which contains diffusive contributions reading (de Boer & Ehlers [32])

$$\mathbf{T} = \sum_\alpha \left(\mathbf{T}^\alpha - \rho^\alpha\, \mathbf{d}_\alpha \otimes \mathbf{d}_\alpha\right). \tag{A.7}$$

Under the action of loads on a femoral head fixed in space, one finds $\ddot{\mathbf{x}} = \mathbf{0}$. Besides, when assuming no mass production, i. e., $\hat{\rho}^\alpha = 0$, and vanishing $\overset{\prime\prime}{\mathbf{x}}_\alpha$, the term $\sum\limits_\alpha \rho^\alpha\, \mathbf{d}_\alpha \otimes \mathbf{d}_\alpha$ in (A.4) sufficiently vanishes, which simplifies equation (A.7) in

$$\mathbf{T} = \sum_\alpha \mathbf{T}^\alpha = \mathbf{T}^S + \mathbf{T}^F\,. \tag{A.8}$$

Appendix B: Polyconvexity of Strain-Energy Functions

B.1 Notion of Polyconvexity

In a general framework, a strain-energy function is *per se* convex if the existence of minimisers is guaranteed. Unluckily, further requirements of material frame indifference and material instabilities render this concept deficient (Ball [16]). A more suitable condition is the concept of quasiconvexity introduced by Morrey [189]. This necessary and sufficient condition claims isothermal stability of an all-round fixed homogeneous body of hyperelastic material and ensures the existence of the minimisers if the strain-energy function is sequentially weakly lower semi-continuous. To have this condition satisfied is important, since violating quasiconvexity can yield the break down of the initially homogeneous bodies into coexisting stable phases (Ball & James [17], Krawietz [150]). However, quasiconvexity as an integral inequality is not really practicable and disallows singularities, which cannot be reconciled with finite material behaviour. In this regard, Ball [16] established the more practical notion of polyconvexity, which is a sufficient condition for quasiconvex functions.

In particular, a scalar-valued function W as the scalar-valued strain energy of the system is said to be polyconvex if it can be expressed as a convex function of subdeterminants of its tensorial variables (Markert *et al.* [176]). Here, one proceeds from

$$W(\mathbf{F}_S) = W_l(\mathbf{F}_S) + W_a(\mathrm{cof}\mathbf{F}_S) + W_v(\det\mathbf{F}_S) \tag{B.1}$$

as an additive polyconvex function, where each part is convex in the associated variable. Assuming a twice differentiable W, the convexity is verified by showing that the second derivatives are positive semi-definite, yielding

$$\left.\begin{aligned} \frac{\partial^2 W}{\partial \mathbf{F}_S \otimes \partial \mathbf{F}_S} \cdot (\mathbf{H} \otimes \mathbf{H}) \geq 0 \\ \frac{\partial^2 W}{\partial \mathrm{cof}\mathbf{F}_S \otimes \partial \mathrm{cof}\mathbf{F}_S} \cdot (\mathbf{H} \otimes \mathbf{H}) \geq 0 \\ \frac{\partial^2 W}{\partial (\det\mathbf{F}_S)} \geq 0 \end{aligned}\right\} \ \forall\, \mathbf{H} \neq \mathbf{0}\,. \tag{B.2}$$

Here, $\mathbf{H}$ represents an arbitrary second-order tensor (see Balzani [18], Ciarlet [50] and Marsden & Hughes [182]). In order to mathematically investigate the polyconvexity of strain-energy functions, some principles of the tensor calculus are required to deal with the following tensor operations. Precise information about the utilised rules and definitions is given by de Boer [29] and in the lecture notes of vector and tensor calculus by Ehlers [64].

B.2 The Non-Equilibrium Anisotropic Strain-Energy Function

Similar to the equilibrium part of the anisotropic strain-energy function, the proposed non-equilibrium contribution $W^{\mathrm{NEQ}}_{\mathrm{ANI}}$ is (Markert [174], Zinatbakhsh [267])

$$\boxed{W^{\mathrm{NEQ}}_{\mathrm{ANI}} = \sum_{m=1}^{M_{fe}} \left[\frac{\widetilde{\mu}^S_m}{\widetilde{\gamma}_m} \, (J_{S4e}^{\widetilde{\gamma}_m/2} - 1) - \widetilde{\mu}^S_m \ln J_{S4e}^{1/2} \right]}\,. \tag{B.3}$$

Here, the only scalar variable is the elastic part J_{S4e} of the squared fibre stretch. Then, the condition (B.2) is evaluated for $W^{\mathrm{NEQ}}_{\mathrm{ANI}}$ yielding

$$\begin{aligned}
\frac{\partial^2 W^{\mathrm{NEQ}}_{\mathrm{ANI}}}{\partial \mathbf{F}_{Se} \otimes \partial \mathbf{F}_{Se}} &= \frac{\partial}{\partial \mathbf{F}_{Se}} \Big(\frac{\partial W^{\mathrm{NEQ}}_{\mathrm{ANI}}}{\partial \mathbf{F}_{Se}} \Big) = \frac{\partial}{\partial \mathbf{F}_{Se}} \Big(\frac{\partial W^{\mathrm{NEQ}}_{\mathrm{ANI}}}{\partial J_{S4e}} \, \frac{\partial J_{S4e}}{\partial \mathbf{F}_{Se}} \Big) \\
&= \frac{\partial}{\partial J_{S4e}} \Big(\frac{\partial W^{\mathrm{NEQ}}_{\mathrm{ANI}}}{\partial J_{S4e}} \, \frac{\partial J_{S4e}}{\partial \mathbf{F}_{Se}} \Big) \, \frac{\partial J_{S4e}}{\partial \mathbf{F}_{Se}} \\
&= \frac{\partial^2 W^{\mathrm{NEQ}}_{\mathrm{ANI}}}{(\partial J_{S4e})^2} \, \frac{\partial J_{S4e}}{\partial \mathbf{F}_{Se}} \otimes \frac{\partial J_{S4e}}{\partial \mathbf{F}_{Se}} + \\
&\qquad + \frac{\partial W^{\mathrm{NEQ}}_{\mathrm{ANI}}}{\partial \mathbf{F}_{Se}} \left[\frac{\partial}{\partial J_{S4e}} \Big(\frac{\partial J_{S4e}}{\partial \mathbf{F}_{Se}} \Big) \right] \otimes \frac{\partial J_{S4e}}{\partial \mathbf{F}_{Se}} \,,
\end{aligned} \tag{B.4}$$

where $\dfrac{\partial J_{S4e}}{\partial \mathbf{F}_{Se}}$ is calculated as

$$\begin{aligned}
\frac{\partial J_{S4e}}{\partial \mathbf{F}_{Se}} &= \frac{\partial}{\partial \mathbf{F}_{Se}} \, [\, \mathrm{tr}\, (\mathbf{C}_{Se} \, \boldsymbol{\mathcal{M}}^S)] = \frac{\partial}{\partial \mathbf{F}_{Se}} \, [(\mathbf{F}^T_{Se} \, \mathbf{F}_{Se}) \cdot \boldsymbol{\mathcal{M}}^S \,] \\
&= \Big[\frac{\partial}{\partial \mathbf{F}_{Se}} \, ((\mathbf{F}^T_{Se} \, \mathbf{F}_{Se}) \Big]^T \boldsymbol{\mathcal{M}}^S + \underbrace{\Big(\cancel{\frac{\partial \boldsymbol{\mathcal{M}}^S}{\partial \mathbf{F}_{Se}}} \Big)^T}_{=\overset{4}{\mathbf{0}}} (\mathbf{F}^T_{Se} \, \mathbf{F}_{Se}) \\
&= \Big[(\mathbf{F}^T_{Se} \otimes \mathbf{I})^{\overset{23}{T}} + (\mathbf{I} \otimes \mathbf{F}_{Se})^{\overset{24}{T}} \Big]^T \boldsymbol{\mathcal{M}}^S \\
&= \Big[\underbrace{(\mathbf{F}_{Se} \otimes \mathbf{I})^{\overset{23}{T}}}_{\text{identical map}} + \underbrace{(\mathbf{F}_{Se} \otimes \mathbf{I})^{\overset{24}{T}}}_{\text{transposing map}} \Big] \, \boldsymbol{\mathcal{M}}^S \\
&= \mathbf{F}_{Se} \, \boldsymbol{\mathcal{M}}^S + \mathbf{F}_{Se} \, (\boldsymbol{\mathcal{M}}^S)^T \\
&= 2 \, \mathbf{F}_{Se} \, \boldsymbol{\mathcal{M}}^S \,.
\end{aligned} \tag{B.5}$$

Inserting (B.5) in (B.4) and evaluating the derivatives of the strain-energy function $W^{\mathrm{NEQ}}_{\mathrm{ANI}}$ with respect to J_{S4e} leads to

$$
\begin{aligned}
\frac{\partial^2 W_{\text{ANI}}^{\text{NEQ}}}{\partial \mathbf{F}_{Se} \otimes \partial \mathbf{F}_{Se}} \;=\; & \sum_{m=1}^{M_{fe}} \widetilde{\mu}_m^S \, J_{S4e}^{-2} \big[(\widetilde{\gamma}_m - 2) \, J_{S4e}^{\widetilde{\gamma}_m/2} \; + \; 2 \big] \mathbf{F}_{Se} \, \boldsymbol{\mathcal{M}}^S \otimes \mathbf{F}_{Se} \, \boldsymbol{\mathcal{M}}^S + \\
& + \sum_{m=1}^{M_{fe}} \widetilde{\mu}_m^S \, J_{S4e}^{-1} \, (J_{S4e}^{\widetilde{\gamma}_m/2} \; - \; 1) \, \mathbf{F}_{S,e}^{T-1} \otimes \mathbf{F}_{Se} \, \boldsymbol{\mathcal{M}}^S \, .
\end{aligned}
\tag{B.6}
$$

Next, the polyconvexity of the strain-energy function is established if the following restriction is respected:

$$
\begin{aligned}
\frac{\partial^2 W_{\text{ANI}}^{\text{NEQ}}}{\partial \mathbf{F}_{Se} \otimes \partial \mathbf{F}_{Se}} \cdot (\mathbf{H} \otimes \mathbf{H}) \;=\; & \sum_{m=1}^{M_{fe}} \widetilde{\mu}_m^S \, J_{S4e}^{-2} \big[(\widetilde{\gamma}_m - 2) \, J_{S4e}^{\widetilde{\gamma}_m/2} \; + \; 2 \big] (\mathbf{F}_{Se} \, \boldsymbol{\mathcal{M}}^S \cdot \mathbf{H})^2 + \\
& + \sum_{m=1}^{M_{fe}} \widetilde{\mu}_m^S \, J_{S4e}^{-1} \, (J_{S4e}^{\widetilde{\gamma}_m/2} \; - \; 1) \, (\mathbf{H} \, \boldsymbol{\mathcal{M}}^S \cdot \mathbf{H}) \overset{!}{>} 0 \, .
\end{aligned}
\tag{B.7}
$$

According to previous works of Karajan [138] and Markert *et al.* [176], the polyconvexity is guaranteed under the following restrictions:

$$
\begin{array}{lll}
(i) & J_{S4e} \geq 1 & : \text{restriction to fibre tension,} \\[2ex]
(ii) & \displaystyle\sum_{m=1}^{M_{fe}} \widetilde{\mu}_m^S \geq 0 & : \text{overall positive fibre stiffness, and} \\[2ex]
(iii) & \widetilde{\mu}_m^S (\widetilde{\gamma}_m - 2) \geq 0 \;\; \rightarrow & \left\{ \begin{array}{lll} \widetilde{\mu}_m^S > 0 & \rightarrow & \widetilde{\gamma}_m \geq 2 \\ \widetilde{\mu}_m^S < 0 & \rightarrow & \widetilde{\gamma}_m \leq 2 \end{array} \right.
\end{array}
$$

Other methods for calculating polyconvex anisotropic strain-energy functions are presented in the works of Balzani [18], Holzapfel *et al.* [122], Itskov *et al.* [127] and Schröder *et al.* [227].

B.3 The Fibre-Matrix Shear-Interaction Strain-Energy Function

B.3.1 Polyconvexity of the Fibre-Matrix Shear-Interaction Function

A further term W_{INT}^S of the strain-energy function is defined as

$$
\boxed{W_{\text{INT}}^S = 0.5 \, \mu_{\text{int}} \, (J_{S5} - J_{S4}^2)^{\alpha_{\text{int}}}} \, .
\tag{B.8}
$$

In this case, the polyconvexity of W_{INT}^S with respect to the solid deformation gradient $\mathbf{F}_S$ is not evaluated by means of the general condition given in (B.2). A calculation using this framework would lead to highly complex derivations of invariants. Instead, existing polyconvex terms given in Ebbing [59] and Schröder & Neff [226] are mathematically combined, leading to an overall polyconvexity of the fibre-matrix interaction strain-energy function.

In this connection, an additional structural tensor $\mathbf{D}^S$ is introduced as (Schröder & Neff [226])

$$\mathbf{D}^S = \mathbf{I} - \boldsymbol{\mathcal{M}}^S\,. \tag{B.9}$$

Next, equation (B.9) is multiplied by $\mathbf{C}_S\,\mathbf{C}_S\,(\,\cdot\,)\,\boldsymbol{\mathcal{M}}^S$, yielding

$$\begin{aligned} \mathbf{C}_S\,\mathbf{C}_S\,\mathbf{D}^S\,\boldsymbol{\mathcal{M}}^S &= \mathbf{C}_S\,\mathbf{C}_S\,\boldsymbol{\mathcal{M}}^S - \mathbf{C}_S\,\mathbf{C}_S\,\boldsymbol{\mathcal{M}}^S\,\boldsymbol{\mathcal{M}}^S \\ &= \mathbf{C}_S\,\mathbf{C}_S\,\boldsymbol{\mathcal{M}}^S - \mathbf{C}_S\,\boldsymbol{\mathcal{M}}^S\,\mathbf{C}_S\,\boldsymbol{\mathcal{M}}^S\,, \end{aligned} \tag{B.10}$$

due to the symmetric nature of $\mathbf{C}_S$ and $\boldsymbol{\mathcal{M}}^S$.

Then, the calculation of the trace of equation (B.10) is

$$\begin{aligned} \mathrm{tr}\,(\mathbf{C}_S\,\mathbf{C}_S\,\mathbf{D}^S\,\boldsymbol{\mathcal{M}}^S) &= \mathrm{tr}\,(\mathbf{C}_S\,\mathbf{C}_S\,\boldsymbol{\mathcal{M}}^S - \mathbf{C}_S\,\boldsymbol{\mathcal{M}}^S\,\mathbf{C}_S\,\boldsymbol{\mathcal{M}}^S) \\ &= \mathrm{tr}\,(\mathbf{C}_S\,\mathbf{C}_S\,\boldsymbol{\mathcal{M}}^S) - \mathrm{tr}\,(\mathbf{C}_S\,\boldsymbol{\mathcal{M}}^S\,\mathbf{C}_S\,\boldsymbol{\mathcal{M}}^S) \\ &= \underbrace{\mathrm{tr}\,(\mathbf{C}_S\,\mathbf{C}_S\,\boldsymbol{\mathcal{M}}^S)}_{J_{S5}} - \underbrace{\mathrm{tr}\,(\mathbf{C}_S\,\boldsymbol{\mathcal{M}}^S)}_{J_{S4}}\,\underbrace{\mathrm{tr}\,(\mathbf{C}_S\,\boldsymbol{\mathcal{M}}^S)}_{J_{S4}} \\ &= J_{S5} - J_{S4}^2\,. \end{aligned} \tag{B.11}$$

After raising equation (B.11) to the power of α_{int} and multiplication by $0.5\,\mu_{\mathrm{int}}$, one calculates

$$0.5\,\mu_{\mathrm{int}}\,[\mathrm{tr}\,(\mathbf{C}_S\,\mathbf{C}_S\,\mathbf{D}^S\,\boldsymbol{\mathcal{M}}^S)]^{\alpha_{\mathrm{int}}} = 0.5\,\mu_{\mathrm{int}}\,(J_{S5} - J_{S4}^2)^{\alpha_{\mathrm{int}}} = W^S_{\mathrm{INT}}\,, \tag{B.12}$$

which is the expression of the fibre-matrix interaction strain-energy term. In other words, proving the polyconvexity of W^S_{INT} is equivalent to proving the polyconvexity of $0.5\,\mu_{\mathrm{int}}\,[\mathrm{tr}\,(\mathbf{C}_S\,\mathbf{C}_S\,\mathbf{D}^S\,\boldsymbol{\mathcal{M}}^S)]^{\alpha_{\mathrm{int}}}$.

This expression can be decomposed as

$$\begin{aligned} W^S_{\mathrm{INT}} &= 0.5\,\mu_{\mathrm{int}}\,[\mathrm{tr}\,(\mathbf{C}_S\,\mathbf{C}_S\,\mathbf{D}^S\,\boldsymbol{\mathcal{M}}^S)]^{\alpha_{\mathrm{int}}} \\ &= 0.5\,\mu_{\mathrm{int}}\,[\mathrm{tr}\,(\mathbf{C}_S)\,\mathrm{tr}\,(\mathbf{C}_S\,\mathbf{D}^S)\,\mathrm{tr}\,(\boldsymbol{\mathcal{M}}^S)]^{\alpha_{\mathrm{int}}} \\ &= 0.5\,\mu_{\mathrm{int}}\,[\mathrm{tr}\,(\mathbf{C}_S)]^{\alpha_{\mathrm{int}}}\,[\mathrm{tr}\,(\mathbf{C}_S\,\mathbf{D}^S)]^{\alpha_{\mathrm{int}}}\,\mathrm{tr}\,[(\boldsymbol{\mathcal{M}}^S)]^{\alpha_{\mathrm{int}}}\,. \end{aligned} \tag{B.13}$$

The term $[\mathrm{tr}\,(\mathbf{C}_S\,\mathbf{D}^S)]^{\alpha_{\mathrm{int}}}$ was shown to be polyconvex with respect to the deformation gradient $\mathbf{F}_S$ with $\alpha_{\mathrm{int}} \geq 1$ by Schröder & Neff [226]. Obviously, both terms $[\mathrm{tr}\,(\mathbf{C}_S)]^{\alpha_{\mathrm{int}}}$ and $\mathrm{tr}\,[(\boldsymbol{\mathcal{M}}^S)]^{\alpha_{\mathrm{int}}}$ are also polyconvex contributions.

Finally, the overall polyconvexity of the fibre-matrix shear-interaction strain-energy function is guaranteed due to the polyconvexity of its components under the following restrictions for the material parameters μ_{int} and α_{int}:

$$
\begin{aligned}
&(i) \quad \alpha_{\text{int}} \geq 1 \text{ and} \\
&(ii) \quad \mu_{\text{int}} \geq 0\,.
\end{aligned}
\tag{B.14}
$$

B.3.2 Derivation of the Fibre-Matrix Shear-Interaction Stresses

The derivation of the fibre-matrix interaction strain-energy function W^S_{INT} leads to the expression of the stresses, yielding

$$
\mathbf{S}^S_{\text{INT}} = \frac{\partial W^S_{\text{INT}}}{\partial \mathbf{E}_S} = 2\,\frac{\partial W^S_{\text{INT}}}{\partial \mathbf{C}_S}\,,
\tag{B.15}
$$

where $\mathbf{S}^S_{\text{INT}}$ is the second *Piola-Kirchhoff* stress tensor related to the fibre-matrix interaction and constitutes a conjugate pair together with the *Green-Lagrange*an solid strain tensor $\mathbf{E}_S$. In particular, the application of the chain rule on equation (B.15) leads to

$$
\mathbf{S}^S_{\text{INT}} = 2\left(\frac{\partial W^S_{\text{INT}}}{\partial J_{S4}}\,\frac{\partial J_{S4}}{\partial \mathbf{C}_S} + \frac{\partial W^S_{\text{INT}}}{\partial J_{S5}}\,\frac{\partial J_{S5}}{\partial \mathbf{C}_S}\right).
\tag{B.16}
$$

Here,

$$
\begin{aligned}
\frac{\partial W^S_{\text{INT}}}{\partial J_{S4}} &= J_{S4}\,\mu_{\text{int}}\,\alpha_{\text{int}}\,(J_{S5} - J^2_{S4})^{(\alpha_{\text{int}}-1)}\,, \\
\frac{\partial W^S_{\text{INT}}}{\partial J_{S5}} &= 0.5\,\mu_{\text{int}}\,\alpha_{\text{int}}\,(J_{S5} - J^2_{S4})^{(\alpha_{\text{int}}-1)}
\end{aligned}
\tag{B.17}
$$

and

$$
\frac{\partial J_{S4}}{\partial \mathbf{C}_S} = \frac{\partial(\mathbf{C}_S \cdot \boldsymbol{\mathcal{M}}^S)}{\partial \mathbf{C}_S} = \boldsymbol{\mathcal{M}}^S\,.
\tag{B.18}
$$

Furthermore,

$$
\begin{aligned}
\frac{\partial J_{S5}}{\partial \mathbf{C}_S} &= \frac{\partial(\mathbf{C}_S \cdot \mathbf{C}_S\,\boldsymbol{\mathcal{M}}^S)}{\partial \mathbf{C}_S} \\
&= \mathbf{C}_S\,\boldsymbol{\mathcal{M}}^S + \left[\frac{\partial(\mathbf{C}_S\,\boldsymbol{\mathcal{M}}^S)}{\partial \mathbf{C}_S}\right]^T \mathbf{C}_S \\
&= \mathbf{C}_S\,\boldsymbol{\mathcal{M}}^S + [\,[\,\mathbf{I} \otimes (\boldsymbol{\mathcal{M}}^S)^T]^{\overset{23}{T}}]^T\,\mathbf{C}_S \\
&= \mathbf{C}_S\,\boldsymbol{\mathcal{M}}^S + [\,\boldsymbol{\mathcal{M}}^S \otimes \mathbf{I}\,]^{\overset{23}{T}}\,\mathbf{C}_S \\
&= \mathbf{C}_S\,\boldsymbol{\mathcal{M}}^S + \boldsymbol{\mathcal{M}}^S\,\mathbf{C}_S\,.
\end{aligned}
\tag{B.19}
$$

Inserting equations (B.17), (B.18) and (B.19) in (B.16), the expression of the second *Piola-Kirchhoff* stress tensor $\mathbf{S}^S_{\text{INT}}$ takes the form

$$
\mathbf{S}^S_{\text{INT}} = \mu_{\text{int}}\,\alpha_{\text{int}}\,(J_{S5} - J^2_{S4})^{(\alpha_{\text{int}}-1)}\,(\,2\,J_{S4}\,\boldsymbol{\mathcal{M}}^S + \mathbf{C}_S\,\boldsymbol{\mathcal{M}}^S + \boldsymbol{\mathcal{M}}^S\,\mathbf{C}_S\,)\,.
\tag{B.20}
$$

After a covariant push-forward transport of $\mathbf{S}^S_{\mathrm{INT}}$, the solid *Cauchy* stress tensor $\mathbf{T}^S_{\mathrm{INT}}$ is obtained as

$$\begin{aligned} \mathbf{T}^S_{\mathrm{INT}} &= J_S^{-1}\,\mathbf{F}_S\,\mathbf{S}^S_{\mathrm{INT}}\,\mathbf{F}_S^T \\ &= \mu_{\mathrm{int}}\,\alpha_{\mathrm{int}}\,J_S^{-1}\,(J_{S5}-J_{S4}^2)^{(\alpha_{\mathrm{int}}-1)}\mathbf{F}_S\,(\,2\,J_{S4}\,\boldsymbol{\mathcal{M}}^S+\mathbf{C}_S\,\boldsymbol{\mathcal{M}}^S+\boldsymbol{\mathcal{M}}^S\,\mathbf{C}_S\,)\,\mathbf{F}_S^T. \end{aligned} \tag{B.21}$$

A more comprehensive overview of the transport mechanisms is given in Acartürk [2], Karajan [138] and Markert [172], amongst others.

Appendix C: Numerical Stability and Physical Behaviour of the Strain-Energy Function for Fibre-Matrix Shear Interaction

In this chapter, some investigations are performed on a simple geometry for a quick evaluation of the influence of the fibre-matrix shear-interaction parameter μ_{int} on the mechanical behaviour. In the following paragraphs, the model response along the non-fibrous directions is investigated to capture the possible non-physical behaviour.

C.1 Influence of Interaction Parameter

In this framework, a pure shear test is performed, since it is widely applied to characterise the stress-strain properties of soft materials (Duong *et al.* [58]). Here, the geometry consists of a single 20-noded, hexahedral *Taylor-Hood* element ($L = 1\,\text{mm}$), yielding 80 DOF (see Figure C.1, left). The element is gripped along one edge to prevent lateral contraction and is extended in the other direction with a displacement $|\bar{\mathbf{u}}_S(t)| = 0.1\,\text{mm}$ applied as a step function (Duong *et al.* [58]). The fibres are parallel oriented to the direction of applied displacement. The element may freely contract in its third dimension and all surfaces are perfectly drained ($\bar{\mathcal{P}} = 0$). The set of material parameters is listed in Table 4.3.

The stress-strain response of the pure shear test is depicted in Figure C.1 (right). The black line indicates the isotropic case. The purely anisotropic case without fibre-matrix shear interaction is represented by the blue curve. The red and the dashed red curves are related to the cases of "low" and "high" interactions, respectively. "Low" and "high" interactions correspond to values of the interaction parameter μ_{int} equal to 0.005 MPa and 0.08 MPa, respectively.

As expected higher stiffness due to anisotropic reinforcement and shear interaction between fibres and matrix is observed. Furthermore, for the given set of material parameters, a purely artificial material stiffening occurs as depicted by the light-blue curve in Figure C.1 (right), after reaching a certain value of the interaction parameter.

C.2 Physical Behaviour Along Non-Fibrous Directions

After evaluating the influence of the interaction parameter on the proposed model response, the model's ability to describe the physical behaviour still needs to be inspected. A well-know non-physical behaviour called "strongly directional behaviour" (SDB) can

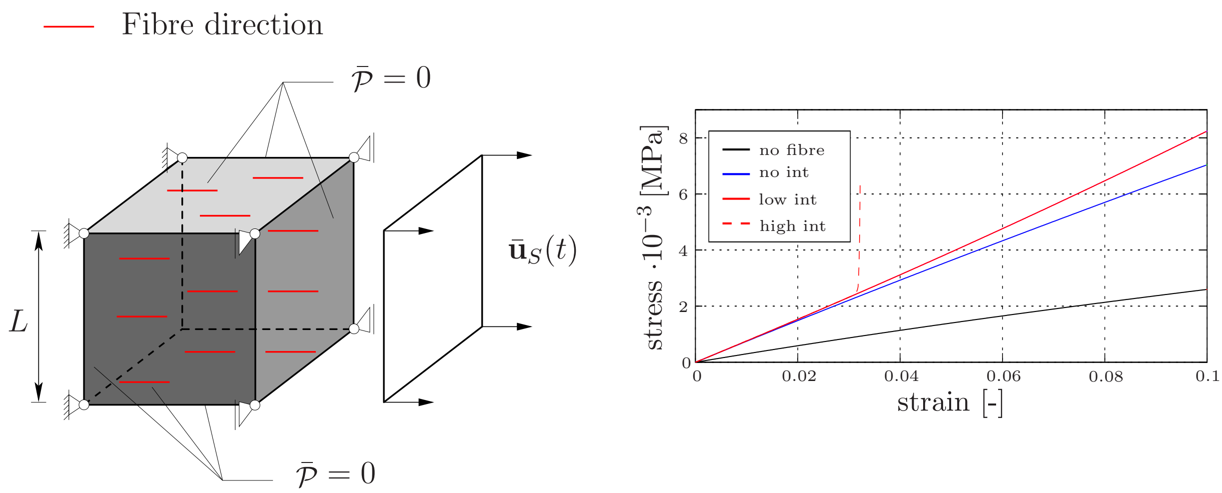

Figure C.1: *IBVP of pure shear loading on hexahedral element of length $L = 1\,\mathrm{mm}$ (left) and stress-strain diagram for isotropic, purely anisotropic and anisotropic with low and high interaction parameters (right).*

lead to an unstable numerical response, known as "fibre rotation" (Gasser *et al.* [95]). When large stretching occurs, the fibres rotate in the loading direction and might create wrong accumulated deformations in the perpendicular direction of the fibre plane. These deformations lead to an artificial thickening of the specimen, when the matrix is too soft to prevent fibre rotation. Duong *et al.* [58] relate the origin of SDB to a numerical aspect. SDB would occur due to ill-conditioning in the system of differential equations implemented in FEM codes. Due to the large difference between isotropic and anisotropic strain-energy values, high loads generating large stretches cannot be carried by a soft matrix. This characteristic leads to failure in the material.

In this regard, the occurrence of SDB is investigated in the presented, anisotropic model considering the fibre-matrix shear interaction. In Figure C.2, the evolution of the strain $\varepsilon_\perp$ in the direction perpendicular to the applied displacement is depicted as a linear function of the strain $\varepsilon_\parallel$ in the direction of applied displacement. Subsequently, the computational model including fibre-matrix interaction effects does not show any bulging, in contrast to other numerical models (Holzapfel *et al.* [123]).

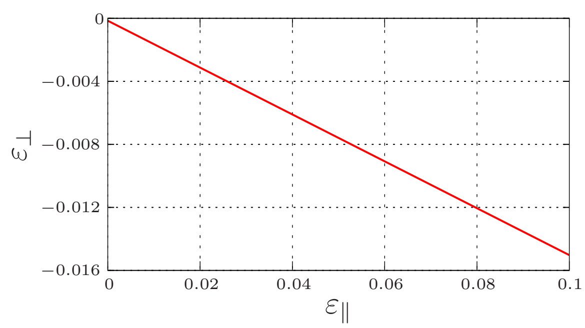

Figure C.2: *Evolution of the strain in the direction perpendicular to the applied strain.*

Bibliography

[1] Abraham, C. L.; Maas, S. A.; Weiss, J. A.; Ellis, B. J.; Peters, C. L. & Anderson, A. E.: A new discrete element analysis method for predicting hip joint contact stresses. *Journal of Biomechanics* **46** (2013), 1121–1127.

[2] Acartürk, A.: *Simulation of charged hydrated porous materials*. Dissertation thesis, Report No. II-18, Institute of Applied Mechanics (CE), University of Stuttgart 2009.

[3] Acartürk, A.; Ehlers, W. & Abbas, I.: Modelling of Swelling Phenomena in Charged Hydrated porous Media. *Proceedings in Applied Mathematics and Mechanics* **4** (2004), 296–297.

[4] Alexopoulos, L. G.; Haider, M. A.; Vail, T. P. & Guilak, F.: Alterations in the mechanical properties of the human chondrocyte pericellular matrix with osteoarthritis. *Journal of Biomechanical Engineering* **125** (2003), 323–333.

[5] Alexopoulos, L. G.; Williams, G. M.; L.Upton, M.; Setton, L. A. & Guilak, F.: Osteoarthritic changes in the biphasic mechanical properties of the chondrocyte pericellular matrix in articular cartilage. *Journal of Biomechanics* **38** (2005), 509–517.

[6] Ammann, M.: *Parallel Finite Element Simulations of Localization Phenomena in Porous Media*. Dissertation thesis, Report No. II-11, Institute of Applied Mechanics (CE), University of Stuttgart 2005.

[7] Andersen, M. S.; Damsgaard, M.; MacWilliams, B. & Rasmussen, J.: A computationally efficient optimisation-based method for parameteridentification of kinematically determinate and over-determinate biomechanical systems. *Computer Methods in Biomechanics and Biomedical Engineering* **13** (2010), 171–183.

[8] Anderson, A. E.; Ellis, B. J.; Maas, S. A. & Weiss, J. A.: Effects of idealized joint geometry on finite element predictions of cartilage contact stresses in the hip. *Journal of Biomechanics* **43** (2010), 1351–1357.

[9] Ascenzi, M.-G.; Kawas, N. P.; Lutz, A.; Kardas, D.; Nackenhorst, U. & Keyak, J. H.: Individual-specific multi-scale finite element simulation of cortical bone of human proximal femur. *Journal of Computational Physics* **244** (2013), 298–311.

[10] Athanasiou, K. A.; Rosenwasser, M. P.; Buckwalter, J. A.; Malinin, I. & Mow, V. C.: Interspecies Comparisons of In Situ Intrinsic Mechanical Properties of Distal Femoral Cartilage. *Journal of Orthopaedic Research* **9** (1991), 330–340.

[11] Athanasiou, K. A.; Thoma, B. S.; Lanctot, D. R.; Shin, D.; Agrawal, C. M. & LeBaron, R. G.: Development of the cytodetachment technique to quantify mechanical adhesiveness of the single cell. *Biomaterials* **20** (1999), 2405–2415.

[12] Azuma, T.; Nakai, R.; Takizawa, O. & Tsutsumi, S.: In vivo structural analysis of articular cartilage using diffusion tensor magnetic resonance imaging. *Magnetic Resonance Imaging* **27** (2009), 1242–1248.

[13] Bachrach, N. M.; Mow, V. C. & Guilak, F.: Incompressibility of the solid matrix of articular cartilage under high hydrostatic pressures. *Journal of Biomechanics* **31** (1998), 445–451.

[14] Bachrach, N. M.; Valhmu, W. B. & Stazzone, E.: Changes in proteoglycan synthesis of chondrocytes in articular cartilage are associated with the time-dependent changes in their mechanical environment. *Journal of Biomechanics* **28** (1995), 1561–1570.

[15] Bae, W. C.; Wong, V. W.; Hwang, J.; Antonacci, J. M.; Nugent-Derfus, G. E.; Blewis, M. E.; Temple-Wong, M. M. & Sah, R. L.: Wear-lines and split-lines of human patellar cartilage: relation to tensile biomechanical properties. *Osteoarthritis Research Society International* **16** (2008), 841–845.

[16] Ball, J. M.: Convexity conditions and existence theorems in nonlinear elasticity. *Archive for Rational Mechanics and Analysis* **63** (1977), 337–403.

[17] Ball, J. M. & James, R. D.: Proposed experimental tests of a theory of fine microstructure and the two-well problem. *Philosophical transactions-Royal Society of London* **338** (1992), 389–450.

[18] Balzani, D.: *Polyconvex anisotropic energies and modeling of damage applied to arterial walls*. Dissertation thesis, Nr. 2, Institute of Mechanics, Faculty of Engineering, Department Civil Engineering, University of Duisburg-Essen 2006.

[19] Bathe, K. J.: *Finite Element Procedures*. Prentice-Hall, New Jersey 1996, 2 edn.

[20] Bauer, L. R. & Hamby, D. M.: On the Statistical Sensitivity Analysis of Models for Chemical Kinetics. *American Institute of Chemical Engineers* **21** (1991), 441–448.

[21] Baykal, D.; Underwood, R. J.; Mansmann, K.; Marcolongo, M. & Kurtz, S. M.: Evaluation of friction properties of hydrogels based on a biphasic cartilage model. *Journal of the Mechanical Behavior of Biomedical Materials* **28** (2013), 263–273.

[22] Benninghoff, A.: Spaltlinien am Knochen, eine Methode zur Ermittlung der Architektur platter Knochen. *Verhandlungen der Anatomischen Gesellschaft* **34** (1925), 189–206.

[23] Berenbaum, F.: Osteoarthritis as an inflammatory disease (osteoarthritis is not osteoarthrosis!). *Osteoarthritis and Cartilage* **21** (2013), 16–21.

[24] Bergmann, G.; Deuretzbacher, G.; Heller, M.; Graichen, F.; Rohlmann, A.; Strauss, J. & Duda, G. N.: Hip contact forces and gait patterns from routine activities. *Journal of Biomechanics* **34** (2001), 859–871.

[25] Bergmann, G.; Graichen, F.; Siraky, J.; Jendrzynski, H. & Rohlmann, A.: Multichannel strain gauge telemetry for orthopaedic implants. *Journal of Biomechanics* **21** (1988), 169–176.

[26] Berryman, J. G. & Berge, P. A.: Critique of two explicit schemes for estimating elastic properties of multiphase composites. *Mechanics of Materials* **22** (1996), 149–164.

[27] Best, B. A.; Guilak, F.; Setton, L. A.; Zhu, W.; Saed-Nejad, F.; Ratcliffe, A.; Weidenbaum, M. & Mow, V. C.: Compressive mechanical properties of the anulus fibrosus and their relationship to biochemical composition. *Spine* **19** (1994), 212–221.

[28] Bock, H. G.; Kostina, E. & Schlöder, J. P.: Numerical Methods for Parameter Estimation in Non-linear Differential Algebraic Equations. *GAMM-Mitteilungen* **30** (2007), 376–408.

[29] de Boer, R.: *Vektor- und Tensorrechnung für Ingenieure*. Springer-Verlag, Berlin 1982.

[30] de Boer, R.: Theory of porous media – Past and Present. *Zeitschrift für Angewandte Mathematik und Mechanik* **78** (1998), 441–466.

[31] de Boer, R.: *Theory of Porous Media*. Springer-Verlag, Berlin 2000.

[32] de Boer, R. & Ehlers, W.: *Theorie der Mehrkomponentenkontinua mit Anwendungen auf bodenmechanische Probleme*. Forschungsberichte aus dem Fachbereich Bauwesen Heft 40, Universität-GH-Essen 1986.

[33] Boskey, A. & Camacho, N.: FT-IR imaging of native and tissue engineered bone and cartilage. *Biomaterials* **28** (2007), 2465–2478.

[34] Bowen, R. M.: Theory of mixtures. In Eringen, A. C. (ed.): *Continuum Physics. Volume III*. Academic Press, New York 1976, pp. 1–127.

[35] Bowen, R. M.: Incompressible porous media models by use of the theory of mixtures. *International Journal of Engineering Science* **18** (1980), 1129–1148.

[36] Box, G. E. P.; Hunter, W. G. & Hunter, J. S.: *Statistics for Experimenters: an Introduction to Design, Data Analysis, and Model Building*. John Wiley & Sons New York 1978.

[37] Braess, D.: *Finite Elemente*. Springer-Verlag, Berlin 1997.

[38] Brent, R. P.: *Algorithms for Minimization Without Derivatives*. Prentice-Hall, Englewoods Cliffs, New Jersey 1973.

[39] Brezzi, F. & Fortin, M.: *Mixed and Hybrid Finite Element Methods*. Springer-Verlag, New York 1991.

[40] Brinckmann, P.; Frobin, W. & Hierholzer, E.: Stress on the articular surface of the hip joint in healthy adults and persons with idiopathic osteoarthrosis of the hip joint. *Journal of Biomechanics* **14** (1981), 149–156.

[41] Broom, N. & Flachsmann, R.: Physical indicators of cartilage health: The relevance of compliance, thickness, swelling and fibrillar texture. *Journal of Anatomy* **202** (2003), 481–494.

[42] Broom, N. D. & Myers, D. D.: Further insights into the structural principles governing the function of articular cartilage. *Journal of Anatomy* **139** (1984), 275–294.

[43] Brown, T. D. & Shawn, D. T.: In vitro contact stress distributions in the natural human hip. *Journal of Biomechanics* **16** (1983), 373–384.

[44] Buschmann, M. D.; Gluzband, Y. A.; Grodzinsky, A. J. & Hunziker, E. B.: Mechanical compression modulates matrix biosynthesis in chondrocyte/agarose culture. *Journal of Cell Science* **108** (1995), 1497–1508.

[45] Caligaris, M. & Ateshian, G. A.: Effects of sustained interstitial fluid pressurization under migrating contact area, and boundary lubrication by synovial fluid, on cartilage friction. *Osteoarthritis and Cartilage* **16** (2008), 1220–1227.

[46] Camacho, C. W.; Tucker, C. L.; Yalvac, S. & McGee, R. L.: Stiffness and thermal expansion predictions for hybrid short fiber composites. *Polymer Composites* **11** (1990), 229–239.

[47] den Camp, O. M. G. C. O.; Oomens, C. W. J.; Veldpaus, F. E. & Janssen, J. D.: An efficient algorithm to estimate material parameters of biphasic mixtures. *International Journal for Numerical Methods in Engineering* **45** (1999), 1315–1331.

[48] Carter, D. R. & Spengler, D. M.: Mechanical properties and composition of cortical bone. *Clinical Orthopaedics and Related Research* **135** (1978), 192–217.

[49] Chen, J. & Lu, G.: Finite element modelling of nanoindentation based methods for mechanical properties of cells. *Journal of Biomechanics* **45** (2012), 2810–2816.

[50] Ciarlet, G. A.: *Mathematical Elasticity: Three-Dimensional Elasticity Vol. 1*. Studies in Mathematics and its Applications, Elsevier Science Publishers B.V., Amsterdam 1988.

[51] Ciavarella, M.; Strozzi, A.; Baldini, A. & Giacopini, M.: Normalisation of load and clearance effects in ball in socket-like replacements. *Proceeding of the Institution of Mechanical Engineers. Part H, Journal of Engineering in Medicine* **221** (2007), 601–611.

[52] Crosetto, M.; Tarantola, S. & Saltelli, A.: Sensitivity and uncertainty analysis in spatial modelling based on gis. *Agriculture, Ecosystems & Environment* **81** (2000), 71–79.

[53] Daniel, M.; Iglic, A. & Kralj-Iglic, V.: The shape of acetabular cartilage optimizes hip contact stress distribution. *Journal of Anatomy* **207** (2005), 85–91.

[54] Day, W. H.; Swanson, S. A. V. & Freeman, M. A. R.: Contact Pressures in the Loaded Human Cadaver Hip. *Journal of Bone and Joint Surgery. British Volume* **57** (1975), 302–313.

[55] Dennis, J. E. & Torczon, V.: Direct search methods on parallel machines. *SIAM Journal on Optimization* **1** (1991), 448–474.

[56] Diebels, S.; Ellsiepen, P. & Ehlers, W.: Error-controlled Runge-Kutta time integration of a viscoplastic hybrid two-phase model. *Technische Mechanik* **19** (1999), 19–27.

[57] Downing, D. J.; Gardner, R. H. & Hoffman, F. O.: An examination of response surface methodologies for uncertainty analysis in assessment models. *Technometrics* **27** (1985), 151–163.

[58] Duong, M. T.; Nguyen, N. H. & Staat, M.: Numerical stability enhancement of modeling hyperelastic materials. *Proceedings of the European Congress on Computational Methods in Applied Sciences and Engineering (ECCOMAS)* **45** (2012), 1–15.

[59] Ebbing, V.: *Design of Polyconvex Energy Functions for All Anisotropy Classes*. Dissertation thesis, Nr. 9, Institute of Mechanics, Faculty of Engineering, Department Civil Engineering, University of Duisburg-Essen 2010.

[60] Eberhardt, A. W.; Keer, L. M.; Lewis, J. L. & Vithoontien, V.: An analytical model of joint contact. *Journal of Biomechanical Engineering* **112** (1990), 407–413.

[61] Eberhardt, A. W.; Lewis, J. L. & Keer, L. M.: Contact of layered elastic spheres as a model of joint contact: effect of tangential load and friction. *Journal of Biomechanical Engineering* **113** (1991), 107–108.

[62] Eberhardt, A. W.; Lewis, J. L. & Keer, L. M.: Normal contact of elastic spheres with two elastic layers as a model of joint articulation. *Journal of Biomechanical Engineering* **113** (1991), 410–417.

[63] Eggli, P. S.; Hunziker, E. B. & Schenk, R. K.: Quantitation of structural features characterizing weight- and less-weight-bearing regions in articular cartilage: a stereological analysis of medial femoral condyles in young adult rabbits. *The Anatomical Record* **222** (1988), 217–227.

[64] Ehlers, W.: *Vector and Tensor Calculus: An Introduction*. Lecture Notes, Institute of Applied Mechanics (Chair of Continuum Mechanics), University of Stuttgart, 1995–2014, URL http://mechbau.uni-stuttgart.de/ls2.

[65] Ehlers, W.: *Poröse Medien – ein kontinuumsmechanisches Modell auf der Basis der Mischungstheorie*. Report No. II-21 of the Institute of Applied Mechanics, University of Stuttgart 2011 (Reproduction of "Forschungsberichte aus dem Fachbereich Bauwesen, Heft 47, Universität-GH-Essen 1989").

[66] Ehlers, W.: Constitutive equations for granular materials in geomechanical context. In Hutter, K. (ed.): *Continuum Mechanics in Environmental Sciences and Geophysics*. Springer-Verlag 1993, CISM Courses and Lecture Notes No. 337, pp. 313–402.

[67] Ehlers, W.: Grundlegende Konzepte in der Theorie Poröser Medien. *Technische Mechanik* **16** (1996), 63–76.

[68] Ehlers, W.: Foundations of multiphasic and porous materials. In Ehlers, W. & Bluhm, J. (eds.): *Porous Media: Theory, Experiments and Numerical Applications.* Springer-Verlag, Berlin 2002, pp. 3–86.

[69] Ehlers, W.: Challenges of porous media models in geo- and biomechanical engineering including electro-chemically active polymers and gels. *International Journal of Advances in Engineering Sciences and Applied Mathematics* **1** (2009), 1–24.

[70] Ehlers, W. & Acartürk, A.: The role of implicit Dirichlet boundary conditions for numerically stable computations of swelling phenomena. *Computational Mechanics* **43** (2009), 545–557.

[71] Ehlers, W. & Ellsiepen, P.: Theoretical and numerical methods in environmental continuum mechanics based on the theory of porous media. In Schrefler, B. A. (ed.): *Environmental Geomechanics*. Springer-Verlag, Wien 2001, CISM Courses and Lectures No. 417, pp. 1–81.

[72] Ehlers, W.; Ellsiepen, P.; Blome, P.; Mahnkopf, D. & Markert, B.: *Theoretische und numerische Studien zur Lösung von Rand- und Anfangswertproblemen in der Theorie Poröser Medien, Forschungsbericht zum DFG-Projekt Eh 107/6-2*. Report No. II-1, Institute of Applied Mechanics (CE), University of Stuttgart 1999.

[73] Ehlers, W.; Karajan, N. & Markert, B.: A porous media model describing the inhomogeneous behaviour of the human intervertebral disc. *Materialwissenschaften und Wekstofftechnik* **37** (2006), 546–551.

[74] Ehlers, W.; Karajan, N. & Markert, B.: An extended biphasic model for charged hydrated tissues with application to the intervertebral disc. *Biomechanics and Modeling in Mechanobiology* **8** (2009), 233–251.

[75] Ehlers, W. & Markert, B.: A linear viscoelastic biphasic model for soft tissues based on the theory of mixtures. *Journal of Biomechanical Engineering* **123** (2001), 418–424.

[76] Ehlers, W.; Markert, B. & Karajan, N.: Continuum mechanical modeling and numerical analysis of spinal discs. In Ehlers, W. & Markert, B. (eds.): *Proceedings of the 1st GAMM Seminar on Continuum Biomechanics*. Report No. II-14, Institute of Applied Mechanics (CE), University of Stuttgart 2005, pp. 35–45.

[77] Ehlers, W.; Markert, B. & Karajan, N.: On the load bearing mechanism of the human intervertebral disc. In Abousleiman, Y. N.; Cheng, A. H.-D. & Ulm, F. J. (eds.): *Poromechanics III, Proceedings of the 3rd Biot Conference on Poromechanics*, Balkema at Taylor & Francis, Leiden 2005, pp. 51–56.

[78] Ehlers, W.; Markert, B. & Karajan, N.: A coupled FE analysis of the intervertebral disc based on a multiphasic TPM formulation. In Holzapfel, G. A. & Ogden, R. W. (eds.): *Mechanics of Biological Tissue*. Springer 2006, pp. 373–386.

[79] Ehlers, W. & Scholz, B.: An inverse algorithm for the identification and the sensitivity analysis of the parameters governing micropolar elasto-plastic granular material. *Archive of Applied Mechanics* **77** (2007), 911–931.

[80] Eipper, G.: *Theorie und Numerik finiter elastischer Deformationen in fluidgesättigten porösen Festkörpern*. Dissertation thesis, Report No. II-1, Institute of Applied Mechanics (CE), University of Stuttgart 1998.

[81] Eisenberg, S. & Grodzinsky, A. J.: Swelling of articular cartilage and other connective tissues: electromechanochemical forces. *Journal of Orthopaedic Research* **3** (1985), 148–159.

[82] Eisenberg, S. & Grodzinsky, A. J.: The kinetics of chemically induced nonequilibrium swelling of articular cartilage and corneal stroma. *Journal of Biomechanical Engineering* **109** (1987), 79–89.

[83] Ellsiepen, P.: *Zeit- und ortsadaptive Verfahren angewandt auf Mehrphasenprobleme poröser Medien*. Dissertation thesis, Report No. II-3, Institute of Applied Mechanics (CE), University of Stuttgart 1999.

[84] Eshelby, J. D.: The determination of the elastic field of an ellipsoidal inclusion, and related problems. *Proceedings of the Royal Society of London, A* **241** (1957), 376–396.

[85] Eshelby, J. D.: The elastic field outside an ellipsoidal inclusion. *Proceedings of the Royal Society of London, A* **252** (1959), 561–569.

[86] Federico, S. & Herzog, W.: On the permeability of fibre-reinforced porous materials. *International Journal of Solids and Structures* **45** (2008), 2160–2172.

[87] Ferguson, S. J.; Bryant, J. T.; Ganz, R. & Ito, K.: The acetabular labrum seal: a poroelastic finite element model. *Clinical Biomechanics* **15** (2000), 463–468.

[88] Fietz, K.: *Towards a Finite Element Model for Fluid Flow in the Human Hip Joint*. Dissertation thesis, Institute of Mechanics and Computational Mechanics, Leibniz University of Hannover 2013.

[89] Fietz, K. & Nackenhorst, U.: A finite element approach for modelling hip joint contact. *Proceedings in Applied Mathematics and Mechanics* **11** (2011), 87–88.

[90] Fietz, K. & Nackenhorst, U.: A Finite Element Approach for Modelling Synovial Joint Contact. In Ehlers, W. & Markert, B. (eds.): *Proceedings of the 3rd GAMM Seminar on Continuum Biomechanics*. 2012, pp. 1–16.

[91] Forcheimer, P.: Wasserbewegung durch Boden. *Zeitschrift des Vereins Deutscher Ingenieure* **50** (1901), 1–34.

[92] Frijns, A. J. H.; Huyghe, J. M. & Janssen, J. D.: A validation of the quadriphasic mixture theory for intervetebral disc tissue. *International Journal of Engineering Science* **35** (1997), 1419–1429.

[93] Gallagher, A. J.; Anniadh, A. N.; Bruyere, K.; Ottenio, M.; Xie, H. & Gilchris, M. D.: Dynamic tensile properties of human skin. *International Research Council on Biomechanics of Injury* **12** (2012), 494–503.

[94] Gardner, R. H.; Huff, D. D.; O'Neill, R. V.; Mankin, J. B.; Carney, J. & Jones, J.: Application of error analysis to a marsh hydrology model. *Water Resources Research* **16** (1980), 659–664.

[95] Gasser, T. C.; Ogden, R. W. & Holzapfel, G. A.: Hyperelastic modelling of arterial layers with distributed collagen fibre orientations. *Journal of Royal Society Interface* **3** (2006), 15–35.

[96] Genda, E.; Iwasaki, N.; Li, G.; MacWilliams, B. A.; Barrance, P. J. & Chao, E. Y. S.: Normal hip joint contact pressure distribution in single-leg standing-effect of gender and anatomic parameters. *Journal of Biomechanics* **34** (2001), 895–905.

[97] Gonzalez-Perez, I.; Iserte, J. L. & Fuentes, A.: Implementation of Hertz theory and validation of a finite element model for stress analysis of gear drives with localized bearing contact. *Mechanism and Machine Theory* **46** (2011), 765–783.

[98] Grodzinsky, A. J.; Roth, V.; Myers, E.; Grossman, W. K. & Mow, V. V.: The significance of electromechanical and osmotic forces in the nonequilibrium swelling behavior of articular cartilage in tension. *Journal of Biomechanical Engineering* **103** (1981), 221–232.

[99] Groves, R. B.; Coulman, S. A.; Birchall, J. C. & Evans, S. L.: An anisotropic, hyperelastic model for skin: Experimental measurements, finite element modelling and identification of parameters for human and murine skin. *Journal of the Mechanical Behavior of Biomedical Materials* **18** (2013), 167–180.

[100] Gründer, W.: MRI assessment of cartilage ultrastructure. *NMR in Biomedicine* **19** (2006), 855–876.

[101] Guilak, F. & Mow, V. C.: The mechanical environment of the chondrocyte: a biphasic finite element model of cell-matrix interactions in articular cartilage. *Journal of Biomechanics* **33** (2000), 1663–1673.

[102] Guilak, F.; Ratcliffe, A. & Mow, V. C.: Chondrocyte deformation and local tissue strain in articular cartilagea confocal microscopy study. *Journal of Orthopaedic Research* **13** (1995), 410–421.

[103] Guilak, F.; Sah, R. L. & Setton, L. A.: Physical regulation of cartilage metabolism. In Mow, V. C. & Hayes, W. C. (eds.): *Basic orthopaedic biomechanics*. Lippincott-Raven, Philadelphia 1997, 2nd edn., pp. 179–207.

[104] Guo, Z. Y.; Caner, F.; Peng, X. Q. & Moran, B.: On constitutive modelling of porous Neo-Hookean composites. *Journal of the Mechanics and Physics of Solids* **56** (2008), 2338–2357.

[105] Guo, Z. Y.; Peng, X. Q. & Moran, B.: A composite-based hyperelastic constitutive model for soft tissue with application to the human annulus fibrosus. *Journal of the Mechanics and Physics of Solids* **54** (2006), 1952–1971.

[106] Guo, Z. Y.; Peng, X. Q. & Moran, B.: Mechanical response of Neo-Hookean fiber reinforced incompressible nonlinearly elastic solids. *International Journal of Solids and Structures* **44** (2007), 1949–1969.

[107] Han, E.; Chen, S. S.; Klisch, S. M. & Sah, R. L.: Contribution of Proteoglycan Osmotic Swelling Pressure to the Compressive Properties of Articular Cartilage. *Biophysical Journal* **101** (2006), 916–924.

[108] Hassanizadeh, S. M. & Gray, W. G.: High velocity flow in porous media. *Transport in Porous Media* **2** (1987), 521–531.

[109] Hayes, W. C.; Keer, L. M.; Herrmann, G. & Mockros, L. F.: A mathematical analysis for indentation tests of articular cartilage. *Journal of Biomechanics* **5** (1972), 541–551.

[110] Hayes, W. C. & Mockros, L. F.: Viscoelastic properties of human articular cartilage. *Journal of Applied Physiology* **31** (1971), 562–568.

[111] Heider, Y.: *Saturated porous media dynamics with application to earthquake engineering*. Dissertation thesis, Report No. II-25, Institute of Applied Mechanics (CE), University of Stuttgart 2012.

[112] Heller, M.; Bergmann, G.; Deuretzbacher, G.; Dürselen, L.; Pohl, M.; Claes, L.; Haas, N. P. & Duda, G. N.: Musculo-skeletal loading conditions at the hip during walking and stair climbing. *Journal of Biomechanics* **34** (2001), 883–893.

[113] Helton, J. C.: Uncertainty and sensitivity analysis techniques for use in performance assessment for radioactive waste disposal. *Reliability Engineering & System Safety* **42** (1993), 327–367.

[114] Helton, J. C.; Davis, F. J. & Johnson, J. D.: A comparison of uncertainty and sensitivity analysis results obtained with random and latin hypercube sampling. *Reliability Engineering & System Safety* **89** (2005), 305–330.

[115] Henak, C. R.; Ellis, B. J.; Harris, M. D.; Anderson, A. E.; Peters, C. L. & Weiss, J. A.: Role of the acetabular labrum in load support across the hip joint. *Journal of Biomechanics* **44** (2001), 2201–2206.

[116] Hewitt, J.; Guilak, F.; Glisson, R. & Vail, T. P.: Regional material properties of the human hip joint capsule ligaments. *Journal of Orthopaedic Research* **19** (2001), 359–364.

[117] Hill, A.: The heat of shortening and the dynamic constants of muscle. *Proceedings of the Royal Society of London. Series B, Biological Sciences* **126** (1938), 136–195.

[118] Hipp, J. A.; Sugano, N.; Millis, M. B. & Murphy, S. B.: Planning acetabular redirection osteotomies based on joint contact pressures. *Clinical Orthopaedics and Related Research* **364** (1999), 134–143.

[119] Hodge, W. A.; Fijan, R. S.; Carlson, K. L.; Burgess, R. G.; Harris, W. H. & Mann, R. W.: Contact Pressures in the Human Hip Joint Measured in vivo. *Proceeding of the National Academy of Sciences* **83** (1986), 2879–2883.

[120] Hoffmann, A. H. & Grigg, P.: Measurements of joint capsule tissue loading in the cat knee using calibrated mechanoreceptors. *Journal of Biomechanics* **22** (1989), 787–791.

[121] Holzapfel, G. A.: *Nonlinear Solid Mechanics. A Continuum Approach for Engineering.* John Wiley & Sons., Chichester 2000.

[122] Holzapfel, G. A.; Eberlein, R.; Wriggers, P. & Weizsäcker, H. W.: A new axisymmetrical membrane element for anisotropic, finite strain analysis of arteries. *Communications in numerical methods in engineering* **12** (1996), 507–517.

[123] Holzapfel, G. A.; Gasser, T. C. & Ogden, R. W.: Comparison of a multi-layer structural model for arterial walls with a Fung-type model, and issues of material stability. *ASME Journal of Biomechanical Engineering* **126** (2004), 264–275.

[124] Huang, C. Y.; Mow, V. C. & Ateshian, G. A.: The role of flow-independent viscoelasticity in the biphasic tensile and compressive responses of articular cartilage. *American Society of Mechanical Engineers* **123** (2001), 410–417.

[125] Iglic, A.; Antolic, V. & Srakar, F.: Biomechanical analysis of various operative hip joint rotation center shifts. *Archives of Orthopaedic and Trauma Surgery* **112** (1993), 124–126.

[126] Iman, R. L.; Johnson, M. E. & Schroeder, T. A.: Assessing hurricane effects. Part 1. sensitivity analysis. *Reliability Engineering & System Safety* **78** (2002), 131–145.

[127] Itskov, M.; Ehret, A. E. & Mavrilas, D.: A polyconvex anisotropic strain-energy function for soft collagenous tissues. *Biomechanics and Modelling in Mechnobiology* **5** (2006), 17–26.

[128] Jin, H. & Lewis, J. L.: Determination of poisson's ratio of articular cartilage by indentation using different-sized indenters. *Journal of Biomechanical Engineering* **126** (2004), 138–145.

[129] Johnson, K. L.: *Contact Mechanics*. Cambridge University Press, Cambridge 1985.

[130] Johnson, M. L. & Faunt, L. M.: Parameter Estimation by Least-Squares Methods. *Methods in Enzymology* **210** (1992), 1–37.

[131] Jones, W. R.; Ting-Beall, H. P.; Lee, G. M.; Kelley, S. S.; Hochmuth, R. M. & Guilak, F.: Alterations in the Young's modulus and volumetric properties of chondrocytes isolated from normal and osteoarthritic human cartilage. *Journal of Biomechanics* **32** (1999), 119–127.

[132] Julkunen, P.; Kiviranta, P.; Wilson, W.; Jurvelin, J. S. & Korhonen, R. K.: Characterization of articular cartilage by combining microscopic analysis with a fibril-reinforced finite-element model. *Journal of Biomechanics* **40** (2007), 1862–1870.

[133] Julkunen, P.; Wilson, W.; Jurvelin, J. S.; Rieppo, J.; Qu, C. J.; Lammi, M. J. & Korhonen, R. K.: Stress-relaxation of human patellar articular cartilage in unconfined compression: prediction of mechanical response by tissue composition and structure. *Journal of Biomechanics* **41** (2008), 1978–1986.

[134] Jurvelin, J. S.; Rasanen, T.; Kolmonen, P. & Lyyra, T.: Comparison of optical, needle probe and ultrasonic techniques for the measurement of articular cartilage thickness. *Journal of Biomechanics* **8** (1995), 231–235.

[135] Juszczyk, M. M.; Cristofolini, L. & Viceconti, M.: The human proximal femur behaves linearly elastic up to failure under physiological loading conditions. *Journal of Biomechanics* **44** (2011), 2259–2266.

[136] Kaab, M.; Ito, K.; Rahn, B.; Clark, J. & Notzli, H.: Effect of mechanical load on articular cartilage collagen structure: A scanning electron-microscope study. *Journal of Anatomy* **167** (2000), 106–120.

[137] Kang, J. J.; Becker, A. A. & Sun, W.: Determining elastic-plastic properties from indentation data obtained from finite element simulations and experimental results. *International Journal of Mechanical Sciences* **62** (2012), 34–46.

[138] Karajan, N.: *An Extended Biphasic Description of the Inhomogeneous and Anisotropic Intervertebral Disc*. Dissertation thesis, Report No. II-19, Institute of Applied Mechanics (CE), University of Stuttgart 2009.

[139] Karajan, N.; Ehlers, W. & Markert, B.: An anisotropic porous media model of the intervertebral disc. *Proceedings in Applied Mathematics and Mechanics* **3** (2003), 180–181.

[140] Kardas, D. & Nackenhorst, U.: Studies on Bone Remodeling Theory Based on Microcracks Using Finite Element Computations. *Proceedings in Applied Mathematics and Mechanics* **9** (2009), 147–148.

[141] Kellgren, J. H. & Bier, F.: Radiological signs of rheumatoid arthritis: a study of observer differences in the reading of hand films. *Annals of the Rheumatic Diseases* **15** (1956), 55–60.

[142] Kellgren, J. H. & Lawrence, F.: Radiological assessment of osteo-arthritis. *Annals of the Rheumatic Diseases* **16** (1957), 494–500.

[143] Kempson, G. E.; Freeman, M. A. R. & Swanson, S. A. V.: The determination of a creep modulus for articular cartilage from indentation tests on the human femoral head. *Journal of Biomechanics* **4** (1971), 231–250.

[144] Khrushchov, M. M. & Berkovich, E. S.: Methods of determining the hardness of very hard materials: the hardness of diamond. *Industrial Diamond Review* **11** (1951), 42–49.

[145] Kim, N. W.; Piatyszek, M. A.; Prowse, K. R.; Harley, C. B.; West, M. D.; Ho, P. L.; Coviello, G. M.; Wright, W. E.; Weinrich, S. L. & Shay, J. W.: Specific association of human telomerase activity with immortal cells and cancer. *Science* **266** (1994), 2011–2015.

[146] Knupp, P. M. & Lage, J. L.: Generalization of the Forchheimer-extended Darcy flow model to the tensor permeability case via a variational principle. *Journal of Fluid Mechanics* **299** (1995), 97–104.

[147] Koay, E. J.; Shieh, A. C. & Athanasiou, K. A.: Creep indentation of single cells. *Journal of Biomechanical Engineering* **125** (2003), 334–341.

[148] Korhonen, R. K.; Julkunen, P.; Rieppo, J.; Lappalainen, R.; Konttinen, Y. T. & Jurvelin, J. S.: Collagen network of articular cartilage modulates fluid flow and mechanical stresses in chondrocyte. *Biomechanics and Modeling in Mechanobiology* **5** (2006), 150–159.

[149] Korhonen, R. K.; Laasanen, M. S.; Töyräs, J.; Rieppo, J.; Hirvonen, J.; Helminen, H. J. & Jurvelin, J. S.: Comparison of the equilibrium response of articular cartilage in unconfined compression, confined compression and indentation. *Journal of Biomechanics* **35** (2002), 903–909.

[150] Krawietz, A.: *Materialtheorie. Mathematische Beschreibung des phänomenologischen thermomechanischen Verhaltens.* Springer-Verlag, Berlin 1986.

[151] Kurrat, H. J. & Oberländer, W.: The thickness of the cartilage in the hip joint. *Journal of Anatomy* **126** (1978), 145–155.

[152] Lai, W. M.; Hou, J. S. & Mow, V. C.: A triphasic theory for the swelling and deformation behaviours of articular cartilage. *Journal of Biomechanical Engineering* **113** (1991), 245–258.

[153] Langelier, E. & Buschmann, M. D.: Increasing strain and strain rate strengthen transient stiffness but weaken the response to subsequent compression for articular cartilage in unconfined compression. *Journal of Biomechanics* **36** (2003), 853–859.

[154] Lanir, Y.: Biorheology and fluid flux in swelling tissues. I. Bicomponent theory for small deformations, including concentration effects. *Biorheology* **24** (1987), 173–187.

[155] Leipzig, N. D. & Athanasiou, K. A.: Unconfined creep compression of chondrocytes. *Journal of Biomechanics* **38** (2003), 77–85.

[156] Li, L. P. & Herzog, W.: The role of viscoelasticity of collagen fibers in articular cartilage: Theory and numerical formulation. *The Official Journal of the International Society of Biorheology* **41** (2004), 181–194.

[157] Li, L. P. & Herzog, W.: Arthroscopic evaluation of cartilage degeneration using indentation testing-influence of indenter geometry. *Clinical Biomechanics* **21** (2006), 420–426.

[158] Li, L. P.; Soulhat, J.; Buschmann, M. D. & Shirazi-Adl, A.: Nonlinear analysis of cartilage in unconfined ramp compression using a fibril reinforced poroelastic model. *Clinical Biomechanics* **14** (1999), 673–682.

[159] Lielens, G.: *Micro-macro modeling of structured materials*. Dissertation thesis, Faculté de Sciences Appliquées, Université catholique de Louvain 2009.

[160] Lieser, B.: *Morphologische und biomechanische Eigenschaften des Hüftgelenks (Articulatio coxae) des Hundes (Canis familiaris)*. Dissertation thesis, Institut für Tieranatomie, Ludwig-Maximilians-Universität München 2003.

[161] Likhitpanichkul, M.; Guo, X. E. & Mow, V. C.: The effect of matrix tension-compression nonlinearity and fixed charges on chondrocyte response in cartilage. *Molecular and Cellular Biomechanics* **2** (2005), 191–204.

[162] Lilledahl, M. B.; Pierce, D. M.; Ricken, T.; Holzapfel, G. A. & de Lange Davies, C.: Structural analysis of articular cartilage using multiphoton microscopy: input for biomechanical modeling. *IEEE Transactions on Medical Imaging* **30** (2011), 1635–1648.

[163] Linn, F. C.: Lubrication of animal joints. I. The arthrotripsometer. *Journal of Bone and Joint Surgery* **49** (1967), 1079–1098.

[164] Linn, F. C. & Radin, E. L.: Lubrication of animal joints. 3. The effect of certain chemical alterations of the cartilage and lubricant. *Arthritis and Rheumatism* **11** (1968), 674–682.

[165] Lipshitz, H.; Etheridge, R. & Glimcher, M.: In vitro wear of articular cartilage. *Journal of Bone and Joint Surgery* **57** (1975), 527–537.

[166] Little, C. B. & Ghosh, P.: Variation in proteoglycan metabolism by articular chondrocytes in different joint regions is determined by post-natal mechanical loading. *Osteoarthritis and Cartilage* **5** (1994), 49–62.

[167] Mabuchi, K.; Ujihiraa, M. & Sasadab, T.: Influence of loading duration on the start-up friction in synovial joints: measurements using a robotic system. *Clinical Biomechanics* **13** (1998), 492–494.

[168] Machado, M.; Moreira, P.; Flores, P. & Lankarani, H. M.: Compliant contact force models in multibody dynamics: evolution of the hertz contact theory. *Mechanism and Machine Theory* **53** (2012), 99–121.

[169] Mak, A. F.: The apparent viscoelastic behaviour of articular cartilage – the contributions from the intrinsic matrix viscoelasticity and interstitial fluid flows. *ASME Journal of Biomechanical Engineering* **108** (1986), 123–130.

[170] Mak, A. F.; Lai, W. M. & Mow, V. C.: Biphasic indentation of articular cartilage?i. theoretical analysis. *Journal of Biomechanics* **20** (1987), 703–714.

[171] Malo, M. K. H.; Rohrbach, D.; Isaksson, H.; Töyräs, J.; Jurvelin, J. S.; Tamminen, I. S.; Kröger, H. & Raum, K.: Longitudinal elastic properties and porosity of cortical bone tissue vary with age in human proximal femur. *Bone* **53** (2013), 451–458.

[172] Markert, B.: *Porous Media Viscoelasticity with Application to Polymeric Foams.* Dissertation thesis, Report No. II-12, Institute of Applied Mechanics (CE), University of Stuttgart 2005.

[173] Markert, B.: A constitutive approach to 3-d nonlinear fluid flow through finite deformable porous continua with application to a high-porosity polyurethane foam. *Transport in Porous Media* **70** (2007), 427–450.

[174] Markert, B.: A biphasic continuum approach for viscoelastic high-porosity foams: Comprehensive theory, numerics, and application. *Archives of Computational Methods in Engineering* **15** (2008), 371–446.

[175] Markert, B.; Ehlers, W. & Karajan, N.: A general polyconvex strain-energy function for fiber-reinforced materials. *Proceedings in Applied Mathematics and Mechanics* **5** (2005), 245–246.

[176] Markert, B.; Monastyrskyy, B. & Ehlers, W.: Fluid penetration effects in porous media contact. *Continuum Mechanics and Thermodynamics* **20** (2008), 303–315.

[177] Markov, M.; Kazatchenko, E.; Mousatov, A. & Pervago, E.: Permeability of the fluid-filled inclusions in porous media. *Transport in Porous Media* **84** (2010), 307–317.

[178] Maroudas, A.: Physicochemical properties of cartilage in the light of ion exchange theory. *Biophysical Journal* **8** (1968), 575–595.

[179] Maroudas, A.: Biophysical chemistry of cartilaginous tissues with special reference to solute and fluid transport. *Journal of Biorheology* **12** (1975), 233–248.

[180] Maroudas, A. & Bannon, C.: Measurement of swelling pressure in cartilage and comparison with the osmotic pressure of constituent proteoglycans. *Biorheology* **18** (1981), 619–632.

[181] Maroudas, A.; Wachtel, E.; Grushko, G.; Katz, E. P. & Weinberg, P.: The effect of osmotic and mechanical pressures on water partitioning in articular cartilage. *Biochimica et Biophysica Acta* **1073** (1991), 285–294.

[182] Marsden, J. E. & Hughes, T. J. R.: *The Mathematical Foundations of Elasticity.* Prentice-Hall, Englewood Cliffs 1983.

[183] Matzat, S. J.; van Tiel, J.; Gold, G. E. & Oei, E. H. G.: Quantitative MRI techniques of cartilage composition. *Quantitative Imaging in Medicine and Surgery* **3** (2013), 162–174.

[184] Mavcic, B.; Iglic, A.; Kralj-Iglic, V.; Brand, R. A. & Vengust, R.: Cumulative hip contact stress predicts osteoarthritis in ddh. *Clinical Orthopaedics and Related Research* **467** (2008), 682–691.

[185] Maxian, T. A.; Brown, T. D. & Weinstein, S. L.: Chronic stress tolerance levels for human articular cartilage: two nonuniform contact models applied to long-term follow-up of CDH. *Journal of Biomechanics* **28** (1995), 159–166.

[186] McCutchen, C.: Mechanism of animal joints. *Nature* **49** (1959), 1284–1285.

[187] Mollenhauer, J.; Aurich, M.; Muehleman, C. & Khelashvilli, T.: X-ray diffraction of the molecular substructure of human articular cartilage. *Connective Tissue Research* **44** (2003), 201–207.

[188] Mori, T. & Tanaka, K.: Average stress in matrix and average energy of materials with misfitting inclusions. *Acta Metallurgica* **21** (1973), 571–574.

[189] Morrey, C. B.: Quasi-convexity and the lower semicontinuity of multiple integrals. *Pacific Journal of Mathematics* **2** (1952), 25?53.

[190] Mow, V. C.; Gibbs, M. C.; Lai, W. M.; Zhu, W. B. & Athanasiou, K. A.: Biphasic indentation of articular cartilage-II. A numerical algorithm and an experimental study. *Journal of Biomechanics* **22** (1989), 853–861.

[191] Mow, V. C.; Holmes, M. H. & Lai, W. M.: Fluid transport and mechanical properties of articular cartilage: A review. *Journal of Biomechanics* **17** (1984), 377–394.

[192] Mow, V. C.; Kuei, S. C.; Lai, W. M. & Armstrong, C. G.: Biphasic creep and relaxation of articular cartilage in compression: theory and experiments **102** (1980), 73–84.

[193] Mow, V. C. & Mansour, J. M.: The non linear interaction between cartilage deformation and interstitial fluid flow. *Journal of Biomechanics* **10** (1977), 31–39.

[194] Mow, V. C. & Ratcliffe, A.: Structure and function of articular cartilage and meniscus. In Mow, V. C. & w. C. Hayes (eds.): *Basic Orthopaedic Biomechanics*. Lippincott-Raven Publishers, Philadelphia 1997, 2nd edn., pp. 113–176.

[195] Mow, V. C. & Schoonbeck, J. M.: Contribution of Donnan osmotic pressure towards the biphasic compressive modulus of articular cartilage. *Transactions of the Orthopaedic Research Society* **9** (1984), 262–272.

[196] Mow, V. C.; Zhu, W. & Ratcliffe, A.: Structure and function of articular cartilage and meniscus. In Mow, V. C. & Hayes, W. C. (eds.): *Basic Orthopaedic Biomechanics*. Raven Press, New York 1991, pp. 143–198.

[197] Muehleman, C.; Majumdar, S.; Issever, A.; Arfelli, F.; Menk, R.-H. & Rigon, L.: X-ray detection of structural orientation in human articular cartilage. *Osteoarthritis and Cartilage* **12** (2004), 97–105.

[198] Myers, E. R.; Lai, W. M. & Mow, V. C.: A continuum theory and an experiment for the ion-induced swelling behavior of articular cartilage. *Journal of Biomechanical Engineering* **106** (1984), 151–158.

[199] Najjar, D.; Behnamghader, A. & Iost, A.: Influence of a foreign body on the wear of metallic femoral heads and polyethylene acetabular cups of total hip prostheses. *Journal of Materials Science* **35** (2000), 4583–4588.

[200] Naresh, D.; Arumugam, V. & Sanjeevi, R.: Mechanical behaviour of shark skin. *Journal of Biosciences* **22** (1997), 431–437.

[201] Nemat-Nasser, S. & Hori, M.: *Micromechanics: Overall Properties of Heterogeneous Materials*. Elsevier Science Publishers, Amsterdam 1999.

[202] Neusch, E.; Dieppe, P.; Reichenbach, S.; Williams, S.; Iff, S. & Juni, P.: All cause and disease specific mortality in people with osteoarthritis of the knee or hip: population based cohort study. *Osteoarthritis and Cartilage* **342** (2011), 11–21.

[203] Nissi, M. J.; Rieppo, J.; Töyräs, J.; Laasanen, M. S.; Kiviranta, I.; Nieminen, M. T. & Jurvelin, J. S.: Estimation of mechanical properties of articular cartilage with MRI - dGEMRIC, T2 and T1 imaging in different species with variable stages of maturation. *Osteoarthritis and Cartilage* **15** (2007), 1141–1148.

[204] Nocedal, J. & Wright, S. J.: *Numerical Optimization*. Springer-Verlag, Wien 1999.

[205] Ogden, R. W.: Large deformation isotropic elasticity – On the correlation of theory and experiment for incompressible rubberlike solids. *Proceedings of the Royal Society of London, Series A* **326** (1972), 565–584.

[206] Pailler-Mattei, C.; Bec, S. & Zahouani, H.: In vivo measurements of the elastic mechanical properties of human skin by indentation tests. *Mechanical Engineering & Physics* **30** (2008), 599–606.

[207] Parsons, J. R. & Black, J.: Mechanical behavior of articular cartilage, quantitative changes with alteration of ionic environment. *Journal of Biomechanics* **12** (1979), 765–773.

[208] Peng, X. Q.; Guo, Z. Y. & Moran, B.: An anisotropic hyperelastic constitutive model with fiber-matrix shear interaction for the human annulus fibrosus. *Transactions of the American Society of Mechanical Engineers* **73** (2006), 815–824.

[209] Pierard, O.; Friebel, C. & Doghri, I.: Mean-field homogenization of multi-phase thermo-elastic composites: a general framework and its validation. *Composites Science and Technology* **64** (2004), 1587–1603.

[210] Powell, M. J. D.: A direct search optimization method that models the objective and constraint functions by linear interpolation. In Gomez, S. & Hennart, J. P. (eds.): *Advances in Optimization and Numerical Analysis*. Kluwer Academic Publishers, Dordrecht 1994, pp. 51–67.

[211] Quinn, T. M.; Dierickx, P. & Grodzinsky, A. J.: Glycosaminoglycan network geometry may contribute to anisotropic hydraulic permeability in cartilage under compression. *Journal of Biomechanics* **34** (2001), 1483–1490.

[212] Radin, E. L.; Burr, D. B. & Caterson, B.: Mechanical determinants of osteoarthrosis. *Semin Arthritis Rheum* **21** (1991), 12–21.

[213] Rasmussen, J.; Damsgaard, M. & Voigt, M.: Muscle recruitment by the min/max criterion – a comparative numerical study. *Journal of Biomechanics* **34** (2001), 409–415.

[214] Rasmussen, J.; Zee, M. D.; Damsgaard, M.; Marek, C. & Siebertz, K.: A general method for scaling musculoskeletal models. *Proceedings of the International Symposium on Computer Simulation in Biomechanics* **24** (2005), 755–756.

[215] Ratcliffe, A. R. & Mow, V. C.: Articular cartilage. In Comper, W. D. (ed.): *Extracellular Matrix*. Harwood Academic Publishers 1996, pp. 234–302.

[216] Reynaud, B. & Quinn, T. M.: Anisotropic hydraulic permeability in compressed articular cartilage **39** (2006), 131–137.

[217] Ricken, T. & Bluhm, J.: Remodeling and growth of living tissue: a multiphase theory. *Archive of Applied Mechanics* **80** (2010), 453–465.

[218] Ridge, M. D. & Wright, V.: Mechanical properties of skin: a bioengineering study of skin structure. *Journal of applied Physiology* **21** (1966), 1602–1606.

[219] Roberts, B. J.; Unsworth, A. & Mian, N.: Modes of lubrication in human hip joints. *Annals of the Rheumatic Disease* **41** (1982), 217–224.

[220] Saad, Y. & Schultz, M. H.: GMRES: A generalized minimal residual algorithm for solving nonsymmetric linear systems. *SIAM Journal on Scientific and Statistical Computing* **7** (1986), 856–869.

[221] Saarakkala, S.; Julkunen, P.; Kiviranta, P.; Mäkitalo, J.; Jurvelin, J. S. & Korhonen, R. K.: Depth-wise progression of osteoarthritis in human articular cartilage:investigation of composition, structure and biomechanics. *Osteoarthritis and Cartilage* **18** (2010), 73–81.

[222] Saarakkala, S.; Laasanen, M. S.; Jurvelin, J. S.; Törrönen, K.; Lammi, M. J.; Lappalainen, R. & Töyräs, J.: Ultrasound indentation of normal and spontaneously degenerated bovine articular cartilage. *Osteoarthritis and Cartilage* **11** (2003), 697–705.

[223] Sah, R. L.; Doong, J. Y. H.; Kim, Y. J.; Grodzinsky, A. J.; Plaas, A. H. K. & Sandy, J. D.: Biosynthetic response of cartilage explants to mechanical and physicochemical stimuli. *Transactions of the Orthopedic Research Society* **13** (1988), 70–86.

[224] Sanjeevi, R.: A viscoelastic model for the mechanical properties of biological materials. *Journal of Biomechanics* **15** (1982), 107–109.

[225] Sanjeevi, R.; Somanathan, N. & Ramaswamy, D.: A viscoelastic model for collagen fibres. *Journal of Biomechanics* **15** (1982), 181–183.

[226] Schröder, J. & Neff, P.: Invariant formulation of hyperelastic transverse isotropy based on polyconvex free energy functions. *International Journal of Solids and Structures* **40** (2003), 401–445.

[227] Schröder, J.; Neff, P. & Balzani, D.: A variational approach for materially stable anisotropic hyperelasticity **42** (2005), 4352–4371.

[228] Schwarz, H. R.: *Methode der finiten Elemente*. Teubner, Stuttgart 1991.

[229] Seifzadeh, A.; Oguamanam, D. C. D. & Papini, M.: Evaluation of the constitutive properties of native, tissue engineered, and degenerated articular cartilage. *Clinical Biomechanics* **27** (2012), 852–858.

[230] Setton, L. A.; Zhu, W. & Mow, V. C.: The biphasic poroelastic behavior of articular cartilage: role of the surface zone in governing the compressive behavior. *Journal of Biomechanics* **26** (1993), 581–592.

[231] Shin, D. & Athanasiou, K.: Biomechanical properties of the individual cell. *Transactions of the Orthopaedic Research Society* **22** (1997), 352–362.

[232] Silver, F. H.; Freeman, J. W. & DeVore, D.: Viscoelastic properties of human skin and processed dermis. *Skin Research and Technology* **7** (2001), 18–23.

[233] Skempton, A. W.: Significance of Terzaghi's concept of effective stress (Terzaghi's discovery of effective stress). In Bjerrum, L.; Casagrande, A.; Peck, R. B. & Skempton, A. W. (eds.): *From Theory to Practice in Soil Mechanics*. Wiley, New York 1960, pp. 42–53.

[234] Smith, H. E. & Mosh, T. J.: Spatial variation in cartilage T2 of the knee. *Journal of Magnetic Resonance Imaging* **14** (2001), 50–55.

[235] Snijders, H.; Huyghe, J. M. & Janssen, J. D.: Triphasic finite element model for swelling porous media **20** (1995), 1039–1046.

[236] Spencer, A. J. M.: *Continuum Theory of the Mechanics of Fibre-Reinforced Composites*. Springer-Verlag, New York 1984.

[237] Stockwell, R. A.: *Biology of Cartilage Cells*. Cambridge University Press 1979.

[238] Stockwell, R. A.: Structure and function of the chondrocyte under mechanical stress. In Helminen, H. J.; Kiviranta, I. & Tammi, M. (eds.): *Joint Loading: Biology and Health of Articular Structures*. Wright and Sons, Bristol 1987, pp. 126–148.

[239] Suh, J. K. & Bai, S.: Finite element formulation of biphasic poroviscoelastic model for articular cartilage. *Journal of Biomechanical Engineering* **120** (1998), 195–201.

[240] Sun, Z. & Hao, C.: Conformal Contact Problems of Ball-Socket and Ball. *Physics Procedia* **25** (2012), 209–214.

[241] Truesdell, C.: Thermodynamics of diffusion. In Truesdell, C. (ed.): *Rational Thermodynamics*. Springer-Verlag, New York 1984, 2nd edn., pp. 219–236.

[242] Truesdell, C. & Noll, W.: The nonlinear field theories of mechanics. In Flügge, S. (ed.): *Handbuch der Physik*. Springer-Verlag, Berlin 1965, Band III/3.

[243] Ugryumova, N.; Attenburow, D.; Winlove, C. & Matcher, S.: The collagen structure of equine articular cartilage, characterized using polarization-sensitive optical coherence tomography. *Journal of Physics D: Applied Physics* **38** (2005), 2612–2619.

[244] Unsworth, A.; Dowson, D. & Wright, V.: The frictional behaviour of human synovial joints. Part–I: Natural joints. *Transactions of the American Society of Mechanical Engineers Series F* **97** (1975), 369–376.

[245] Urban, J. P. G.; Maroudas, A. & Dillon, J.: Swelling pressures of proteoglycans at the concentrations found in cartilagenous tissues. *Biorheology* **16** (1979), 447–464.

[246] Urban, J. P. G. & McMullin, J. F.: Swelling pressures of the lumbar intervertebral discs: influence of age, spinal level, composition and degeneration. *Spine* **13** (1981), 179–187.

[247] Vetterling, W. & Press, W.: Routine Implementing the Simplex Method. In Press, W. (ed.): *Numerical Recipes in C: the Art of Scientific Computing*. Cambridge University Press, Cambridge 1992, pp. 439–443.

[248] Viéville, P. & Lipinski, P.: Application du schéma autocohérent par étapes à la modélisation des propriétés viscoélastiques des composites. *Proceedings of 9èmes Journées Nationales des Composites* **9** (1994), 545–554.

[249] de Visser, S.; Crawford, R. & Pope, J.: Structural adaptations in compressed articular cartilage measured by diffusion tensor imaging. *Osteoarthritis Cartilage* **16** (2008), 83–89.

[250] Wagner, D. R. & Lotz, J. C.: Theoretical model and experimental results for the nonlinear elastic behavior of human annulus fibrosus. *Journal of Orthopaedic Research* **22** (2004), 901–909.

[251] Wang, Y.; Ding, C.; Wluka, A. E.; Davis, S.; Ebeling, P. R.; Jones, G. & Cicuttini, F. M.: Factors affecting progression of knee cartilage defects in normal subjects over 2 years. *Annals of the Rheumatic Diseases* **45** (2006), 79–84.

[252] Wieners, C.; Ammann, M.; Ehlers, W. & Graf, T.: Parallel Krylov methods and the application to 3-d simulations of a tri-phasic porous media model in soil mechanics. *Computational Mechanics* **36** (2005), 409–420.

[253] Wieners, C.; Ehlers, W.; Ammann, M.; Karajan, N. & Markert, B.: Parallel solution methods for porous media models in biomechanics. *Proceedings in Applied Mathematics and Mechanics* **5** (2005), 35–38.

[254] Wilson, W.; van Donkelaar, C. C. & Huyghe, J. M.: A comparison between mechano-electrochemical and biphasic swelling theories for soft hydrated tissue **127** (2005), 158–165.

[255] Wilson, W.; Huyghe, J. M. & van Donkelaar, C.: Depth-dependent compressive equilibrium properties of articular cartilage explained by its composition. *Biomechanics and Modeling in Mechanobiology* **6** (2007), 43–53.

[256] Wilson, W.; Huyghe, J. M. & van Donkelaar, C. C.: A composition-based cartilage model for the assessment of compositional changes during cartilage damage and adaption. *Osteoarthritis and Cartilage* **14** (2006), 554–560.

[257] Wingstrand, H. & Wingstrand, A.: Biomechanics of the hip joint capsule – a mathematical model and clinical implications. *Clinical Biomechanics* **22** (1997), 273–280.

[258] Wu, G.; Siegler, S.; Allard, P.; Kirtley, C.; Leardini, A.; Rosenbaum, D.; Whittle, M.; D'Lima, D. D.; Cristofolini, L.; Witte, H.; Schmid, O. & Stokes, I.: ISB recommendation on definition of joint coordinate system of various joints for the reporting of human joint motion–part I: ankle, hip, and spine. *Journal of Biomechanics* **35** (2002), 543–548.

[259] Wu, J.; Kirk, T. & Zheng, M.: Study of the collagen structure in the superficial zone and physiological state of articular cartilage using a 3-d confocal imaging technique. *Journal of Orthopaedic Surgery and Research* **3** (2008), 1–11.

[260] Wu, J. Z.; Herzog, W. & Epstein, M.: Joint contact mechanics in the early stages of osteoarthritis. *Medical Engineering & Physics* **22** (2000), 1–12.

[261] Xia, Y.; Moody, J.; Burton-Wurst, N. & Lust, G.: Quantitative in situ correlation between microscopic MRI and polarized light microscopy studies of articular cartilage. *Osteoarthritis and Cartilage* **9** (2001), 393–406.

[262] Yoshida, H.; Faust, A.; Wilckens, J.; Kitagawa, M.; Fetto, J. & Chao, E. Y. S.: Three-dimensional dynamic hip contact area and pressure distribution during activities of daily living. *Journal of Biomechanics* **39** (2006), 1996–2004.

[263] Yosibash, Z.; Padan, R.; Joskowicz, L. & Milgrom, C.: A CT-based high-order finite element analysis of the human proximal femur compared to in-vitro experiments. *Journal of Biomechanical Engineering* **129** (2007), 297–309.

[264] Zhupanska, O. I.: Contact problem for elastic spheres: applicability of the Hertz theory to non-small contact areas. *International Journal of Engineering Science* **49** (2011), 576–588.

[265] Zienkiewicz, O. C.; Qu, S.; Taylor, R. L. & Nakazawa, S.: The patch test for mixed formulations **23** (1986), 1873–1883.

[266] Zienkiewicz, O. C. & Taylor, R. L.: *The Finite Element Method, Vol. 1*. Butterworth-Heinemann, Oxford 2000, fifth edn.

[267] Zinatbakhsh, S.: *Continuum mechanical modeling of fiber reinforcements*. Master thesis, Report No. II-3, Institute of Applied Mechanics (CE), University of Stuttgart 2008.

[268] Zipfel, W.; Williams, R. & Webb, W.: Nonlinear magic: Multiphoton microscopy in the biosciences. *Nature Biotechnology* **21** (2003), 1368–1376.

Nomenclature

Symbols

Symbol	Unit	Description
$\mathbf{A}_\alpha$	[-]	*Almansi*an strain tensor of the constituent φ^α
α	[-]	constituent identifier i. e., $\alpha = \{S, F\}$
α_{int}	[-]	parameter of the interaction part of the strain-energy function
α_M	[-]	scalar parameter
$\mathbf{a}_0^S$, $\mathbf{a}^S$	[-]	vector of orientation of fibres in the solid reference and actual configurations
$\mathbf{A}$		regular identity matrix
$\mathbf{B}_\alpha$	[-]	left *Cauchy-Green* deformation tensor of the constituent φ^α
$\mathcal{B}$		aggregate body
β	[-]	deformation-dependent factor
β_M	[-]	scalar parameter
B_{0S}^S, B^S	[mm]	tortuosity parameter in the solid reference and actual configurations
$\mathbf{B}_{Se}$, $\mathbf{B}_{Si}$	[-]	elastic and inelastic part of left *Cauchy-Green* deformation tensor of the constituent φ^S
$\mathbf{C}_\alpha$	[-]	right *Cauchy-Green* deformation tensor of constituent φ^α
$\bar{c}_m$	[mol/l]	molar concentration of the external salt solution
$c_{m,0S}^{fc}$, c_m^{fc}	[mol/l]	initial and actual concentration of fixed charges
$\bar{c}_{m,0S}^{fc}$	[mol/l]	average concentration of fixed charges
$c_{m,\text{eff}}^{fc}$	[mol/l]	effective concentration of fixed charges
$\boldsymbol{\chi}_\alpha$		motion function of the constituent φ^α
$\mathbf{C}_S$	[-]	right *Cauchy-Green* deformation tensor of the constituent φ^S
$\mathrm{d}a$	[mm^2]	area element
$\mathrm{d}\bar{\mathbf{a}}_\alpha$	[mm^2]	oriented weighted area element in reference configuration of the constituent φ^α
$\mathbf{D}_\alpha$	[1/s]	deformation velocity tensor
$\mathrm{d}\mathbf{a}$	[mm^2]	oriented area element in actual configuration

$\mathrm{d}\mathbf{A}_\alpha$	$[\,\mathrm{mm}^2\,]$	oriented area element in reference configuration of the constituent φ^α
D_C	$[\,\mathrm{mm}\,]$	diameter of a chondron
$\Delta\, p$	$[\,\mathrm{MPa}\,]$	pressure difference
$\delta\mathcal{P}$	$[\,\mathrm{MPa}\,]$	test function for $\mathcal{P}$
$\Delta\pi_{0S}$, $\Delta\pi$	$[\,\mathrm{MPa}\,]$	initial and actual osmotic pressure difference
$\Delta\mathbf{q}_n$		local increment of the intern variables
Δt	$[\,\mathrm{s}\,]$	time increment
$\delta\mathbf{u}_S$	$[\,\mathrm{mm}\,]$	testfunction of $\mathbf{u}_S$
δ_0^C	$[\,\mathrm{MPa}\,]$	compression modulus of chondron
δ_0^S	$[\,\mathrm{MPa}\,]$	compression modulus of ECM
δ_0^P	$[\,\mathrm{MPa}\,]$	compression modulus of PCM
$\delta_{0,\mathrm{eff}}^S$	$[\,\mathrm{MPa}\,]$	effective compression modulus
δ_0^Z	$[\,\mathrm{MPa}\,]$	compression modulus of cell
$\dfrac{\mathrm{d}\phi_n}{\mathrm{d}\mathbf{s}}$		sensitivity vector
$\mathrm{d}v$	$[\,\mathrm{mm}^3\,]$	actual volume element of φ
$\mathrm{d}v^\alpha$	$[\,\mathrm{mm}^3\,]$	local volume element of the constituent φ^α
$\mathrm{d}\mathbf{X}_\alpha$	$[\,\mathrm{mm}\,]$	reference line element of the constituent φ^α
$\mathrm{d}\mathbf{x}$	$[\,\mathrm{mm}\,]$	actual line element of the constituent φ
D_Z	$[\,\mathrm{mm}\,]$	diameter of the chondrocyte
e	[-]	notch length ratio
E	$[\,\mathrm{MPa}\,]$	overall *Young*'s modulus
$\mathbf{E}_\alpha$	[-]	*Green-Lagrange*an strain tensor of the constituent φ^α
ε_{tol}	[-]	tolerance value
η_f	$[\,\mathrm{MPa\,s}\,]$	fibre viscosity parameter
η_n^S	$[\,\mathrm{MPa\,s}\,]$	shear viscosity related to the n-th *Maxwell* element
ζ_C	[-]	scalar parameter
ζ_n^S	$[\,\mathrm{MPa\,s}\,]$	bulk viscosity related to the n-th *Maxwell* element
$\mathbf{F}_\alpha$	[-]	deformation gradient of the constituent φ^α
F_c	$[\,\mathrm{N}\,]$	contact force value
$\mathbf{F}_c$	$[\,\mathrm{N}\,]$	oriented contact force
$\mathbf{F}_{Se}$, $\mathbf{F}_{Si}$	[-]	elastic and inelastic part of the deformation gradient of the constituent φ^S
$f(\mathbf{s})$		objective function
$\mathbf{F}_S$	[-]	deformation gradient of the constituent φ^S
$\mathbf{f}$		generalised external force vector
$\mathbf{F}_V$	$[\,\mathrm{N}\,]$	vertically oriented force

Γ		overall domain boundary
γ^{FR}	[N/m^3]	effective fluid weight
γ_0^S	[-]	parameters governing the volumetric response of φ^S
γ_n^S	[-]	parameters governing the volumetric response of φ^S related to the n-th *Maxwell* element
$\widetilde{\gamma}_m$	[-]	parameters of the equilibrium part of the anisotropic strain-energy function
$(\widetilde{\gamma}_m)_n$	[-]	parameters of the non-equilibrium part of the anisotropic strain-energy function related to the n-th *Maxwell* element
$\mathbf{g}$	[m/s^2]	constant gravitation vector with $\lvert g\rvert = 9.81\,\mathrm{m/s^2}$
$\mathbf{G}_n$		global numerical system
$\mathbf{G}$		space-discrete function vector
$\mathcal{H}^1(\Omega)$		*Sobolev* function space
$\boldsymbol{\mathcal{H}}_{0S}^S$, $\boldsymbol{\mathcal{H}}^S$	[-]	initial and actual hydraulic anisotropy
$\mathbf{I}$	[-]	identity tensor (2$^{\mathrm{nd}}$-order fundamental tensor)
J_α	[-]	*Jacobi*an of φ^α
$J_{S4i,n}^k$	[-]	inelastic counterpart of the fibre stretch at the n-th time step after the k-th local *Newton* iteration
$\mathbf{J}_n$		*Jacobi*an (tangent) matrix
J_S	[-]	*Jacobi*an of φ^S
J_{S4}	[-]	fourth invariant
J_{S4e}, J_{S4i}	[-]	elastic and inelastic part of the fourth invariant (fibre stretch)
J_{S5}	[-]	fifth invariant (mixed invariant)
J_{Se}, J_{Si}	[-]	elastic and inelastic part of the *Jacobi*an of φ^S
κ	[-]	exponent governing the nonlinear dependency of the permeability
K_C	[mm^4/N s]	permeability of the chondron
K_{0S}^F, K^F	[mm^4/N s]	initial and actual specific permeability
$\bar{K}_{0S}^F$	[mm^4/N s]	average initial specific permeability
K_F^F	[mm^4/N s]	nonlinear specific permeability
$\mathbf{K}^F$	[mm^4/N s]	anisotropic permeability tensor
k_{ij}	[-]	covariance coefficient of i-th parameter with j-th parameter
K_P	[mm^4/N s]	permeability of PCM
$\boldsymbol{\mathcal{K}}^S$	[-]	deformation-induced anisotropy
$\mathbf{k}$		generalised stiffness vector
K_0^C	[mm^4/N s]	initial permeability of the chondron

K_0^P	$[\mathrm{mm}^4/\mathrm{N\,s}]$	initial permeability of the PCM
K_0^Z	$[\mathrm{mm}^4/\mathrm{N\,s}]$	initial permeability of the cell
$\mathbf{L}_\alpha$	$[1/\mathrm{s}]$	spatial velocity gradient of φ^α
λ_0^S	[MPa]	first *Lamé* constant
$\lambda_{0,\mathrm{eff}}^S$	[MPa]	effective first *Lamé* constant
$\lambda_{S(k)}$, $\lambda_{Se(k)}$	[-]	eigenvalues of $\mathbf{C}_S$ and $\mathbf{C}_{Se}$
λ_n^S	[MPa]	first *Lamé* constant related to the n-th *Maxwell* element
$\mathbf{L}$		local vector
M_f, M_{fe}	[-]	number of polynomial terms
$\boldsymbol{\mathcal{M}}^S$, $\boldsymbol{\mathcal{N}}^S$	[-]	structural tensors in solid reference and actual configuration
$\mathbf{M}$		generalised mass matrix
μ_0^C	[MPa]	second *Lamé* constant of chondron
μ_{int}	[MPa]	parameter of the interaction part of the strain-energy function
μ_k	[-]	coefficient of friction
μ_0^P	[MPa]	second *Lamé* constant of PCM
μ_0^S	[MPa]	second *Lamé* constant of ECM
$\mu_{0,\mathrm{eff}}^S$	[MPa]	effective shear modulus or effective second *Lamé* constant
$\widetilde{\mu}_m$	[MPa]	fibre stiffness
$(\widetilde{\mu}_m)_n$	[MPa]	fibre stiffness related to the n-th *Maxwell* element
μ_0^Z	[MPa]	second *Lamé* constant of chondrocyte
n^α	[-]	volume fraction of constituent φ^α
n_0^C	[-]	volume fraction of chondron
n_{coll}^S	[-]	solid fraction of collagen fibres
n_{ECM}^S	[-]	solid fraction of ECM
N_e	[-]	number of FE elements
n_{0S}^F, n^F	[-]	initial and actual porosity
$\bar{n}_{0S}^F$	[-]	average porosity
$n_{\mathrm{extra},0S}^F$	[-]	extrafibrillar part of porosity
N_{inq}	[-]	number of inequality constraints
N_n	[-]	number of nodes
n_0^P	[-]	volume fraction of PCM
n_{0S}^S, n^S	[-]	initial and actual solidity
$\mathbf{N}_{S(k)}$, $\mathbf{N}_{Se(k)}$	[-]	eigenvectors of $\mathbf{C}_S$ and $\mathbf{C}_{Se}$

n_{Si}^S	[-]	solid volume fraction $(n_{Si}^S)_n$ related to the n-th *Maxwell* element
ν	[-]	overall *Poisson*'s ratio
$\mathbf{n}$	[-]	outward-oriented unit normal vector
n_0^Z	[-]	volume fraction of chondrocyte
Ω		spatial domain
$\mathit{\Omega}_e$, $\mathit{\Omega}^h$		one finite element and the discretised finite element mesh
p	[MPa]	overall pore-fluid pressure
P		material point in actual configuration
P^α		material point of φ^α
P_c	[N]	contact force value
$\mathcal{P}$	[MPa]	hydraulic pore-fluid pressure (primary variable)
$\bar{\mathcal{P}}$	[MPa]	*Dirichlet* boundary condition for $\mathcal{P}$
$\hat{\mathbf{p}}_E^F$	[J/mm^2 s]	extra momentum production of φ^F
$\hat{\mathbf{p}}^F$	[J/mm^2 s]	momentum production of φ^F
$\hat{\mathbf{p}}^S$	[J/mm^2 s]	momentum production of φ^S
ϕ_0^S	[rad]	fibre angle in the solid reference configuration
$\phi_n(\mathbf{s})$		output after parameter fluctuation around reference state
$\tilde{\phi}_n$		exact solution of inverse problem
$\tilde{p}$	[-]	normalised pressure
$\mathbf{q}_{\mathrm{ISO}}$, $\mathbf{q}_{\mathrm{ANI}}$		isotropic and anisotropic entries of vector of internal variables
$\bar{q}$	[mm/s]	volume efflux of φ^F over the boundary
$\mathbf{q}$		vector of internal variables
r	[mm]	indenter radius
R	[J/mol K]	universal gas constant
r_c		contact zone radius
ρ^α	[kg/mm^3]	partial density of φ^α
$\rho^{\alpha R}$	[kg/mm^3]	effective density of φ^α
r_c	[mm]	radius of contact zone
ρ^{FR}	[kg/mm^3]	effective fluid density
r_{ij}	[-]	correlation coefficient of i-th parameter with j-th parameter
r_n		local residuum value
$\mathbf{r}$		local residuum vector
$\mathbf{S}^\alpha$	[MPa]	second *Piola-Kirchhoff* stress tensor of φ^S

σ_c	[MPa]	contact stress
$\sigma_{c,max}$	[MPa]	peak of contact stress
σ_v	[MPa]	*von Mises* stress
$\mathbf{S}_n^S$	[MPa]	second *Piola-Kirchhoff* non-equilibrium stress tensor contribution related to the n-th *Maxwell* element
t	[s]	time
t_0	[s]	initial time
$\mathbf{T}^\alpha$	[MPa]	*Cauchy* stress of φ^α
$\mathbf{t}^\alpha$	[$\mathrm{N/m^2}$]	surface traction vector of φ^α
τ^α	[MPa]	*Kirchhoff* stress tensor of φ^α
$\bar{\mathbf{t}}$	[MPa]	external load vector acting on the boundary
$\mathbf{T}_{\mathrm{ANI}}^{\mathrm{EQ}}$, $\mathbf{T}_{\mathrm{ANI}}^{\mathrm{NEQ}}$	[MPa]	equilibrium and non-equilibrium part of anisotropic *Cauchy* solid stresses
$\mathbf{T}_{\mathrm{ISO}}^{\mathrm{EQ}}$, $\mathbf{T}_{\mathrm{ISO}}^{\mathrm{NEQ}}$	[MPa]	equilibrium and non-equilibrium part of isotropic *Cauchy* solid stresses
$\mathbf{T}_E^F$	[MPa]	extra *Cauchy* fluid stress
$\mathbf{T}^F$	[MPa]	*Cauchy* fluid stress
θ	[-]	deformation-dependent factor
Θ	[K]	overall temperature
Θ^α	[K]	temperature of φ^α
$\mathbf{T}_{\mathrm{ANI}}^S$, $\mathbf{T}_{\mathrm{ISO}}^S$	[MPa]	isotropic and anisotropic *Cauchy* solid stresses
$\mathbf{T}_E^S$	[MPa]	extra *Cauchy* solid stress
$\mathbf{T}_{\mathrm{INT}}^S$	[MPa]	interaction part of *Cauchy* solid stress
$\mathbf{T}_{\mathrm{mech}}^S$	[MPa]	purely mechanical part of *Cauchy* solid stress
$\mathbf{T}_{\mathrm{osm}}^S$	[MPa]	osmotic part of *Cauchy* solid stress
$\mathbf{T}^S$	[MPa]	*Cauchy* solid stress
$\mathbf{T}$	[MPa]	overall *Cauchy* stress
$\bar{\mathbf{u}}_S$	[mm]	*Dirichlet* boundary condition for $\mathbf{u}_S$
$\mathbf{u}_S$	[mm]	solid displacement vector (primary variable)
$\lvert\mathbf{u}_S\rvert$	[mm]	absolute value of solid displacement
$\mathbf{u}$		vector of unknowns
V	[$\mathrm{mm^3}$]	overall volume
V^α	[$\mathrm{mm^3}$]	volume of φ^α
W_{ANI}	[$\mathrm{J/mm^3}$]	anisotropic part of the strain-energy function
$W_{\mathrm{ANI}}^{\mathrm{EQ}}$, $W_{\mathrm{ANI}}^{\mathrm{NEQ}}$		equilibrium and non-equilibrium part of the anisotropic strain-energy function
$\mathbf{w}_F$	[mm/s]	seepage velocity vector
w_k, w_n	[-]	weight factors

W^S_{INT}	[J/mm^3]	interaction part of the strain-energy function
$\mathbf{x}$	[mm]	actual position vector of φ
$\dot{\mathbf{x}}$	[mm/s]	aggregate velocity vector of φ
$\ddot{\mathbf{x}}$	[mm/s^2]	aggregate acceleration vector of φ
$\overset{\prime}{\mathbf{x}}_\alpha$ or $\mathbf{v}_\alpha$	[mm/s]	velocity vector of φ^α
$\overset{\prime\prime}{\mathbf{x}}_\alpha$	[mm/s^2]	acceleration vector of φ^α
$\mathbf{X}_\alpha$	[mm]	reference position vector of P^α
$\mathbf{X}_S$	[mm]	initial position vector of φ^S
$\overset{\prime}{\mathbf{x}}_F$ or $\mathbf{v}_F$	[mm/s]	velocity of φ^F
$\overset{\prime}{\mathbf{x}}_S$ or $\mathbf{v}_S$	[mm/s]	velocity vector of φ^S
ξ	[-]	local element coordinate
ξ_k		discrete *Gauß* point
$\mathbf{y}$		general vector of unknown
$\tilde{z}$	[-]	normalised depth

Acronyms

Selected Acronym	Definition
COBYLA	Constrained Optimization BY Linear Approximation
DAE	Differential Algebraic Equation
DEA	Discrete-Element Analysis
DIRK	Diagonally Implicit *Runge-Kutta*
DOF	Degree Of Freedom
ECM	Extra-Cellular Matrix
FE	Finite Element
FEM	Finite-Element Method
GMRES	Generalized Minimal RESidual method
IBVP	Initial-Boundary-Value Problem
JCS	Joint Coordinate System
MBS/MKS	Multi-Body System/Mehrkörpersystem
MPM	Multi-Photon Microscope
MRI/MRT	Magnetic Resonance Imaging/Magnetresonanztomographie
OA	Osteoarthritis/Osteoarthrose
OCT	Optical Coherence Tomography
ODE	Ordinary Differential Equation

PANDAS	Porous media Adaptive Nonlinear finite element solver based on Differential Algebraic Systems
PCM	Peri-Cellular Matrix
PG	Proteoglycan
PDE	Partial Differential Equation
QLV	Quasi-Linear Viscoelasticity
REV	Representative Elementary Volume
SDB	Strong Directional Behaviour
SEM	Scanning Electron Microscopy
TPM	Theory of Porous Media/ Theorie der Porösen Medien

List of Figures

List of Tables

Curriculum Vitae

Personal Data:

Name:	Joffrey Mabuma
Date of birth:	May 19, 1984
Place of birth:	Lille, France
Nationality:	Belgian
Marital status:	unmarried

School Education:

1990 – 1996	elementary school Saint-Amand, Jupille (Belgium)
1996 – 2002	secondary/high school Saint-Benoît Saint-Servais, Liège (Belgium)
06/2002	degree: "Allgemeine Hochschulreife" (high school diploma)

University Education:

2002 – 2008	double diploma (T.I.M.E.) in civil engineering at the University of Stuttgart (Germany) and University of Liège major subject: "Konstruktiver Ingenieurbau"
06/2008	degree: "Doppeldiplom-Ingenieur (DDipl.-Ing.) Bauingenieurwesen"
since 07/2008	research associate and doctoral candidate at the Institute of Applied Mechanics (Civil Engineering), University of Stuttgart

Released Report Series

II-1 Gernot Eipper: *Theorie und Numerik finiter elastischer Deformationen in fluid-gesättigten porösen Festkörpern*, 1998.

II-2 Wolfram Volk: *Untersuchung des Lokalisierungsverhaltens mikropolarer poröser Medien mit Hilfe der Cosserat-Theorie*, 1999.

II-3 Peter Ellsiepen: *Zeit- und ortsadaptive Verfahren angewandt auf Mehrphasenprobleme poröser Medien*, 1999.

II-4 Stefan Diebels: *Mikropolare Zweiphasenmodelle: Formulierung auf der Basis der Theorie Poröser Medien*, 2000.

II-5 Dirk Mahnkopf: *Lokalisierung fluidgesättigter poröser Festkörper bei finiten elastoplastischen Deformationen*, 2000.

II-6 Heiner Müllerschön: *Spannungs-Verformungsverhalten granularer Materialien am Beispiel von Berliner Sand*, 2000.

II-7 Stefan Diebels (Ed.): *Zur Beschreibung komplexen Materialverhaltens: Beiträge anläßlich des 50. Geburtstages von Herrn Prof. Dr.-Ing. Wolfgang Ehlers*, 2001.

II-8 Jack Widjajakusuma: *Quantitative Prediction of Effective Material Parameters of Heterogeneous Materials*, 2002.

II-9 Alexander Droste: *Beschreibung und Anwendung eines elastisch-plastischen Materialmodells mit Schädigung für hochporöse Metallschäume*, 2002.

II-10 Peter Blome: *Ein Mehrphasen-Stoffmodell für Böden mit Übergang auf Interface-Gesetze*, 2003.

II-11 Martin Ammann: *Parallel Finite Element Simulations of Localization Phenomena in Porous Media*, 2005.

II-12 Bernd Markert: *Porous Media Viscoelasticity with Application to Polymeric Foams*, 2005.

II-13 Saeed Reza Ghadiani: *A Multiphasic Continuum Mechanical Model for Design Investigations of an Effusion-Cooled Rocket Thrust Chamber*, 2005.

II-14 Wolfgang Ehlers & Bernd Markert (Eds.): *Proceedings of the 1st GAMM Seminar on Continuum Biomechanics*, 2005.

II-15 Bernd Scholz: *Application of a Micropolar Model to the Localization Phenomena in Granular Materials: General Model, Sensitivity Analysis and Parameter Optimization*, 2007.

II-16 Wolfgang Ehlers & Nils Karajan (Eds.): *Proceedings of the 2nd GAMM Seminar on Continuum Biomechanics*, 2007.

II-17 Tobias Graf: *Multiphasic Flow Processes in Deformable Porous Media under Consideration of Fluid Phase Transitions*, 2008.

II-18 Ayhan Acartürk: *Simulation of Charged Hydrated Porous Materials*, 2009.

II-19 Nils Karajan: *An Extended Biphasic Description of the Inhomogeneous and Anisotropic Intervertebral Disc*, 2009.

II-20 Bernd Markert: *Weak or Strong – On Coupled Problems In Continuum Mechanics*, 2010.

II-21 Wolfgang Ehlers & Bernd Markert (Eds.): *Proceedings of the 3rd GAMM Seminar on Continuum Biomechanics*, 2012.

II-22 Wolfgang Ehlers: *Poröse Medien – ein kontinuumsmechanisches Modell auf der Basis der Mischungstheorie*, 2012.

II-23 Hans-Uwe Rempler: *Damage in multi-phasic Materials Computed with the Extended Finite-Element Method*, 2012.

II-24 Irina Komarova: *Carbon-Dioxide Storage in the Subsurface: A Fully Coupled Analysis of Transport Phenomena and Solid Deformation*, 2012.

II-25 Yousef Heider: *Saturated Porous Media Dynamics with Application to Earthquake Engineering*, 2012.

II-26 Okan Avci: *Coupled Deformation and Flow Processes of Partial Saturated Soil: Experiments, Model Validation and Numerical Investigations*, 2013.

II-27 Arndt Wagner: *Extended Modelling of the Multiphasic Human Brain Tissue with Application to Drug-Infusion Processes*, 2014.

II-28 Joffrey Mabuma: *Multi-Field Modelling and Simulation of the Human Hip Joint*, 2014.